Pyrazine Based Ligands:

Supramolecular Structures

A thesis presented in partial fulfilment of the requirements for the degree of

Master of Science

In

Chemistry

At Massey University, Manawatu, New Zealand.

Marryllyn Emma Donaldson

2021

Abstract

Pyrazine based ligands have been found to facilitate electronic communication between metal centres, within polynucleated structures. The control of spin states can lead to controllable bistable states of metal centres, in multinucleated supramolecular structures, possibly leading to a physical-materials, with binary analogous properties. These areas are especially of interest to many industries due to the rapidly approaching upper limit in conventional magnetic data storage.[1]

The aim of this research is the creation of new pyrazine-based ligands, which can form metal-organic supramolecular complexes, and then investigate the architectures that can be built. The design and synthesis of a new series of ligands based around a central, symmetric, pyrazine-units with functionality on the 2,5- positions was achieved including azide, alkyne and aldehyde groups. These units were than used to synthesise four novel-ligands to contribute to the ever-expanding library of ligands used in supramolecular chemistry.

New pyrazine ligands were reacted with a wide range of 3*d* metal salts, which assembled into eleven 1D polymer chain complexes, and a 3D polymer network. NMR spectroscopy, Mass spectroscopy, ART-IT, X-ray crystallography, and other techniques was utilised to analyse the structural aspects of the ligands and complexes.

Acknowledgements

I would like to acknowledge and thank my supervisor Prof. Paul Plieger for his consistent support and feedback throughout my research project. I would like to thank my co-supervisor Assoc. Prof. Gareth Rowlands.

I would especially like to thank Tyson Dais, and Sydney Woodhouse for their work with the screening and collection of SXRD crystal structures. I'd like to thank them for their support in the lab; and am grateful to the Plieger/Rowlands research groups for their friendship, support and encouragement throughout my Masters' research.

I would like to thank Brodie Matheson for putting up with my mess and the water in the fume hood, and for giving up a day of summer as chief ozonator. I'd also like to thank anyone who took a turn at being an NMR gopher for me, and crossing that magnetic line.

I'd like to thank Sydney Woodhouse and Prof. Paul Plieger for their help in editing and cleaning up my thesis, and all the time put into re-reading it.

I would also like to thank Suraj Patel for his friendship and support during this research, and for the pick ups for weekend work and writing.

Finally, I would like to thank my mum, dad, and brother for their continual love and support throughout this research project, and enjoying lockdown with me.

Table of Contents

Acknowledgements ..... **v**

Table of Contents ..... **vii**

List of Tables ..... **xiii**

Abbreviations ..... **xv**

1.0 Introduction **1**

1.1.0 Metal-Metal Communication **1**
1.1.1 Magnetism **1**
1.1.2 Super-Exchange **2**
1.1.3 Spin-Crossover **3**
1.1.4 Single Molecule Magnets **4**
1.2 Pyrazine **5**
1.3 Metallo-Organic Complexes **6**
1.3.1 Metallo-Organic Supramolecular Structures **6**
1.3.2 Supramolecular Chemistry **8**
1.3.3 Ligand Design **9**
1.3.4 Metal Coordination **11**
1.3.5 Solvent and other Environmental Factors **13**
1.4 Supramolecular Structures **14**
1.4.1 Helicates **14**
1.4.3 Tetrahedral Cages **16**
1.4.4 Cyclohelicate Squares and Triangles **17**
1.4.5 1D Polymer Chains **22**
1.4.5 2D and 3D Metal Organic Frameworks **24**
1.5 Aims of Research **25**
1.6.1 Thesis Outline **26**
1.6.2 Ligand Design and Synthesis Summary **26**
2.0: New Click Chemistry Ligands **27**
2.1 Introduction to Click Ligands: (L3) and (L4) **27**
2.2 Synthesis and Characterisation of L3 ..... **32**
2.3 Comparisons of L3 to Previous Work **37**
2.4 Metal Complexation of L3 ..... **38**
2.4.1 Octahedral Metal Ions **38**
2.4.2 Tetrahedral Copper ions **40**
2.4.3 Silver Complexes **44**
2.6 Synthesis of L4 ..... **52**
2.6.1 Williamson Ether Reaction **52**
2.6.2 Synthesis of D3 ..... **52**
2.6.3 Synthesis of L4 ..... **53**

2.6.4 Conclusions on L4 54

2.7 Future work from di-azide 'click' ligands 55
3.0 Synthesis and Characterisation: L5 and L6 57

3.1 Comparisons to previous works 58
3.2 Isolation of Novel bis-alkyne E1 59
3.3 Synthesis of capping azides. E2 and E3 60
3.5 Future Analogues of L5R 64
4.0 Metal Complexations with L5 and L6 65

4.1 General Complexation Synthesis and Characterisation 65
4.2 ATR-FTIR of Complexes 5A1 – 5F2 67
4.3 Mass Specs of Complexes 5A1 – 5F2 68
4.4 UV-Vis of Complexes 5A1 – 5C6 69
4.5 Conductivity of Complexes 5A1 – 5C6 70
4.6 Seven Coordinate Mn Complexes 5A1 and 5A3 71
4.6.1 X-Ray Structural Determination 5A1 and 5A3 71

4.6.2 1D Single chain polymer of 5A1 {[Mn L5 $(H_2O)_2$]$(ClO_4)_3$}$_\infty$ 73
4.9 Complexations with L6 97

4.9.1 General Complexation Synthesis 97
4.10 Conclusions of L5 and L6 complexes 100
5.0 Imine Ligands 101

5.1 Endo- and Exo- Imine Pyrazine Ligands 101

5.2 Schiff Base Condensation 102
5.3 Pyrazine Centre: 2,5-diformyl pyrazine (B1) 103
5.4 Remaking of ($L1^{endo}$) 105
5.5 Oxidation of ($L1^{endo}$) – (L1b) 106

5.5 Synthesis and Characterisation of L2 109
5.5.2: Attempted Synthesis of L2 Complexes 111

5.5.3 General synthesis of complexes 111

5.6 Imine Ligands: Conclusions 113
6.0 Synthesis Pathway for Exo Imine centre (C6) 114

6.10 Introduction 114
6.11 Full Synthesis Pathway 115
6.2 The 2,5-di(hydroxymethyl) pyrazine Pathway (C1) (C2) (C3) 116
6.3 Chlorination of (C3) to 2,5-di(chloromethyl) pyrazine (C4) 118

6.4 Azide Synthesis of 2,5-di(azidomethyl) pyrazine (D1) 119

6.5 Synthesis of the C5 Intermediate 121
6.5.1 Gabriel Synthesis via (C4) 121

6.5.2 Gabriel Synthesis via (C3) 122

6.6 Ing-Manske Reduction of (C5) to produce the goal amine (C6) 124
7.0 Conclusions 127

8.0 Future Work 129
References ..... Error! Bookmark not defined.

List of Figures

Figure 1: Direct exchange and Super-exchange 2
Figure 2: A linker which held Mn(II) 180 apart, with overlapping orbitals. 2
Figure 3: Schematic representation of classes I to III. 3
Figure 4: Potential curves for the three primary Robin–Day classes 3
Figure 5: Numbered six-membered diazine heterocycles 5
Figure 6: Diagram of various SCC architectures. 6
Figure 7: Diagram of generic ligands leading to helicates and tetrahedrons. 9
Figure 8: aspect ratio of ligands contributes to the self-assembly of coordination cages 10
Figure 9: Metal coordination geometries 12
Figure 10: Interconvertible grid-helicate structures 12
Figure 11: Conversion of complexes between a Grid and Pincer arrangements 13
Figure 12: A Schematic of various helicates 14
Figure 13: A bimetallic triple stranded helicate 16
Figure 14: A schematic showing tetrahedral cage geometries 17
Figure 15: Possible discrete polygon shapes 18
Figure 16: The formation of cyclohelicate squares and triangles 19
Figure 17: A diagram of a cyclohelicate square, $[M_4L_4]$ with **L1b** 19
Figure 18: Cyclohelicate triangle 20
Figure 19: Diagrams of 1D polymer chains 23
Figure 20: MOF ligands 24
Figure 21: Summary of the central ligand units synthesised 26
Figure 22: General structure of ligands made from **D1** using click reactions. 27
Figure 23: The various supramolecular interactions of 1,2,3-triazoles 29
Figure 24: Previous simple CuACC 1,2,3-triazoles 30
Figure 25: The competitive binding between the N2 and N3 nitrogen atoms of triazoles. 32
Figure 26: **L3** assigned with ^{1}HNMR and ^{13}CNMR peaks, (ppm) 34
Figure 27: Crystal structure of the full **L3** molecule 34
Figure 28: The crystal structure of stacks of **L3**. 35
Figure 29: Crystal structure showing the CH-π bonds. 36
Figure 30: The 010 cell face of the **L3** packing. 36
Figure 31: Previous ligands similar to **L3**. 37
Figure 32: Tetrahedral cage example 38
Figure 33: Simple Geometric model of the hypothetical $[L_6M_4]$ tetrahedral, $\mathbf{L3}_6Fe(II)_6$. 39
Figure 34: Geometric model, PM3 in Spartan, of the hypothetical [2x2] square, $\mathbf{L3}_4Cu(I)_4$ 40
Figure 35: The precipitate resulting from reaction **L3** and $[Cu(MeCN)_4]PF_6$. 42
Figure 36: Photo of the gel result from the cryo-diffusion of **L3** and $[Cu(MeCN)_4]PF_6$ salt 43
Figure 37: Ligands and Ag(I) complexes previously synthesised 44
Figure 38: A single chain section of the crystal structure of the $\{[Ag_2(\mathbf{L3})](NO_3)_2\}_\infty$ complex 45
Figure 39: **L3** in the **L3Ag,** coordinated to Ag(I) ions and uncoordinated **L3.** 47
Figure 40: The crystal structure of three 1D polymer chains, with the Tz-Ph rings. 48
Figure 41: The crystal structure of three 2D sheets. 48
Figure 42: sphere packing of the 3D stacking of the 2D sheets 49
Figure 43: The offset stacking of 2D sheets of polymers resulted in a repeating pattern 50
Figure 44: **L4** 52

Figure 45: Possible alkynes that could be clicked to **D1** 55
Figure 46: Chelation sites built from two N-heterocycles. 57
Figure 47: Examples of previously synthesised molecules from literature, with a P_-O-Tz..... 58
Figure 48: Future molecules to click to **E1** (Central).. 64
Figure 49: Crystal structure of the asymmetric unit of {[Mn **L5** $(H_2O)_2$]$(ClO_4)_3$}$_\infty$ **5A1**..... 72
Figure 50: Crystal structure of the monomer [Mn_2(**L5**)]$(NO_3)_2(H_2O)_4$]$(NO_3)_2$, **5A3**. 72
Figure 51: Alternation between linear and contorted ligands 73
Figure 52: The mercury crystal structure of **5A1**: mono-capped trigonal prism geometry. 75
Figure 53: The crystal structures of the complexes **5A1** and **5C1**. 76
Figure 54: The crystal structure of **5A1** 77
Figure 55: The mercury crystal structure of **5A3** 79
Figure 56: The crystal structure of the hydrogen bonding network. 80
Figure 57: The crystal structure of the hydrogen bonding network between the **5A3** 82
Figure 58: The crystal structure of the asymmetric unit of **5B1** {[Co(**L5**)]$(ClO_4)_3$}$_\infty$ 85
Figure 59: The crystal structure of the asymmetric unit of **5C1** {[Fe(**L5**)]$(ClO_4)_3$}$_\infty$..... 85
Figure 60: The crystal structure of two asymmetric unit of **5C1**-hydrogen bonding..... 86
Figure 61: The crystal structure of two asymmetric units of **5C2** {[Fe(**L5**)]$(BF_4)_2$}$_\infty$..... 86
Figure 62: The crystal structure of the asymmetric unit of **5B2** {[Co(**L5**)]$(BF_4)_2$}$_\infty$ 87
Figure 63: The crystal structure of the asymmetric unit of **5C2** {[Fe(**L5**)]$(BF_4)_2$}$_\infty$ 87
Figure 64: The crystal structure of the asymmetric unit of **5D1** {[Ni(**L5**)]$(ClO_4)_3$}$_\infty$..... 88
Figure 65: The crystal structure of the asymmetric unit of **5E2** {[Zn(**L5**)]$(BF_4)_2$}$_\infty$ 88
Figure 66: The crystal structure of the asymmetric unit of **5F1** {[Cu_2(**L5**)]$(ClO_4)_3$}$_\infty$ 89
Figure 67: The crystal structure of the asymmetric unit of **5F2** {[Cu(**L5**)]$(BF_4)_2$}$_\infty$ 89
Figure 68: Crystal structures of **L5** complexes. **5F1** and **5F2**. 93
Figure 69: Cross-sections of the 3D packing of the **L5** complexes, of the 001 cell view. 94
Figure 70: PM3 semiempirical Spartan examples of positive and negative electronegativity ... 95
Figure 71: The crystal structure of **6F1** 98
Figure 72: The crystal structures of **6F1** cross-section of the 3D structure. 99
Figure 73: The general chemical structures of Endo-Imine and Exo-imine pyrazine ligands .. 101
Figure 74: **L1b** Ligand isolated from crystal growth. 106
Figure 75: The crystal structure of the **L1b** ligand, with the asymmetric unit labelled. 107
Figure 76: The crystal structure of **L1b**. Hydrogen bonds..... 108
Figure 77 The assignments of the ^{1}H NMR and ^{1}C NMR peaks (ppm) **L2.**..... 110
Figure 78: Characterisation of **C5** and assignment of ^{1}H NMR, ^{13}C NMR 122
Figure 79: **C6** (central) and the potential future primary carbonyls 125
Figure 80: Successfully synthesised ligands **L2**, **L3**, **L5** & **L6**. 127
Figure 81: Novel molecules, **C5** and **E1** 127

Schemes

Scheme 1: The variety of 5-membered N-heterocycles available. 28
Scheme 2: Click mechanism 31
Scheme 3: Simplified Glaser coupling reaction scheme to form 1,4-diphenylbuta-1,3-diyne. 31
Scheme 4: Reaction scheme for the synthesis of **L3** 33
Scheme 5: **D3**; Williamson Ether Synthesis: NaH 0 ºC, DMF, RT, 16h 52
Scheme 6: Click synthesis of **L4**, from **D1** and **D3**: DCM, tBuOH, $Cu(OAc)_2.2H_2O$, RT, 18h. 53
Scheme 7: **E1** from the Williamson Ether Reaction of **C3** and **D5:** 57
Scheme 8: Preparation of Azide click units. a) 1-azido butane (**E2**) NaN_3, (1:3) H_2O:DMSO, 50 ºC, 4h. b) 3-azido-1-propene (**E3**): NaN_3, DMF, RT 48h. 60
Scheme 9: Synthesis of Pz-O-Tz bis-tridentate ligands:. 61
Scheme 10: Mechanism for Schiff Base Condensation, based of Hossain et al.[119] 102
Scheme 11: The reaction scheme for the synthesis of, **A2** and **B1**. 103
Scheme 12: Ozonolysis oxidation reaction mechanism of **A2** to **B1** 104
Scheme 13: Reaction Scheme for the synthesis of **L1.** 105
Scheme 14: The Schiff base condensation of **B1** and **B3** to synthesise **L2b**. 109
Scheme 15: The overall route in the pathway to **C6**.. 115
Scheme 16: Proposed Mechanism of an Acetate addition to a Pyrazine N-oxide 117
Scheme 17: The chlorination mechanism of **C4**. 118
Scheme 18: Schematic of **D1** synthesis. 119
Scheme 19: Synthesis of **C5**. Gabriel Synthesis - Mitsunobu reaction 121
Scheme 20: Mitsunobu Mechanism of **C3**, DIAD and Phth, to form **C5**. 123
Scheme 21: The Ing-Manske Reduction Mechanism, adapted from Curley et al.[137] 124

List of Tables

Table 1: ^{1}H NMR and ^{13}C NMR characterisation of **L3**. 34
Table 2: The intermolecular bond distances and angles in the arrangement of **L3**. 35
Table 3: Solubility of **L3** in solvents at RT and with heat. 38
Table 4: Complexations of **L3** with octahedral 3d ions. 39
Table 5: Attempts at complexation of **L3** and **L3Cu** 41
Table 6: Reactions of **L3** with in $AgNO_3$ 1:1 ratios, stirred at heat under argon. 44
Table 7: The selected bond lengths and angles related to the coordination of Ag(I) cations. 46
Table 8: Hydrogen Bonding within the **L3Ag** HOF network. 47
Table 9: The intermolecular bonds between the 2D sheet layers of the complex. 49
Table 10: Assignment of **E1** ^{1}H and ^{13}C NMR in DMSO (ppm). 59
*Table 11: Assignment of **L5** ^{1}H and ^{13}C NMR in DMSO (ppm).* 62
Table 12: Assignment of **L6** ^{1}H and ^{13}C NMR in DMSO (ppm). 63
Table 13: (m/z) data for **L5** and **L6** 63
Table 14: Selected **L5** and **L6** IR data (cm^{-1}) 63
Table 15: Complexation Codes of 3d transition metal salts, with **L5**. **Bolded Green**, codes indicate successful isolation of crystallised complex. Italicise and underlining indicates the crystal isolated was the metal salt. 66
Table 16: Complexation codes of 4f transition metal salts, with **L5**. **Bolded** codes indicate successful isolation of crystallised complex. Italicise and underlining indicates the crystal isolated was the metal salt. 66
Table 17: Selected average IR peaks present in the **L5** complexes. 67
Table 18: The Mass determined in SCXRD and the MS values of the **L5** complexes. (g/mol) 68
Table 19: UV-Vis peak wavelengths (λ) and Absorbances (A), of **L5** complexes. 69
Table 20: The conductivity results for the **L5** Complexes. 70
Table 21: The bond distances from the atoms coordinated to the central Mn(II) in **5A1** (Å). 74
Table 22: Angles around the Mn(II) centre in **5A1** (º). 74
Table 23: Hydrogen Bond data (Å), for **5A1** 77
Table 24: The Angles around the Mn(II) centre in **5A3** (º) 79
Table 25: The Distances from the Mn(II) centre to the chelated atoms in **5A3** (Å) and the comparative bond lengths from the Mn(II) centre to the chelated atoms in **5A1** (Å) 80
Table 26: Hydrogen Bond lengths (Å) and Angles (º) of **5A3** complex. 80
Table 27: The colours of the single block shaped crystals of **L5** complexes. 83
Table 28: The Metal-atom bond lengths (Å) in the **5B1-5F1** perchlorate complexes. 90
Table 29: The Metal-atom bond lengths (Å) in the **5B2-5F2** fluoroborate complexes. 90
Table 30: Bond angles from metal centres in complexes **5B1-5F1,** (º) and distortions from octahedral. 91
Table 31: Bond angles from metal centres in complexes **5B2-5F2,** (º) and distortions from octahedral 92
Table 32: Results of **L5** complexation reactions with additional counter ions and metal salts. 96
Table 33: The 3d metal salts reacted with **L6**, and their complex codes. **Bold** metal salts have resulted in successful crystal structures. 97
Table 34: Selected bond lengths (Å) and angles (º) of **6F1**. 98

Table 35: Complexations of **L1** and various metal salts, with the respective solvent system used, the colour changes observed and the complexation code 106
Table 36: Selected intermolecular bond lengths (Å)and angles (º) for the **L1b** ligand. 108
Table 37: The ^{1}H and ^{13}C NMR Assignment of **L2**. 110
Table 38: **L2** Complexation Results with various metal salts, the resulting colour change, ppt and ms. 111
Table 39: Solubility investigation of **L2** complexes. 112
Table 40: Recrystallisation attempts with **L2** complexes 112
Table 41: Assignments of **C5**, ^{1}H NMR, ^{13}C NMR 122

Abbreviations

3*d*	first row transition metal
4*f*	lanthanide metal ions
Ac_2O	acetic anhydride
ATR-IR	attenuated total reflectance – infrared spectroscopy
BF_4^-	tetrafluoroborate Anion
Bnz	benzaldehyde
BzO_2	benzoyl peroxide
$C_6H_7NaO_7$	sodium citrate
CCl_4	tetrachloromethane
$CDCl_3$	deuterated chloroform
ClO_4^-	perchlorate anion
CuAAC	Cu(I)-catalyzed 1,4-dipolar azide-alkyne cycloaddition
DCE	1,2-dichloroethane
DCM	aichloromethane
DIAD	diisopropyl azodicarboxylate
DMSO	dimethyl sulfoxide
DMF	dimethyl formaldehyde
Et_2O	diethyl ether
EtOAc	ethyl acetate
Et_3N	triethylamine
HMTA	hexamethyl tetra amine
IPA	isopropyl alcohol
m-CPBA	*m*-chloroperoxybenzoic acid
MeCN	acetonitrile
Me_2CO	acetone
MeOH	methanol
$MgSO_4$	magnesium sulfate
NaOMe	sodium methoxide
$Na_2S_2O_5$	sodium metabisulfite

NCS	N-chlorosuccinimide
NEt_3	triethyl amine
NO_3^-	nitrate anion
OAc^-	acetate anion
O_3	ozone
Phth	phthalimide
$POCl_3$	phosphoryl chloride
Ppt	precipitate
Pz	pyrazine
Pyr	pyridine
RF	retention factor
SCC	supramolecular coordination complex
SCXRD	single crystal X-ray diffraction
$SOCl_2$	thionyl chloride
^{t}Bu	tert-butyl group
TBAHS	tetrabutylammonium hydrogensulfate
THF	tetrahydrofuran
TLC	thin layer chromatography
Tz	triazole
XRD	X-ray diffraction

Metal Salts

$AgNO_3$	silver nitrate
AgCl	silver chloride
AgOTf	silver trifluoromethanesulfonate
$AgPF_6$	silver hexafluorophosphate
$Co(CH_3COO)_2 \cdot 4H_2O$	cobalt acetate tetrahydrate
$Co(BF_4)_2 \cdot 6H_2O$	cobalt tetrafluoroborate hexahydrate
$Co(ClO_4)_2 \cdot 6H_2O$	cobalt perchlorate hexahydrate
$Cu(ClO_4)_2 \cdot 6H_2O$	copper perchlorate hexahydrate
$Cu(BF_4)_2 \cdot 6H_2O$	copper tetrafluoroborate hydrate
$[Cu(MeCN)_4]PF_6$	tetrakis(acetonitrile)copper(I) hexafluorophosphate
$Fe(ClO_4)_2 \cdot 6H_2O$	iron perchlorate hexahydrate
$Fe(BF_4)_2 \cdot 6H_2O$	iron tetrafluoroborate hexhydrate
$Ni(ClO_4)_2 \cdot 6H_2O$	nickle perchlorate hexahydrate
$Ni(BF_4)_2 \cdot 6H_2O$	nickle tetrafluoroborate hexhydrate
$Mn(ClO_4)_2 \cdot 6H_2O$	manganese perchlorate hexahydrate
$Mn(NO_3)_2 \cdot 4H_2O$	manganese nitrate tetrahydrate
$Pb(ClO_4)_2 \cdot H_2O$	lead perchlorate hydrate
$Zn(ClO_4)_2 \cdot 6H_2O$	zinc perchlorate hexahydrate
$Zn(BF_4)_2 \cdot 6H_2O$	zinc tetrafluoroborate hexhydrate

1.0 Introduction

1.1.0 Metal-Metal Communication

One of the hopes of this research is that the ligands designed and synthesised will be able to facilitate metal-metal electronic communication.

The development of electronic communication between metal centres by spin-crossover and super-exchange leads to interesting sensing, photophysical, and magnetic behaviours.[2] There is interest in the ability to create materials where magnetic and electronic properties can be manipulated, such as single molecule or chain magnets, magnets that can superconduct at high critical Curie (TC) or Neel (T_N) temperatures and stimulated magnets, for application in high-density information storage, spintronics and quantum computing.[3]

Metal–metal communication is typically assessed, by measuring the difference between the redox potentials shown by the metals comprised in the polymetallic compound. [4]

The control of spin states can lead to controllable bistable states of metal centres, possibly leading to a physical-materials, with binary analogous properties. These areas are especially of interest to many industries due to the rapidly approaching upper limit in conventional magnetic data storage.[1]

1.1.1 Magnetism

Magnetism is described by the coupling of individual magnetic moments, generated from electron spin, through an exchange interaction. Randomly orientated electron spins in a material will align with an applied magnetic field, in an attractive or repulsive sum response, creating magnetisation (M) in the material.[5] Attractive interactions arise from paramagnetic species, containing unpaired electrons, while electrons repel against the applied field in diamagnetic materials, with no unpaired electrons. This order will dissipate to chaos over time when the material is removed from the applied field.

1.1.2 Super-Exchange

One of the bases for electronic communication between metal centres is super-exchange. Paramagnetic metal ions can exhibit intramolecular magnetic coupling, either directly, where there is direct overlap of partially occupied adjacent metal orbitals, or through an anionic ligand bridge, which allows an exchange between metal centres that are held at a greater distance, and would not otherwise have any orbital overlaps (Figure 1). Unpaired electrons on a metal centre interact with a fully occupied orbital on a bridging ligand with an overlapping orbital. Partial electron density, of opposite spin according to Pauli Principle, is then donated to the metal centres.[6]

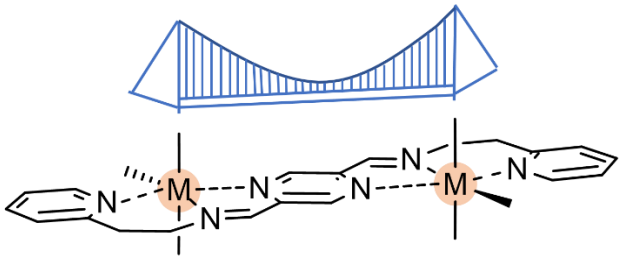

Figure 1: Direct exchange is observed in spin-polarised metals in close proximity. Super-exchange is mediated by a diamagnetic bridging motif, provided as the ligand.

This forms a magnetic ordering of metal centres, that have successive spin polarisations that align parallel (ferromagnetism) or antiparallel (antiferromagnetism), through either σ- or π-type ligand orbitals.[7] For example, in an Mn-Link-Mn bridge, the 3*d* Mn(II) centres are, arranged at 180º, the Mn e_g orbitals overlap with the oxides 2p orbitals, allowing for long range superexchange between the two Mn(II), shown in Figure 2.[8]

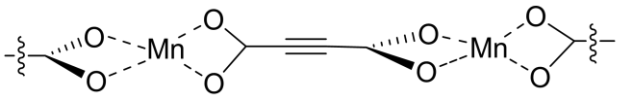

Figure 2: A linker by Tiana *et al.* which held Mn(II) 180 apart, with overlapping orbitals.

The strength of the superexchange between metal centres depends on; the metal and ligand orbital overlap; the electronic transfer properties; and the length of the bridging ligand pathway. The degree of the coupling can be described with the Robin-Day classification, Class I having no communication, Class II partial communication and Class III full communication (Figure 2).[9] These classifications describe the strength of influence on a whole system, when an external stimulus affects one metal centre.

Class I molecular systems act as completely decoupled redox states for each metal centre, while moderate electronic coupling between the centres in Class II creates a double-well ground state and the strong coupling for Class III creates a single ground state for the redox transitions for the whole system (Figure 3).[10]

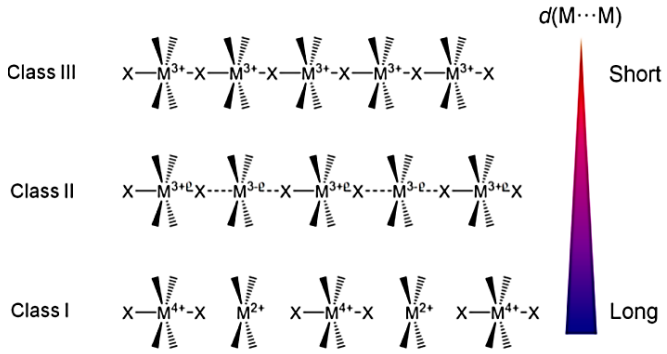

Figure 3: Schematic representation of classes I to III. Figure used with permission from Kumagai *et al.*[9] Copywrite 2018 American Chemical Society.

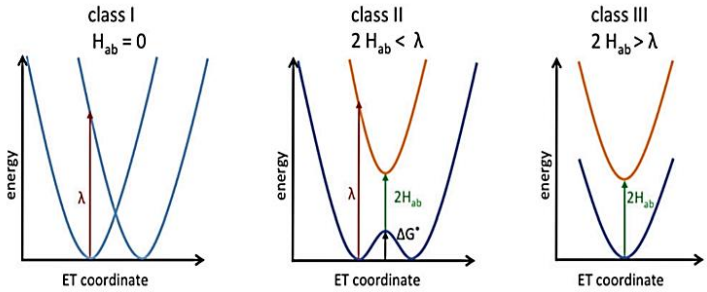

Figure 4: Potential curves for the three primary Robin–Day classes: class I (left), class II (middle) and class III (right). Figure used with permission from Parthey *et al.*[10]

1.1.3 Spin-Crossover

The spin-crossover (SCO) effect is a reversible crossover and switching of electrons in inorganic materials. SCO is observed for metal ions with $3d^4$–$3d^7$ electronic configurations, where there are two ways for the electrons to populate the t_2g and eg orbitals.[11] The distribution of octahedral *d* electron spin states between t_2g and *eg* orbitals, and the magnetic moment of a central d-block metal ion can be switched between two well-defined diamagnetic low-spin (LS) and paramagnetic high-spin (HS) states, in association with diamagnetic-to-paramagnetic switching.[12] This is controlled by external stimuli such as a change in temperature, pressure or by irradiation with light. [11b, 13]

The transition between the two states can result in measurable changes; in magnetism, dielectric constant, bond vibrations and lengths, and often also in the colour of the

complex, which can be monitored by a superconducting quantum interference device (SQUID), IR, Raman and UV spectroscopy.[11b, 12b]

With thoughtful ligand selection, successful SCO can also be monitored by luminescence, with the energy transfer from an excited energy donor to the LS state, causing a switch to HS and quenching the donor emission, indicating successful SCO.[13b]

Future data storage, processing technology and molecular electronics require a bistability of two distinct states, analogous to binary, in the aim of improving density storage compared to contemporary devices.[1, 14] Polynuclear SCO complexes, especially as grids, with interchangeable fixed states and magnetic multistability, have potential in this area.[12a] This has led to interest in designing complexes and arrays, where the geometric and electronic changes of individual SCO events can be propagated between metal ions and exchange pathways, altering the electronic states of metal centres, creating an overall cooperative SCO.[12b, 13b]

1.1.4 Single Molecule Magnets

An emerging range of single molecule magnets (SMMs), have been made with polynuclear 3*d* and/or 4*f* metal complexes. The slow relaxation of magnetisation of these complexes, allow them to act with macro-magnetic properties, creating unique bulk magnetic and quantum regime qualities.

The overall magnetic coupling, within these systems, is controlled by an appropriate choice of bridging groups, and paramagnetic metal ions, with consideration to their redox properties.[15] Diamagnetic metal ions can result luminescent properties, while paramagnetic metal ions can result in electron transfer in donor-acceptor systems.[16] Examples of [2 × 2] grids with these properties can be found throughout the literature, typically with Mn(II), Ni(II) and Co(II). [14b]

It is the careful design of these single molecules, that produce behaviour analogous to bulk counterparts; with interesting magnetic properties that have potential application in nanoelectronics and spintronics.[13b, 17]

1.2 Pyrazine

Pyrazine is a six-membered nitrogen heterocycle, containing a 1,4-diazine in a carbon ring. Others in this group of six-membered diazine heterocycles are pyrimidine (1,3-diazine) and pyridazine (1,2-diazine), (Figure 5).

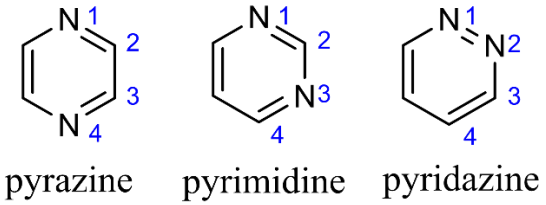

Figure 5: Numbered six-membered diazine heterocycles: pyrazine, pyrimidine and pyridazine.

Pyrazine has previously been used as a bridging ligand in coordination chemistry.[14b, 18] and incorporated as the aromatic centre of different symmetric chelating ligands. [15, 19] Pyrazine is a good π-acceptor and its electronegativity can support spin-spin and electronic interactions between metal centres, facilitating electronic communication and antiferromagnetic coupling.[20] For these reasons *N*-donor heterocycles, like pyrazine, have been used to create magnetic frameworks and grids. [8]

1.3 Metallo-Organic Complexes

1.3.1 Metallo-Organic Supramolecular Structures

The use of metallosupramolecular self-assembly is of interest to bypass tedious 'top-down' nanofabrication and nanomanipulation procedures, saving time and increasing efficiency.[1] As supramolecular chemistry relies on self-assembly, a large focus is put on the suitable design of ligands, and how they combine with appropriate metal-ions so that polynuclear coordination arrays are generated in a controlled fashion.[21]

Combinations of organic ligands and metal centers can be organised in a myriad of different ways to produce a wide variety of polynuclear, supramolecular coordination complexes (SCCs). [22] These different structures retain the intrinsic properties of their metal components such as the, magnetic,[23] optical,[19] electronic, redox,[24] and luminescence[25] properties with future potential for crystal engineering and design of molecular based nano-scale devices.[14b, 26]

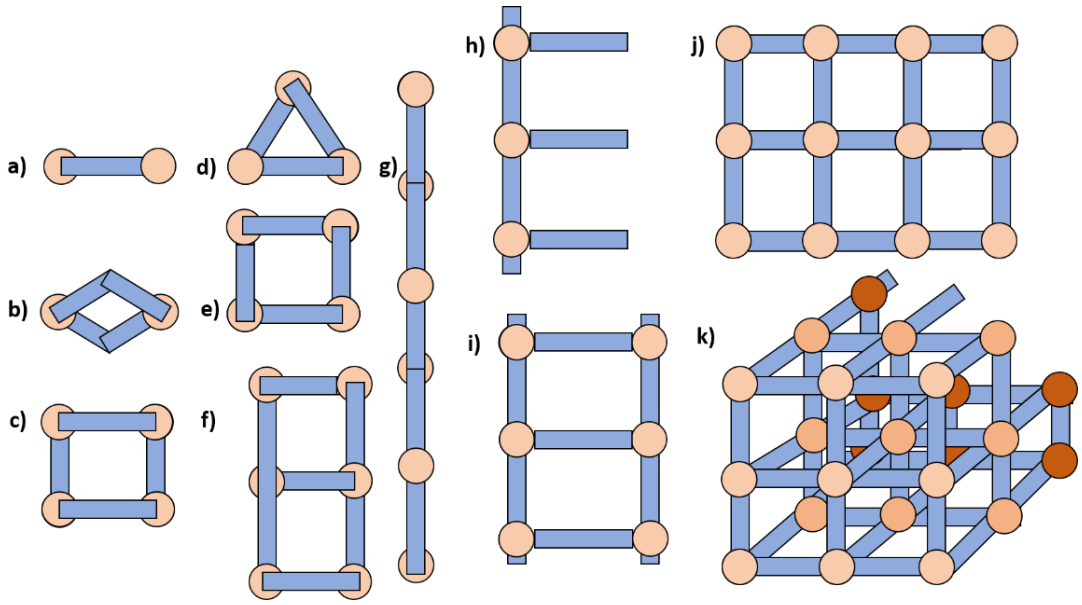

Figure 6: Diagram of various SCC architectures, with metal circles and ligand rectangles.
a) di-nuclear monomer b) di-nuclear helicate c) square [2 x2] grid d) cyclohelicate triangle
e) cyclic [2 x 2] grid f) [2 x 3] grid g) 1D polymer chain h) [3]-rack i) [2.3]-ladder j) 2D grid
k) 3D MOF (differing shades of metals indicate depth in grid)

SCC architectures spontaneously assemble, forming a wide range of architectures of different nuclearity, such as; racks, [27] ladders, [19] grids,[21, 28] polygons, 1D polymers and 3D Metal-organic frameworks (MOFs). Well-ordered [n × n] grid-like arrays of metal ions, such as polynuclear squares, and helicates are receiving particular attention (Figure 6).[23, 29] Numerous discrete SCCs of different shapes and sizes have been synthesised, with different ligands having been contributed to this growing library of structures.

Monolayer grid assemblies, 2D [n × n] or larger interconnected grids, could have the potential for intramolecular ferromagnetic exchange. There is also the potential for the slow relaxation of magnetic properties, which could even be activated selectively, providing application in 'qubit' building blocks for quantum computing, spintronics, and high-density information storage devices.[14b] These areas are especially of interest to many industries due to the rapidly approaching upper limit in conventional magnetic data storage.

While much is known about their design principles, and a high degree of synthetic control is now achievable, ample information and application potential is still to be uncovered.

1.3.2 Supramolecular Chemistry

Self-assembly is the fundamental technique employed by nature to construct the elegant and intricate molecular machinery. In recent years, self-assembly has been harnessed to automatically assembled materials, to create new molecular materials. [30]

Inorganic supramolecular chemistry is the term that describes self-assembly of SCCs, from subcomponents of rationally-designed ligands and appropriate metal ions.[21] As a consequence the electronic, magnetic and photophysical properties of these building block components is transferred to the SCC. This metal-directed self-assembly is then used to create higher-order architectures, with an increased stability compared to structures held with hydrogen bonding.[31] The favourability of the formation of the final overall structure is determined by a few key factors; angle of chelation, hard-soft-acid-base considerations, solvent, and other environmental factors.

The enthalpic and entropic balances needs to be considered in the formation of SCCs.[32] Enthalpically, the lowest energy structure possible is assembled, initially favouring oligomers and polymers. However, this would not have the greatest number of metal-ligand interactions possible. The reversibility of the intermolecular bonds and lability of the metal bonds, allow for greater specificity, leading to the formation of the entropically favoured, small discrete architectures. These will create a greater number of individual structures compared to oligomers or networks. [16, 32] The structures will balance between filling all possible metal-ion and ligand coordination sites, complying with the principle of "maximum coordination site occupation"[21] while still being entropically favourable. These energetic parameters can also be altered by environmental factors, such as solvent, counterions, or other species present.[17]

1.3.3 Ligand Design

The position of chelating coordination sites on the ligand, and their functional groups control the final arrangements of complex architectures.[31a, 32] The positioning of the chelation sites also produce consistent binding angles, that have been well documented, creating a predictable molecular library, coined by Stang *et al.* [33]

The directional-bonding approach of SCC self-assembly is provided by the well-defined shapes, sizes, rigidity and geometries of the organic components under the control of the researcher. The shape of the building block components is dominated by the angle formed between the two open coordination sites; the turning angle.

The turning angle determines the final SCCs as seen in, (Figure 6), the ligand with a 180° turning angle arranges into a tetrahedral [M_4L_4], while the ligand with coordination sites held at a 120° angle, will form a dinuclear triple stranded helicate. (Figure 7.)

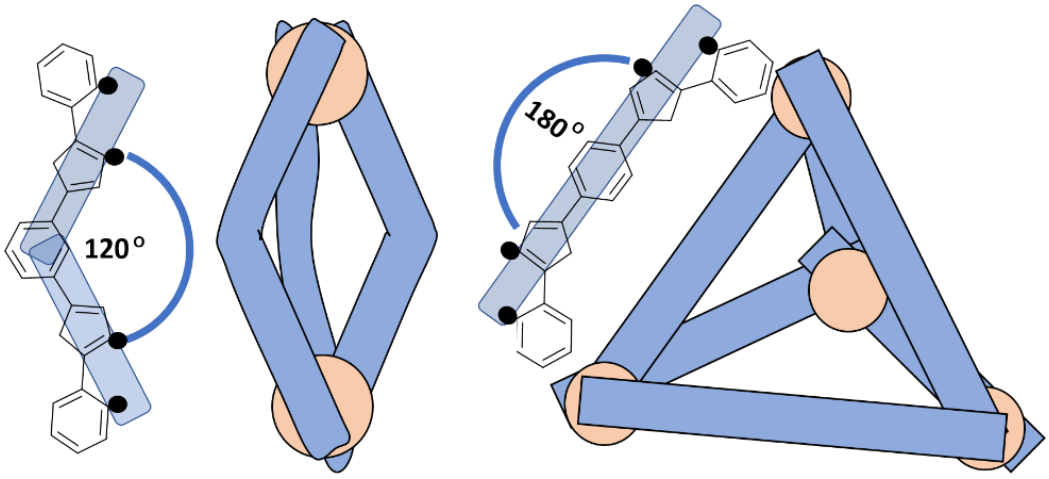

Figure 7: Diagram of generic ligands, with coordination sites positioned away from each other at angles of, 120º (left) and 180º (right), leading to preferred structures of helicates and tetrahedrons respectively.

An investigation by Jansze *et al.* revealed how the relative aspect ratios (length and thickness) of linkers between matching chelation groups affected the self-assembly of coordination cages.[34] For one ligand set, both long-thick ligands and short thin ligands, with similar size ratios, formed tetrahedral cages, whereas a short-thick ligand was found to form a denser cubic cage arrangement (Figure 8).

Ligands that are too long and flexible, based on enthalpic arguments, form single nucleated structures instead of multi-nucleated structures. Generally, the greater the rigidity of the ligand the more it will coordinate to separate metal centres.[1] Incorporating aromatic systems into a ligand designs has the benefit of increased rigidity, creating kinetically labile intermediates and thermodynamically stable end products. Aromatic π- π interactions also aid in forming stable, communicative systems.[1, 16] Ultimately, all aspects of the overall structure of the ligand contribute to the final arrangement of the SCCs formed.

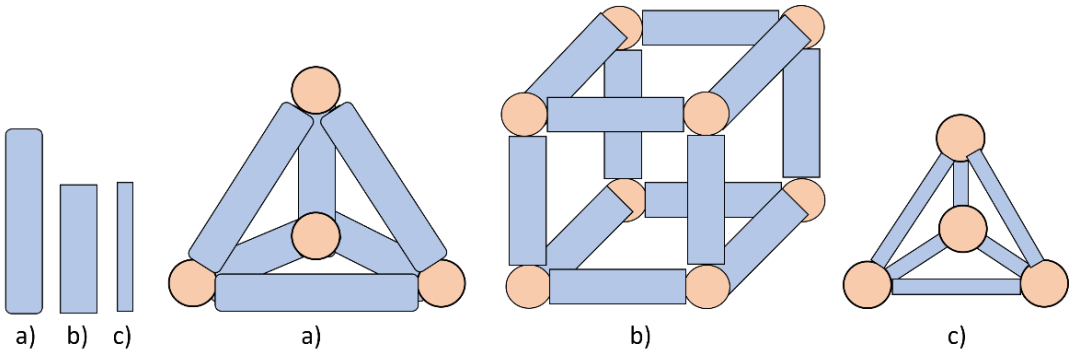

Figure 8: A diagram summarising some of the work by Jansze *et al.* on how the aspect ratio of ligands contributes to the self-assembly of coordination cages. a) long-thick = tetrahedral cage b) short-thick = cubic cage c) short-thin = tetrahedral cage. [34]

1.3.4 Metal Coordination

The successful directing, formation and facilitating self-correction of a particular SCC depend heavily on the ligand design, choice of metal ion and the metal–ligand.[35] If attraction between the ligand coordination site and the metal ions is too weak, bonds and corresponding structures will not form. If the bonds are too strong, ligands will not be able to self-correct into discrete shapes, but create continuous chains of ligands and metal ions, into large entanglements.

Metal ions have predictable geometric coordination preferences, such as, octahedral, square planar or tetrahedral (Figure 9). [36] These differences control not only the overall architecture of a complex, but also subtle changes within one type of structure. The structural properties of the metal ions and ligands provide predictability in structures. Transition metal-ions most commonly have four or six coordination, at fixed angles, square planar (90º), tetrahedral (109.5º), octahedral (180º and 90º), etc.[14b, 33] The angles between the coordination sites in the ligands and the 3*d* coordination geometry, control the angles of approach between these building blocks and so control internal geometry.[33] This coordination geometry of the metal ions and ligand field theory, controls which of the ligands functional groups, and the metal ions are more likely to coordinate. Hence, structural organisation depends on designing ligands with suitable types, numbers and geometry of coordination sites.[1, 14b]

Sumby and Steel[37] investigated the effect of metal ion selection in the construction of helicates. The changing coordination geometry of metal ions resulted in a difference in torsion of the ligands, and therefore also changed the distance between the metal ions. With octahedral nickel, the ligand adopts a large twist and brought the metal ions closer, while the distorted square pyramidal shape of copper atoms, meant that the ligand did not twist as much, and so extended further in length, increasing the metal-metal distance.

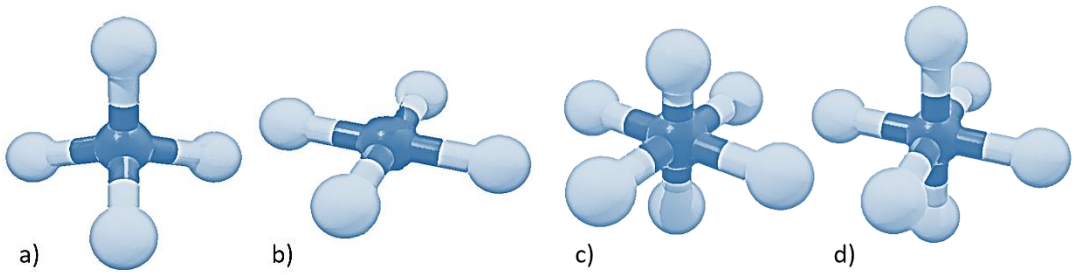

Figure 9: Metal coordination geometries: a) tetrahedral, b) square planar, c) octahedral, d) distorted square pyramidal.

The substituents of the ligand will then also determine fundamental properties of the structures. Tailoring the nature of the bridging ligands controls chemical and physical properties,[2, 21] required by the ligand to support electronic communication between the metal centres. Shorter ligands, with a close proximity between the metals, are also predisposed to better handle magnetic exchange coupling between paramagnetic metal ions.[14b] Coordinating ligands are most commonly based on nitrogen, oxygen or sulphur donor ligands.[1]

As an example, the ligand developed by Stadler *et al.* was able to convert between a binuclear double helicate, with tetrahedral Cu(I) and a tetranuclear grid with octahedral Cu(II).[29] (Figure 10.) The forced change in the geometry in the metal centre through the oxidation and reduction of the Cu clearly shows the importance of the metal geometry in the overall arrangement of SCCs.

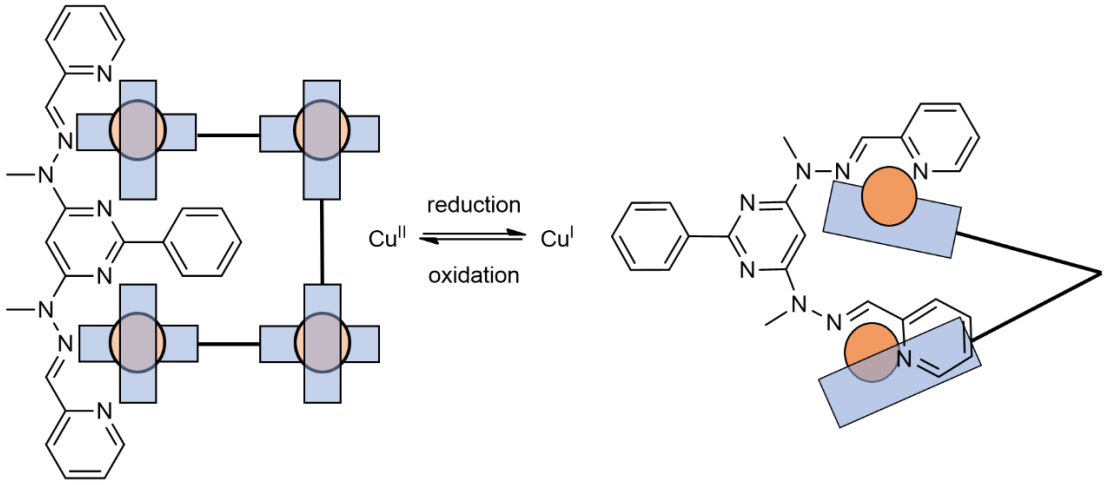

Figure 10: A summary diagram of the work by Stadler *et al.* on interconvertible grid-helicate structures due to the oxidation/reduction of Cu (pink circles).[29] The pink circles indicate Cu(II) ions, and the brown circles indicate the Cu(I) ions.

1.3.5 Solvent and other Environmental Factors

External factors can also affect the final SCC arrangement, for instance, by contributing to the entropy-enthalpy balance. As mentioned before, ligands will occupy as many coordination sites as possible, but there is a balance between filling all coordination sites and forming the largest number of molecules, entropically. Altering a coordination environment with counter ions or solvents can alter this balance.

Ramirez *et al.*[38] reported a reversible structural system that converted between an enthalpically favourable Co(II) [2x2] square grid in nitromethane and a entropically favourable mononuclear pincer-like Co(II) complex, when an excess of acetonitrile was introduced into the environment (Figure 11).

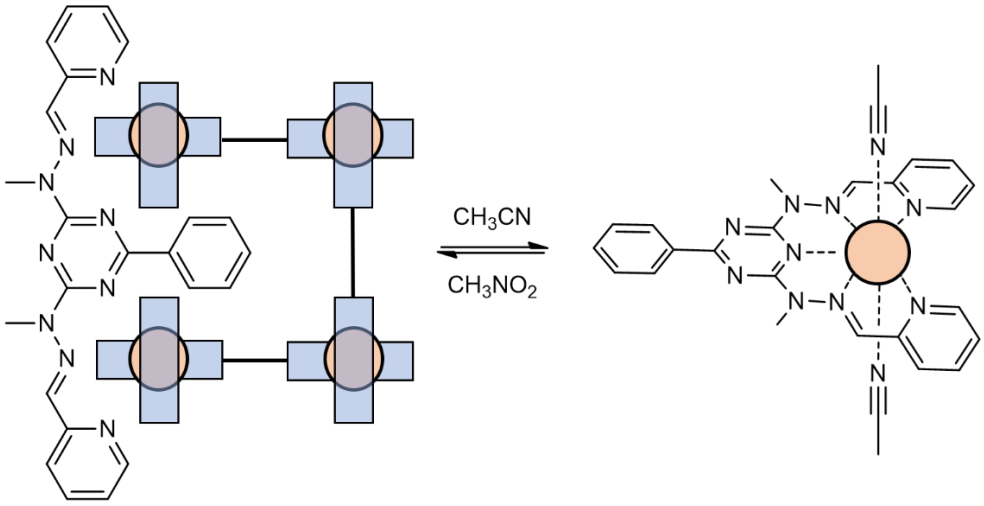

Figure 11: A diagram summarising the conversion of complexes between a Grid and Pincer arrangements due to solvent choice, image adapted from, Ramirez, *et al. [46]* [38] The pink circles indicate Co(II) ions.

The nature of the solvents determined which structure was thermodynamically favourable in each situation, modulated by external/medium effects, effector-induced facilitation of interconversion; and dual ligand structural plasticity. [38]

A ligand system produced by Schweiger *et al.* formed a crystallised equilibrium of 54:46 square:triangular structures in nitromethane. This equilibrium could be controlled with anions, as the introduction of small triflates or large cobalticarboranes, forced a selective crystallisation and allow for a higher degree of control over the final reaction outcome.[39] The counter ion size can alter which shape is preferential in the packing process, meaning that anions have a templating effect.

1.4 Supramolecular Structures

The previously described contributing factors on ligand design and metal choice, lead to the assembly of various discrete structures, as well as larger 2D and 3D structures. Some of the possible arrangements, and previous examples of them are included in the following sections.

1.4.1 Helicates

Aside from simple one-ligand, mono-metallic [M_1L_1] structures, helicates are the simplest discrete SCCs. The term helicate was introduced by Lehn and co-workers in 1987 for the description of these discrete, polymetallic mono-directional, helical complexes, of one or more covalent ligand strands wrapped about and coordinated to a series of metal ions, with a defined helical axis.[40]

The formation of helicates is controlled by the metal ion coordination and other factors, such as hydrogen bonding, entropy, etc.[30] If the 'spacer' section, between coordination sections, of the ligands is too long and flexible, a single nucleated structure would enthalpically form, with both chelation sites attaching to a singular metal centre, instead of forming a multi-nucleated structure. The greater the rigidity of the ligand the more it will coordinate to separate metal centres.[1]

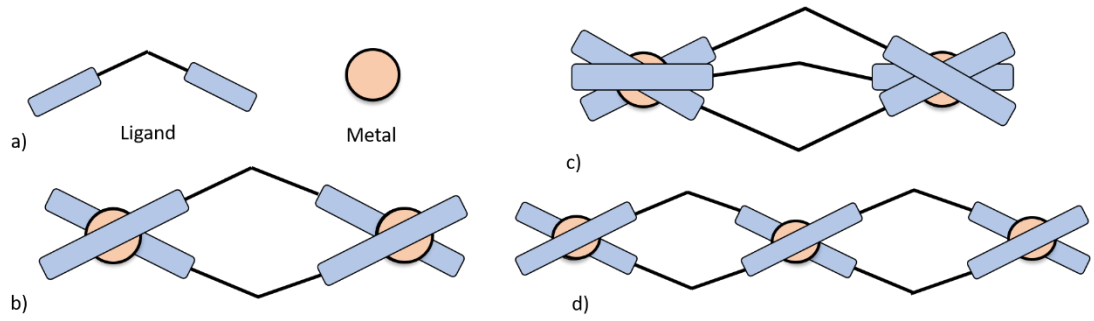

Figure 12: A Schematic of various helicates a) The linear structure represents the organic ligand and the circle represent the metal centres, b) [M_2L_2] bimetallic double stranded helicate, c) [M_2L_3] bimetallic triple stranded helicate, and d) [M_3L_2] trimetallic double stranded helicate

Different types of helicates of different metal/ligand proportions include, triple-helicates, which can be formed by taking a suitable (oligo)bidentate ligand and coordinating to metal ions that prefer an octahedral coordination geometry, [40c] first structurally characterised triple-stranded helicate was obtained in 1991 by Williams *et al.*[41] Bidentate chelating ligands introduced to tetrahedrally or octahedrally

coordinated metal ions lead to double- or triple-stranded helicates. Tridentate ligands can form double-stranded complexes with octahedral or triple-stranded systems with a tricapped trigonal prismatic geometry at the metal.[42] (Figure 12.) Longer ligands with multiple chelation sites can even form extended helices, from trimetallic double stranded helicates [M_3L_2] to longer [M_xL_2].[43]

In bimetallic triple stranded helicates [M_2L_3] and quadruple stranded helicates [M_2L_4], (with oligo-monodentate ligands and square planar metals) and utilizing ligands with appropriate length and flexibility, larger cavities between the ligand strands can be made. The creation of cavities in SCCs that can encapsulate small molecules, have with potential applications in medicine in drug delivery,[44] as gas storage, [45] and can be utilised as catalytic sites.[46] The maturity of the research field in this area has meant that literature has moved away from 'just' synthesis, with more of a focus on purposeful design with the intent of more complex function. An example of this can be seen in the work of von Krbek *et al.* which contains a bis-bidentate chelation sites within the ligand, (red, Figure 13) coordinate to two octahedral Fe(II) ions in a [M_2L_3] helicate, and the (blue) functional groups in the spacer unit, catalyze the conversion between α- and β- D-glucose.[44]

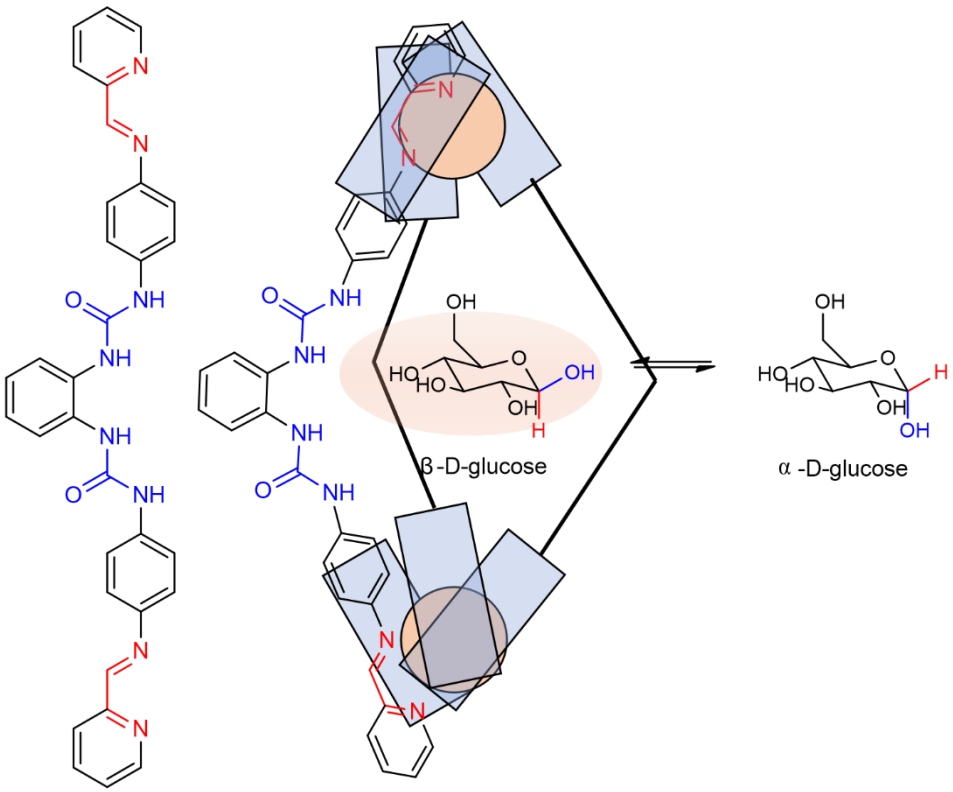

Figure 13: A bimetallic triple stranded helicate developed by von Krbek *et al.* which catalyses the conversion between α- and β- D-glucose. [44]

1.4.3 Tetrahedral Cages

Tetrahedral cages, are discrete [M_4L_6] polygons with internal cavities. The functionalisation of ligands in these complexes provide non-bonding interactions complimentary to specific guests. The main interest of these structures is the selective encapsulation of guests, which can contribute to: reaction specificity; isolation and protection of volatile components from outside interactions;[46b] host-guest[47] and catalytic chemistry.[46a] These cavities are incredibly versatile, with changeable volume, topography and internal chemistry that create complementary environments capable of encapsulating a variety of size, shape, and types of guests.

Symmers, *et al.* successfully synthesised a tetrahedral cage utilising bis-bidentate ligand, with a cis-conformation of N_{Pyr}-N_{Tz} chelation sites coordinated with octahedral Co(III) ions (Figure 14a).[48]

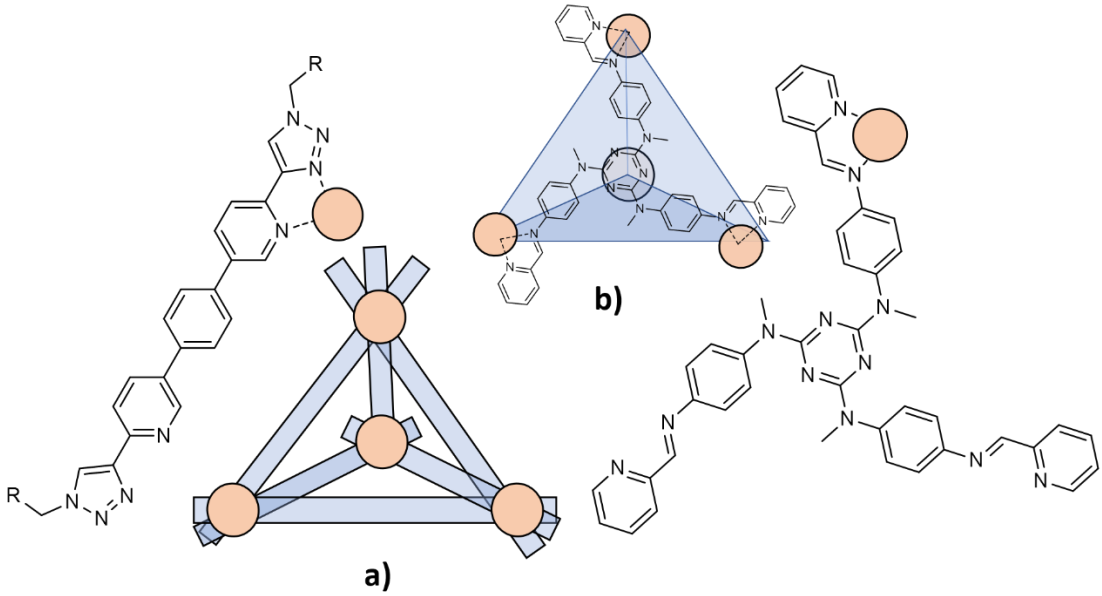

Figure 14: A schematic showing tetrahedral cage geometries; a) The bis-bidentate ligand forming the edges of the cage [M_4L_6], coordinated to Co(III), reported by Symmers, *et al.*[48] b)The terdentate ligand forms the face tetrahedral [M_4L_4], coordinated to Fe(II) reported by Bolliger *et al.*[49]

In the work of Bolliger *et al.* a tetrahedral capsule was structured so that the ligand forms a 'face' of the tetrahedral pyramid.[49] The ligand has three 'binding sites' which diverge 60° away from each other to coordinate with metal ions and form a tetrahedral [M_4L_4], as seen in (Figure 14 b). As seen in the previous section on ligand design, it is the turning angle of coordination, that determines the formation of polyhedral cages versus helicates.

1.4.4 Cyclohelicate Squares and Triangles

These are popular target architectures due to the close proximity of the metal ions, which often allow electronic or magnetic communication between appropriate centres.[50] This feature makes these structures desirable candidates for the future design of novel materials in crystal engineering, nano-scale devices, information storage and processing technology.[51]

Cyclohelicate structures consist of parallel and perpendicular ligands that coordinate in a 'paddle wheel' around the metal ions.[35] This is done either with bidentate ligands and tetrahedral metal ions, or with tridentate ligands and octahedral metal ions.[33] The combinations of these symmetric di-nucleating ligands and metal ions spontaneously self-assemble into discrete even numbered cyclohelicate, [n×n], polygon architectures, grids and squares, and have even led to rarer triangular structures.[14b, 52] This

spontaneous assembly occurs if the metal ions satisfy the condition of filling the most coordination sites,[14b] while being thermodynamically favourable.[16, 53]

For cyclic structures the chelation sites are arranged *trans*- to each other on the ligand, with metal ions coordinating above and below.[1, 14b, 16, 21] Ligands with a cis-chelation site arrangement coordinate into non-cyclic structures, with no 'twist' in the ligand arrangement, such as [2x2] square grids (Figure 15). Most metallogrids synthesised have been homometallic, with some heterometallic structures synthesised, though these are still relatively rare due to the more challenging synthesis, these result in *anti*- and *syn*-topisomer arrangements.[16, 23, 54]

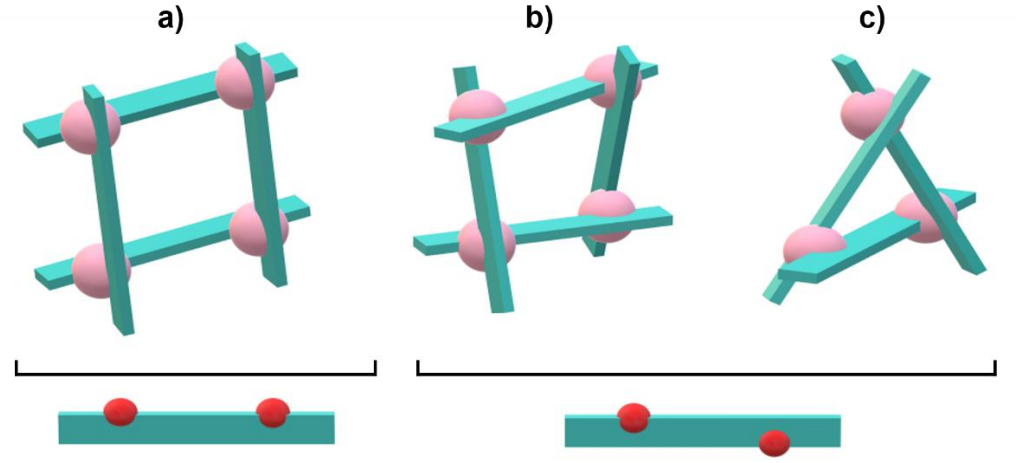

Figure 15: Possible discrete polygon shapes. a) [2x2] square grid, utilises *cis*-bidentate ligands, while b) cyclic [2x2] square grid, and c) cyclic triangle, utilise *trans*-bisdentate ligands. Pink spheres represent metal ions, red spheres represent chelation sites on ligands.

Work reported by Wu and Chen, *et al.* shows how alterations to the internal geometry of ligands can alter the final formation.[55] The only difference in the two ligands in Figure 16 is where the R groups were attached relative to each other on the central benzene ring, (either 1,3- or 1,4-). When these ligands were coordinated with tetrahedral Zn(II) ions; the 1,2- benzene ligand (not shown) formed a bimetallic double stranded helicate, while the 1,4- benzene ligand (Figure 16(a)) formed cyclohelicate squares and the 1,3- benzene appended ligand (Figure 16(b)) generated cyclohelicate triangles.

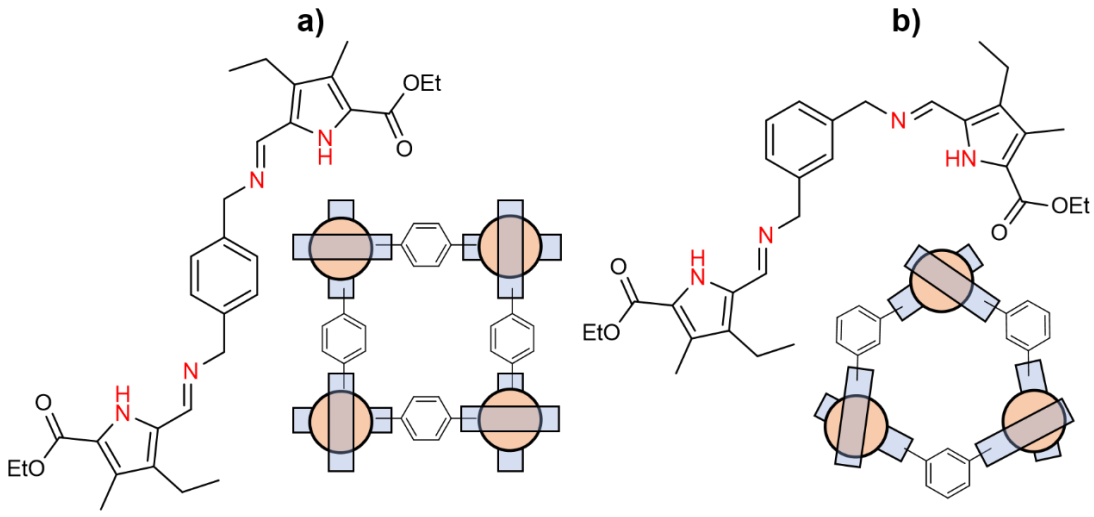

Figure 16: The formation of cyclohelicate squares and triangles dependant on the internal geometry of the ligand, when assembled with tetrahedral Zn(II) ions. a) 1,4-R benzene ligand assembled into cyclohelicate squares b) 1,3-R benzene ligand assembled into cyclohelicate triangles. Diagram of relevant results from Wu, *et al.*[55]

An example of a successful pyrazine-based ligand, which was used in the assembly of a cyclic [2x2] square grid, was reported by Hausmann *et al.*[56] (Figure 17.) A bis-terdentate ligand (**L1b**) assembled with octahedral Co(III). When one of the amide moieties was protonated, only a $[M_1H_2L_2]$ complex formed, displaying the environment sensitivity of complex assembly.

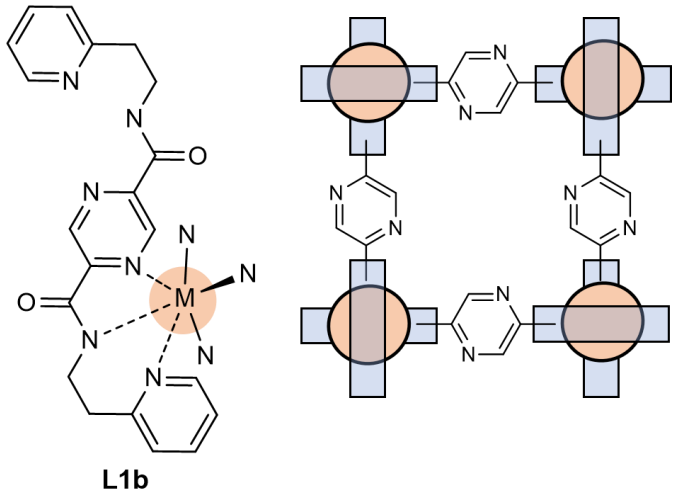

Figure 17: A diagram of a cyclohelicate square, $[M_4L_4]$ with **L1b** ligands and Co(III). Reported by Hausmann *et al.*[56]

Cyclohelicate triangles are trinuclear metallacycles $[M_3L_3]$, with three metal ions most often equidistant, arranged at 60º angles. Three ligands coordinate in the same above and below arrangement as seen in squares, in an anti-parallel fashion. Cyclohelicate

triangles, however, are much less common than cyclohelicate squares.[57] Cyclohelicate triangles are double stranded like squares, but have a more compressed internal angle geometry. Triangles are more entropically favourable than square geometry, as more molecules are created than squares, but squares are usually favoured due to the reduced angular strain on the ligands being held close together. Triangle formation requires an alteration in this balance, which can be done through an increase in the flexibility of the ligand. Trinuclear metallacycles are most often obtained serendipitously.[57]

One of the simplest cyclic triangle complexes in this style, was reported by Neels and Stoeckli-Evans, where the bidentate ligand (Figure 18-A) coordinated to three octahedral Zn(II) ions.[58]

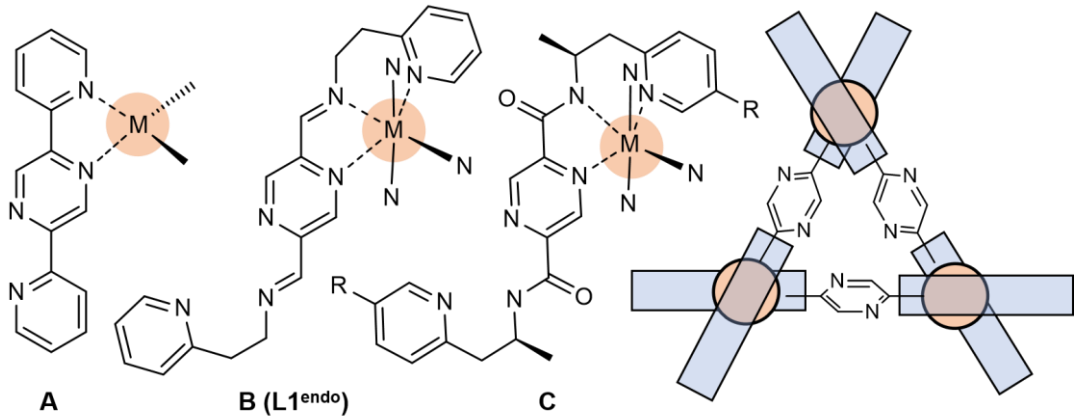

Figure 18: Cyclohelicate triangles. **A**: simple ligand by Neels and Stoeckli-Evans[58] assembled into Zn(II) cyclohelicate triangles; **B** (**L1^{endo}**): a relatively recent ligand assembled into triangles by Brooker, *et al*.[59] and Dais *et al*.[60] **C**: An analogue of ligand **L1b**, R = $OCH_2CH_2CH{=}CH_2$ reported by Zhong *et al*.[61] which assembled into cyclohelicate triangles with Co(III).

A more recent cyclohelicate triangle [M_3L_3], reported by Zhong *et al.* [61] in **C**, made a slight alteration to **L1b**, with the introduction of a stereospecific methyl group, and an R group of $OCH_2CH_2CH{=}CH_2$. This slight change to the chelation site assembled cyclohelicate triangles, when coordinated with Co(III), rather than squares. That both ligands coordinated with Co(III) shows that the metal was not involved in the different structural outcomes. This highlights just how a small change in internal geometry, in the ligand, or even just the chelation site, can change the outcome of the overall complex architecture.

Another pyrazine-based ligand, **B** (**L1^{endo}**) reported by Brooker *et al.*[59] and Dais *et al.*[60] differed from **L1b** by having an imine as the bridge, rather than the amide group, and resulted in a triangle. The nitrogen atoms in both of these moieties are utilised in chelating to the octahedral metal ions, but the dianionic amide resulted in a cyclohelicate square. This **B** (**L1^{endo}**) ligand complexed with Mn, Fe, Zn and Co(II) ions, to form a triangle, while the **L1b** dianionic amide complexed with Co(III), to form squares. Here the difference in the cyclohelicate structure could be due to the difference in charge of the ligand, of the difference in the flexibility in the *N*-moieties utilised, again this shows how architectures change with small changes to the ligands used.

1.4.5 1D Polymer Chains

Some ligands, with chelation sites that are predicted to form discrete architectures, can assemble into one-dimensional (1D) polymer chains. Some examples here, show how metal ions with less restricted geometries, such as silver, can lead to a flexibility in the angles between ligands. This more malleable angle means that the ligands are not restricted to convergent angle, but can diverge and lead to 1D polymer chains.

The various structural motifs in these coordination polymers can be divided into (1D), two-dimensional (2D) and three-dimensional (3D) categories.[62] Included in these frameworks are long singular 1D coordination polymers, held together in larger 3D structures, by weak, non-covalent interactions such as hydrogen bonding, π–π stacking interactions, and van der Waals forces.[62-63]

There is an area of interest in developing 1D polymeric chain metalloorganic complexes, as they often contain similar properties as those in discrete structures. In the last two decades, progress has been made in the synthesis of coordination polymers with flexible structures, motivated by their potential applications, due to their distinctive characteristics such as nanoscale and tuneable thickness, high-aspect-ratio, large surface area, more exposed accessible active site, favourable mechanical flexibility, and optical transparency.[62-64] Layered structures formed by the stacking of 1D and 2D materials offer a great opportunity for fundamental studies as well as practical applications.

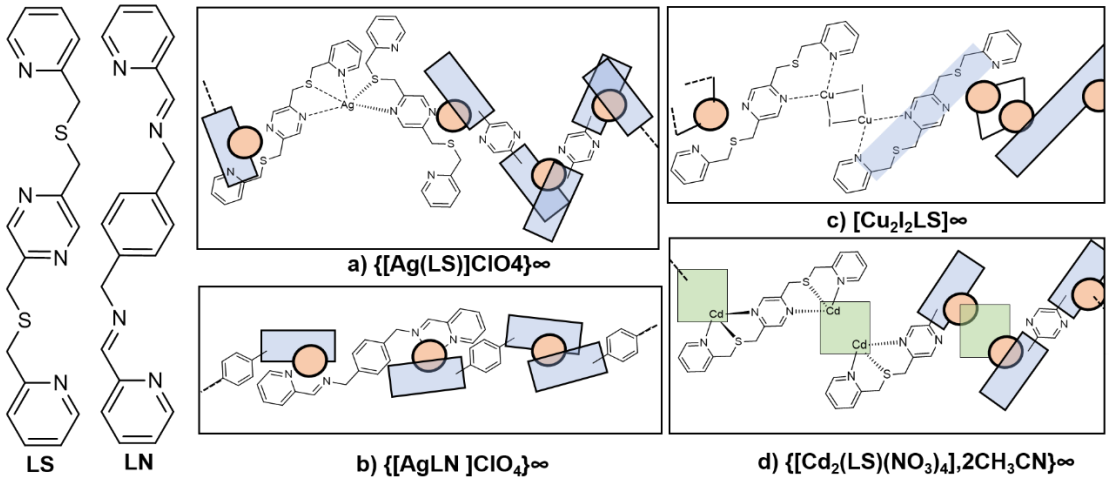

Figure 19: Diagrams of 1D polymer chains. a) $\{[AgLS]ClO_4\}_\infty$ reported by Caradoc-Davies *et al.* [65] b) $\{[AgLN]ClO_4\}_\infty$ reported by Chakraborty, *et al.*[66] c) $[Cu_2I_2LS]_\infty$ reported by Chakraborty, *et al.*[67] d) $\{[Cd_2(\mathbf{LS})(NO_3)_4],2CH_3CN\}_\infty$ reported by Cordes *et al.*[68]
The pink spheres indicate the corresponding metal ion, the blue rectangle indicates the chelating end of the corresponding ligand, the green squares indicate the $Cd_2(NO_3)_4$ moiety structures.

The bis-bidentate ligand (**LN**) was reported by Chakraborty, *et al.*[66] to form 1D polymer chains, {[Ag**LN**]ClO_4}∞ when reacted with anhydrous silver perchlorate. The flexibility in this coordination with the distorted tetrahedral coordinated Ag(I) ions resulted in the formation of a continuous polymer. Likewise, when the thiol pyrazine-based ligand (**LS**), reported by Caradoc-Davies *et al.*[65] with anti-bis-terdentate chelation sites, was introduced to silver perchlorate, the Ag ions expressed a five-coordinate geometry. A 1D polymer chain assembled, {[Ag**LS**]ClO_4}∞ with **LS** ligands alternating between all three atoms in the chelation site coordinating to the Ag ion, and only the N-Pz nitrogen and the sulphur coordinating, forming a zig-zag polymer. (Figure 19-b.)

When **LS** was introduced to CuI, the counterion was incorporated in the final complex. An intermittent symmetric Cu_2I_2 moiety, created a strictly planar coordination between the two Cu ions and the adjacent **LS** ligands, leading to a side-to-side polymer chain, [Cu_2I_2**LS**] ∞.[67] (Figure19-c) Finally, when $Cd(NO_3)_2.4H_2O$ was introduced to LS, the counter ions were incorporated into the structure and the Cd ions formed an eight coordinate geometry, with a less controllable final angle outcome. This led to a $\{[Cd_2(\mathbf{LS})(NO_3)_4],2CH_3CN\}\infty$ polymer of alternating **LS** ligands and $Cd_2(NO_3)_4$ moiety structures, where all of the **LS** ligands are held in the same orientation.[68] (Figure 19-d.)

1.4.5 2D and 3D Metal Organic Frameworks

Simple 2D polygon shapes can be expanded upon into 2D sheets and 3D architectures such as MOFs (Metal Organic Frameworks). The unique physiochemical properties and multiscale organisation of layered materials draw the attention of researchers across a wide range of interdisciplinary research due to their potential applications in magnetics,[69] optics,[70] catalysis, gas adsorption[62] and general guest–host interactions.[71]

MOF nanosheets have been extensively prepared with two main methods. From the top-down, breakdown of a bulk product, or bottom-up step-wise methods.[63] The ligands used in covalent 2D and 3D networks have divergent chelation sites, with a wider range of angles to expand connections to, compared to the previously discussed ligands, that have more convergently arranged chelation sites. Some examples of ligands used in MOFs are shown in, (Figure 20). The architecture of MOF is dependent on the combination of arrangements of multiple ligand components and metals ions.

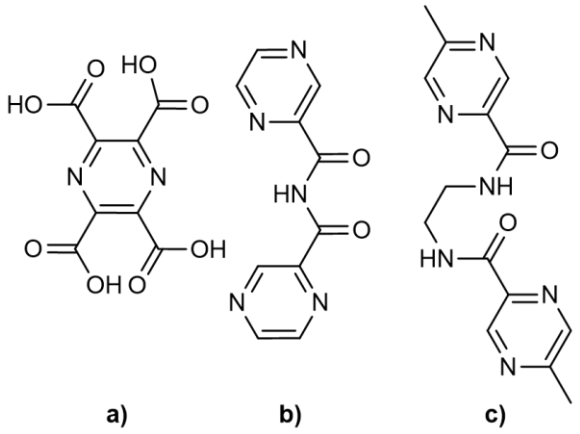

Figure 20: MOF ligands demonstrating the more divergant arrangement of coordination sites on ligands. a) a pyrazine ligand involved in a MOF reported by Gosh *et al.*[72] b) a ligand used as one of a set of reversible redox and MOF building blocks, reported by Cowan *et al.*[73] c) a ligand involved in a functionalized POM-based MOF reported by Cui *et al.*[74]

1.5 Aims of Research

The overall aim of this research is the design and synthesis of a collection of novel symmetric pyrazine-based ligands capable of coordinating to 3*d* metal ions, and to characterise the resulting structures to develop an understanding of the factors involved.

This will require the investigation into the synthesis of central, symmetric pyrazine units with functional groups on the 2,5- positions.

The first target is the synthesis of 2,5-dimethylamino pyrazine (**C6**). The primary amines on the pyrazine will then be used to synthesise exo-imine pyrazine-based ligands. This style of imine pyrazine ligand does not appear to have been reported before, however endo-imine based ligands have been, for example a endo-imine ligand previously discussed, by Brooker *et al.*[59] and Dais, *et al*.[60]

Within the synthesis plan for **C6**, is the isolation of the di-azide **D1**. With the isolation of a pyrazine with azide moieties, ligands utilising 'click' chemistry can be explored.

Finally, following any development of novel ligands, complexation reactions with a wide range of metal salts, will investigate the ligands' ability to form complexes. NMR and X-ray crystallography will be utilised to analyse the structural results of these future ligands and $[M_xL_x]$ complexes. This research will contribute to the ever-expanding library of ligands used in supramolecular chemistry.

1.6.1 Thesis Outline

Section 1 – Background information into this area of research.

Section 2 – 'Click' ligands from - 2,5-bis(aminomethyl)pyrazine (**D1) - L3. L4.**

Section 3 – Pz-O-Tz ligands from - 2,5-bis(aminomethyl)pyrazine (**E1**) - **L5**. **L6**.

Section 4 – Pz-O-Tz ligands X-ray crystallography discussion.

Section 5 – Endo-Imine ligands from 2,5-diformyl pyrazine (**B1**) - **L1^{exo}. L1b. L2.**

Section 6 – Development of synthetic route - 2,5-bis(aminomethyl)pyrazine (**C6**)

Section 7 – Conclusion

Section 8 – Future Work

1.6.2 Ligand Design and Synthesis Summary

Over the course of this research, several pyrazine-based centres were synthesised. These centres could then be joined to 'peripheral' groups through reactions that will be discussed and expanded upon in the upcoming sections of this report. Shown below, are the central pyrazine groups isolated, the general ligand design they form and the section under which they are discussed. The pyrazine acts as part of a pair of antiparallel coordinate vectors, which will then go on to coordinate to 3*d* ions.

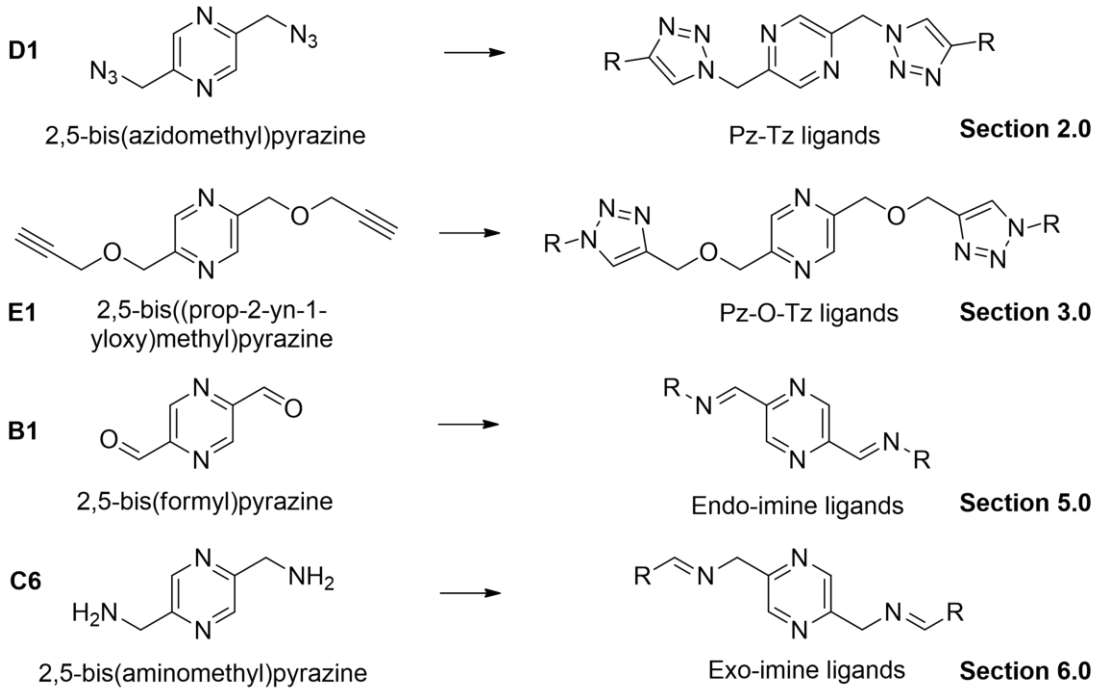

Figure 21: Summary of the central ligand units synthesised, the generic ligand structure they form. The section these ligands are discussed in are labelled. (Pz, pyrazine, Tz, triazole.)

For ease of reference the molecule and ligand codes are listed on a fold out page at the end of the thesis.

2.0: New Click Chemistry Ligands

2.1 Introduction to Click Ligands: (L3) and (L4)

With the isolation of the **D1** molecule, a pyrazine centre with symmetric, terminal azides, (Section 6.3.2) a different field of ligand synthesis could be explored, triazoles formed through 'click chemistry'.

A general ligand shape shown in (Figure 22), introduces the functionality of the 1*H*-1,2,3-triazole functional group. This group, can act as a coordination site, to transition and other metals. This group can be formed by the reaction of terminal azides, (e.g. **D1**) with terminal alkyne reagents. The versatility of this approach means other functional groups can 'click' onto this **D1** central unit, opening up many functional and structural options for ligand synthesis.

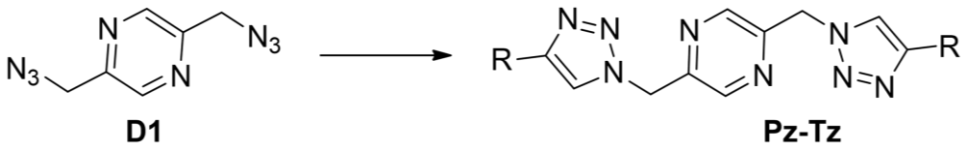

Figure 22: General structure of ligands made from **D1** using click reactions.

The concept of 'click chemistry' was coined by Sharpless and co-workers in 2001,[75] and introduced a branch of powerful, highly reliable, and selective reactions.[76] These reactions had high yields, generated easily removable (or no) side products, are stereospecific, exhibit a large thermodynamic driving force, and have simple reaction conditions.[77] The establishment of this reaction methodology opened up a new repertoire of functionalisation and synthesis, for use in bioconjugation, materials science,[78] and drug discovery.[76] Triazoles are particularly suited to construct various multidentate ligand systems due to the high synthetic flexibility brought by click chemistry; making triazoles a valuable tool in ligand synthesis for metal-organic complexes. Lewis *et al.* used click reactions to functionalise, already assembled, bimetallic quadruple stranded cages.[79]

The Cu(I)-catalyzed 1,4-dipolar azide–alkyne cycloaddition (CuAAC) leading to 1,2,3-triazoles has been established as one of the most useful and valuable examples of click chemistry, providing 1,4-substituted 1,2,3-triazoles with such efficiency and scope that the transformation has been described as the synonymous "click" chemistry

reaction.[77a, 80] CuAAC is a type of Huisgen 1,3-dipolar cycloaddition based on the formation of 1,4-substituted 1,2,3-triazoles between a terminal alkyne and an aliphatic azide in the presence of Cu(I).[77b] This reaction owes its usefulness in part to the ease with which azides and alkynes can be introduced into a molecule and their relative stability under a variety of conditions.[80]

Numerous papers have been published on CuAAC reactions that give 1,4-disubstituted 1,2,3-triazoles under mild conditions, in very high selective yields; opposed to the classical Huisgen-type thermal 1,3-dipolar cycloaddition, which afforded mixtures of 1,4- and 1,5-disubstituted triazoles.[76]

Triazoles make up some of the five membered *N*-heterocycles, the range of which is shown in Scheme 1. The triazoles make up the variations with three nitrogen atoms in the ring. It is the 1,2,3-triazole that was explored within this research.

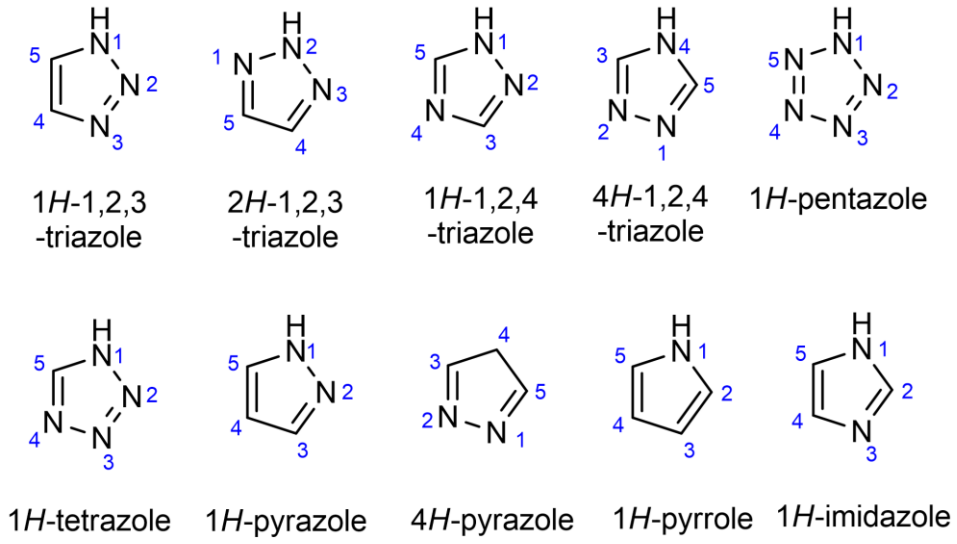

Scheme 1: The variety of 5-membered *N*-heterocycles available. The 1*H*-1,2,3-triazole is used in this research.

Applications of this CuAAC reaction have been developed to, not only link two units together, but also to intentionally synthesise the triazole moiety. A growing range of ligand architectures based on triazoles are available; with applications of the triazole in coordination chemistry reported; metal ion sensing,[81] medicinal chemistry,[82] catalysis,[83] magnetic materials,[84] and photovoltaic.[85]

Some the most relevant target structures are 1,4-disubstituted *1H*-1,2,3-triazoles, (Scheme 1) emerging as powerful "click chelators".[86] Their facile and modular synthesis allowing for the fine-tuning of steric and electronic, properties of these ligands, with established *N* coordination available.[87]

An exclusive feature of the 1,2,3-triazole derivatives, in comparison to pyridine or imidazole derivatives, is the presence of an additional nitrogen atom adjacent to the nitrogen donor reducing the steric demand of the ligand, altering the flexibility and lability.[87] The N3 donor of 1,2,3-triazole is readily available to coordinate to metal cations, with coordination also possible at the N2 and C5. The C5-H is also able to interact with counter anions in complexes via hydrogen bonds, that are as strong as for classical, intrinsically polarized hydrogen bond donors (N–H and O–H), due to the extrinsic polarization of a carbon atom.[87] These possible coordination arrangements are shown in Figure 23.

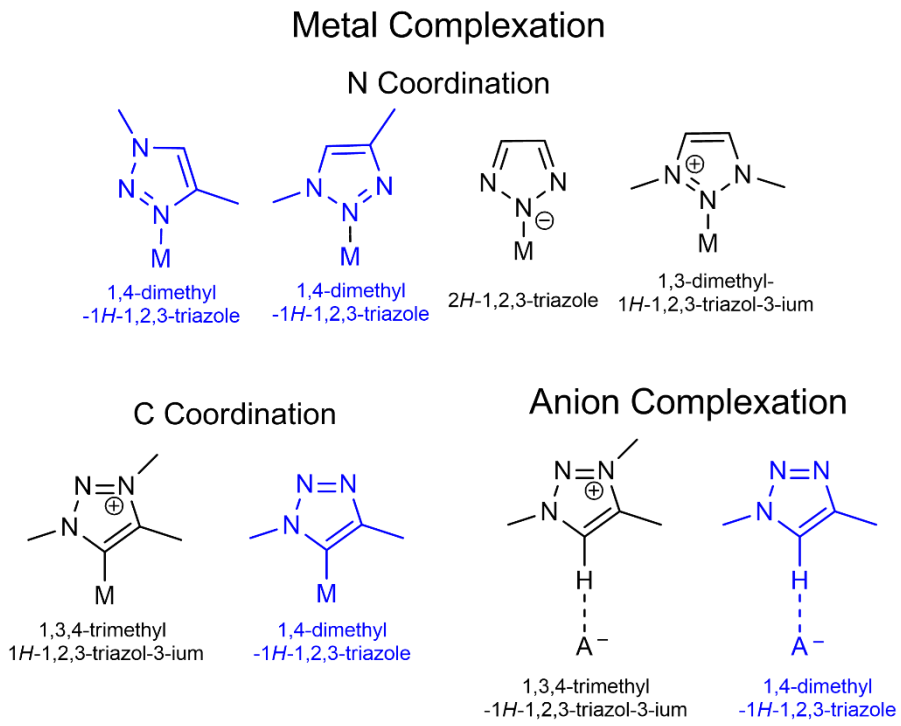

Figure 23: The various supramolecular interactions of 1,2,3-triazoles and their derivatives, with the 1*H*-1,2,3-triazoles expected to be made, highlighted in blue.[87]

Some of the simplest examples of CuACC triazoles being utilised in supramolecular chemistry are shown in Figure 24. Urankar *et al.* complexed (a), with Rh, coordinating only to the pyridine N, while Pd complexes, coordinated to the N3 of the triazole.[86] Herzigkeit, *et al.* introduced $[Cu(MeCN)_4]PF_6$ to (b), (c) and (d), with all three ligands coordinating to the metal cation with both the pyridine N and N2 of the triazole.[88] It is the successful coordination of this moiety, that proved promising for the work with **L3** discussed next.

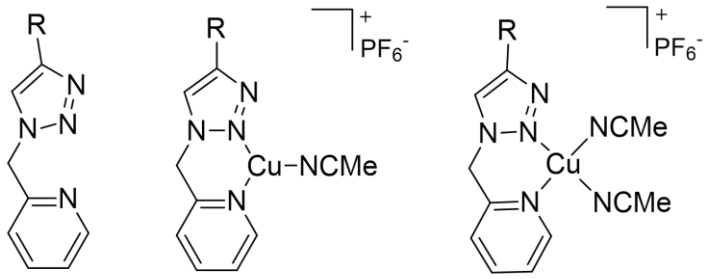

Figure 24: Previous simple CuACC 1,2,3-triazoles used in supramolecular chemistry. (a) Urankar *et al.*[86] and, (b), (c), and (d) Herzigkeit, *et al.*[88]

(a) = 2-((4-phenyl-1H-1,2,3-triazol-1-yl)methyl)pyridine
(b) = 2-((4-tolyl)-1H-1,2,3-triazol-1-yl)methyl)pyridine
(c) = 2-((4-(4-methoxyphenyl)-1H-1,2,3-triazol-1-yl)methyl)pyridine
(d) = 2-((4-(4-(tert-butyl)phenyl)-1H-1,2,3-triazol-1-yl)methyl)pyridine

The mechanism for this reaction was initially explored computationally by Himo *et al. in* 2005,[89] closely followed with Rodionov *et al.*[90] and Bock *et al.*[80] exploring the mechanism experimentally. It was already known that Cu(I) readily inserts into terminal alkynes in the presence of base, as seen in the Sonogashira coupling reaction.[91] This CuAAC mechanism can be seen in Scheme 2. which shows how the Cu(I) catalyst facilitates the cyclisation of the azide and alkyne groups to form the triazole moiety.

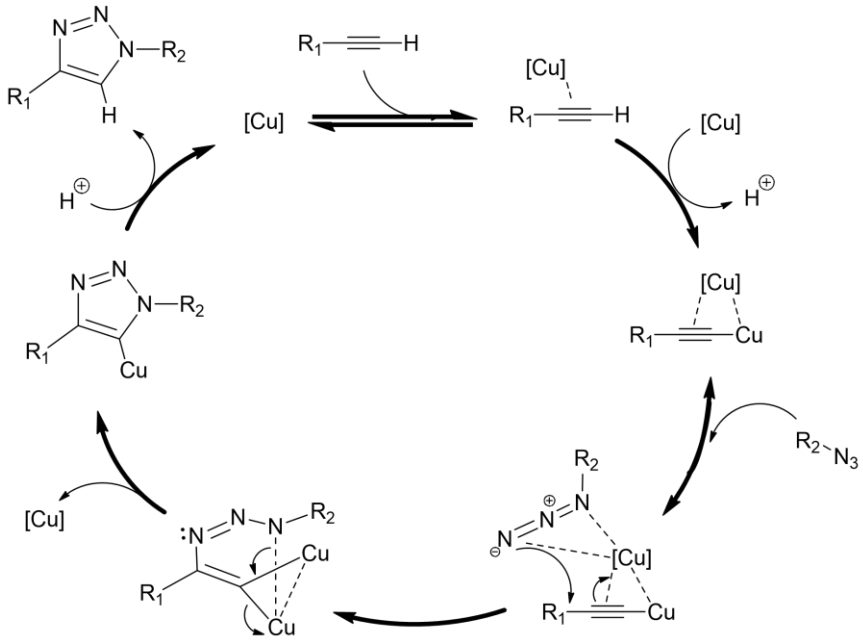

Scheme 2: Click mechanism, adapted from Castro, *et al.*[77b] The cycloaddition of alkynes and azides to 1,2,3-triazoles, with catalytic Cu(I) retention.

A secondary outcome, that needs to be accounted for, is the possibility of Glaser coupling. This acetylenic formation, via Cu(I) catalyst, means that the two equivalences of phenylacetylene starting reagent will need to be marginally compensated for, with the possible formation of 1,4-diphenylbuta-1,3-diyne. The reaction environment should also minimise any exposure to base, to prevent the initial deprotonation of the phenylacetylene reagent. The reaction for the generation of this side product is shown in (Scheme 3).

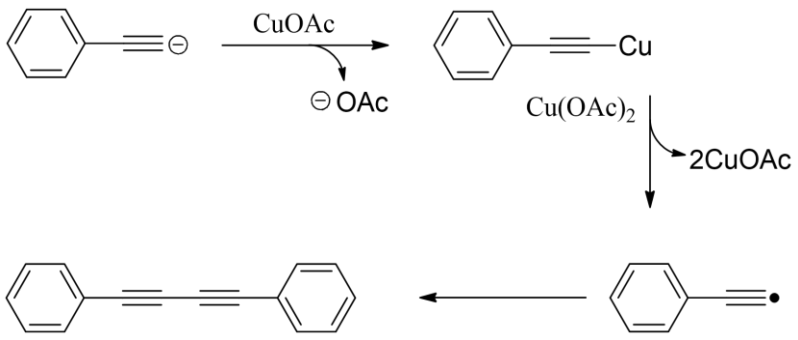

Scheme 3: Simplified Glaser coupling reaction scheme to form 1,4-diphenylbuta-1,3-diyne.

2.2 Synthesis and Characterisation of L3

This section describes the synthesis of **L3** using the CuACC reaction with **D1** and phenylacetylene (**D2**) (Scheme 4). The new ligand is capable of coordinating to 3*d* transition metal ions.

Phenylacetylene was chosen as it was readily available and did not possess any competing coordination sites. It has been shown by Crowley *et al.*[92] and Shatruk, Zhu *et al.*[86], that the N2 and N3 nitrogen atoms of triazoles can participate in metal coordination and that there is a preference depending of substituents present. Their findings, summarised in Figure 25. below, showed that if a secondary coordination site, involving N3, is available, then the N3 will be the preferential binding site. However, if there is no secondary site to create a cavity with N3 available; then the N2 atom will coordinate to the metal. The use of phenylacetylene, **D2**, with no secondary coordination cavity, was therefore hypothesised, to coordinate to using the N2 atom. It was found that for Ag(1) coordination that this was not the case, with both N2 and N3 nitrogen atoms involved in the coordination, see Section 2.4.3.

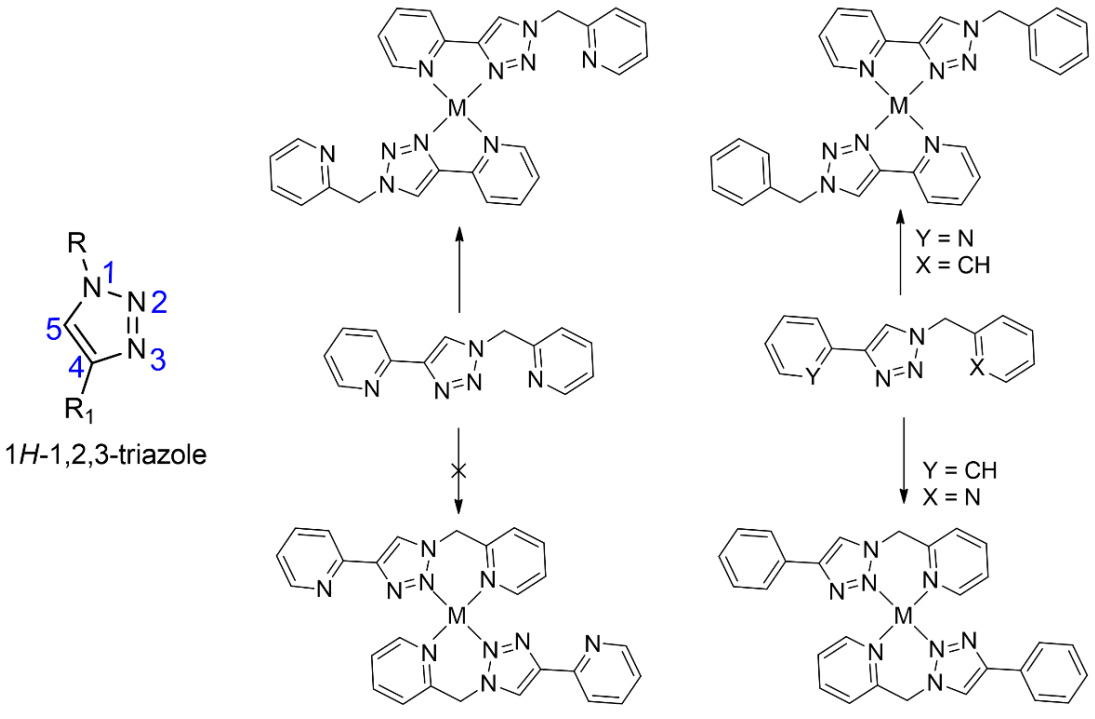

Figure 25: Summary of the work by Crowley *et al.*[92] and Shatruk, Zhu *et al.*[84] demonstrating the competitive binding between the N2 and N3 nitrogen atoms of triazoles. Diagram, adapted from the summary by Schulze and Schubert.[87]

The method for synthesising the new ligand **L3**, was adapted from Herzigkeit *et al.*[88] and Brotherton, *et al.*[93] with some modifications based on reagent availability, for instance, even though $CuSO_4 \cdot 5H_2O$ is preferentially used in many literature examples, $Cu(CH_3COO)_2$, was used here due to its immediate availability and literature evidence that higher yields are obtained with this catalyst when performed at sites that were directly next to a pyridine.[93] Likewise, citrate was used instead of the typical sodium ascorbate, again favoured due to availability of the reagent.[94]

This resulting CuAAC reaction, summarised in Scheme 4, was performed in DCM/tBuOH (3:1) and used 0.5 mol% $Cu(OAc)_2.H_2O$ (0.5M) catalyst. The reaction, performed overnight at RT, resulted in a light brown-white solid powder was collected in a 56 % yield. This resulting **L3** was characterised and complexed with metal salts.

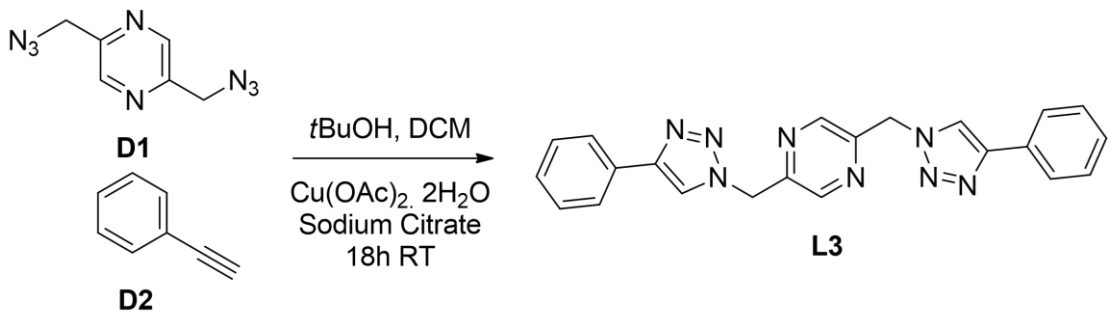

Scheme 4: Reaction scheme for the synthesis of **L3**

The structure of **L3** was characterised by ^{1}H NMR and ^{13}C NMR, along with SCXRD, MS and IR. The disappearance of **D2**'s 3.08 ppm ^{1}H NMR alkyne peak, and the appearance of the 8.68 ppm ^{1}H NMR and 122.8 ppm ^{13}C HNMR peaks indicated the successful formation of the triazole units. The assignment of the ^{1}H NMR and ^{13}C NMR is shown in the (Figure 26 and Table 1). The assigned ^{1}H NMR, ^{13}C NMR, COSY, and HMQC spectra can be found in (Apx12.3.1-3).

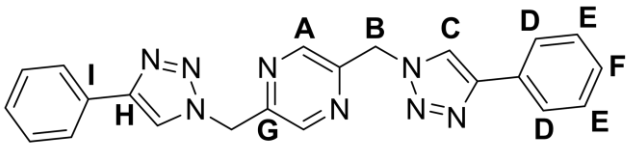

Figure 26: **L3** assigned with ^{1}HNMR and ^{13}CNMR peaks, (ppm).

Table 1: ^{1}H NMR and ^{13}C NMR characterisation of **L3**.

	A	**B**	**C**	**D**	**E**	**F**	**G**	**H**	**I**
*^{1}H NMR**	8.75	5.88	8.68	7.85	7.46	7.34	-	-	-
	s 2H	s 4H	s 2H	d 4H	t 4H	t 2H			
J (Hz)				7.50	7.28	7.32			
^{13}C NMR$^{\intercal}$	144.0	52.8	122.8	123.6	129.4	128.3	150.5	147.0	131.1

**(500 MHz, DMSO): δ ppm* $^{\intercal}$ *(126 MHz; DMSO): δ ppm*

White needle-shaped crystals of **L3** of suitable quality for SCXRD, could be isolated either by vapour diffusion of Et_2O or by hot recrystallisation from DCM. These crystals, were also obtained during crystalisation attempts from metal complexation reactions. The full crystal data can be found in Apx10.0.

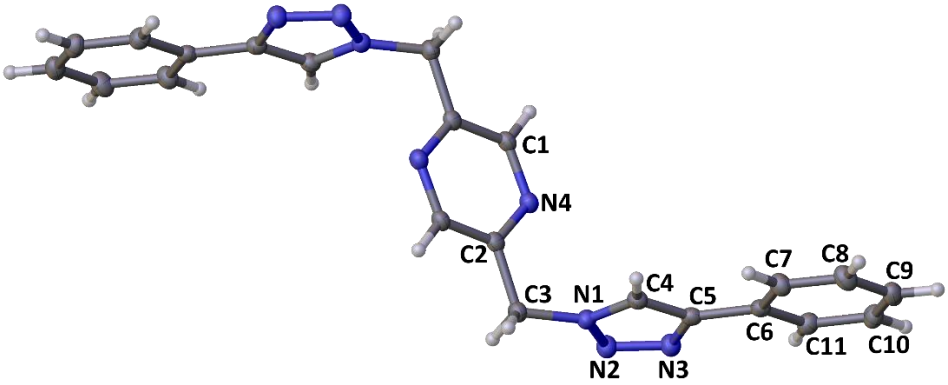

Figure 27: Crystal structure of the full **L3** molecule, angled to show the whole ligand. The asymmetric unit of half a ligand, with labelled atoms. Colour Code: grey = C, blue = N, white = H.

The **L3** crystallised in a monoclinic space group P $2_1/c$. The solved X-ray crystallography solution was consistent with the other collected experimental data. The asymmetric unit consists of a half of the ligand, (labelled in Figure 27), with the full ligand generated by an inversion centre positioned in the centre of the pyrazine ring. The phenyl-triazole arms lie parallel to each other, while the pyrazine is held almost perpendicular to the arms, at an angle of 112.43º for the N1-C3-C2 angle.

Table 2: The intermolecular bond distances and angles in the arrangement of **L3**.

Pz-N2: π-π bonds in a single stack of **L3** ligands			
Pz^{Cent} - N2 (Å)	3.116	C2-Pz-N2 (º)	88.53
C4-H^{C4} – Ph: CH-π bonds between stacks of **L3** ligands			
H^{C4} - Ph^{Cent} (Å)	2.978	C4- H^{C4}-Ph^{Cent} (º)	128.08
C4 - Ph^{Cent} (Å)	3.642	- Ph^{Cent}-H^{C4} (º)	87.13

This Z shape conformation of the ligand then stack on top of each other, with perpendicular T-shaped π bonding at a distance of 3.12 Å bond, between the N2 of the triazole and the centroid (cent) of the pyrazine of the ligands in front and behind within the same stack, (Table 2 and Figure 28). This distance is much shorter than the estimated distance between the N of a pyridine bound to the centroid of a second pyridine, 4.7 Å, proposed by Hohenstein *et al.*[95] which indicates a relatively strong T-shaped π bond between the ligands.

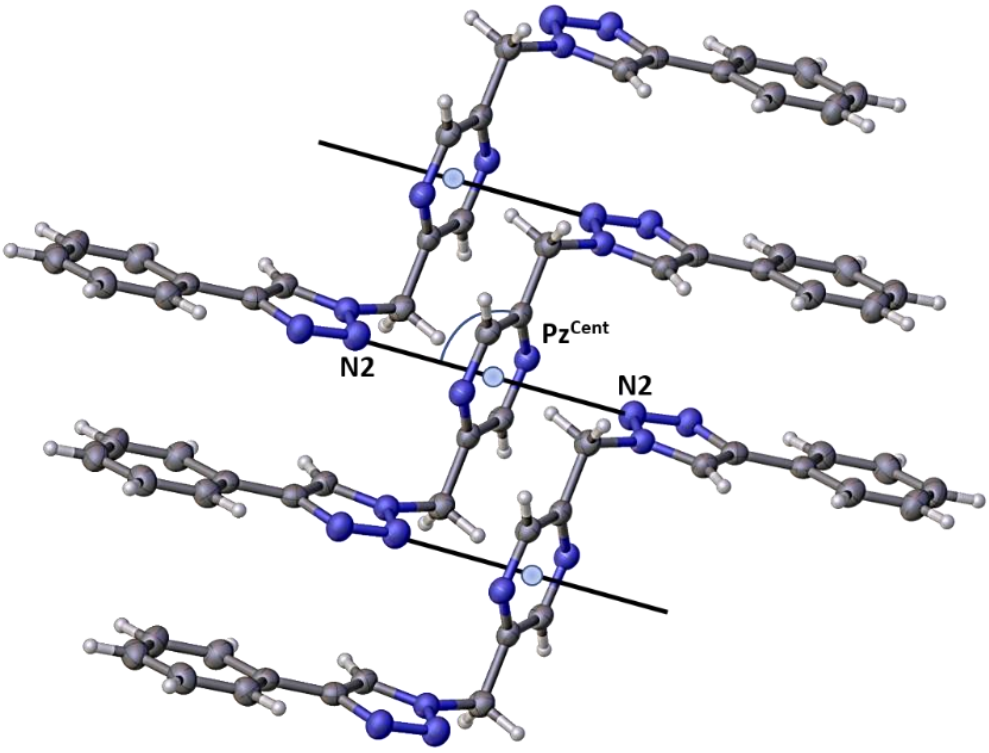

Figure 28: The crystal structure of stacks of **L3**, held by T-shaped bonding, between the N2 of a triazole and the pyrazine centroid (Pz^{cent}) of adjacent ligands with a distance of 3.116 Å.

The layers of ligands stacked in alternating directions, are held by, the non-conventional hydrogen bonds, namely intermolecular aromatic CH-π bonds, between the C4 of the triazole group and the phenyl group of an adjacent layer of ligands (Figure 29). Nishio *et al.* reported that the average distance in intermolecular CH- π bonds was 2.91±0.12 Å,[96] a range that the H^{C4}-Ph distance of 2.98 Å fell within (Table 2). All of this culminates in the tight packing of the **L3** ligands, and close arrangement of pyrazines and triazoles (Figure 30).

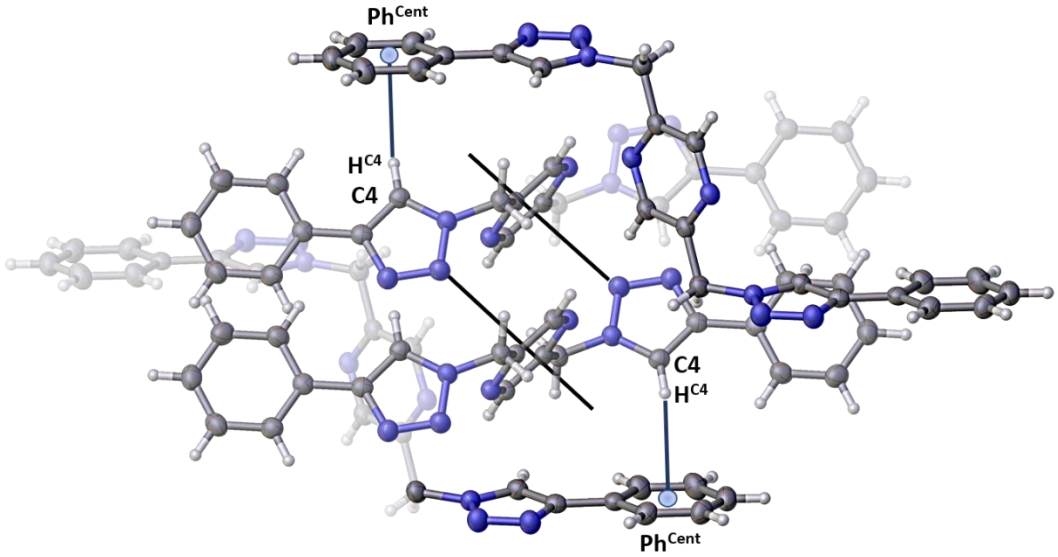

Figure 29: Crystal structure showing the CH-π bonds, (blue lines) between the phenol rings and the C4 of the triazole of the ligand above or below. The separate rows of ligands, held by N2- π bonds between the pyrazines, are stacked together.

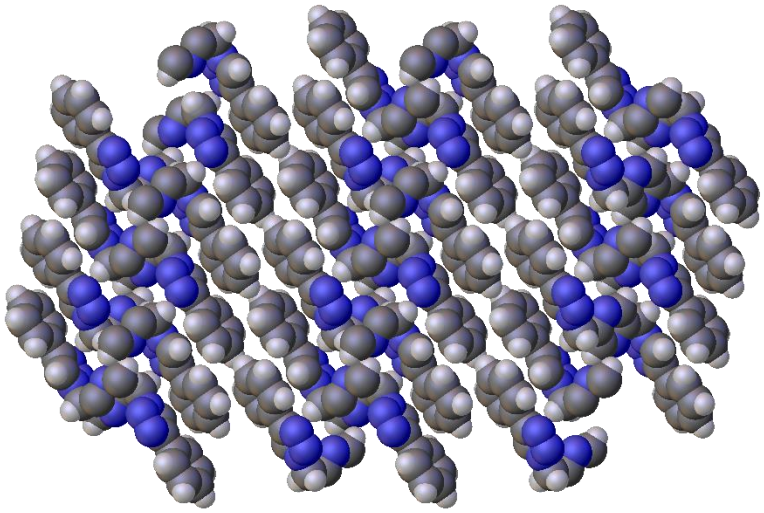

Figure 30: The 010 cell face of the **L3** packing. Upper: a ball and stick representation. Bottom: a space filling representation of the extended stacking present within the crystal.

2.3 Comparisons of L3 to Previous Work

There have been similar ligands, consisting of 1,2,3-triazoles and *N*-heterocycles, published previously in the literature, as shown in Figure 31. However, **L3** itself hasn't been reported, with the azides of the triazoles coming from a central pyrazine, which would allow for the coordination of metals at a closer proximity than these previous ligands. It appears as if **L3** rounds out a series of linear, rigid ligands synthesised via click chemistry.

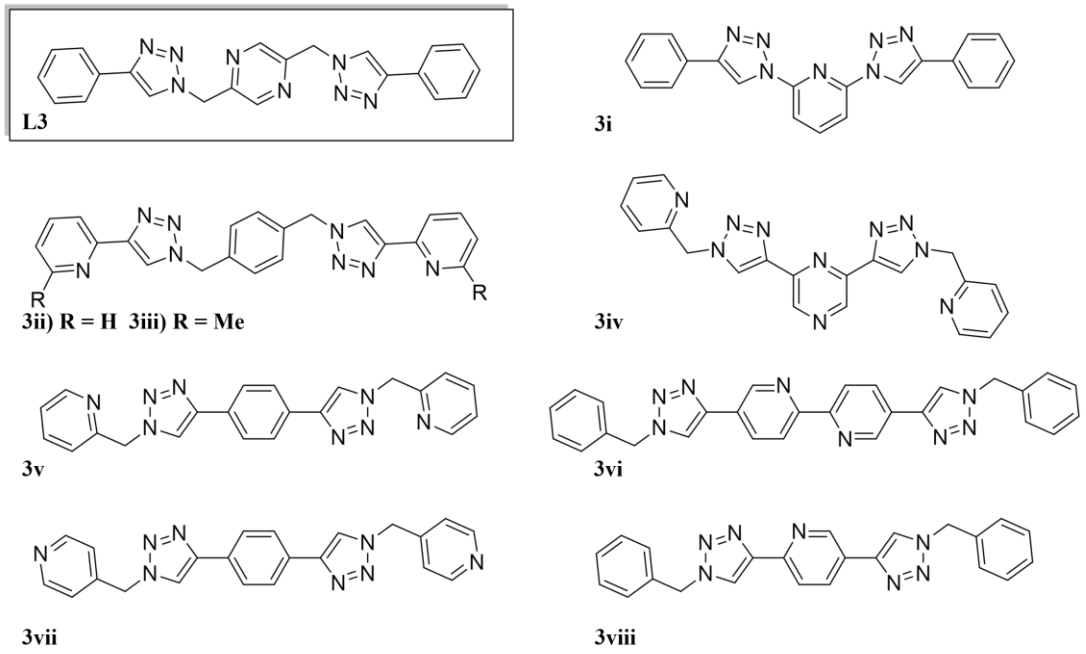

Figure 31: Previous ligands similar to **L3**.

The ligand 3i molecule, by Anderson *et al.*[97], and 3ii[98] and 3iii, by Nan *et al.*[98-99] are similar to **L3** in the arrangement of the click, having the azides coming from the central aryl group, although here this is a benzene, not a pyrazine. Scattergood, *et al.*[100] 3iv, did use a pyrazine as its central aryl component, but in a 2,6- orientation opposed to the 2,5- of **L3**, leaving a tridentate chelation site in 3iv and 3i, opposed to the bidentate site of **L3**.

Finally, 3v,[101] 3vi,[101] 3vii,[102] and 3viii[102], were all variations on this click ligand system, with the central aryl group having alkyl functional groups that click to azides on a secondary aryl molecule.

2.4 Metal Complexation of L3

With the synthesis and characterisation of **L3** confirmed, metal complexation reactions were attempted. Initially, the solubility of **L3** was investigated. The results, shown below, in Table 3, found that **L3** was insoluble in most typical solvents. This observation is also in keeping, with similar published ligands. Based on these findings, THF was chosen as the solvent for the complexation attempts for of **L3**.

Table 3: Solubility of **L3** in solvents at RT and with heat.

	MeOH	DCM	$CHCl_3$	MeCN	EtOAc	Hexane	THF	DMSO
RT	X	X	X	X	X	X	P	P
H	X	X	X	X	X	X	P	P

H = at reflux; X = **L3** was not soluble in solvent; P = **L3** was partially soluble in solvent – colour seen in solvent, but solid **L3** never fully disappeared.

2.4.1 Octahedral Metal Ions

In an attempt to produce tight tetrahedral cages (Figure 32), octahedral 3*d* ions, were mixed with **L3** in a 4:6 metal: ligand ratio, with the estimated outcome in (Figure 33).

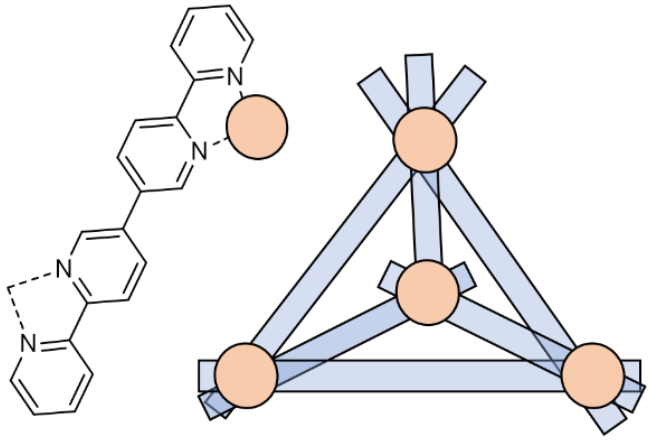

Figure 32: Tetrahedral cage example, with a ligand reported by Burke, *et al.*[103]

Burke, et al. reported the success of their ligand in the assembly of tetrahedral cages.[103] Like **L3**, Burke's ligand is relatively short, and has two nitrogen groups in a cis-arrangement of bidentate chelation sites. In Burke's case, the ligands coordinated with Co(III) ions in an L_6M_4 ratio.

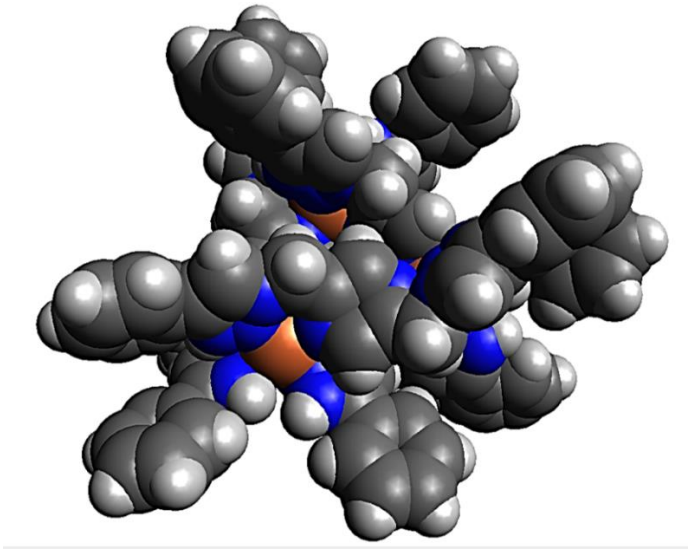

Figure 33: Simple Geometric model, in Avogadro, of the hypothetical $[L_6M_4]$ tetrahedral, $\mathbf{L3}_6Fe(II)_6$.

Table 4: Complexations of **L3** with octahedral 3*d* ions.

	Equiv.	Colour Δ		Crystal	(m/z) Result
$Mn(ClO_4)_2.6H_2O$	0.67	6:4.00	to yellow/red	√	394 (100) 395 (24) 396 (3)[**L3**] 647.0 (100) 649.0 (66) 648.0 (27) [Mn$\mathbf{L3}_2$] 843 (100) 844 (53) 845 (11) [Mn$\mathbf{L3}_2$](ClO_4^-)
$Co(ClO_4)_2.6H_2O$	0.70	6:4.21	to muddy pink	√	394 (100) 395 (24) 396 (3) [**L3**] 651.0(100) 652.99(64) 652.0 (23) [Co$\mathbf{L3}_2$] 847 (100) 848 (48) 849 (11) [Co$\mathbf{L3}_2$](ClO_4^-)
$Fe(ClO_4)_2.6H_2O$	0.68	6:4.08	to muddy orange	√	394 (100) 395 (24) 396 (3) [**L3**] 764.32

The first attempts were done at RT, with no success. The attempts were then repeated, with the complexation solutions heated to 60 ºC for half an hour. All of these complexations resulted in the **L3** crystalising out, and not coordinating with any of the metal anions. The reactions were attempted again, for longer time periods and higher temperatures, but for temperatures above 80 ºC, the **L3** ligand crashed out as the solution cooled, and the other reactions resulted in crystals of **L3**.

The results of these attempts are shown in Table 4. The results of the mass spec show that while the ligand is crystalising out, there is indication of the ligands coordinating to 3d ions, as M_1L_2 monomers. The coordination sites could be too close together for tetrahedral cages to form, six ligands may not be able to pack that tightly together, resulting the **L3** ligand consistently crystalising out.

2.4.2 Tetrahedral Copper ions

The introduction of 3*d* ions with tetrahedral geometry, to **L3** in a 1:1 ratio had the potential to create discrete [2x2] squares. This hypothetical outcome can be seen in the Figure 34. A tetrahedral metal ion should coordinate to the *N* of the pyrazine and the N2 of the triazole, as discussed previously, which should result in two ligands being held perpendicularly to each other. This could ultimately form a discrete square complex, fulfilling the aim of this research, or, the ligands could form a continuous zig-zag 1D polymer chain, if the strain to close the ring is too unfavourable.

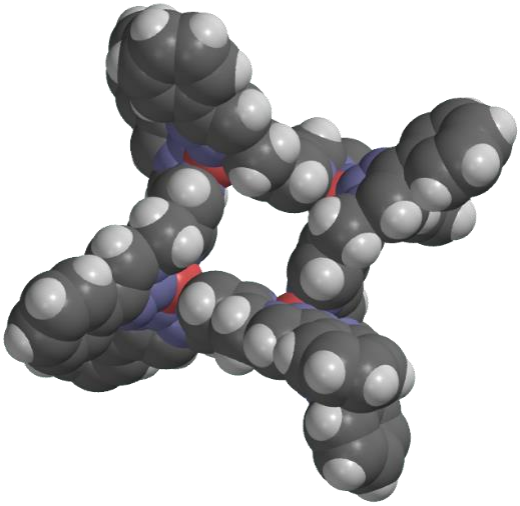

Figure 34: Geometric model, PM3 in Spartan, of the hypothetical [2x2] square, $\mathbf{L3}_4Cu(I)_4$.

The coordination geometry of this coordination cavity has previously been reported.[88] Herzigkeit, *et al.* introduced $[Cu(MeCN)_4](PF_6)$ to a similarly arranged chelation site, successfully coordinating the tetrahedral inclined Cu(I) to their pyridine-triazole site.

To attempt this reaction, a Cu(I) salt was required. $[Cu(MeCN)_4](PF_6)$ was first synthesised from Cu_2O, according to Equation 1, using a method from Kubas. *et al.*[104] shown in Apx5.1. This white crystalline salt needed to be tightly stored in a sealed container, flushed with Ar, and stored in the freezer. When a sample was left, in a desiccator, sections would become a bright, light blue, as the copper oxidised.

Equation 1: The synthesis for the Cu(I) as a $[Cu(MeCN)_4](PF_6)$ salt.

$$Cu_2O + 2HPF_6 \xrightarrow{MeCN} 2[Cu(MeCN)_4)][PF_6] + H_2O$$

Table 5: Attempts at complexation of **L3** and **L3Cu**

L3:[Cu(MeCN)$_4$]PF$_6$ (1:1)			**Colour Δ**	**Ppt**	**Crystal**	**Result**
RT Solvent	MeOH	A	Stayed a white suspension	-	White, Needle	**L3**
	DCM	B	White to yellow sus.	Yellow	White, Needle	**L3**
	$CHCl_3$	C	White to yellow sus.	Yellow	White, Needle	**L3**
	THF	D	White to yellow sus.	Yellow	White, Needle	**L3**
At 66 ºC	DCM	E	White to bright yellow With some orange sus.	Yellow	White, Needle	**L3**
	$CHCl_3$	F	White to bright yellow With some orange sus.	Yellow	White, Needle	**L3**
	THF	G	White to bright yellow sus.	Yellow	White, Needle	**L3**
***L3Cu** in MeOH injected into sealed **L3** in THF under Ar.*		H	Turned slightly yellow, sus. not as bright as the previous reactions	Yellow	White, Needle	**L3**
*Slow diffusion of **L3** and **L3Cu** across THF and MeOH*		I	The THF layer turned yellow.			**Yellow Gel**

***L3** dissolved in THF, frozen in bevel of liquid N, with* **L3Cu** in MeOH added, frozen, then *Et_2O added on top, frozen. The container was then left to thaw to RT with the slow diffusion of reagents across layer boundaries.*

The ligand **L3** was combined with [Cu(MeCN)$_4$](PF$_6$) in different solvents at RT and at 65 ºC, for an hour (Table 5). There was no colour change in the suspension in MeOH, but in DCM, $CHCl_3$ and THF reactions the white suspension became bright yellow, indicating some form of coordination to the Cu(I) ion. These precipitates were collected by filtration, (Figure 35). If this yellow precipitate was put into a solution of MeCN the precipitate would turn white. This indicated that the Cu(I) would preferentially coordinate to MeCN and release the **L3** ligand, and further indicate that **L3** can coordinate to Cu(I) in some way.

Reaction (H) was prepared by putting **L3** in THF in a bunged scintillation vial flushed with an argon balloon. The suspension was heated to 70 ºC and a 1:1 equivalence of [Cu(MeCN)$_4$](PF$_6$) in MeOH was injected into the reaction, and stirred at heat for an hour. The suspension again turned from white to bright yellow.

The yellow precipitate that was collected in reactions B-G, was insoluble in common solvents at room temperature but was partially soluble in hot THF. The precipitate never fully dissolved, but more white needles of **L3** crystallised out, as confirmed by SCXRD. The solution was filtered and the filtrate layer was vapour diffused with Et_2O, where white crystals of **L3** grew and more yellow precipitate appeared. If the reaction solution was put into the crystalising vial before being allowed to cool, white crystals of **L3** would crash out.

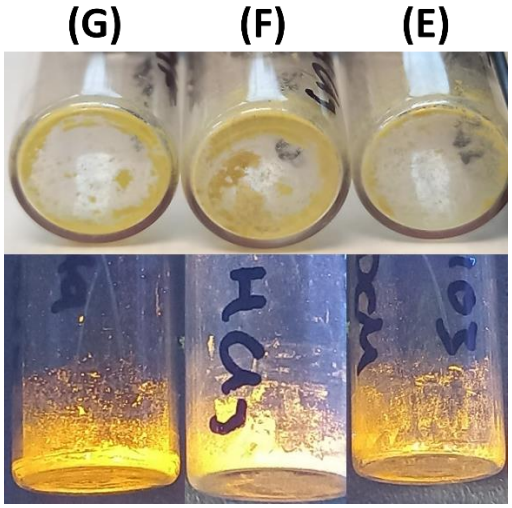

Figure 35: The precipitate resulting from reaction **L3** and $[Cu(MeCN)_4]PF_6$ in different hot solvents, G) THF F) $CHCl_3$ E) DCM. The pale yellow in the upper image, taken three weeks after synthesis, is a less intense than on immediate formation. The lower image shows the bright yellow emission under UV – nm.

In reaction (H), the complexation reaction was attempted in THF under argon. A large amount of fine white/clear needle crystals appeared, which SCXRD revealed to be **L3** again, but there were also some off white plate crystal, however, upon X-ray crystallography, this was determined to be the $[Cu(MeCN)_4]PF_6$ salt.

One of the final attempts at crystallisation, Reaction (I) was done via a slow diffusion of solid THF and MeOH, with a top layer Et_2O frozen in liquid nitrogen temperatures. The thawing of these layers was an attempt to slow the rate of complexation, in an aim to create crystals rather than a precipitate. Instead, this resulted in a tacky, yellow, gel, (Figure 36). The gel could be stretched below around 0.4 cm, with the tip of a glass pipette, and return to its original shape, when stretched further than this, a portion of the gel would break off. The formation of this gel was a strong indication that **L3** was forming a polymer network under these conditions. Organo-metallic gels are an area that have been researched on their own, to incorporated coordinated metals into a

polymer network to conserve the available properties, such as magnetism, catalysis and sensing.[105] However, further investigation into this gel product was not continued at this time.

Figure 36: Photo of the gel result from the cryo-diffusion of **L3** and $[Cu(MeCN)_4]PF_6$ salt in THF and Et_2O. The gel, stuck to the side of a scintillation vial, is being stretched by glass capillary tube. Photo taken three weeks after complexation, with a more saturated yellow colour than the original isolation.

A sample of this gel was submerged in MeCN, to determine whether the ligand could be removed from the Cu and exchanged with MeCN ligands, repeating what occurred when the yellow ppt product turned white upon addition of MeCN.

The gel lost intensity of yellow colour over time. The photo of the gel was taken after three weeks had passed, and was not as yellow as originally seen. This again indicates that any complexation that is occurring between **L3** and the $[Cu(MeCN)_4]PF_6$ salt is degrading either just over time or in exposure to air.

In conclusion, it seems like there is a possibility of forcing a complexation with $[Cu(MeCN)_4]PF_6$ if more reaction conditions are tested, but otherwise **L3** seems to preferentially self-sort into white crystals of the ligand.

2.4.3 Silver Complexes

With the consistent trouble occurring when attempting to complex tetrahedral Cu, attempts were made to complex with an alternative tetrahedral species. Silver(I) ions have been used extensively in the construction of supramolecular architectures.[106] Bodman *et al.* even formed [2x2] squares.[35] The d^{10} electronic configuration of silver(I) means that its complexes are diamagnetic, labile and can adopt a variety of coordination numbers ranging from two to six.[98] Crowley *et al.*[98] have previously shown the assembly of various polynuclear complexes with bi and tridentate pyridyl-1,2,3-triazole ligands, shown in (Figure 37), where the Ag(I) formed tetrahedral geometries, and square planar geometry. This led to the use of this more versatile metal being used, as no other metal complexation had been isolated to this point.

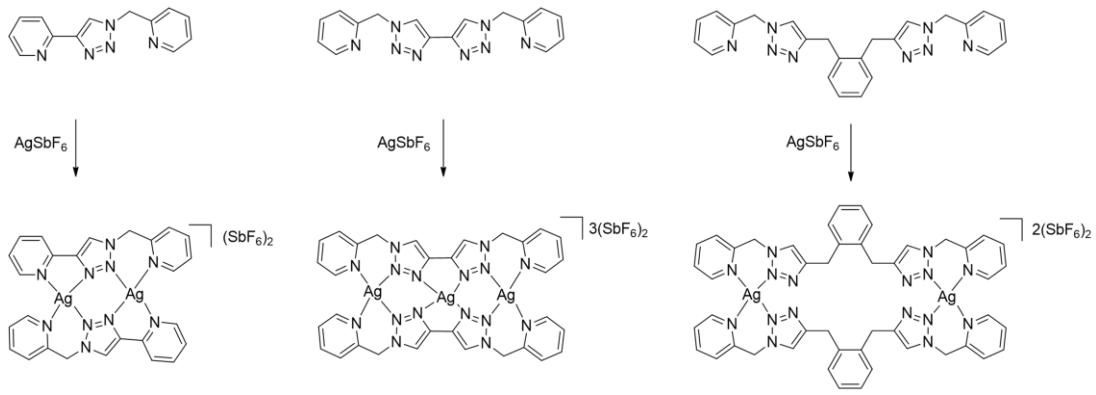

Figure 37: Ligands and Ag(I) complexes previously synthesised by Crowley *et al.*[98]

The metal salt, $AgNO_3$ was readily available, and so was used in an attempt to make a complex with **L3**. Given the results of the solubility tests in the reactions in Section 2.4.2, the reactions here were heated. The **L3** in the corresponding solvent, (Table 6) was heated to 70 °C, and $AgNO_3$ was added in a 1:1 ratio to **L3**, dissolved in MeOH. These reactions A-D were then cooled and vapour diffused with Et_2O. However, only uncoordinated **L3** crystallised out again.

Table 6: Reactions of **L3** with in $AgNO_3$ 1:1 ratios, stirred at heat under argon.

		Colour Δ	**Ppt**	**Crystal**	**Result**
MeOH	A	Stayed a white suspension		White	**L3**
$CHCl_3$	B	Stayed a white suspension		White	**L3**
DCM	C	Stayed a white suspension		White	**L3**
THF	D	Stayed a white suspension		White	**L3**
THF (Ar)	E	Stayed a white suspension	white	Pink/red	**L3Ag**

Success was achieved by taking, **L3**, suspended in THF, in a sealed argon flushed container, and adding $AgNO_3$ dissolved in MeOH by injection. The resulting solution was stirred for two hours. Isolation of the complex was achieved by either slow evaporation, or vapour diffusion of Et_2O into a THF solution containing the crude material resulting in very small red/pink, block-shaped crystals after one week. The crystals were barely sufficient quality to be characterised by X-ray crystallography. The polymeric $\{[Ag_2(\mathbf{L3})](NO_3)_2\}_\infty$ crystallised in a monoclinic, $P2_1/n$ space group, with a final R1 value of 18.8%, which allowed connectivity to be established. The asymmetric unit contained half of the **L3** ligand, a silver cation coordinated to one ligand, on the N3 on the triazole and to N1 on the pyrazine, and to a second ligand on the N4 of the triazole, and a fourth coordination site is occupied by the O3 oxygen of a NO_3^- counter ion (Figure 38). Each NO_3^- anion coordinated to the two Ag(I) atoms, of each side of the ligand, sit above and below the plane of the Tz rings. This counterion forms hydrogen bonding to the hydrogen atoms of the C3 and C4 of separate **L3** ligands, with a counter ion. The full molecule is generated by an inversion operation at the mid-point between the Ag-Ag atoms. The two adjacent Ag(I) ions are separated by 3.960 Å.

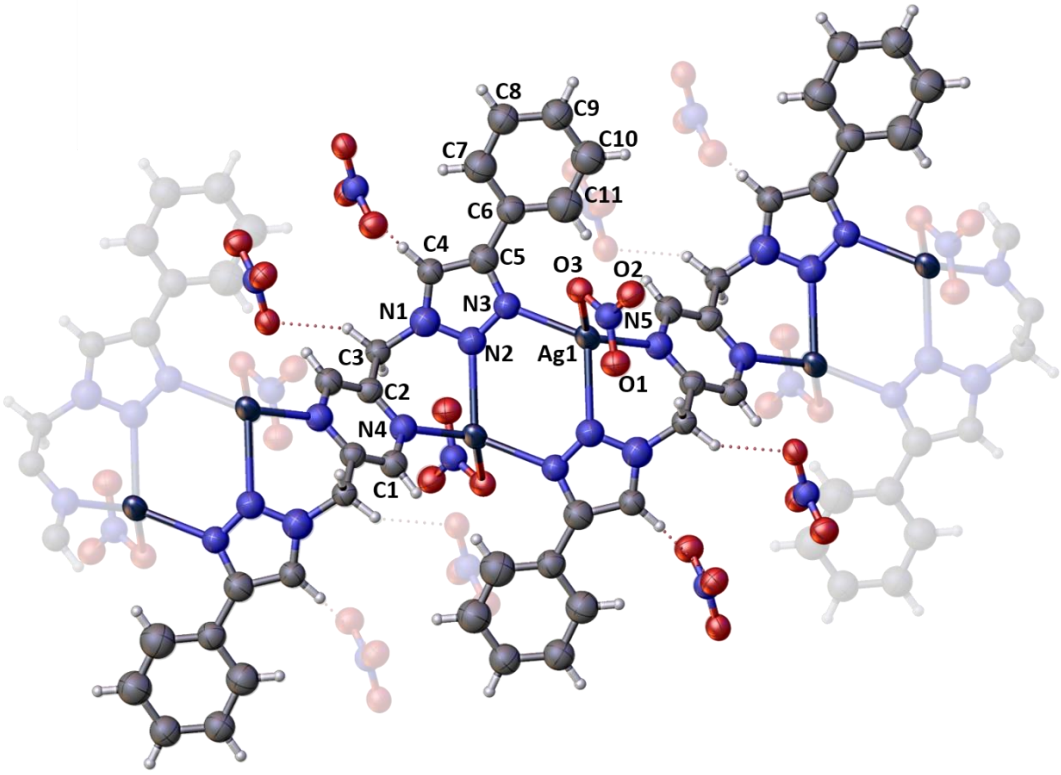

Figure 38: A single chain section of the crystal structure of the $\{[Ag_2(\mathbf{L3})](NO_3)_2\}_\infty$ complex, showing the side to side bonding of **L3** ligands by two Ag(I) ions, with the atoms of the asymmetric unit labelled. Colour Code: C = grey, N = blue, O = red, H = white, and Ag = dark blue.

Table 7: The selected bond lengths and angles related to the coordination of Ag(I) cations.

Bond Length Å		**Bond Angle °**	
Ag1 – N3[1]	2.23 (3)	N4[2]-Ag1-N3[1]	136.4 (10)
Ag1 – N2[2]	2.46 (3)	N4[2]-Ag1-N2[2]	79.7 (10)
Ag1 – N4[2]	2.28 (3)	N2[2]-Ag1- N3[1]	112.3 (9)
Ag1 – O3[NO3]	2.51 (3)	N3[1] – Ag1-O3 [NO3]	79.9 (10)
		N4 – Ag1-O3 [NO3]	128.5 (10)
		N2– Ag1-O3 [NO3]	125.5 (10)
Ag1 – Ag1[2]	3.96	C2-C2-C6	127.9

(1 = the atom is on the first ligand coordinated to the Ag(I) centre; 2 = the atom is on the first ligand coordinated to the Ag(I) centre; NO3 = the coordinated NO_3^- counter ion.)

The bond angles of the atoms coordinated to the silver centre are not the expected 109.5º of a metal ion in a tetrahedral arrangement, but the angles also don't quite match the expected $\theta_{1\text{-}3}$ = 120º and $\theta_{4\text{-}6}$ = 90º of a trigonal pyramidal geometry. A four-coordinate geometry index, τ_4 was developed by Yang, *et al.*[107] to determine the most appropriate geometry to describe a four-coordinate metal centre. The geometry index that results from Equation 2, shown below, results in a τ_4 factor, where τ_4 = 1.00 for a perfect tetrahedron, through to τ_4 = 0.00 for a perfectly square planar. A τ_4 = 0.85 is indicative of a trigonal pyramidal geometry.

Equation 2: The four-coordinate τ_4 index, by Yang, *et al.* [107]

$$\tau_4 = \frac{360^o - (\alpha + \beta)}{141^o}$$

This equation was applied to the geometry of the Ag complex, using the largest of the six angles of the four-coordinate metal ion, as the α and β values; in this case, 136.7º and 128.5º. For this complex the τ_4 value was calculated to be 0.67 indicating that this Ag(I) centre had a seesaw geometry (τ_4 = 0.64), to trigonal pyramidal than square planar geometry.

The triazole-phenol (Tz-Ph) ends of the ligands in this complex are bent at an angle of 127.98º to the pyrazine ring, as compared to 107.59º present in the free ligand structure, due to the Ag(I) coordination. Coordination of the Ag(I) also accounts for the observation that the pyrazine ring lies flat relative to the Tz-Ph arms of the ligand, rather than perpendicular as observed in the uncoordinated ligand (Figure 39).

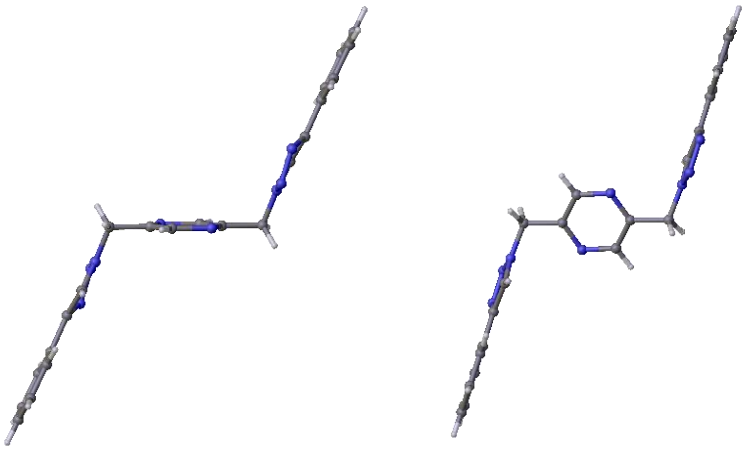

Figure 39: Left: a side on view of, **L3** in the **L3Ag,** coordinated to Ag(I) ions. Right: a side view of the uncoordinated **L3.**

The structure of this complex was both interesting and unexpected. It had been expected that a tetrahedral geometry of Ag(I) would preferentially coordinate to N3 over N4, rather than coordinating to both, as seen in the solved structure. The donor atoms that are available from **L3**, have turned out not to be discerning enough to form discrete structures.

Table 8: Hydrogen Bonding within the **L3Ag** HOF network.

D-H-A	D-H (Å)	H ··· A (Å)	D ··· A (Å)	D-H ··· A(°)
C3 - H_{c3} - O3	0.99	2.18	3.04	145.6
C4 - H_{C4} - O2	0.95	2.04	2.99	175.6

This complex resulted in a polymeric chains of $\{[Ag_2(\mathbf{L3})](NO_2)_2\}_\infty$ (**L3Ag**), as ligands coordinate to Ag cations. Each of the 1D chains are held, slightly overlapping, in a 2D sheets through moderate strength hydrogen bond interactions,[108] from the C3, and C4(Tz) hydrogens to the O3 and O2 coordinated oxygens of the NO_3^- anions respectively (Table 8 and Figure 40). Each NO_3^- anions is involved in three bonds, as the O3 oxygen of each intermediate NO_3^- anions, is coordinated to a Ag(I) of an adjacent 2D sheet, as well as the O3 hydrogen bond, ultimately forming a large 3D HOF structure (Figures 41 and 42).

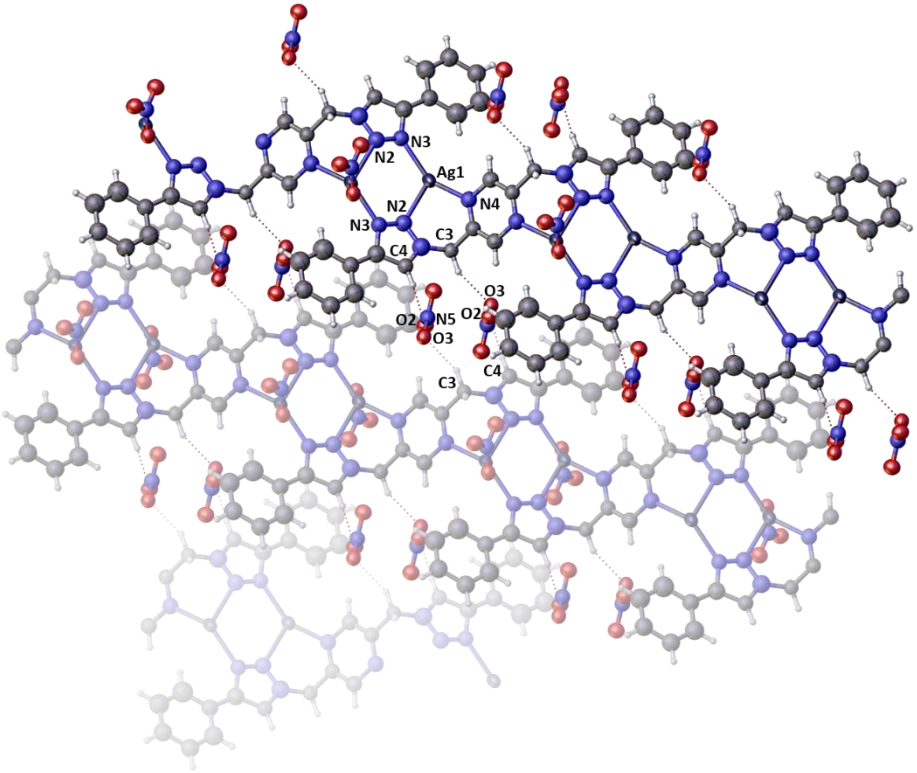

Figure 40: The crystal structure of three 1D polymer chains, with the Tz-Ph rings of the chains overlapping, held by π-π bonds, and C3-O3 and C4-O2 hydrogen bonds in 2D sheets. The separate 1D chains are gradated for clarity.

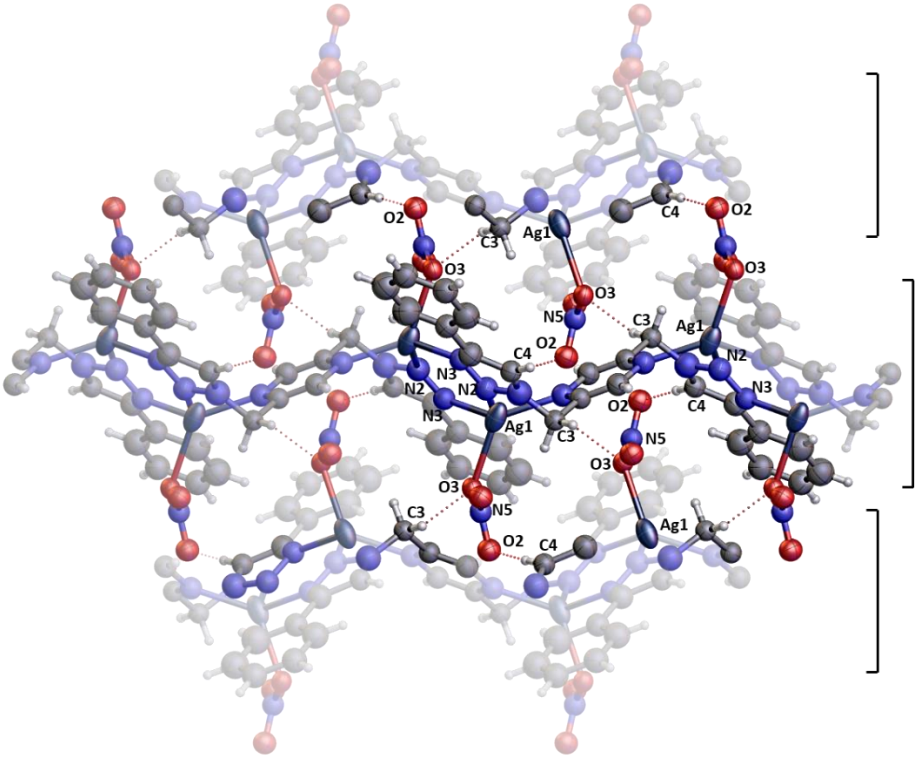

Figure 41: The crystal structure of three 2D sheets, indicated by brackets, stacked in a 3D network, held by hydrogen bonds. The upper and lower sheets are gradated for clarity.

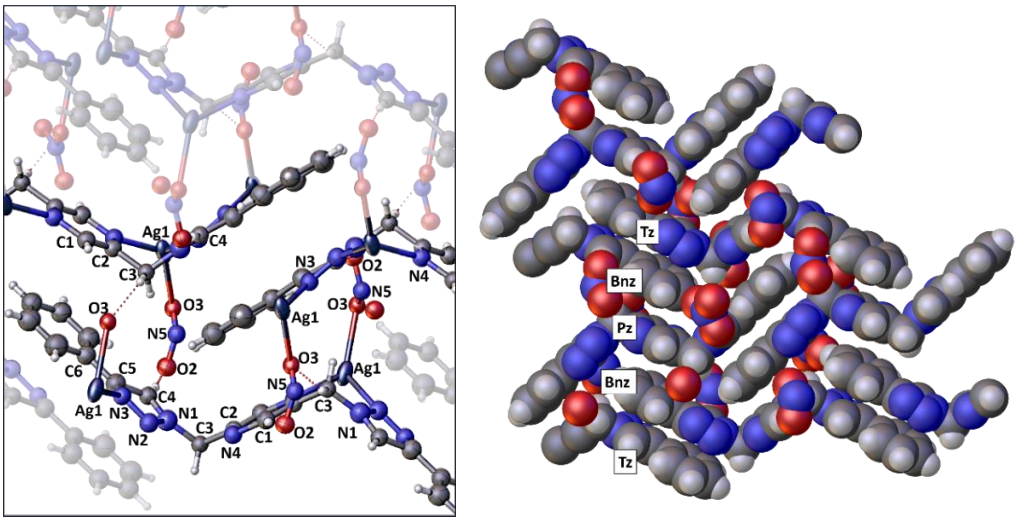

Figure 42: a) side of view of the 3D stacking of the 2D sheets, with the NO_3^- atoms not invovled in the bonds removed for clarity. b) the side on view of the sphere packing of the 3D stacking of the 2D sheets, with the Ag(I) ions rmoved for clarity. The offset layering of the ligands results in the π-π bonds of overelapping of rings in order of a triazole, benzene, pyrazine, benzene, and triazole, before the triazoles then facing the edge face of another benzene.

In the 3D layering, the **L3** ligands lie in an offset repeating pattern that results in the overelapping order of rings in a triazole, benzene, pyrazine, benzene, and triazole, before the triazoles then facing the edge face of another benzene. This overlay indicates that π-π bonds are involved in the 3D packing of the complex.

Along with the hydrogen bonds holding the vertical stacks together, there is also a repeating series of weak π- π and CH- π interactions, that appear in an offset pattern between the layers (Figures 42 and 43. Table 9).

Table 9: The intermolecular bonds between the 2D sheet layers of the complex.

	Distances (Å)		Angles(º)	
1	Ph^{cent} – C2			
2	C9 (Ph) – Pz^{cent}	3.74	C6 – Ph – C2(Pz)	93.9
			Ph^{cent} – C6 – C2(Pz)	64.4
3	Ph^{cent} – C4 (Tz)	3.33		81.6
4	H^{C9} – Tz^{cent}	2.86	C9(Ph) – H^{C9} – Tz^{cent}	
	C9(Ph) – Tz^{cent}	3.75	C9(Ph) – Tz^{cent}- N1	98.7

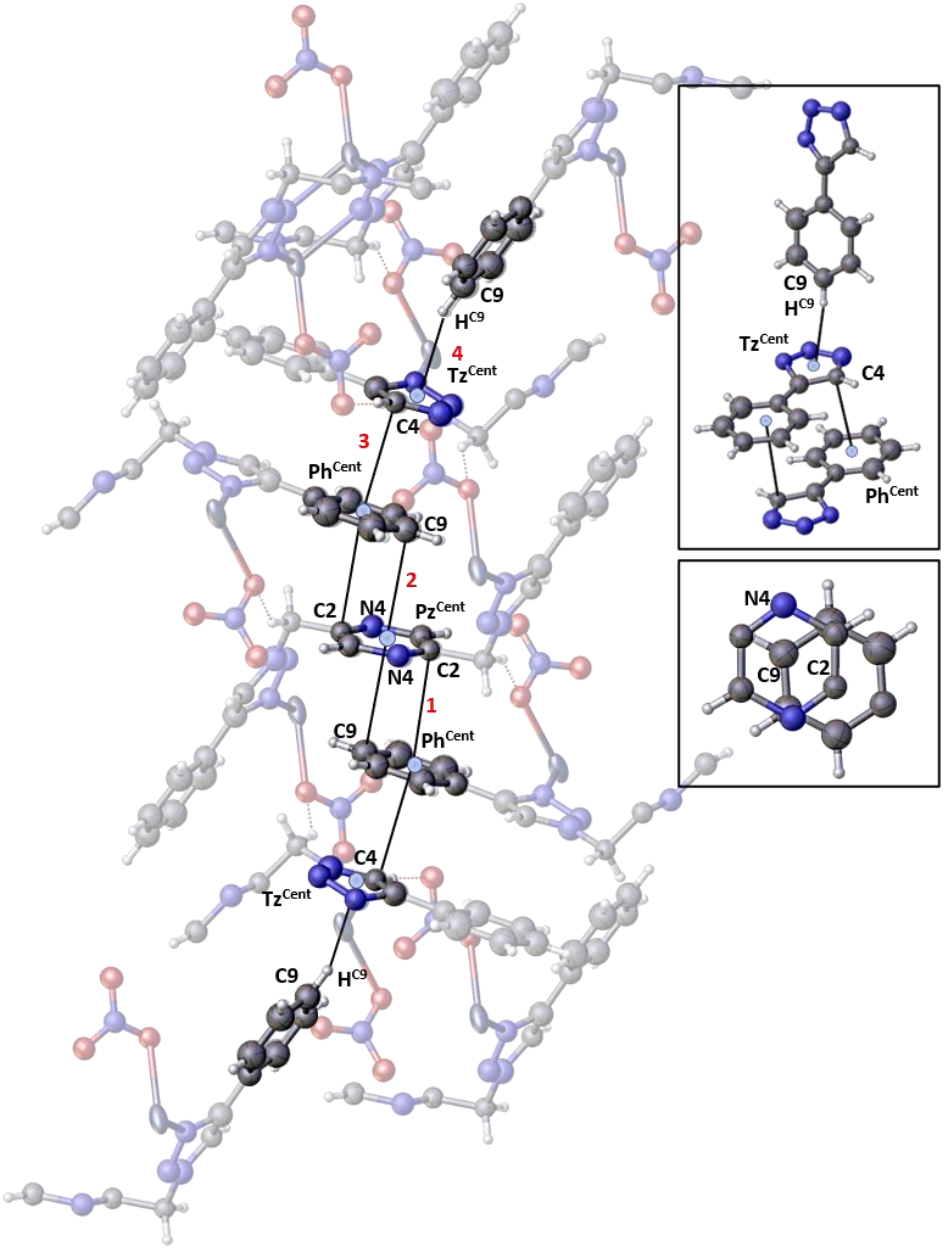

Figure 43: The offset stacking of 2D sheets of polymers resulted in a repeating pattern of intermolecular bonds between sheet layers. The pattern of a C9-H of a phenol, to a triazole, to a phenol, to a pyrazine, to a phenol, to a triazole to a phenol.

2.5 Conclusions on L3

The **L3** ligand was successfully synthesised from **D1**, via the versatile CuACC click reaction, and isolated as a single crystal in high enough quality for X-ray spectroscopy. The lone **L3** ligand arranged in opposing lines of zig-zag arranged ligands.

The complexation of **L3** with octahedral 3*d* transition metal ions, was unsuccessful. This could be because the two bidentate chelation sites are too close, and the overlap of the benzene tail of three ligands would be too great. The tetrahedral $[M_4L_6]$ arrangement of this ligand might not be physically possible, or the strain could be too great to ever be favourable. If these attempts formed crystals, they were isolated **L3**, it is also possible that the **L3** ligand is too insoluble to work with.

When **L3** was introduced to tetrahedral $[Cu(MeCN)_4]PF_6$, the solutions would go from white to a bright yellow, indicating the coordination of **L3** to Cu. The disappearance of this yellow with the addition of excess MeCN, confirmed that there was a complex forming. When a liquid-liquid diffusion of frozen THF and Et_2O was tried, a tacky, yellow, metalo-organic gel was formed. **L3** is likely forming a polymer network, with Cu(I), that will be difficult to isolate.

The tendency of **L3** to form polymer networks was confirmed with the isolation of red **L3Ag** crystals; $\{[Ag_2(\mathbf{L3})](NO)_4\}_\infty$. Polymer chains of **L3** and Ag(I) were held together in a hydrogen bond network. The expectation was that, coordination would occur at the N of the pyrazine and the second N of the triazole did not occur. The tetrahedral Ag(I) did not preferentially coordinate to the N3 over N4, rather than coordinating to both, as seen here. The hydrogen bonding from C3 was also unexpected. The bonds that are available from **L3**, have turned out not to be discerning enough to from discrete structures.

Herzigkeit, *et al.* obtained the desired tetrahedral coordination with $[Cu(MeCN)_4]PF_6$, when the click was closed with ^{t}Bu, rather than a phenol.[88] If it was the size of the ligand arm preventing discrete complex formation, altering the size of the capping section of the ligand could result in success.

Another option for the future would be to use silver salts with larger counterions. They would be less likely to become involved in the complexation with the **L3**, as is what happened with the nitrate ions.

2.6 Synthesis of L4

2,5-bis((4-((pyridin-2-ylmethoxy)methyl)-1H-1,2,3-triazol-1-yl)methyl)pyrazine

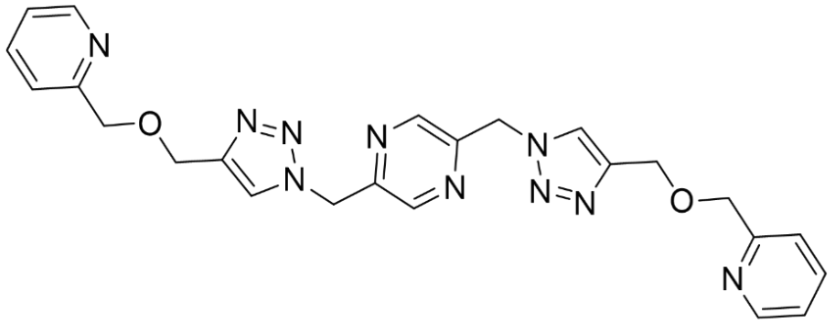

Figure 44: **L4** -2,5-bis((4-((pyridin-2-ylmethoxy)methyl)-1H-1,2,3-triazol-1-yl)methyl)pyrazine

A second direct 'click' ligand that was designed was **L4** (Figure 44). This would produce a ligand with a bi-tridentate coordination sites, which would hypothetically be suitable for coordination with octahedral 3*d* metal cations.

2.6.1 Williamson Ether Reaction

To create the molecule with a terminal alkyne, that would also contribute to the chelation of the ligand to a 3*d* transition metal, a terminal alkyne would be added to a pyridine. This would be done via a Williamson Ether reaction, for the ether to enable the formation of a tridentate chelation site. The mechanism for a Williamson ether Reaction follows a general S_N2 reaction mechanism.

2.6.2 Synthesis of D3

This ligand began with the synthesis of 2-((prop-2-yn-1-yloxy)methyl)pyridine (**D3**), (Scheme 5) the method for which, was adapted from Delso *et al*.[109]

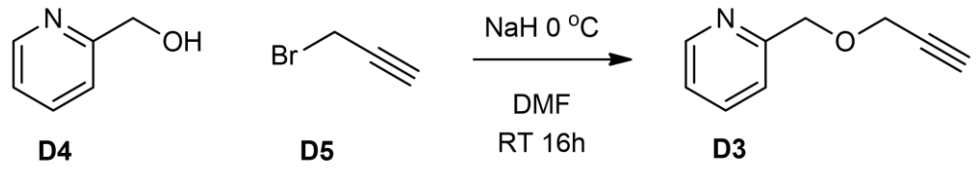

Scheme 5: **D3**; Williamson Ether Synthesis: NaH 0 ºC, DMF, RT, 16h

Pyridin-2-ylmethanol (**D4**) was dissolved in DMF, bubbled with Ar, and cooled to 0 ºC, upon which NaH was carefully measured and added in portions. This produced gaseous H_2 and so was done in small portions and kept away from heat. When

hydrogen production ended, the vessel was covered in foil to prevent the degredation of the propargyl bromide (**D5**) which was then added. The solution was stirred overnight at RT. An extraction work up resulted in the isolation of the **D3** product as an oil.

An almost colourless, faint yellow oil, (the intensity of yellow being dependant on the concentration of Br side product extracted with the crude product) **D3** was isolated in up to 0.12 g in up to 90 % yield. The full method is found in Apx5.2.

The ^{1}H NMR of **D3** agreed with the literature values[109] 8.55 (d, 1H, J = Hz), 7.68 (t, 1H, J = Hz), 7.44 (d, 1H, J = Hz), 7.20 (t, 1H, J = Hz), 4.73 (s, 2H), 4.28 (d, 2H, J = Hz), 2.46 (t, 1H, J = Hz). The fully assigned spectra is found in Apx12.3.4.

2.6.3 Synthesis of L4

The synthesis of **D3**, created an available terminal alkyne, ready for a click reaction, with **D1**. The synthesis of **L4**, (Scheme 6) used the same conditions are those described in the synthesis of **L3**, seen previously, as the reaction was similarly an alkyne clicking to an azidomethyl group attached to a pyrazine. The details of the method are found in full in Apx5.3.

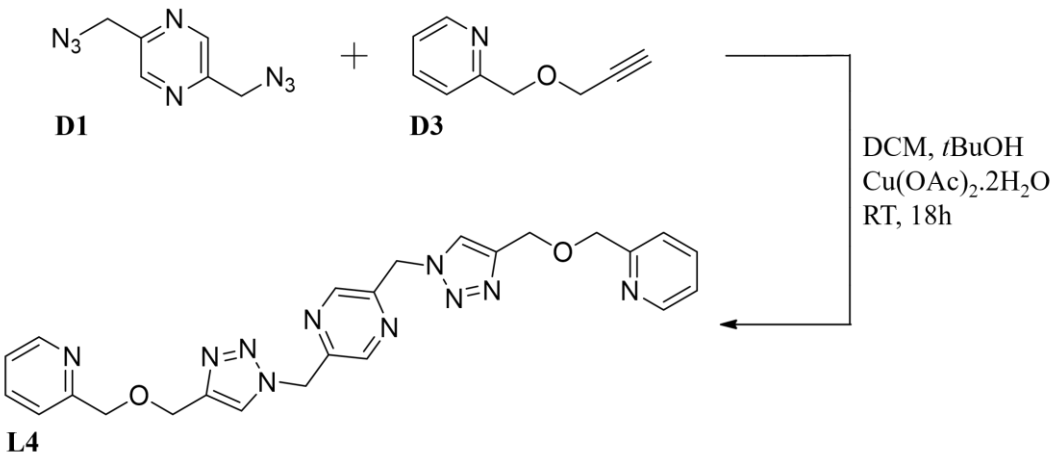

Scheme 6: Click synthesis of **L4**, from **D1** and **D3**: DCM, tBuOH, $Cu(OAc)_2.2H_2O$, RT, 18h

The initial ppt isolated through filtration, was a tacky, green/brown sludge. It was assumed that the green colour in the crude product was due to an excess lingering of copper catalyst. It is also possible that this could have been due to **L4** coordinating

with some of the copper catalyst forming some type of organo-metallic gel; the likes of which was discussed previously in Section 2.4.2.

The crude product was washed with MeCN and DCM, and subsequently dried again, forming a light brown solid, in a very small amount, with a crude yield of 84%.

The ^{1}H NMR recorded, below, are what are presumed to be the presence of **L4**, however, this ligand was never isolated in a large enough quantity to confirm the exact peak splitting, these results can be seen in Apx12.3.5. Thus, the full confirmation of the success of the method of **L4** synthesis, and whether the ^{1}HNMR itself were successful, could not be determined. Further investigation would be required to characterise this ligand.

^{1}H NMR (400 MHz, DMSO): δ = 8.65 (s, 1H), 8.51 (m, 1H), 8.26, (s, 1H), 7.78 (m, 1H), 7.42 (m, 1H), 7.29 (m, 1H), 5.81 (s, 2H), 4.65 (s, 2H), 4.60 (s, 2H).

2.6.4 Conclusions on L4

At this point in time, the **D1** was only being produced in small quantities due to its explosive nature. The success and ease of synthesis of **L3** resulted in efforts being focussed on **L3** synthesis, upon the isolation of **D1**, to further complexation studies. This, ultimately, led to exploration into **L4** synthesis being shelved for the time being.

The investigation into **L4** was done concurrently with **L3**. The unexpected, extended polymerisation of **L3**, with coordination to the N2 of the triazole, could also be a possibility for the triazole in **L4**. The two coordination sites could be more likely to both coordinate to 3*d* metals, rather than the initial expectation that the Pyr-O-Tz would be more favourable to coordination with octahedral metals than the Tz-Pz site.

The yields of the **L4** synthesis were too low to begin investigation into **L4** coordination with 3*d* metal salts, but this could still be a possible route of investigation for another time.

2.7 Future work from di-azide ‘click’ ligands

With the isolation of **D1**, there is the possibility for this central pyrazine unit to create a variety of ligands within this family. Any molecule with a terminal alkyne moiety can be added to this central unit and can be used to introduce different functionalities to the ligand. If this central unit is able to form a discreet polygon organo-metallic complex in the future, very tightly built units could be created with a range of functions. Some of these possible alkyl units are shown in Figure 45.

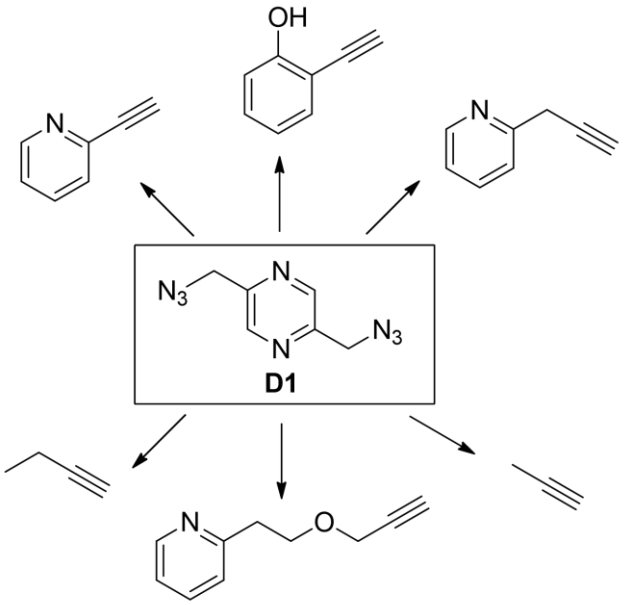

Figure 45: Possible alkynes that could be clicked to **D1** (central) to form possible future ligands. Clockwise, from the top left (TL): 2-ethynylpyridine, (TC) 2-ethynylphenol, (TR) 2-(prop-2-yn-1-yl)pyridine, (BR) prop-1-yne, (BC) 2-(2-(prop-2-yn-1-yloxy)ethyl)pyridine, (BL) but-1-yne.

3.0 Synthesis and Characterisation: L5 and L6

The investigations into the synthesis of **L3** and **L4** provided a new familiarity with click reactions. From here a more efficient triazole synthesis was designed. The introduction of two propargyl groups to the bis-hydroxymethyl, **C3,** using a Williamson-ether reaction, produced **E1**, (Scheme 7). The isolation of a molecule with two terminal alkynes, required fewer steps than the synthesis of the bis-azide component for **L3** and **L4**.

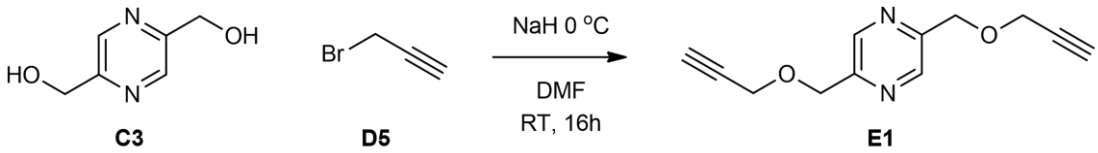

Scheme 7: **E1** from the Williamson Ether Reaction of **C3** and **D5:** NaH, 0 °C, DMF, RT, 16h.

When the bis-alkyne, **E1**, was reacted using click chemistry with a primary azide, it produced a ligand **L5R** with two anti-parallel, terdentate, ether linked pyrazine/triazole (Pz-O-Tz) chelation sites. These have the potential to create a coordination cavity similar to the ether linked pyrazine/triazole (Pyr-O-Tz) site proposed in **L4**, (Figure 46).

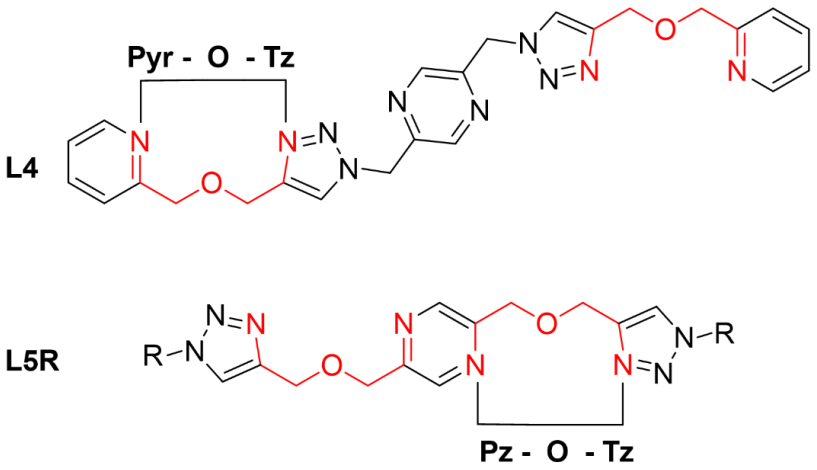

Figure 46: Chelation sites built from two *N*-heterocycles joined by a bridging ether. Top: the second chelation site of **L4**, a pyridine, bridging ether, and triazole (Pyr-O-Tz) unit. Bottom: the general structure of **L5R** and its analogues, with a pyrazine, bridging ether, triazole (Pz-O-Tz) chelation site.

These Pz-O-Tz trimeric chelation sites will provide three of the six required donor atoms, to coordinate with octahedral 3*d* ions, potentially allowing the formation of

metal-organic complexes, with two ligands held perpendicular to each other. This expected perpendicular arrangement, of ligands with structural rigidity provided by the central pyrazine unit, should lead to discrete complexes. This turned out not to be the case for the newly synthesised **L5** and **L6** ligands; as explained in Section 4.0.

3.1 Comparisons to previous works

With the successful synthesise of **L5** and **L6**, discussed in the upcoming Section 3.4, this chelation site was investigated for any appearance in literature. Previous published literature with similar chelation sites can be found, but none with this exact coordination arrangement, Pz-O-Tz.

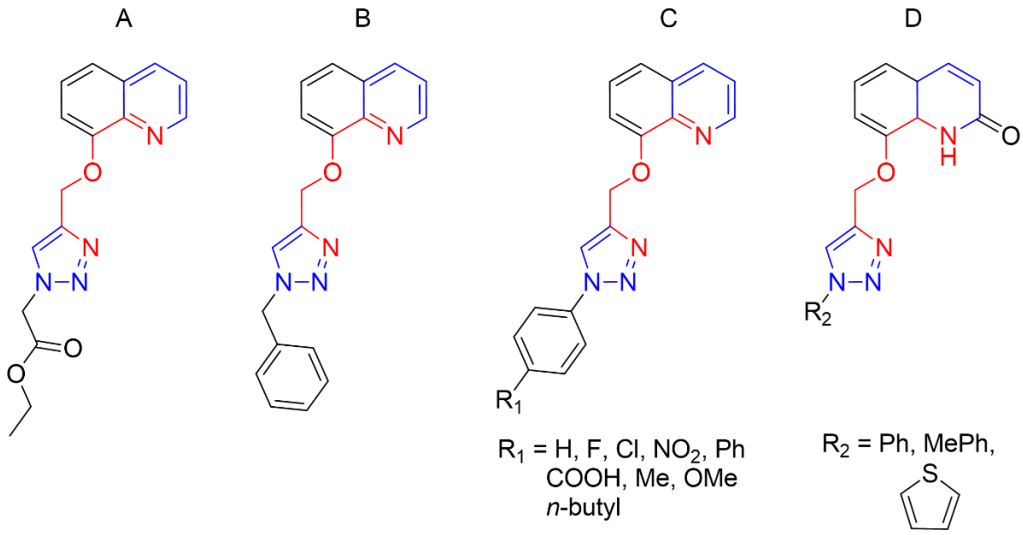

Figure 47: Examples of previously synthesised molecules from literature, with a P_-O-Tz arangement. A) Hao *et al.*[110] B) Irfan *et al.*[111]C) Aneja *et al.*[112] D) Gümüş *et al.*[113]

Some molecules, with a similar, Px-O-Tz, sequencing were found, (Figure 47), however, these molecules were not synthesised for the purposed of supramolecular chemistry with 3*d* ions. Molecule (B) was synthesised for antifungal purposes,[111] while, the (C)[112] and (D)[113] molecule derivatives, were investigated for their anti-bacterial properties.

Molecule (A) produced by Hao *et al.*[110] was one that was coordinated to transition metals; Fe^{3+} and Zn^{2+} as mononuclear complexes. This was done to investigate the fluorescent properties of a 1,2,3-triazole linked 8-hydroxyquinoline chemosensors, to test whether these biologically present metals would quench biological sensors.

3.2 Isolation of Novel bis-alkyne E1

The synthesis of **E1**, and the two alkynes necessary for the click reactions that followed, began with the introduction of **D5** to **C3**, via a Williamson Ether reaction. This reaction, (Scheme 5) was adapted from the method used to produce **E1**, which combined a propargyl with a 2-hydroxymethyl pyridine, based on the work by Delso *et al.*[109] The same conditions as the **D3** reaction in Section 2.6.2, were used, with the stoichiometry altered for the bis-ether formation, to produce 2,5-bis((prop-2-yn-1-yloxy)methyl)pyrazine (**E1**).

This reaction resulted in a very faint yellow oil, (the intensity of yellow corresponding to the concentration of Br_2 in the crude product collected). This reaction produced a yield of 74 %. The full details of this can be found in Apx6.1. The success of the synthesis of this molecule, was confirmed though Mass Spec, ^{1}H NMR, and ^{13}C NMR; shown in Table 10, and assigned in Apx12.4.01-03. The appearance of the triplet at 3.25 ppm in the ^{1}H NMR, and a signal at 78.29 ppm in the ^{13}C NMR, both indicate the presence of the alkynes. The (*m/z*): 239.14 (100) 240.14 (14) [**E1**, Na], indicates the presence of the **E1** molecule, and the absence of any, M (100), M+2 (97), M+1 (3), splitting typical of Br, meaning the Br has been substituted from the molecule.

Table 10: Assignment of **E1** ^{1}H and ^{13}C NMR in DMSO (ppm).

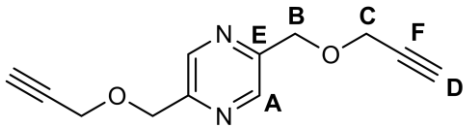

E1 assigned with ^{1}HNMR and ^{13}CNMR peaks						
	A	**B**	**C**	**D**	**E**	**F**
*^{1}H NMR**	8.63	4.68	4.30	3.52	-	-
	s 2H	s 4H	d 4H	t 2H		
J (Hz)			2.33	2.23		
^{13}C NMR$^{\intercal}$	142.97	70.29	58.16	78.29	152.21	80.31

**(500 MHz, DMSO): δ ppm* *$^{\intercal}$ (126 MHz; DMSO): δ ppm*

With the successful synthesis of **E1**, a final click reaction with a terminal azide, would cap the ligand with a H-1,2,3-triazole formation. This step could be done with a wide range of azides. This opens up a ligand system that can be used to create discrete structure that can be functionalised, with different properties, though the addition of different end molecules.

3.3 Synthesis of capping azides. E2 and E3.

To test the utility of the ligand system, azido butane (**E2**), and 3-azido-1-propene (**E3**) were synthesised (Scheme 8). These molecules were used as simple end units, to click to the alkyne appended to pyrazine **E1**. At this stage simple azides, without other function groups, were used to keep subsequent coordination steps simple, with 3*d* ions.

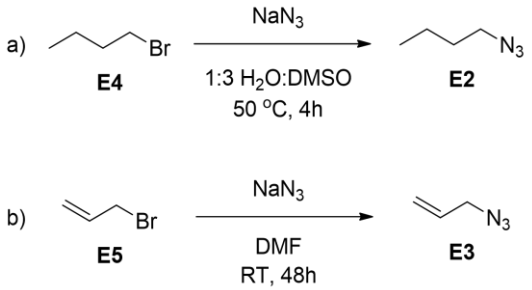

Scheme 8: Preparation of Azide click units. a) 1-azido butane (**E2**) NaN_3, (1:3) H_2O:DMSO, 50 °C, 4h. b) 3-azido-1-propene (**E3**): NaN_3, DMF, RT 48h.

As with other parts of this research, the C:N ratios of these molecules were acknowledged. In this case **E2** had a C:N ratio of with 4:3 and in **E3** a ratio of 1:1. Due to the potential explosive nature of organic azides, the synthesis of these molecules was never done in quantities of reagent of more than 0.8 g, and for the higher ratio of **E3**, this was kept dilute in DCM. The reagents were also stored in temperatures below RT.

A simple method for the synthesis of **E2** was adapted from Darrah *et al.*[114] who synthesised azido propane. This method only took four hours, and the clear oil, isolated itself as a decantable layer on top of the DMSO, in isolated yields of 97 %. that could be used without further purification; the **E2** could be stored in the freezer with no risk of degradation.

The synthesis of **E3** was initially attempted with the chemical conditions used by Darrah *et al.*[114] but at RT, over 48 hours. From this, **E3** could be isolated, but in very low yields, with only 5 mg ultimately isolated. A second method for the synthesis of **E3** was from Yang *et al.*[115], replacing the literature roto-evaporation step with liquid extraction. The resulting solution was reduced in volume and the product was not isolated from the concentrated solution. This method successfully obtained 0.28 g **E3** in DCM, in a yield of 42 %, calculated from ^{1}H NMR. This solution could then be utilised in the next step of ligand synthesis.

The full details of these methods are found in, **E2** (Apx6.2.) and **E3** (Apx6.3.). The ^{1}H NMR spectra of **E2** and **E3** can be found in Apx12.4.04-06, and both agree with values found in literature.[115-116]

3.4 Synthesis of Pz-O-Tz bis-tridentate Ligands: L5 and L6

The final step of the Pz-O-Tz ligand synthesis was to perform the click reaction of the novel **E1**, with the capping azide molecules **E2** and **E3**. For the synthesis of **L5**, the click reaction of **E2** with **E1** was initially done using the conditions used in the synthesis of **L3**. This produced low yields, between 27-35 %; however, neither the alkyne, nor azide groups were not as closely associated to the pyrazine as they had been in the synthesis of **L3**. As a result, the method was modified from that of Brotherton *et al.*[93] and a higher 10% mol sodium citrate was included in the reaction, increasing to a 63-70 % yield.

The synthesis of **L6**, also adopted the this method, with the only difference being a greater ratio of DCM in the synthesis of **L6**, due to **E3** being kept in a DCM dilution. Scheme 9, shows these reactions below.

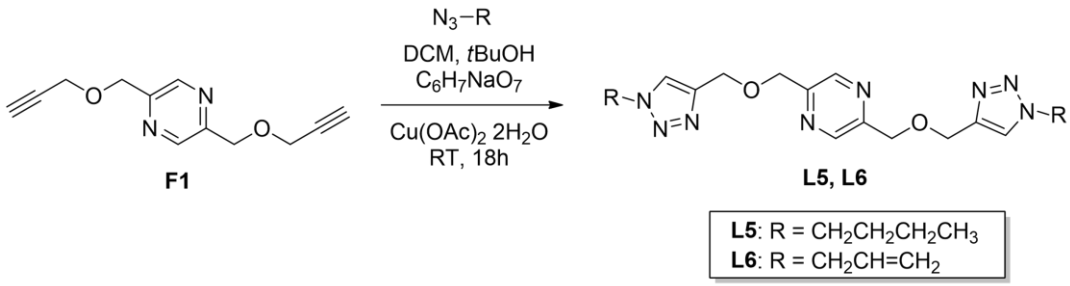

Scheme 9: Synthesis of Pz-O-Tz bis-tridentate ligands: DCM, *t*BuOH, Sodium Citrate, $Cu(OAc)_2.2H_2O$, RT, 18h. **L5** and **E2**: R = *n*-butyl, **L6** and **E3**: R = 1-propene.

The ligand **L5** could be isolated in reasonable yields by the precipitation of a greyish-light brown ppt, after filtration of the organic layer. The isolated **L5** was pure by ^{1}H NMR so was able to be utilised without further purification. This reaction gave 0.2614 g in a 78 % yield. (Apx6.4)

No precipitate was formed from the **L6** reaction, so the organic layer was concentrated *in vacuo*, and dried, resulting in the isolation of a dark brown, tacky solid, with a crude product yield of 440 mg, (102%). (Apx6.5) The ^{1}H NMR of **L6**, showed the presence of **L6**, along with DMF and a small amount of some unknown waste products.

Although impurities were present, some test complexation reactions were performed with no further purifications. In the future, eluents will be tested for the purification via chromatography, that will be required for **L6** to be further purified.

For both **L5** and **L6** ligands, the disappearance of the alkyne triplet 3.52 ppm of **E1** and the presence of a new 2H singlet at ~8.15 ppm, indicated the successful formation of the 1,2,3-triazole groups. A correlated ^{13}C NMR peak at ~124 ppm of the -*CH*- of the triazole, confirmed this, along with the appearance of a peak around ~144 ppm, of the non-protonated C of the triazole, next to the already present ~142 ppm peak of the pyrazine.

In **L5**, the N_3-CH_2 ^1H peak in **E2** shifted from a triplet at 3.26 ppm to a triplet at 4.34 ppm when the azide became a triazole. In **L6**, the doublet of quartets 5.87 ppm peak of CH=, of the allyl azide, shifted to a 6.02-6.07 ppm doublet of quartets peak, when the triazole formed. The full NMR data for **L5** is shown in Table 11, and in Table 12, for **L6**. The ^{1}HNMR, ^{13}CNMR, COSY, and HMQC spectra of **L5** and **L6** are assigned in Apx12.4.07-14.

*Table 11: Assignment of **L5** ^1H and ^{13}C NMR in DMSO (ppm).*

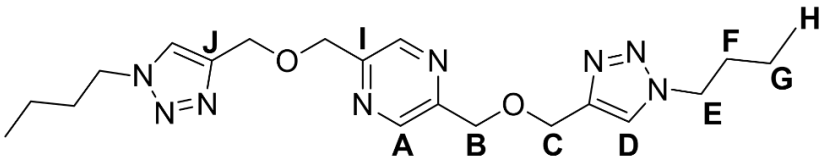

	A	B	C	D	E	F	G	H	I	J
*^1H NMR**	8.63	4.68	4.67	8.17	4.34	1.78	1.22	0.89	-	-
	s 2H	s 4H	s 4H	s 2H	t 4H	q 4H	m 4H	t 6H		
J (Hz)					7.05	7.33 7.11	7.45	7.38		
^{13}C NMR$^{\intercal}$	142.8	70.7	64.1	124.5	46.5	32.1	19.5	13.8	152.5	143.9

**(500 MHz, DMSO): δ ppm* $^{\intercal}$ *(126 MHz; DMSO): δ ppm*

Table 12: Assignment of **L6** ^{1}H and ^{13}C NMR in DMSO (ppm).

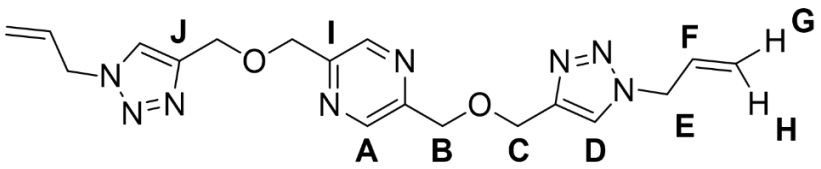

	A	B	C	D	E	F	G	H	I	J
*^{1}H NMR**	8.63	4.68		8.14	5.00-5.02	6.02-6.07	5.14-5.18	5.24-5.26	-	-
	s 2H	s 8H		s 2H	d 4H	dq 2H	d 2H	d 2H		
J (Hz)					5.93	6.29 10.38 5.26	16.94	10.2		
*^{13}C NMR*ᵀ	142.82	70.76	63.99	124.66	52.10	133.23	119.17		152.52	144.14

**(500 MHz, DMSO): δ ppm* ᵀ *(126 MHz; DMSO): δ ppm*

The m/z and IR spectra corroborated the formation of these ligands. The (m/z) results, summarised in Table 13, show the presence of the successfully synthesised **L5** and **L6**. As shown in Table 14, an aromatic N=N stretch around 1450 cm^{-1}, a C-N (Tz) stretch between 1270-1400 cm^{-1} and a C=C (Tz) stretch around 1500 cm^{-1}, all indicate the formation of the triazole groups. The C-O-C stretches around 1090 cm^{-1} and 850-900 cm^{-1} confirm the presence of the ether groups. The full IR spectrum for **L5** and **L6** are summarised in Apx12.5.

With the successful synthesis of **L5** and **L6**, attempts were then made to complex these ligands with 3*d* ions and 4*f* ions. The methods, results and conclusions of which are discussed in Section 4.1.

Table 13: (m/z) data for **L5** and **L6**

	[**L**H]	[**L**Na]	[**L**K]	[2**L** Na]
L5	415.21(100) 416.18 (22)	437.19 (100) 438.19 (20)		851.37 (100) 852.36 (50)
L6	383.05 (100)	405.12 (100)	420.99 (100)	787.28 (100)

Table 14: Selected **L5** and **L6** IR data (cm^{-1})

	C-H (Tz)	C=C	C=C (Tz)	N = N (Ar)	C-N	C-O-C	C-O-C (sym str)
L5	3118.84	1669.37	1484.80	1458.67	1349.86	1091.34	870.35
L6	3143.29	1664.71	1490.69	1463.86	1338.13	1095.00	886.43

3.5 Future Analogues of L5R

The arrangement of **E1**, with symmetrical terminal alkynes, means that any primary azide can be used in a click reaction to complete a ligand, allowing for the development of a new family of ligands. Different end groups could be added to promote different arrangements of supramolecular structures, or facilitate different chemical properties.

Some primary azides, that future research could start from, are illustrated in Figure 48. This new **E1** core molecule could lead to endless new ligands.

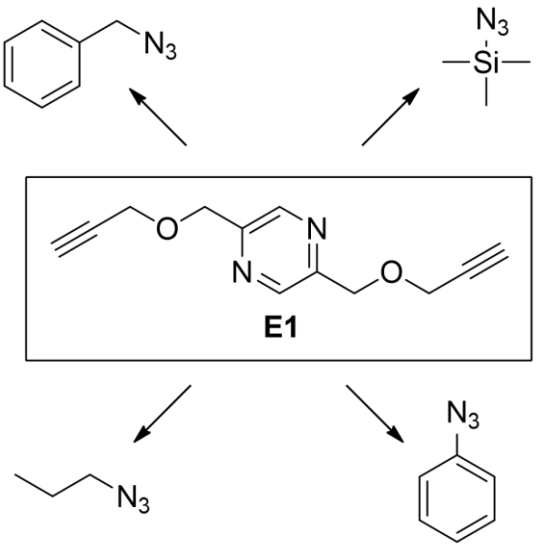

Figure 48: Future molecules to click to **E1** (Central). Clockwise from top left (TL): (azidomethyl)benzene; (TR) azidotrimethylsilane; (BR): azidobenzene; (BL) 1-azidopropane.

4.0 Metal Complexations with L5 and L6

4.1 General Complexation Synthesis and Characterisation

The principal aim of this research was to synthesise a series of metal-organic complexes, using newly developed ligands, with different 3*d* and 4*f* metals. The bis-terdentate Pz-O-Tz chelation sites, successfully synthesised in the ligands **L5** and **L6**, were very promising for coordination with octahedral 3*d* transition metals.

A variety of 3*d* and 4*f* salts, with different counter anions, were introduced to **L5**. The full range of metal salts, including ratios used, observations, and complexation results, is available in Apx10.0. The complexes attempted, and their complex codes are displayed in Tables 15 and 16. The **L5** ligand did not coordinate to any of the 4*f* metals, but did coordinate to a range of 3*d* metals.

Ten **L5** complexes were successfully synthesised and characterised. For the majority of these, the complex isolated formed a 1D polymer chains $[M_1L_1]_\infty$ held in layers of 2D sheets by non-covalent interactions. The one exception was complex, **5A3**, which formed a $[M_2L_1]$ monomer. The results of the characterisations of these complexes are discussed in this following section.

Complexations were performed by combining the ligand (**L5** or **L6**), dissolved in MeCN, in a 1:1 ratio with metal salt dissolved in MeOH (or MeCN as necessary for solvation). The reaction mixture was then, heated at 60 ºC for 30 minutes. Confirmation that some form of coordination had occurred was observed with colour changes in the reactions, as noted in Apx7.0.

Table 15: Complexation Codes of 3*d* transition metal salts, with **L5**. **Bolded Green**, codes indicate successful isolation of crystallised complex. Italicise and underlining indicates the crystal isolated was the metal salt.

	3*d* Metals						
Anions in salts	**Mn**	**Co**	**Fe**	**Ni**	**Zn**	**Cu**	**Cr**
ClO_4^-	**5A1**	**5B1**	**5C1**	**5D1**	5E1	**5F1**	5G1
BF_4^-	-	**5B2**	**5C2**	5D2	**5E2**	**5F2**	-
NO_3^-	**5A3**	-	-	-	-	5F3	-
Cl^-	*5A4*	5B4	-	5D4	-	*5F4*	5G4
acac	5A5	5B5	5C5	5D5	FE5	5F5	-
OAc	5A6	-	-	5D6	5E6	-	-
SO_4^-	-	5B8	5C8	-	5F8	5F8	-

Table 16: Complexation codes of 4*f* transition metal salts, with **L5**. **Bolded** codes indicate successful isolation of crystallised complex. Italicise and underlining indicates the crystal isolated was the metal salt.

	4f Metal Salts					
Anions in salts	**La**	**Dy**	**Er**	**Eu**	**Gd**	**Ho**
NO_3^-	5B9	5B7	-	-	5B8	-
Cl^-	5D7	5C7	*5C8*	*5D8*	-	*5F3*

Isolation of crystallised complexes were achieved by vapour diffusion of Et_2O into the reaction solutions over a period of four weeks. The resulting crystals, were produced in a variety of shapes and colours, fully described in Apx7.0. The arrangements of these complexes were confirmed by X-ray crystallography and analysed by IR, UV and ESI-MS.

4.2 ATR-FTIR of Complexes 5A1 – 5F2

ATR-FTIR spectroscopy of the complexes was performed in the range 700 – 4000 cm^{-1} to compare the various stretching and bending modes of the complexes and their corresponding ligand, **L5**. The peaks corresponding to the coordinated atoms showed a shift in wavelength as expected. The full table of IR peak data can be found in Apx12.5.00-10.

Table 17: Selected average IR peaks present in the **L5** complexes.

N-H stretch	3430.81 br	C=C (Tz)	1484.67 m	C-O	1218.73 m
C-H Ar Stretch	3118.84 s	N=N (Tz)	1458.67 m	C-O-C ether stretch	1091.34 s
N-H stretch	2955.45 s	C-N	1349.86 m	C-O-C Sym stretch	870.35 w
C=C stretch	1669.37 w	C-N aromatic	1255.46 m		

When **L5** is coordinated, there is a decrease in intensity of the 2800 – 3150 cm^{-1} peaks, and a decrease in intensity of the 1450 cm^{-1} peak, as any N-H stretching disappears with the coordination of the pyrazine, indicating deprotonation. But, the 1250 C-N aromatic stretch is consistent, between the free and coordinated **L5**.

There is also a broadening of the strong, 1050< x >1100 cm^{-1} peak from the C-O stretching within the ether group, as the oxygen in the ether coordinates to the corresponding metal cation.

The coordination modes of all the ligands resembled each other, with slight variations from the Mn^{2+} based complexes, (**5A1** and **5B1**). In **5B1**, there is a pronounced strong 1290 – 1490 cm^{-1} peaks, compared to the other complexes, due to its coordination to NO_2, creating N-O stretching.

4.3 Mass Specs of Complexes 5A1 – 5F2

The mass spectroscopy of the complexes, all resulted in masses that corresponded to the lone **L5** and various arrangements of the breakdown of the extended polymer chain, as the structure was broken upon characterisation in the MS.

Table 18: The Mass determined in SCXRD and the MS values of the **L5** complexes. (g/mol)

	MS: (m/z)
5A1	414.65 [L], 441.77, 648.6, 828.92, 981.81 [[Mn^{2+}(2L)](ClO_4^-)(H^+)]
5B1	414.15 [L], 443.65[Co^{2+}(2L)] 603.41, 650.79, 779.97 [2Co^{2+}(3L)](2ClO_4^-)]], 857.80, 985.81[[Co^{2+}(2L)](ClO_4^-)]
5C1	414.02 [L], 442.27 [Fe^{2+}(2L)], 649.29, 829.05, 982.81 [[Fe^{2+}(2L)](ClO_4^-)]
5D1	415.16 [L], 437.08 [LNa], 585.13, 650.95, 698.18, 764.50, 851.42, 999.25
5F1	414.27 [L], 445.77 [Cu^{2+}(2L)], 577.78 [Cu^{2+}(L+H)](ClO_4^-)], 652.91, 783.92 [2 Cu^{2+}(3L)](2 ClO_4^-)], 991.43 [[Cu^{2+}(2L+H)](ClO_4^-)].
5A3	266.89, 414.27 [L], 441.65, 531.03, 648.66, 709.79 [Mn^{2+}(L)](H_2O)(2ClO_4^-), 792.05, 855.80, 944.93
5B2	268.89, 443.65 [Co^{2+}(2L)], 650.66 [[Co^{2+}(L+2H)](2BF_4^-)], 857.80, 973.93 [[Co^{2+}(L)](BF_4^-)]
5C2	414.15 [L], 437.02[LNa], 649.16, 850.92, 996.93.
5E2	414.02 [L], 437.02 [LNa], 446.27 [Zn^{2+}(2L)], 653.79 [Zn^{2+}(LH)](2BF_4^-)], 828.92, 978.93
5F2	445.65 [Cu^{2+}(2L)], 522.03, 653.16 [Cu^{2+}(LH)](2BF_4^-)], 771.79[2Cu^{2+}(3L)], 890.80, 977.93

4.4 UV-Vis of Complexes 5A1 – 5C6

The UV-Vis spectral data resulted in the same pattern of peaks, at 309.5-310.5 nm, 269.5-271.0 nm, and 209.0-213.0 nm, shown in Table 19. It is likely that the peaks are produced from the ligand itself, as they remain constant between the different complexes, and no absorption is occurring due to metal interactions to the ligand.

Table 19: UV-Vis peak wavelengths (λ) and Absorbances (A), of **L5** complexes.

	A1	**A2**	**A3**	**A4**	**A6**	**B1**	**C2**	**C3**	**C5**	**C6**
g/mol *	686.37	825.78	669.27	672.13	671.62	844.47	647.07	1305.99	653.51	651.68
C (mol/L) x10^{-4}	5.558	4.38	5.09	6.65	3.48	4.54	4.60	1.14	2.60	4.90
λ nm				373.0						
A				2.56						
λ nm	309.5	310.5	310.5	310.0		310.5	310.5	310.5	310.5	310.5
A	489.27	1057.05	947.60	215.11		919.49	503.98	1078.56	43.00	937.246
λ nm	270.0	269.5	269.0	270.0	271.5	269.5	270.0	270.0	270.0	271.0
A	3984.04	8700.66	6743.31	1576.50	6293.14	7430.87	4096.98	7582.00	3394.00	5437.66
λ nm	210.2	221.0		210.0			212.2	210.0	209.0	213.0
A	7064.81	8428.98		3080.79			8437.24	15178.78	7102.84	8167.72

***** *= molar mass calculated by X-ray crystallography used for these polymer chains. C = concentration of crystal dissolved in MeOH (mol/L) x10^{-4}. A : (ε, L/mol cm)*

4.5 Conductivity of Complexes 5A1 – 5C6

The conductivity of the complexes was measured, by dissolving a crystal in MeOH. The molar conductivity (Λ) of these complexes, are used to investigate the ion ratio of the complex. The intermolecular forces holding the 1D chains together are quite labile, meaning there is the possibility the anions could not be static within these structures, and the X-ray crystallography only provided a snap shot of the crystal arrangement.

A comparison of values obtained by Geary[117] indicate a correlation between the molar conductance, Λ of coordination complexes in a particular solvent and the number of counterions present. Using methanol as the solvent system, the expected approximate molar conductivity for a particular complex:counterion ratio given by Geary are as follows: 80-115 S cm^2 mol^{-1} for 1:1 systems, 160-220 S cm^2 mol^{-1} for 1:2 systems, and 290-350 S cm^2 mol^{-1} for 1:3 systems.[117] The discrete M_2L_1 **A31** monomer complex, has a 1:2 ratio, as the 190.52 S cm^2 mol^{-1} fell within the 160-220 S cm^2 mol^{-1} range for 1:2 systems, which was what was expected and agrees with the other data collected on the physical structure.

These results of the other complexes resulted, show a less than 1:1 ion ratio that could be because the counter ions are entangled within these large 1D polymer chain complexes, limiting the mobility of the anions in solution. The anions would be slow to move between these chains, resulting in a lower conductivity result.

Table 20: The conductivity results for the **L5** Complexes.

	Formula	MeOH Conductivity	Conductivity	Molar Conductivity (Λ)	Ion Ratio
		μS cm^{-1}	μS cm^{-1}	S cm^2 mol^{-1}	
5A1	$\{[Mn_2(\mathbf{L5})(H_2O)](ClO_4)_2\}_\infty$	7.89	44.6	65.79	<1:1
5B1	$\{[Co_2(\mathbf{L5})](ClO_4)_2\}_\infty$	7.73	66.7	134.63	1:1
5C1	$\{[Fe_2(\mathbf{L5})](ClO_4)_2\}_\infty$	7.65	23.4	44.14	<1:1
5D1	$\{[Ni_2(\mathbf{L5})](ClO_4)_2\}_\infty$	7.32	34.2	40.44	<1:1
5F1	$\{[Cu_2(\mathbf{L5})](ClO_4)_2\}_\infty$	7.68	18.17	42.92	<1:1
5A3	$[Mn_2(\mathbf{L5})](NO_3)_2(H_2O)_4](NO_3)_2$	9.19	69.8	190.52	2:1
5B2	$\{[Co_2(\mathbf{L5})](BF_4)_2\}_\infty$	7.26	23.8	51.22	<1:1
5C2	$\{[Fe_2(\mathbf{L5})](BF_4)_2\}_\infty$	7.45	9.11	20.75	<1:1
5E2	$\{[Zn_2(\mathbf{L5})](BF_4)_2\}_\infty$	7.67	13.2	30.27	<1:1
5F2	$\{[Cu_2(\mathbf{L5})](BF_4)_2\}_\infty$	8.22	24.1	46.22	<1:1

4.6 Seven Coordinate Mn Complexes 5A1 and 5A3

The syntheses of the 1D polymer chain complex, **5A1** {[Mn **L5** $(H_2O)_2$]$(ClO_4)_3$}$_\infty$ and the mononuclear complex, **5A3** [Mn_2(**L5**)]$(NO_3)_2(H_2O)_4](NO_3)_2$, followed the same general procedure; the reaction between **L5** and a corresponding metal salt (for example, ($Mn(ClO_4)_2 \cdot 6H_2O$, or $Mn(NO_3)_2 \cdot 4H_2O$) combined in a 1:1 ratio, which resulted in, a change in solution colour from pink to yellow solutions. Isolation was achieved by the vapour diffusion of diethyl ether into the reaction solutions over a period of three weeks, resulting in the formation of yellow block crystals of **5A1** and very pale-yellow block crystals of **5A3**. The formulations were established by elemental analysis, IR, and ESI-MS, and confirmed by X-ray crystallography.

4.6.1 X-Ray Structural Determination 5A1 and 5A3

The X-ray crystallography data is shown in Apx11.0. The **5A1** complex was monoclinic and crystallised in the C2/*c* space group, while the **5A3** complex was triclinic and crystallised in the $P\bar{1}$ space group.

The asymmetric unit for **5A1** consisted of two half ligands coordinated to a seven-coordinate, mono-capped trigonal prism Mn (II), which is also coordinated to a water molecule, which in turn, forms a hydrogen bound to a perchlorate counterion. There is a second perchlorate ion present to balance the charge (Figure 49). The full polymer is generated by inversion at each half pyrazine, (C1-N4-C2) and (C11-N8-C12).

The asymmetric unit for **5A3** contains half an **L5** ligand coordinated to a Mn(II) cation, which is then coordinated to two axial water molecules and an equatorial bifurcated nitrate ion, with a second nitrate counterion forming a hydrogen bond to one of the water molecules. The full structure is generated by an inversion symmetry operation through the central pyrazine ring (Figure 49).

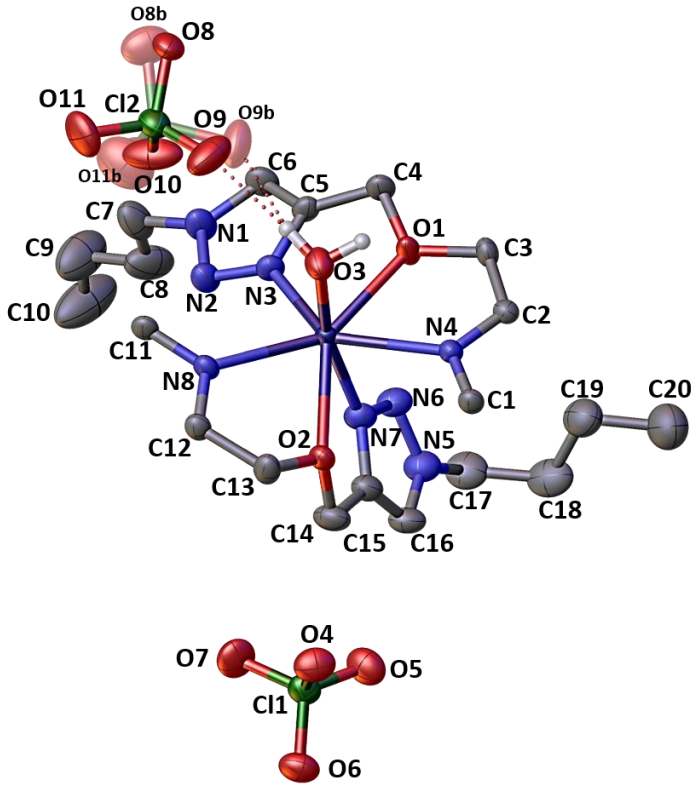

Figure 49: Crystal structure of the asymmetric unit of {[Mn **L5** $(H_2O)_2$]$(ClO_4)_3$}$_\infty$ **5A1** complex: Colour Code: C = grey, N = blue, Cl = green, O = red, H = white, H not involved with hydrogen bonds, omitted for clarity. Hydrogen bonding indicated by a red line. The Cl1 perchlorate counterions were solved wih an 0.81 occupancy (O8-O11) and an 0.18 occupancy (O8b-O11b).

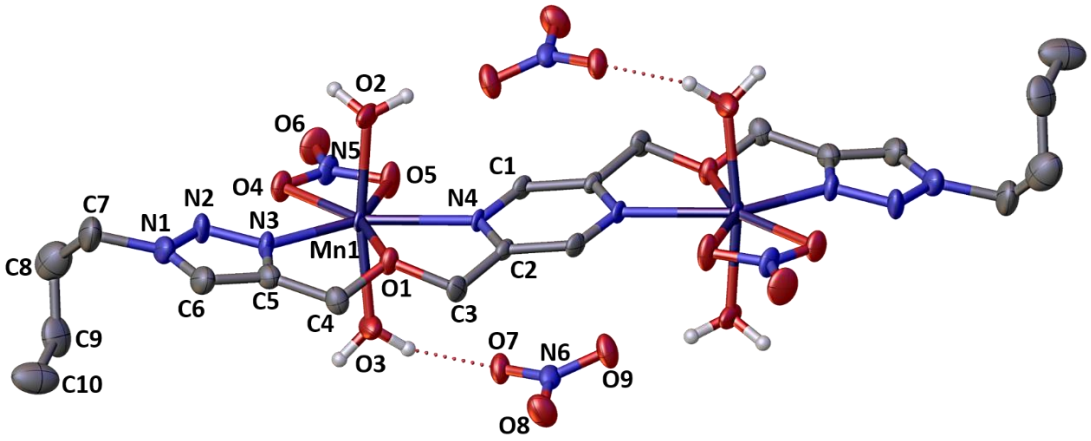

Figure 50: Crystal structure of the monomer [Mn_2(**L5**)]$(NO_3)_2(H_2O)_4](NO_3)_2$, **5A3** complex, with the asymmetric unit labelled. Atoms are represented as ellipsoids, Colour Code: C = grey, N = blue, Cl = green, O = red, H = white. Hydrogen bonding indicated by a red dotted line; hydrogen atoms not involved with bonding omitted for clarity.

4.6.2 1D Single chain polymer of 5A1 $\{[Mn\ L5\ (H_2O)_2](ClO_4)_3\}_\infty$

Filling the seven coordinate mono-capped trigonal prism Mn(II), are two halves of two **L5** ligands, coordinated to the Pz-O-Tz chelation sites. The 1D polymer chain is built by alternating conformations of ligands, linear and contorted, illustrated in (Figure 51).

The linear ligands chelation site coordinates to three equatorial sites, at 135.4 (12)º [$N3_{(Tz)}$–Mn–$N4_{(Pz)}$], a ($N3_{(Tz)}$– $N4_{(Pz)}$) distance of 4.273 (4) Å and has a mostly linear backbone angle of 170.75 (17)º [C2-O1-C5] with distances between (C2-C5) of 4.676 (5) Å, and (C3-C4) 2.392 (5) Å. Both halves of the linear ligand have this outcome.

The second ligand is bent, in an almost 'Z' conformation. The O2 oxygen atoms are the most in plane with the linear Pz-O-Tz site, while both $N8_{(Pz)}$ nitrogen atoms of the contorted ligand lie out of plane, and the Mn-N7 bonds are axial, opposite to the Mn-$O3_{(H2O)}$ bond. The contorted ligand, is left with an angle of 109.3 (13)º [$N7_{(Tz)}$–Mn–$N8_{(Pz)}$]. The $N_{(Tz)}$ and $N_{(Pz)}$ are held 0.55 Å closer together compared to the linear ligand with a ($N7_{(Tz)}$– $N8_{(Pz)}$) distance of 3.719 (4), compared to the 4.273 (4) Å ($N3_{(Tz)}$–$N4_{(Pz)}$). This bend has a Pz-O-Tz backbone angle of 129.07 (16)º [C(12)-O(2)-C(15)] with a (C12–C15), distance of 4.260 (5) Å; 0.42 Å closer than in the linear ligand, and a 2.409 (6) Å (C13-C14). More of these differences are shown in Tables 21 and 22.

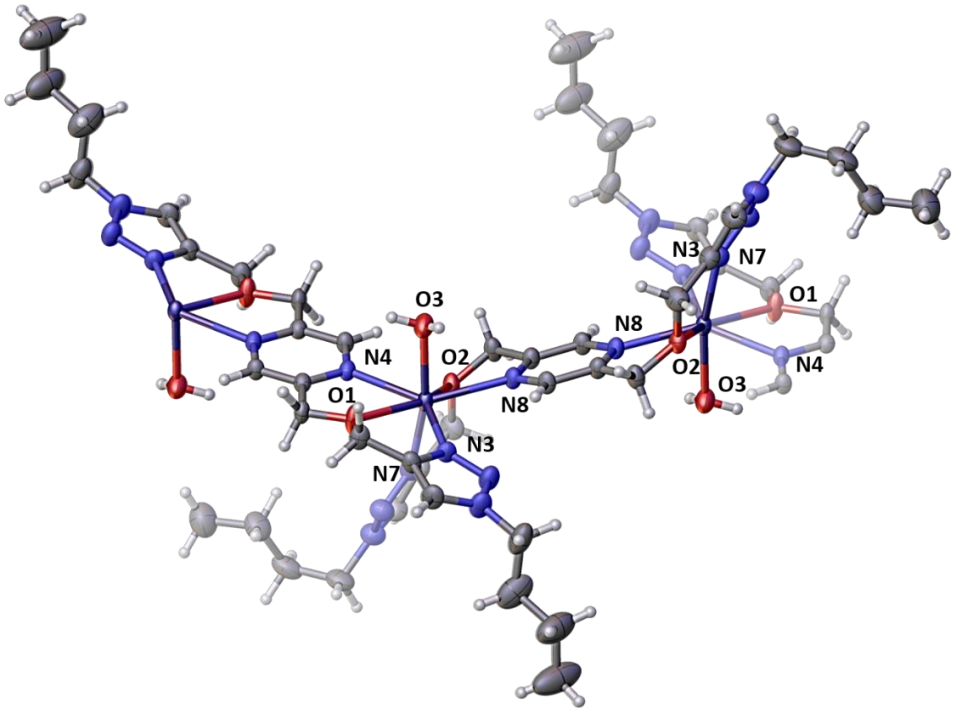

Figure 51: Crystal structure illustrating the alternation between linear and contorted ligands. Perchlorate counterions removed for clarity.

Table 21: The bond distances from the atoms coordinated to the central Mn(II) in **5A1** (Å).

M-X (H_2O) distances		**Linear Ligand distances**		**Bent Ligand distances**	
Mn-O3	2.185 (3)	Mn-N3	2.252 (3)	Mn-N7	2.203 (3)
		Mn-O1	2.326 (3)	Mn-O2	2.393 (3)
		Mn-N4	2.367 (3)	Mn-N8	2.354 (3)
Distances between atoms					
		N4-N3	4.273 (4)	N8-N7	3.719 (4)
		C2-C5	4.676 (5)	C12-C15	4.260 (5)
		C3-C4	2.392 (5)	C13-C14	2.409 (6)

Table 22: Angles around the Mn(II) centre in **5A1** (º).

Angles from $O3^{ax}$		Angles from $N7^{ax}$		Planar Pentagonal Angles ^{eq}	
Atoms	Angle (º)	Atoms	Angle (º)	Atoms	Angle (º)
O3-Mn-O2	105.72 (10)	N7-Mn-O2	70.06 (10)	O2-Mn-N8	67.81 (9)
O3-Mn-N8	79.74 (10)	N7-Mn-N8	109.31 (11)	N8-Mn-N3	87.84 (10)
O3-Mn-N3	100.27 (11)	N7-Mn-N3	90.33 (11)	N3-Mn-O1	68.71 (9)
O3-Mn-O1	85.18 (10)	N7-Mn-O1	90.92 (11)	O1-Mn-N4	67.17 (9)
O3-Mn-N4	82.16 (10)	N7-Mn-N4	84.38 (10)	N4-Mn-O2	78.79 (9)
average	90 ± 10		89 ± 13		74 ± 8
Δd	9.78		9.22		6.99
Linear Bond Angles ~180º					
O3-Mn-N7	166.46 (11)	N8 – M – O1	149.29 (11)	N4– M – N3	135.40 (12)

The seven-coordinate, mono-capped trigonal prism geometry of these Mn(II) complexes differ in their spatial arrangements as compared to the complexes formed from other 3*d* ions, which all formed six-coordinate octahedral geometries.

In a perfect pentagonal bipyramidal geometry, there is a 180º angle between the two axial sites and angles around 72º between each of the five in equatorial coordinated atoms. In the **5A1** polymer chain, the expected 90º axial angles (from O3, and N7 to equatorial atoms) had a total distortion (Σd) of 95.0º with an average deviation of 9.5º. There was a range of deviations of 0.33º to 19.9º (Table 22). The sum of 370.3º of the five pentagonal chelate angles indicated that the structure does not have a true pentagonal bipyramidal arrangements, and was distorted.

It is the placement of the N8 nitrogen and O2 oxygen that indicate that this Mn(II) centre has a mono-capped trigonal prism geometry, opposed to a pentagonal bipyramidal one. The N7-Mn-N8 angle is 19.3º more than 90º, while the N7-Mn-O2 angle is 19.9º less than 90º, both angle differences are more than just slight deviations. When N8 is compared to the plane generated by the mean of the other coordinated atoms and Mn, the N8 atom lies far out of plane. The mono-capped trigonal prism geometry can be clearly seen in (Figure 52).

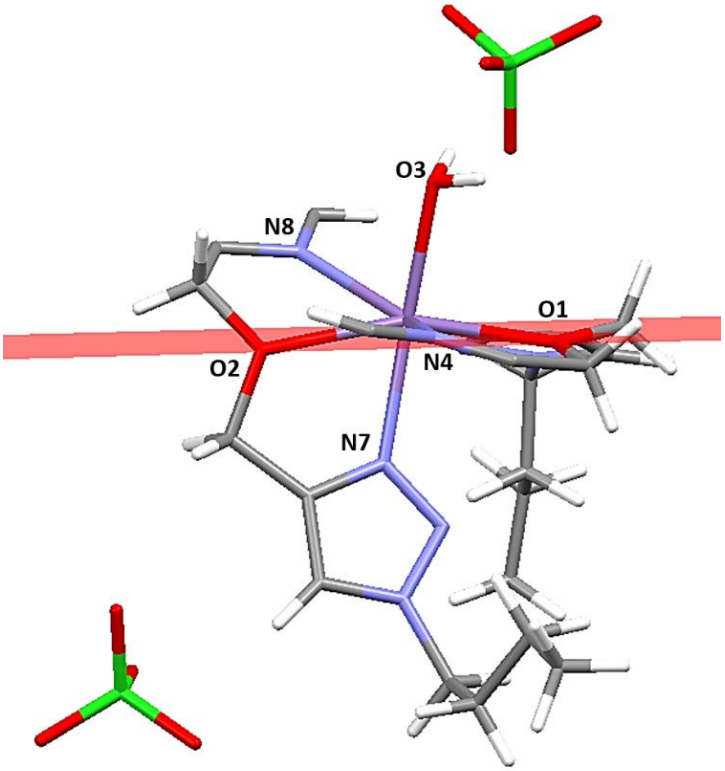

Figure 52: The mercury crystal structure of **5A1**: average plane of the atoms coordinated to the central Mn (excluding N8), demonstrates mono-capped trigonal prism geometry.

The average distortion (Δd) for each section of angles (axial or equatorial) around the Mn(II) centre was calculated by dividing the sum, of the differences between the measured angle (Φ) and the expected angle (A), (which for a pentagonal bipyramidal geometry was 90º for the axial (^{ax}) angles and 72º for the equatorial (^{eq}) angles) by the number of angles in that section (n). The equation used to derive the distortions in the pentagonal bipyramidal geometries was altered from the distortion measurement equation for octahedral geometries presented by Buron-Le Cointe *et al.* [118]

Equation 3: The average angle distortion of a set of angles within a set of angles (º).

$$\Delta d = \left(\frac{1}{n}\right) \Sigma_{i=1}^{n} [\pm(\Phi_i - A)]$$

In **5A1**, this seven-coordinate, ono-capped trigonal prism geometry resulted in more obtuse angles (a 137.1º for [N4($L5^2$) – Mn1 – N8($L5^1$)] between the ligands in the 1D polymer chain) as compared to the other polymer complexes, where the ligands are coordinated close to perpendicular to each other, 91.1º for [N4($L5^2$) – Fe1 – N8($L5^1$)], in **5C1**, (from Section 4.7) as shown in Figure 53.

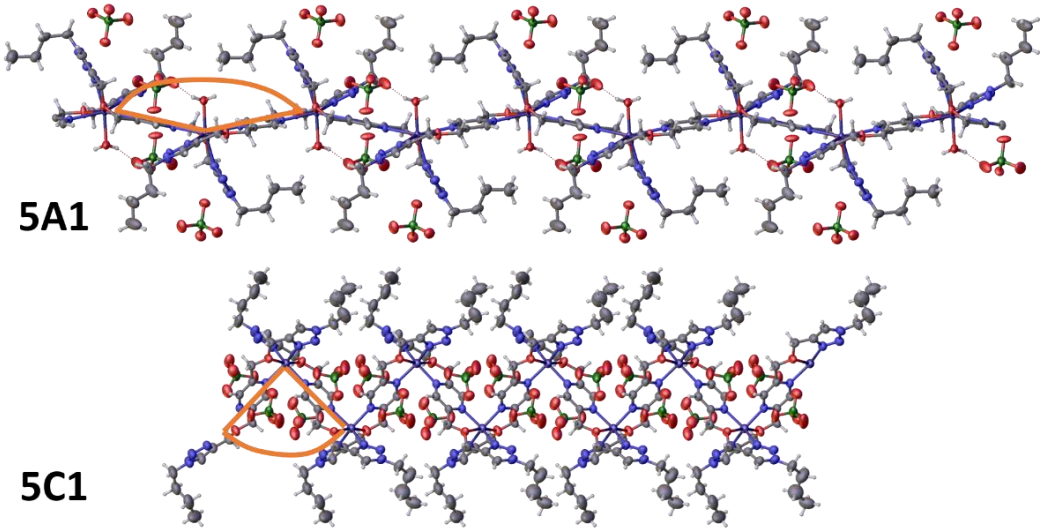

Figure 53: The crystal structures of the complexes **5A1** and **5C1**, over a nine ligand repeating units. Angles are indicated with orange lines.

This wider angle created larger gaps between the 1D chains, resulting in the butyl groups sitting further apart from one another. These void spaces house the secondary ClO_4^- counterions, in contrast to the other single chain polymer complexes, (Section 4.7-4.8) where the anions are packed around the pyrazines. The difference in the how tightly the 'zig-zag' of the 1D chain is packed as shown in (Figure 53), the perpendicular ligands in **5C1** hold the chain quite tightly, while the polymer chain of **5A1** is more stretched out.

The **5A1** 1D polymer complex has strong hydrogen bonds forming 2D sheets, with weak van der Waal interactions between the butyl groups creating a 3D network. Each Mn(II) coordinated water molecule forms hydrogen bonds to two perchlorate anions, $Ha^{O3}{}_{(H2O)}$ to O9 (H-A distance of 1.972 (9) Å), and $Hb^{O3}{}_{(H_2O)}$ to the O8 (H-A 1.982 (12) Å), meaning each ligand within the 1D polymer chain forms four hydrogen bonds. The two bonds, from the water ions, are repeated on the opposite side of the perchlorate ions and from bonds to the adjacent 1D polymer chain (Figure 54). The

hydrogen-acceptor distances for these bonds, (Table 23) are between 1.5-2.2 Å, which indicate moderate strength, mostly electrostatic hydrogen bonds.[108]

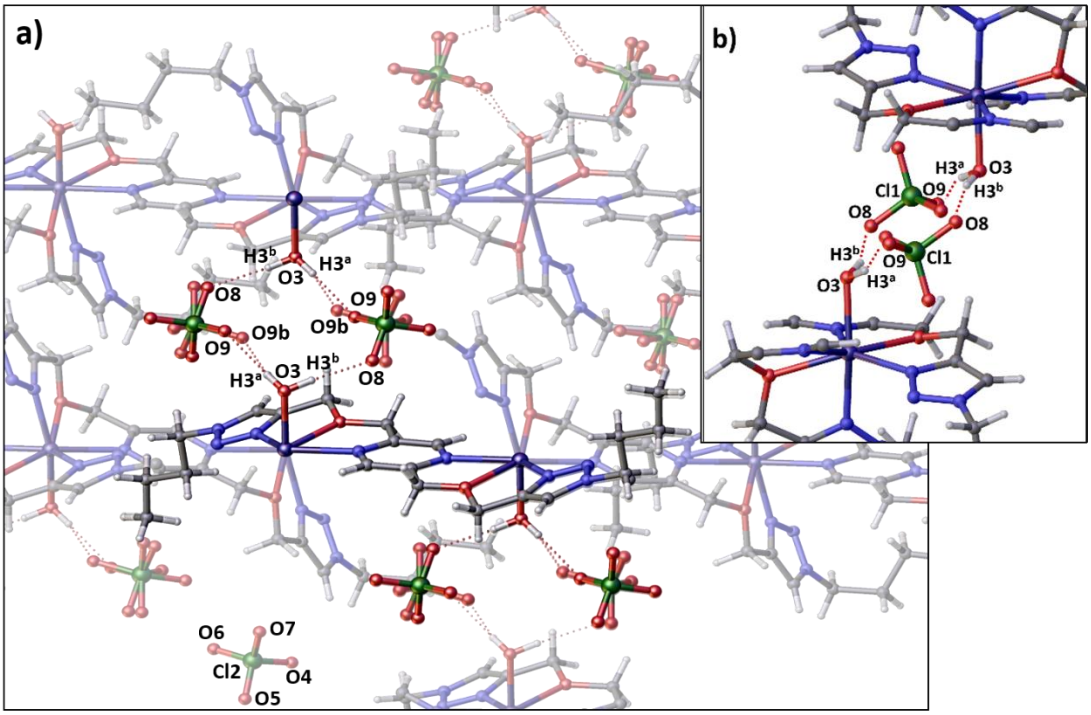

Figure 54: The crystal structure of **5A1.** a) two adjacent 1D polymer chains in separate 2D sheets, forming a 3D network with the associated perchlorate ions. b) side on view of the hydrogen bond network. Ball and stick view for clarity. One free ClO_4^- ion is left as an example, but others have been removed for clarity. Colour Code: C = grey, N = blue, Cl = green, O = red, and H = white.

Table 23: Hydrogen Bond data (Å), for **5A1**

D-H-A	D-H(Å)	H ··· A (Å)	D ··· A (Å)	D-H ··· A (°)
O3A - H3a - O9*	0.8707	1.972 (9)	2.800 (5)	158.3 (19)
O3A - H3a - O9b*	0.8707	1.88 (2)	2.74 (2)	167 (4)
O3A - H3b – O8'	0.8705	1.982 (12)	2.828 (7)	164 (3)
O3A - H3b – O8b'	0.8705	2.347	3.189	162.9

The perchlorate anions involved in this hydrogen bonding network are disordered over two sites, with occupancies of 0.815 and 0.185, meaning that the full hydrogen bonding within the framework is only present for 81.5% of Mn centres within the structure, while the other 18.5% were arranged in a way that only lead to hydrogen bonding to one water molecule, O3A - H3a – O9b, with the O8b oxygen being too far away with a D-A distance of 3.189 Å. This percentage is high enough to assume that the network is still being strongly held together. The second, minor occupancy perchlorate (0.185) has been excluded to help clarify the above hydrogen bonding network.

4.6.3 Monomer Complex 5A3 $[Mn_2(L5)](NO_3)_2(H_2O)_4](NO_3)_2$

When **L5** was reacted with $Mn(ClO_4)_2 \cdot 6H_2O$, it resulted in the polymeric chain **5A1**, where three equatorial coordination sites of the seven coordinate Mn(II) cations are occupied by a linear **L5** ligand. The other two equatorial sites and one of the axial sites are occupied by a second contorted **L5** ligand, leading to the generation of polymers. The remaining axial site is occupied by a water molecule. The ClO_4^- counter anions are non-coordinating in this case.

When **L5** was reacted with $Mn(NO_3)_2 \cdot 4H_2O$ in **5A3**, the NO_3^- counter anions are now incorporated into the coordination sphere of the Mn(II) cation in contrast to the non-coordinating ClO_4^- anions. The linear **L5** ligand, in this complex, occupies three equatorial sites of the seven coordinate Mn(II), with the remaining equatorial coordination sites occupied by a bifurcated nitrate ion, with an angle of 55.89 (10)º [O4-Mn-O5]. As well as one axial bond occupied by a water molecule, the second axial bond, (Mn-N7 bond in **5A1**) was occupied by a coordinated water molecule. The availability of coordinating anions resulted in **5A3** having a $[M_2L_1]$ monomer arrangement, a discrete unstrained complex with a less contorted metal ion geometry. This outcome was more enthalpically favourable than the Mn(II) coordinating to two continuous ligands in 1D polymer chains.

In the **5A3** complex, a seven coordinate Mn(II) has its five equatorial sites filled by the (Pz-O-Tz) chelation site of the ligand and two filled by an equatorial bifurcated nitrate ion, in a planar pentagonal arrangement. The sum of the intra equatorial angles measure 360.1º, which is much less distorted than the **5A1** (a sum of 370.3º of pentagonal angles).

The axial angles of **5A3** (from O3 and O2), are also much closer to 90, (Table 24) with only a total distortion measurement (Σd) of 33.65º and an average deviation of 3.37º, compared to **5A1** with a total distortion measurement (Σd) of 95.03º and an average deviation of 9.50º. The distortions (***Δd***) were derived from Equation 3.

The range of deviation from 90º in **5A3**, of 0.22º to 7.57º is also much smaller than the 0.33º to 19.9º in **5A1**. The metal centre geometry in **5A3** is much closer to a true pentagonal bipyramidal arrangement, as seen with the plane generated by the average of the Mn(II) and the coordinated atoms maintaining the coordinated atoms much

closer in line than in **5A1**, (Figure 55). The O2-Mn-O3 angle of 169.80 (10)º rather than 180º, indicates that that this is a distorted pentagonal bipyramidal geometry.

Table 24: The Angles around the Mn(II) centre in **5A3** (º)

Angles ~Perpendicular to O2 (H_2O)		Angles ~Perpendicular to O3 (H_2O)		Angles in the equatorial pentagonal arrangement	
O2-Mn-O3	169.80 (11)				
O2-Mn-N3	90.22 (11)	O3-Mn-N3	93.88 (12)	O4-Mn-O5	55.89 (10)
O2-Mn-O1	85.16 (11)	O3-Mn-O1	87.51 (10)	O5-Mn-N4	83.07 (10)
O2-Mn-N4	86.94 (10)	O3-Mn-N4	83.82 (10)	N4-Mn-O1	69.04 (9)
O2-Mn-O4	97.57 (11)	O3-Mn-O4	92.24 (10)	O1-Mn-N3	69.72 (10)
O2-Mn-O5	92.74 (12)	O3-Mn-O5	90.43 (12)	N3-Mn-O4	82.35 (10)
average	91 ± 4		90 ± 4		72 ± 10
Δd	3.69		3.04		8.55

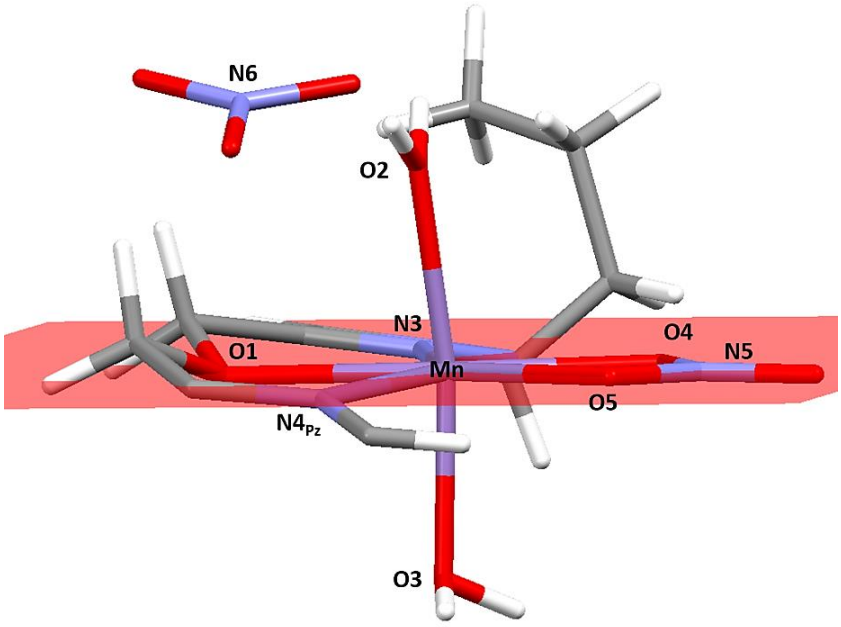

Figure 55: The mercury crystal structure of **5A3** showing the plane generated from the Mn and its coordinated atoms.

This distorted pentagonal bipyramidal arrangement of **5A3** also led generally to shorter metal-ligand bond lengths compared to **5A1** (Table 25). The Mn-H_2O decreased from 2.185 (3) Å in **5A1** to 2.161 (3) in **5A3**. The linear ligand in **5A1** had distances of Mn-N3 (2.252 (3) Å); Mn-O1 (2.326 (3) Å) and Mn-N4 of (2.367 (3) Å), while the ligand in **5A3** had distances of Mn-N3 (2.186 (3) Å); Mn-O1 (2.379 (2) Å) and Mn-N4 of (2.303 (3) Å).

Table 25: The Distances from the Mn(II) centre to the chelated atoms in **5A3** (Å) and the comparative bond lengths from the Mn(II) centre to the chelated atoms in **5A1** (Å)

5A3	**M-X (H_2O) distances**		**M-X (NO_3^-) distances**		**M-X (L5) distances**	
	Mn-O3	2.161 (3)	Mn-O4	2.308 (2)	Mn-N3	2.186 (3)
	Mn-O2	2.163 (3)	Mn-O5	2.262 (3)	Mn-O1	2.379 (2)
					Mn-N4	2.303 (3)
5A1	**M-X (H_2O) distances**		**Bent (L5) distances**		**Linear (L5) distances**	
	Mn-O3	2.185 (3)	Mn-N7	2.203 (3)	Mn-N3	2.252 (3)
			Mn-O2	2.393 (3)	Mn-O1	2.326 (3)
			Mn-N8	2.354 (3)	Mn-N4	2.367 (3)
5A3 Ligand atom distances			**5A1 Bent (L5) distances**		**5A1 Linear (L5) distances**	
	N4-N3	4.201 (4)	N8-N7	3.719 (4)	N4-N3	4.273 (4)
	C2-C5	4.662 (5)	C12-C15	4.260 (5)	C2-C5	4.676 (5)
	C3-C4	2.381 (5)	C13-C14	2.409 (6)	C3-C4	2.392 (5)

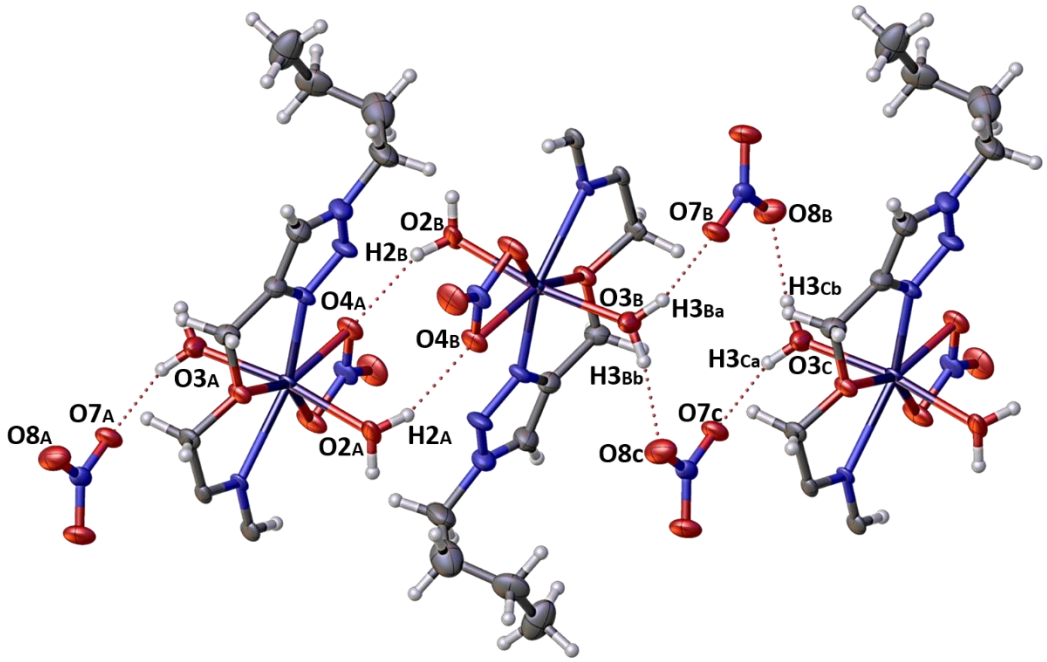

Figure 56: The crystal structure of the hydrogen bonding network on both side of the monomer, **5A3**, shown between three asymmetrical units. Colour Code: C = grey, N = blue, Cl = green, O = red, H = white. Hydrogen bonds indicated by a red dotted line.

Table 26: Hydrogen Bond lengths (Å) and Angles (º) of **5A3** complex.

	D-H-A	**D-H**	**H ··· A**	**D ··· A**	**D-H ··· A (º)**
1	$O2_A$-$H2_A$-$O4_B$	0.883	2.12 (3)	2.861 (4)	142 (4)
2	$O3_B$-$H3_{Ba}$-$O7_B$	0.870	1.929 (10)	2.772 (4)	163 (3)
3	$O3_B$-$H3_{Bb}$-$O8_C$	0.870	1.903 (7)	2.765 (4)	171 (3)

The two water molecules coordinated, above and below the Mn(II) are used to create two sets of hydrogen bonds that create a large hydrogen bonded 2D network of **5A3** monomers.

Each monomer has eight hydrogen bonds connecting to four other monomers, as seen in (Figures 56 and 57). The discrete monomers are interlocked into brick-laying like stacks, with each face, of the asymmetric units, orientated towards the same face of a separate asymmetric unit.

For the face with the (O2) water ligand, two (O2) water ligands lay parallel to each other, next to the NO_3^- anion ((N5) coordinated to the Mn(II)) on the opposing monomer. Two identical hydrogen bonds (Table 26: 1) form between the water ligand of one monomer O2-H to the $O4_{(NO3)}$ of the second monomer, with a H-A distance of 2.12 (3) Å, forming a rectangular network.

On the opposite face of the asymmetric unit, the O3 water ligand facilitates two hydrogen bonds. The first, from $Ha^{O3}{}_{(H2O)}$ to O7 of an associated (N6) NO_3 anion, with a H-A distance of 1.929 (10) Å; and a second hydrogen bond from the same water ligand, O3-Hb to the O8 of a second NO_3^- (N6) anion, with a H-A distance of 1.903 (7) Å. These hydrogen bonds form again, on the other side of the associated nitrate$^-$ anions, to corresponding a third monomer, forming a diamond shaped network of four hydrogen bonds. This holds two ligand halves via two associated nitrate anions, as shown in Figure 56.

These repetitive hydrogen bond patterns create an alternate, off-set stacking of the monomers to form strongly connected 2D sheets. The distances and angles of these hydrogen bonds shown in (Table 26), are between 15-2.2 Å, indicating a moderate hydrogen bond strength, that's mostly electrostatic,[108] so this network of bonds is held together relatively strongly.

The 010 cell view of the overall packing of this structure, seen in (Figure 57), shows how the butyl tail groups fold into the spaces left by the hydrogen bond networks. These 2D sheet networks are layered on top of each other, with the butyl side groups associating through weak interactions and acting as a barrier between these sheets.

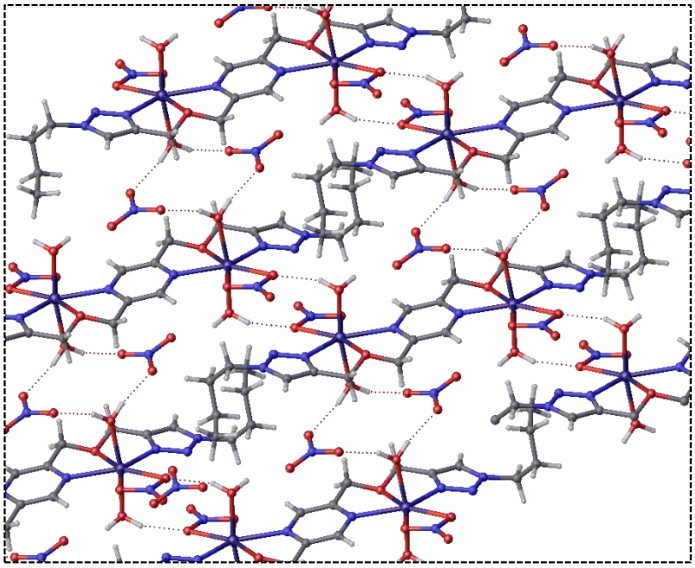

Figure 57: The crystal structure of the hydrogen bonding network between the **5A3** monomer complexes, to 2D sheets. Colour Code: C = grey, N = blue, Cl = green, O = red, H = white. Hydrogen bonds indicated by a red line.

4.7 Single Chain Polymer Complexes (5B1-5F1) and (5B2-5F2)

The following complexes **5B1**, **5C1**, **5D1**, and **5F1**, were synthesised from the complexation reaction between **L5** and ClO_4^- metal salts of Co, Fe, Ni and Cu, respectively, while **5B2**, **5C2**, **5E2**, and **5F2**, were synthesised from the complexation reaction between **L5** and BF_4^- metal salts of Co, Fe, Zn and Cu, respectively. These complexes assembled into 1D 'zig-zig' metal-organic polymer chains, arranged into stacked 2D sheets held by non-covalent interactions.

The synthesis of these complexes all followed the general reaction procedure, with **L5** dissolved in MeCN and the corresponding metal salts in MeOH, being heated to 60 ºC for half an hour. The specifics for each complex reaction are shown in Apx7.0. The success of coordination was indicated by the colour change of the reaction solution. The isolation of these complexes was done by the slow diffusion of Et_2O into the reaction solutions over four weeks, which resulted in the formation of single block shaped crystals (Table 27).

Table 27: The colours of the single block shaped crystals of **L5** complexes.

	Code	Complex	colour	Code	Complex	colour	
monoclinic	**5B1**	$\{[Co(\mathbf{L5})](ClO_4)_2\}_\infty$	pink	**5B2**	$\{[Co(\mathbf{L5})](BF_4)_2\}_\infty$	pink	*triclinic*
P2₁/c s.g.	**5C1**	$\{[Fe(\mathbf{L5})](ClO_4)_2\}_\infty$	orange	**5C2**	$\{[Fe(\mathbf{L5})](BF_4)_2\}_\infty$	orange	$P\bar{1}$ s.g
monoclinic	**5D1**	$\{[Ni(\mathbf{L5})](ClO_4)_2\}_\infty$	blue	**5E2**	$\{[Zn(\mathbf{L5})](BF_4)_2\}_\infty$	clear	
C2/c s.g.	**5F1**	$\{[Cu_2(\mathbf{L5})](ClO_4)_2\}_\infty$	green	**5F2**	$\{[Cu_2(\mathbf{L5})](BF_4)_2\}_\infty$	turquois	

The formulations were established by elemental analysis, IR, and ESI-MS, and confirmed by X-ray crystallography. The **5B1** and **5C1** complexes are monoclinic and crystallise in the $P2_1/c$ space group; and the **5D1**, **5F1**, **5E2**and **5F2** complexes are monoclinic and crystallise in the C2/*c* space group. The **5B2** and **5C2** complexes are triclinic and crystalise in the $P\bar{1}$ space group.

The asymmetric unit of the **5B1** complex, consisted of two ligand halves coordinated to a Co(II) ion, with two associated ClO_4^- anions (Figure 58). The **5C1** complex had an asymmetric unit consisting of one full **L5** ligand coordinated to one Fe(II) cation in a Pz-O-Tz chelation site, with two associated ClO_4^- counter anions and a water (Figures 59). The water and the (Cl2) ClO_4^- anion have a hydrogen bond of H-A 2.1 (3) Å and D-H-A 130 (30) º, connecting them (Figure 60).

The **5B2** and **5C2** complexes had asymmetric units of; two halves of an **L5** ligand, coordinated to a metal ion (Co(II) and Fe(II) respectively), with two BF_4^- counter anions associated. (Figure 62 and 63) However, the **5C2** crystal structure, also has an associated water molecule, which the other complexes don't have. This water molecule also forms a hydrogen bond, with the counter BF_4^- anion, with a H-A distance of 1.745 Å, between the hydrogen of the water molecule and the F6-B2 of a BF_4^- counter anion of a separate asymmetric unit, with a O3-H-F6 angle of 156.22º. (Figure 61). However, this does not affect the packing of the 1D chains. This asymmetric unit, again shows, how the alternate sides of the **L5** ligand coordinate to a metal centre to assemble in a polymer chain arrangement.

The **5C1** complex polymer chains differed from the other complexes, due to the arrangement of paired strands, bordered by ClO_4^- metal anions, producing a double molecule layer sheet. Comparatively, **5B1**, **5D1** and **5F1** arranged as a single chain strands bordered by ClO_4^- metal anions.

The asymmetric units of **5D1**, **5E2**, **5F2** and **5F1** consist of a half ligand, coordinated to a corresponding, Ni(II), Zn(II) and Cu(II) cations, with the complexes having one associated counter anion (Figures 64-67). The **5F2** and **5F1** complexes are isostructural, with the complexes arranging in identical space groups, with only the counter anions differing.

The butyl tail in the **5F1** and **5F2** asymmetric ligand halves, if present in different orientations. C8B and C9B have 0.8 occupancies, while C8 and C9 have 0.2 electron occupancies, hence, the butyl tail is bent in different directions, at these ratios, throughout the crystal structure.

There is some splitting within the butyl tails, in **5B1** and **5F1**. In **5B1** there is splitting within both butyl tail, separately, on each end of the ligand, (C8-C10 = 0.7), (C8b-C10b = 0.3), (C18-C20 = 0.65), and (C18b-C20b = 0.35). In **5F1** C8 and C9 having an occupancy of 0.8, while C8b and C9b have an occupancy of 0.2. The changes in orientation of the butyl tail here are very minor, and does not appear to have a substantial effect on the overall packing of this crystal structure.

Monoclinic - $P2_1/c$ space groups

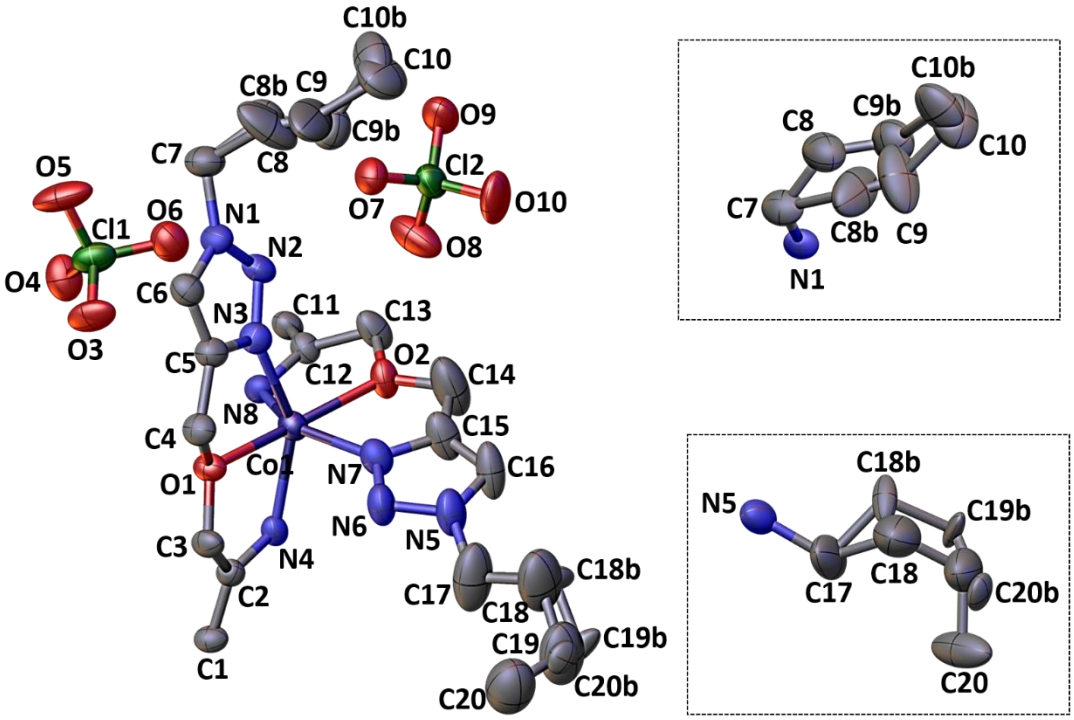

Figure 58: The crystal structure of the asymmetric unit of **5B1** {[Co(**L5**)]$(ClO_4)_3\}_\infty$, complex., of two half **L5** ligands coordinated to a Co(II) metal with two associated ClO_4^- anions. The butyl tails show the split: (C8-C10 = 0.7), (C8b-C10b = 0.3), (C18-C20 = 0.65), (C18b-C20b = 0.35). Colour Code: C = grey, N = blue, Cl = green, O = red, Co = dark blue, with, hydrogens omitted for clarity.

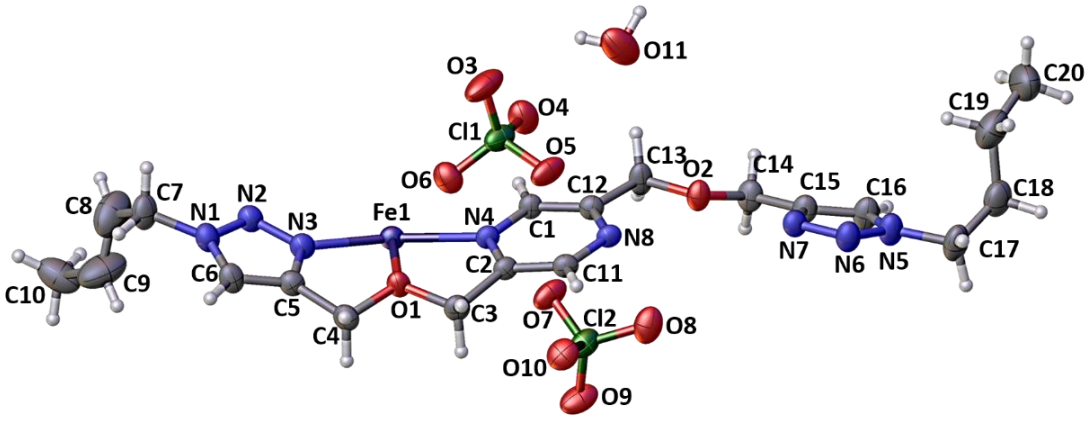

Figure 59: The crystal structure of the asymmetric unit of **5C1** {[Fe(**L5**)]$(ClO_4)_3\}_\infty$, consisting of one **L5** ligand coordinated to one Fe(II) ion, with two associated ClO_4^- anions. Colour Code: C = grey, N = blue, Cl = green, O = red, H = white, Fe = dark blue.

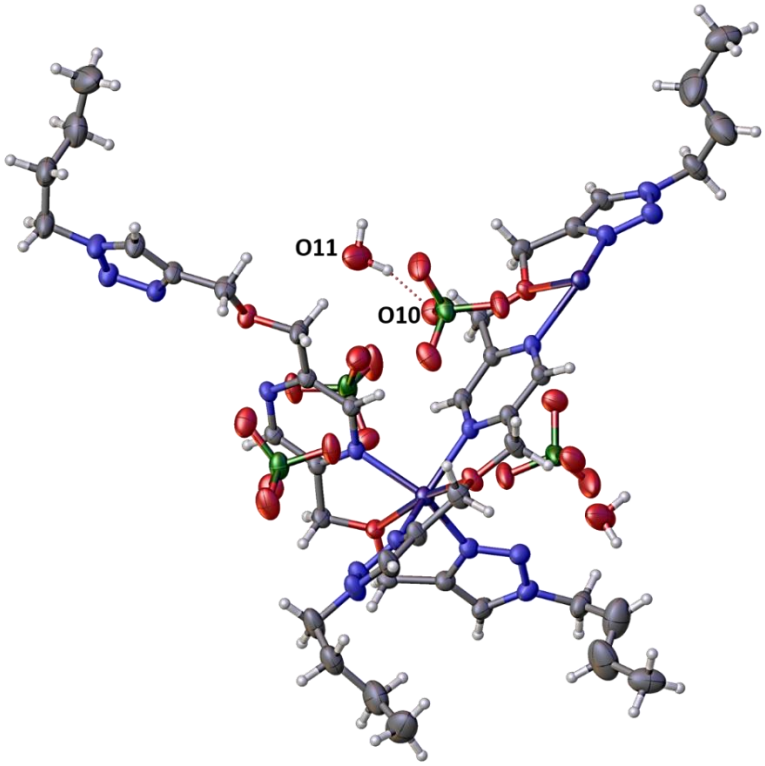

Figure 60: The crystal structure of two asymmetric unit of **5C1**, to show the hydrogen bonding between the associated water molecule and one of the perchlorate counterions. Colour Code: C = grey, N = blue, Cl = green, O = red, H = white, Fe = dark blue.

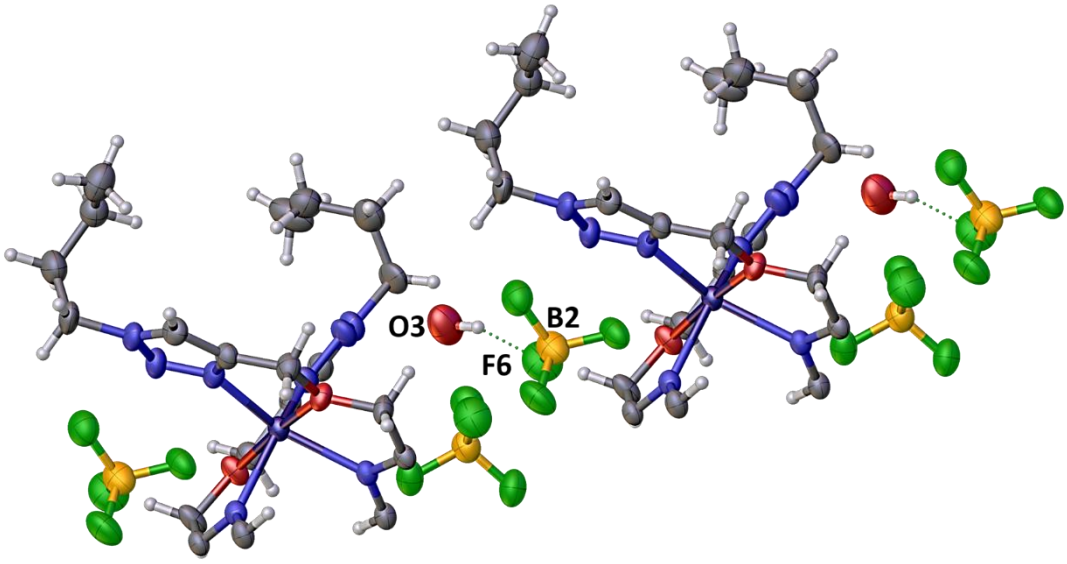

Figure 61: The crystal structure of two asymmetric units of **5C2** $\{[Fe(\mathbf{L5})](BF_4)_2\}_\infty$, complex, showing the hydrogen bond between the associated H_2O ligand and the **B2**-BF_4^- associate anion. Colour Code: C = grey, Fe = dark blue, N = blue, F = green, B = yellow O = red, H = white. Hydrogen bond shown with a dotted line.

Triclinic - $P\bar{1}$ space groups

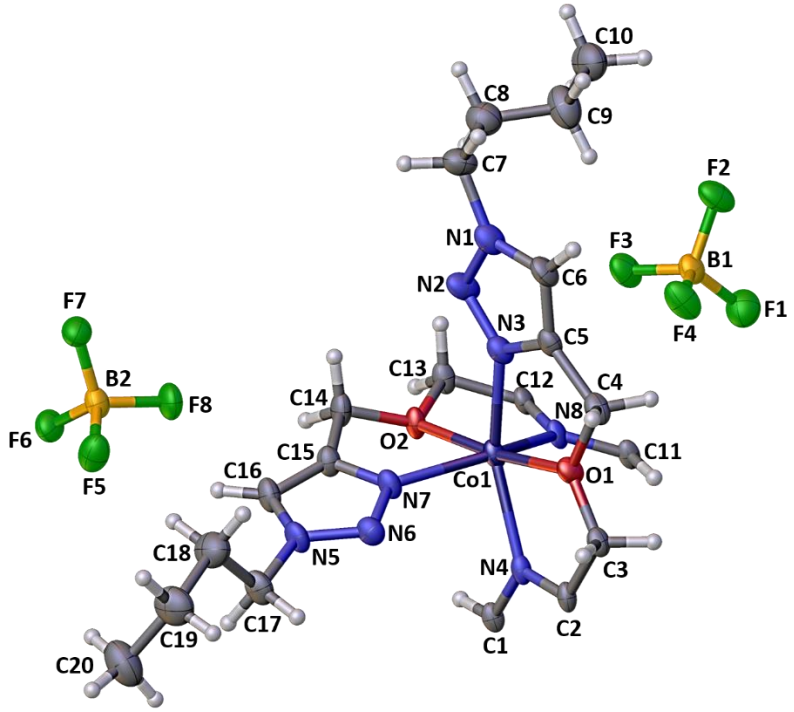

Figure 62: The crystal structure of the asymmetric unit of **5B2** $\{[Co(\mathbf{L5})](BF_4)_2\}_\infty$, complex., of two half **L5** ligands coordinated to a Co(II) metal with two associated BF_4^- anions. Colour Code: C = grey, Co = dark blue, N = blue, F = green, B = yellow O = red, H = white.

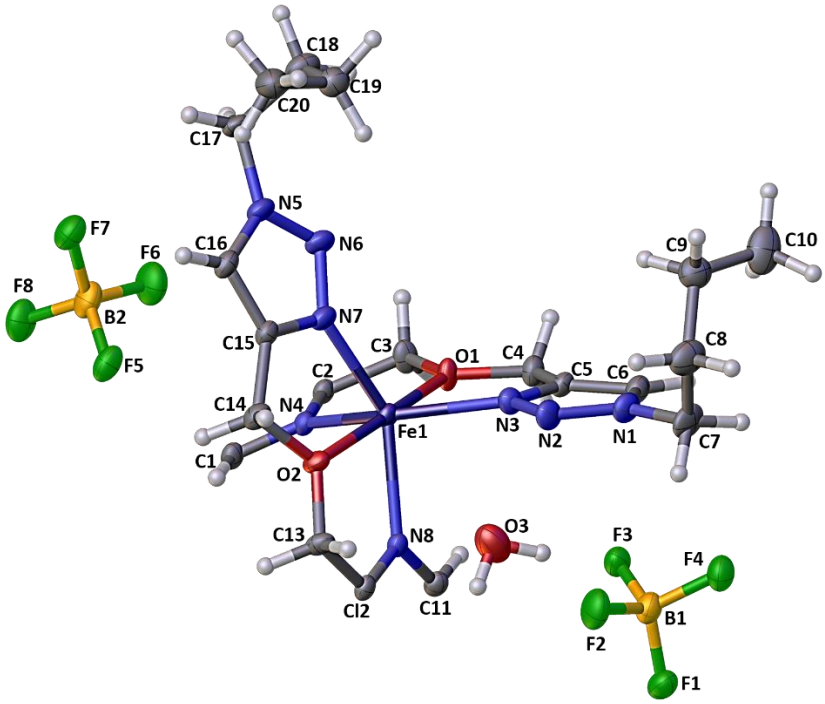

Figure 63: The crystal structure of the asymmetric unit of **5C2** $\{[Fe(\mathbf{L5})](BF_4)_2\}_\infty$, complex., of two half **L5** ligands coordinated to a Fe(II) metal, with two associated BF_4^- anions, and an associated water molecule. Colour Code: C = grey, Fe = dark blue, N = blue, F = green, B = yellow O = red, H = white.

Monoclinic - C2/*c* space groups

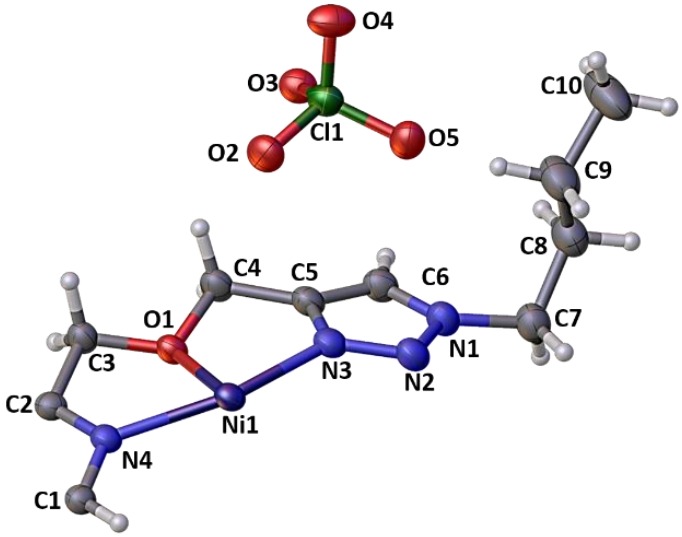

Figure 64: The crystal structure of the asymmetric unit of **5D1** {[Ni(**L5**)]$(ClO_4)_2\}_\infty$, complex., of a half **L5** ligand coordinated to a Ni(II) metal with an associated ClO_4^- anion: . Colour Code: C = grey, N = blue, Cl = green, O = red, H = white, Ni = dark blue.

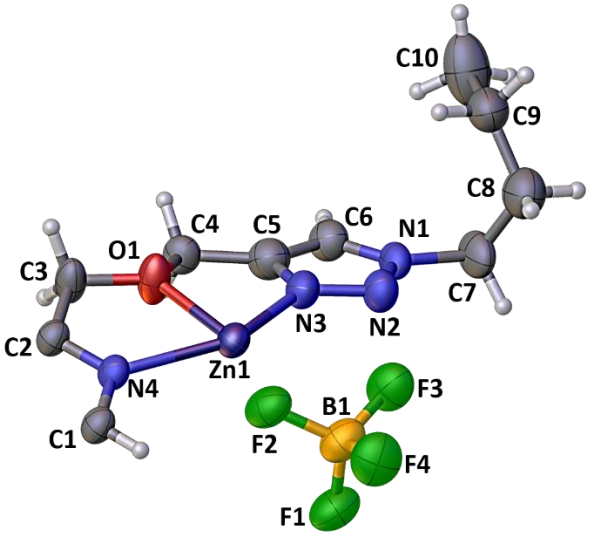

Figure 65: The crystal structure of the asymmetric unit of **5E2** {[Zn(**L5**)]$(BF_4)_2\}_\infty$, complex, of a half **L5** ligand coordinated to a Zn(II) metal, with an associated BF_4^- anion. Colour Code: C = grey, Zn = dark blue, N = blue, F = green, B = yellow O = red, H = white.

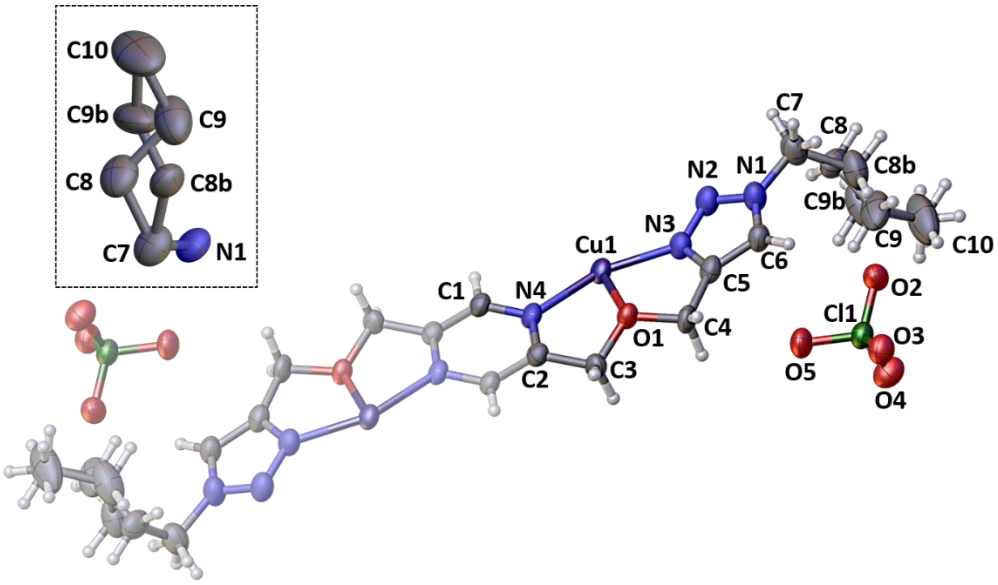

Figure 66: The crystal structure of the asymmetric unit of **5F1** $\{[Cu_2(\mathbf{L5})](ClO_4)_2\}_\infty$. complex., of a half **L5** ligand coordinated to a Cu(II) metal with an associated ClO_4^- anion. The butyl tails show the split: (C8-C10 = 0.8), (C8b-C10b = 0.2). Colour Code: C = grey, N = blue, Cl = green, O = red, Cu = dark blue. with hydrogens omitted for clarity.

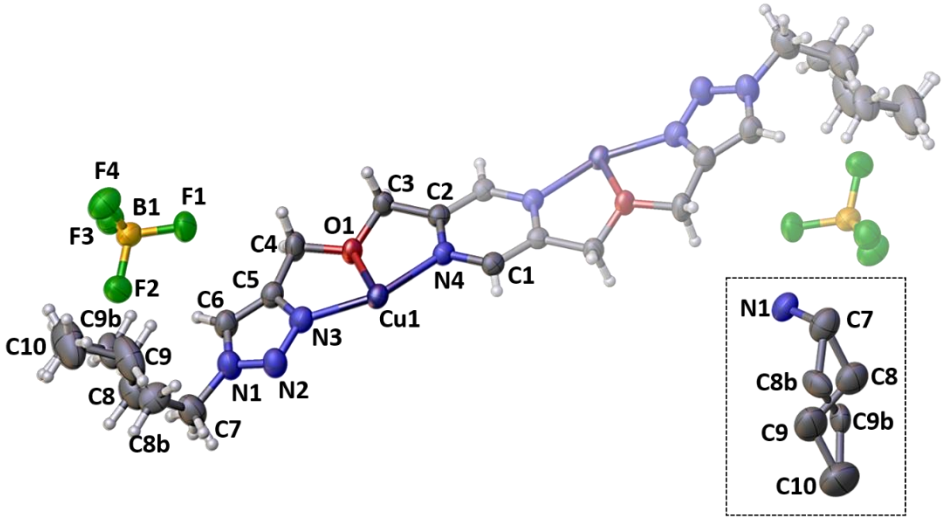

Figure 67: The crystal structure of the asymmetric unit of **5F2** $\{[Cu(\mathbf{L5})](BF_4)_2\}_\infty$, complex., of a half **L5** ligand coordinated to a Cu(II) metal, with an associated BF_4^- anion. The butyl tails show the split: (C8-C10 = 0.8), (C8b-C10b = 0.2). Colour Code: C = grey, Cu = dark blue, N = blue, F = green, -B = yellow O = red

Table 28: The Metal-atom bond lengths (Å) in the **5B1-5F1** perchlorate complexes.

	5B1	**5C1**	**5D1**	**5F1**
$N3_{(Tz)}$ - M	2.083 (5)	2.094 (5)	2.052 (4)	1.995 (3)
O1- M	2.137 (4)	2.184 (4)	2.060 (3)	2.254 (3)
$N4_{(Pz)}$ - M	2.120 (5)	2.149 (4)	2.072 (3)	2.038 (3)
$N7_{(Tz)}$ - M	2.066 (6)	2.107 (5)		
O2- M	2.130 (4)	2.175 (4)		
$N8_{(Pz)}$ - M	2.119 (5)	2.166 (5)		

Table 29: The Metal-atom bond lengths (Å) in the **5B2-5F2** fluoroborate complexes.

	5B2	**5C2**	**5E2**	**5F2**
$N3_{(Tz)}$ - M	2.070 (5)	2.177 (4)	2.067 (4)	1.997 (3)
O1- M	2.059 (4)	2.166 (4)	2.218 (3)	2.263 (3)
$N4_{(Pz)}$ - M	2.137 (5)	2.129 (4)	2.158 (3)	2.037 (3)
$N7_{(Tz)}$ - M	2.078 (4)	2.132 (4)		
O2- M	2.162 (4)	2.168 (4)		
$N8_{(Pz)}$ - M	2.107 (4)	2.178 (4)		

The corresponding [Co(II), Fe(II), Ni(II), and Cu(II)] metal centres in complexes **5B1-5F1** have very similar bond lengths between the metal centres and coordinated atoms, with **5D1** having the shortest distances, **5C1** having the longest bond lengths, while **5F1** had the largest range in bond lengths (Table 28).

The corresponding [Co(II), Fe(II), Zn(II), and Cu(II)] metal centres in complexes **5B2-5F2** have very similar bond lengths between the metal centres and coordinated atoms, with **5B2** having the shortest distances, **5C2** having the longest bond lengths, while **5F2** had the largest range in bond lengths (Table 29).

Table 30: Bond angles from metal centres in complexes **5B1-5F1,** (º) and distortions from octahedral.

	5B1 (º)	**5C1(º)**	**5D1(º)**	**5F1(º)**
O1-M-O2	169.18 (19)	167.39(16)	175.73 (15)	172.08 (14)
N3-M-N4	147.4 (2)	142.25 (17)	155.13 (14)	149.88 (14)
N7-M-N8	147.4 (2)		155.13 (14)	149.88 (14)
N4-M-O1	74.76 (17)	72.31 (14)	76.87 (12)	74.45 (11)
N4-M-N8	87.3 (2)	89.50 (16)	88.02 (18)	90.15 (18)
N4-M-N7	93.2 (2)	93.39 (17)	92.35 (13)	92.99 (14)
N4-M-O2	112.22 (19)	113.29 (15)	100.00 (12)	99.82 (12)
N3-M-O1	75.24 (18)	72.36 (15)	78.59 (12)	75.50 (12)
N3-M-O2	99.0 (2)	104.05 (16)	104.30 (13)	109.88 (13)
N3-M-N7	100.3 (2)	103.88 (19)	97.50 (2)	99.0 (2)
N3-M-N8	96.1 (2)	96.56 (16)	92.35 (13)	92.99 (14)
N7-M-O1	96.42 (19)	97.09 (16)	104.30 (13)	109.88 (13)
N7-M-O2	73.34 (19)	71.81 (15)	78.59 (12)	75.50 (12)
N8-M-O1	115.00 (18)	119.82 (14)	100.00 (12)	99.82 (12)
N8-M-O2	74.39 (18)	72.31 (14)	76.87 (12)	74.45 (11)
Average angle	91.44	92.20	90.81	91.20
Σd octahedral distortion	17.27	26.37	9.74	14.46
Total distortion	147.21	169.79	111.86	134.66
Mean Σd	74 ± 14	92 ± 16	92 ± 10	91 ± 13
Δd range	2.7-22.22	0.5-29.82	1.98-14.3	0.16-19.88

Table 31: Bond angles from metal centres in complexes **5B2-5F2,** (º) and distortions from octahedral

	5B2	**5C2**	**5E2**	**5F2**
O1-M-O2	173.56 (16)	173.33 (14)	178.86 (19)	172.64 (13)
N3-M-N4	152.45 (18)	142.78 (17)	142.72 (14)	150.36 (13)
N7-M-N8	143.89 (17)	143.68 (17)	142.72 (14)	150.36 (13)
N4-M-O1	73.34 (16)	71.58 (14)	71.65 (12)	74.6 (10)
N4-M-N8	89.77 (17)	88.83 (15)	89.11 (17)	90.45 (17)
N4-M-N7	88.20 (18)	92.14 (16)	92.93 (13)	93.14 (13)
N4-M-O2	111.06 (16)	101.95 (15)	107.49 (14)	100.09 (11)
N3-M-O1	77.24 (18)	72.34 (15)	72.26 (13)	75.80 (11)
N3-M-O2	96.40 (18)	113.74 (16)	108.45 (15)	109.23 (12)
N3-M-N7	97.91 (19)	108.07 (17)	107.12 (14)	98.0 (2)
N3-M-N8	100.33 (18)	92.20 (16)	92.93 (13)	93.14 (13)
N7-M-O1	108.17 (17)	109.13 (17)	108.45 (15)	109.24 (12)
N7-M-O2	73.44 (15)	72.19 (15)	72.26 (13)	75.80 (11)
N8-M-O1	106.12 (16)	105.59 (15)	107.49 (14)	100.09 (11)
N8-M-O2	73.76 (14)	72.11 (14)	71.65 (12)	74.6 (10)
Average angle	91.31	91.66	91.82	91.18
Σd octahedral distortion	144.24	165.77	167.93	132.58
Mean Σd	15.74	19.87	21.79	14.18
Δd range (º)	0.23-21.06	1.17-23.74	0.89-18.45	0.45-19.23

In these complexes, the average bond angle in each of the complexes are close to the 90º expected in a true octahedral metal geometry. But, the Σd octahedral distortion measurement, calculated from the sum of the differences from 90º, (Equation 4)[118]and the range of distortions from 90º, were quite large (Table 30 and Table 31). This indicated that all of the perchlorate complex metals had distorted octahedral geometries.

Equation 4: The octahedral distortion measurement Σd. Buron-Le Cointe *et al.*[118]

$$\Sigma d = \Sigma_{i=1}^{12} |90 - \Phi_i|$$

All the **L5** complexes that were successfully isolated, (excluding Mn(II) complexes) formed one general structure of a 1D polymer chain. These polymers consist of the 3d ion, occupying a distorted octahedral geometry which is occupied by the Pz-O-Tz chelation sites of two ligands, as shown by the Cu(II) isocomplexes in (Figure 68). The individual polymer chains are arranged into 2D sheets, separated by the hydrophobic interactions between the butyl side groups of the polymer chains.

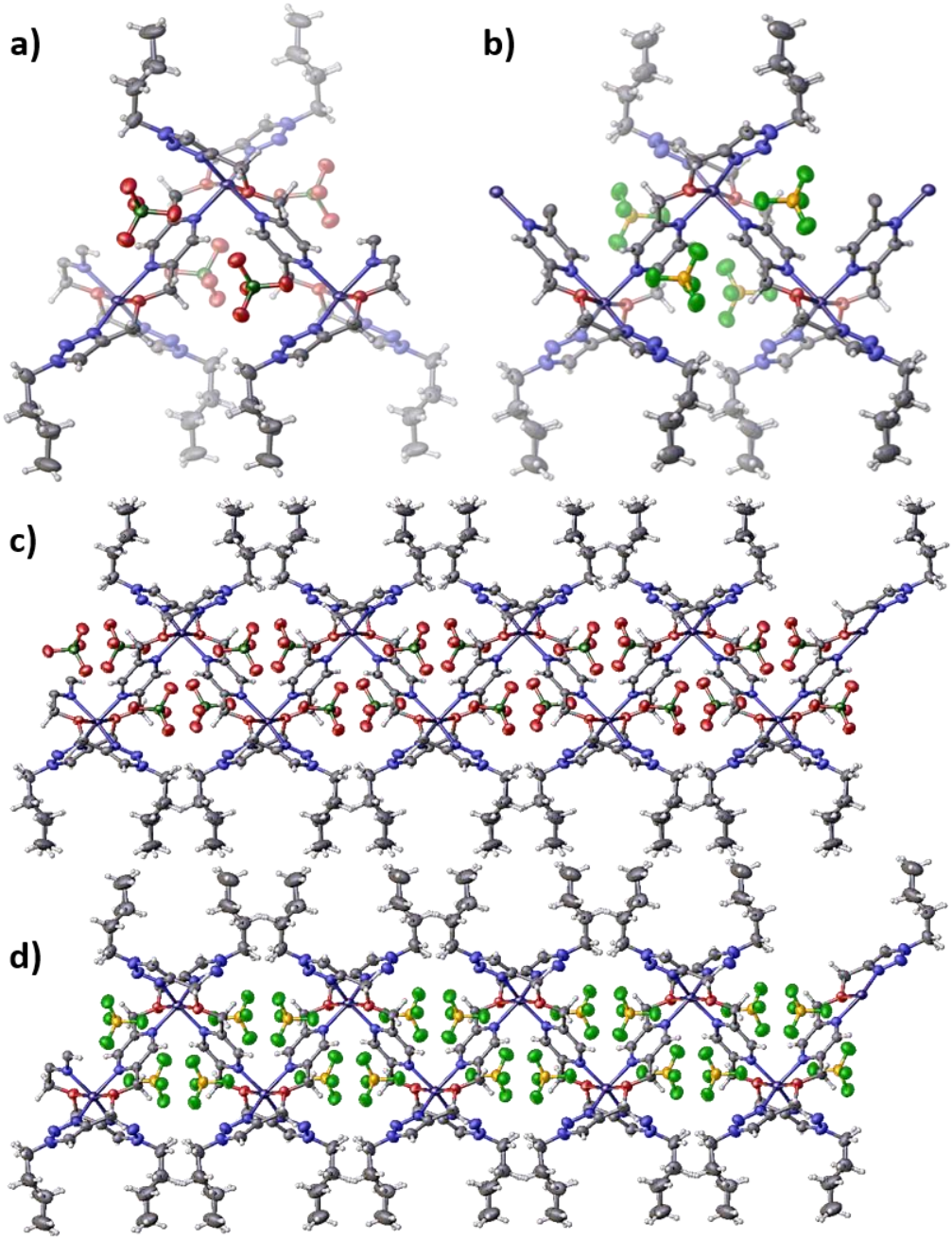

Figure 68: Crystal structures of **L5** complexes. Close ups of the over-under coordination of the polymer chains a) **5F1** and **5F2**. Sections of the polymer chains of c) **5F1** and d) **F52**, with a counterion arranged on each face of the pyrazines of the complex, perchlorate and fluoroborate respectively.

The general formation of the 2D sheets was consistent across the different complexes. The arrangement of the butyl tails, appeared to be random, with the butyl groups occupying different locations even within the same complex. It is the length and flexibility of the butyl group that introduced this inconsistent element; a shorter or more rigid azide click group would lead to more consistent architectures and packing.

The 2D sheets arranged on top of each other. Cross sections of this packing is shown in Figure 69.

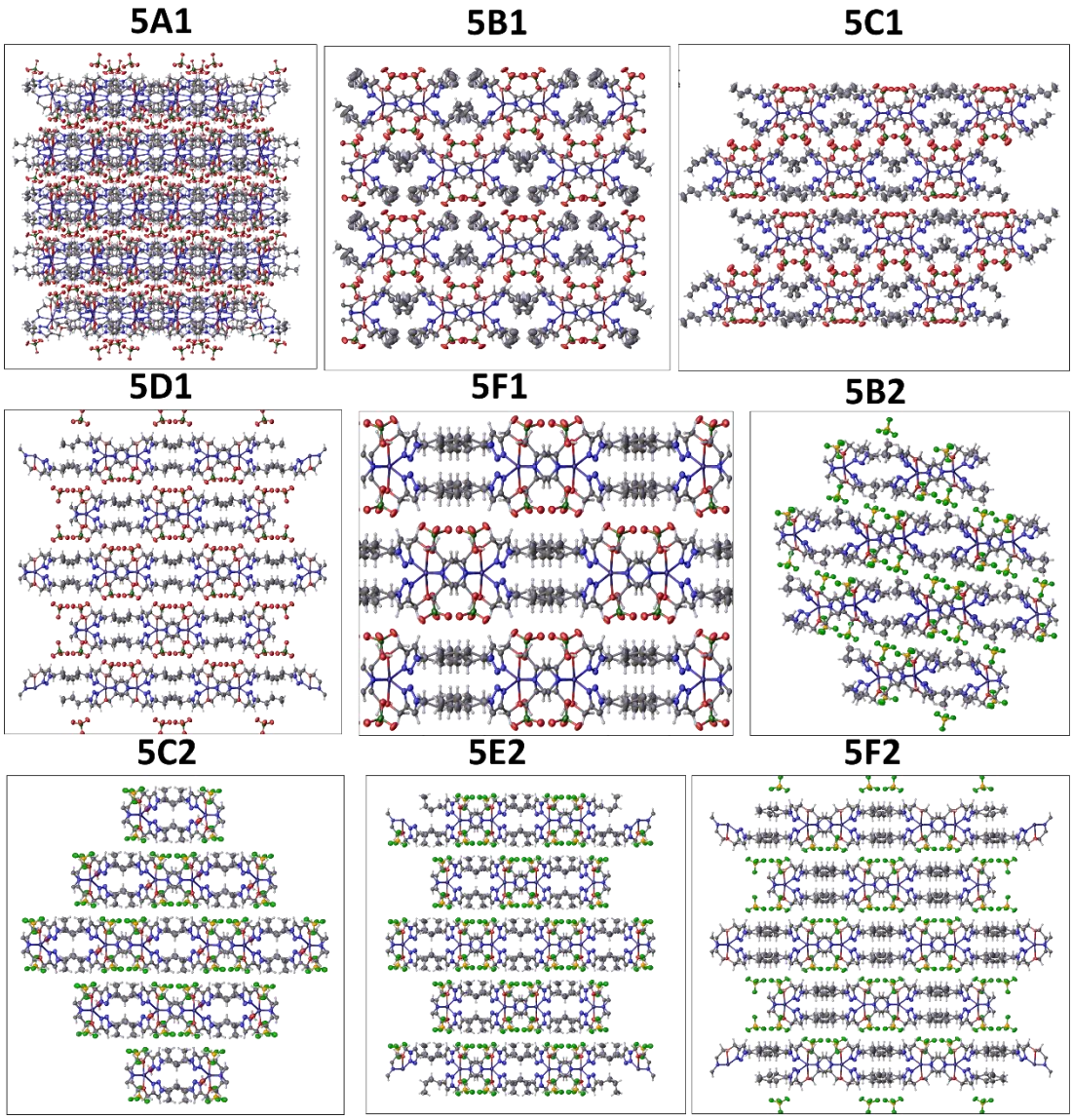

Figure 69: Cross-sections of the 3D packing of the **L5** complexes, of the 001 cell view.

4.8 Influence of templating ions to on L5 complex formation

With the consistent synthesis of single polymer chains, the next step was to investigate whether the resulting complex structure ligand system could be altered through the influence of ions. The range of ions introduced, and their results can be seen in Table 32. The introduction of excess counter anions during complexation was done, in order to see if these ions could influence the final structure by acting as a template, driving the equilibrium towards discrete complexes.

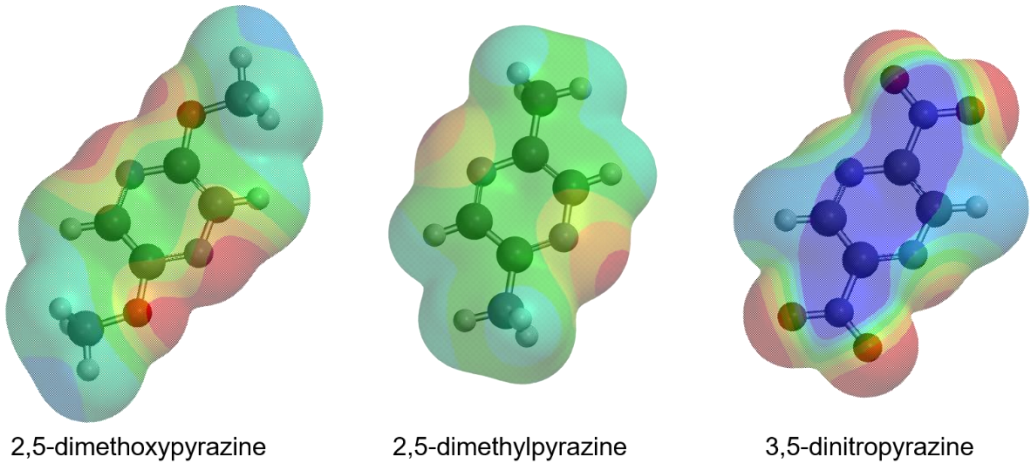

Figure 70: PM3 semiempirical Spartan examples of positive and negative electronegativity environments around pyrazine groups. Key: red indicates an electronegative surface, blue represents an electropositive surface.

If the large void spaces within the 'zig-zag' of the final polymer were electronegative spaces, (example shown in Figure 70.) the introduction of larger positive cations (Ba and Pb) could have filled these spaces during assembly and forced the ligands to build around these cations as templates.

The introduction of other larger anions, PF_6^- and I^-, could fill possible electronegative void spaces and again could then force the ligands to build around them, or could possibly disrupt the layering between the polymer sheets into a different arrangement.

Table 32: Results of **L5** complexation reactions with additional counter ions and metal salts.

	5G1	**5G2**	**5G3**	**5G4**	**5H1**	**5H2**
Metal Salt	$Co(BF_4)_2.H_2O$	$Fe(ClO_4)_2.6H_2O$	$Co(BF_4)_2.H_2O$	$Fe(BF_4)_2.H_2O$	$Co(BF_4)_2.H_2O$	$Fe(ClO_4)_2.6H_2O$
M equiv.	0.96	0.76	1.06	0.99	0.96	1.02
Introduced Ion	$Na(ClO_4)_2.H_2O$	$Na(ClO_4)_2.H_2O$	BF4	BF4	$Ba(ClO_4)_2$	$Ba(ClO_4)_2$
Introduced ion equiv.	2.50	1.96	1.94	1.83	1.04	1.06
Colour Δ						
Crystal	√	√	√	X	√	X
	pink	orange	pink		pink	
	5H3	**5J1**	**5J2**	**5J3**	**5J4**	
Metal Salt	$Co(BF_4)_2.H_2O$	$Co(BF_4)_2.H_2O$	$Fe(ClO_4)_2.6H_2O$	$Co(BF_4)_2.H_2O$	$Fe(ClO_4)_2.6H_2O$	
M equiv.	1.06					
Introduced Ion	$Pb(ClO_4)_2.3H_2O$	KI	KI	PF_6	PF_6	
Introduced ion equiv.	0.88	0.96	0.98	0.87	0.94	
Colour Δ						
Crystal	√ pink	√ pink	√ orange	√ pink	X	
Ppt		Brown	Brown			

The single crystal results from these experiments resulted in cell data that matched the original **L5** complexes, and were isolations of the original corresponding polymer chains. The introduction of other ions did not impact the self-assembly of the 3*d* 1D polymer chains, and that these complexes are self-sorting.

4.9 Complexations with L6

4.9.1 General Complexation Synthesis

With the successful synthesis of **L6**, a variety of 3*d* salts, were introduced. The full range, of metal salts, their ratios, and their results, is available in Apx10.0. The complexes attempted, and their complex codes are displayed in Table 33.

Following the general pattern of the results of the **L5** complexes, the successfully isolated **L6** complex, with $Cu(ClO_4)_2.6H_2O$, **6F1** arranged into 1D polymer chains $[M_1L_1]_\infty$ held in layers of 2D sheets by non-covalent interactions,

Table 33: The 3*d* metal salts reacted with **L6**, and their complex codes. **Bold** metal salts have resulted in successful crystal structures.

6A1	$Mn(ClO_4)_2.6H_2O$	6A3	$Mn(NO_3)_2.4\ H_2O$
6B1[*]	**$Co(ClO_4)_2.H_2O$**	**6B2**[*]	**$Co(BF_4)_2.6H_2O$**
6C1	$Fe(ClO_4)_2.6H_2O$	6C2	$Fe(BF_4)_2.6H_2O$
6D1	$Ni(ClO_4)_2.6H_2O$	6E2	$Zn(BF_4)_2.H_2O$
6F1	**$Cu(ClO_4)_2.6H_2O$**	6F2	$Cu(BF_4)_2.6H_2O$

(*) Crystals of complexes isolated but not yet analysed.

4.9.2 Characterisation of 6F1 complex

The syntheses of the 1D polymer chain complex, **6F1** $\{[Cu\mathbf{L6}](ClO_4)_2\}_\infty$ followed the general procedure; the reaction between **L6** and $Cu(ClO_4)_2.6H_2O$ in both a 1:1 ratio, which resulted in a green to blue to yellow solution colour change. Isolation was achieved by vapour diffusion of Et_2O into the reaction solutions over a period of three weeks, resulting in the formation of green block crystals of **6F1**. The formulations were established by elemental analysis, IR, and ESI-MS, and confirmed by X-ray crystallography. The X-ray crystallography, data shown in Apx11.0. However, although the crystals were able to be used to collect SCXRD data, what was collected only had an R_1 value of 22.80%, which was enough to allow for connectivity to be established, but higher quality crystals are needed for publication in the future.

The **6F1** complex was monoclinic and crystallised in the C2/*c* space group. The asymmetric unit consists of a half ligand coordinated to an octahedral Cu(II) with a perchlorate ion associated (Figure 71), the remainder of the complex extends into a continuous metalloorganic 1D polymer chain.

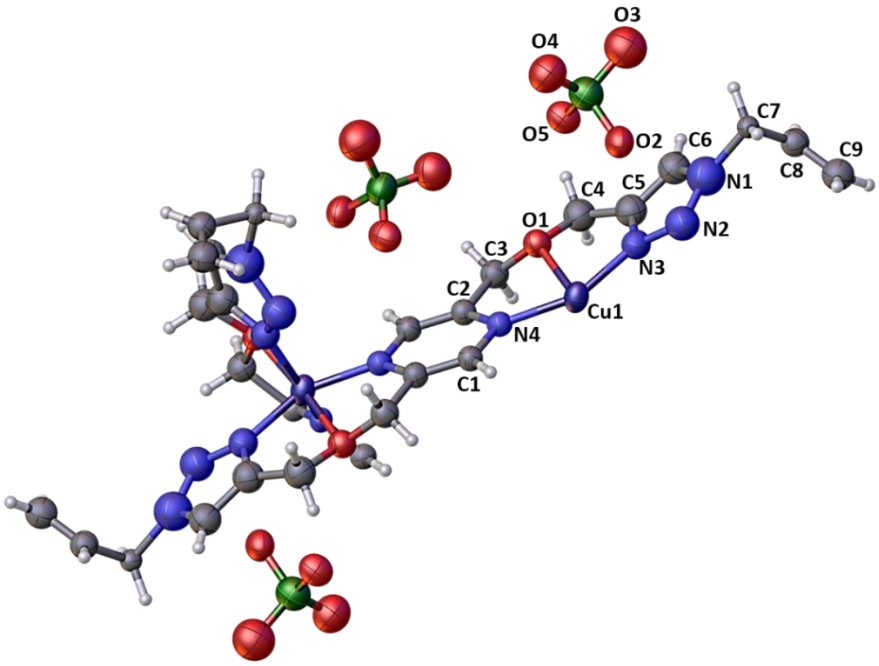

Figure 71: The crystal structure of **6F1**, illustrating the polymer bonding between L6 ligands and coordinated Cu(II) ions. The assymetrical unit is labelled. Colour Code: C = grey, N = blue, O = red, Cl = green, Cu = dark blue, H = white.

Table 34: Selected bond lengths (Å) and angles (º) of **6F1**.

Bond lengths (Å)					
N3-M	1.920 (15)	O1-M	2.241 (16)	N4-M	1.926 (17)
Angles (º)					
O1-M-O2	174.46	N3-M-N4	149.9 (8)	N7-M-N8	149.9 (8)
N4-M-O1	73.2 (6)	N3-M-O1	76.7 (8)	N7-M-O1	99.2
N4-M-N8	91.6	N3-M-O2	99.2	N7-M-O2	76.7 (8)
N4-M-N7	97.8	N3-M-N7	88.21	N8-M-O1	110.8
N4-M-O2	110.8	N3-M-N8	97.8	N8-M-O2	73.2 (6)
Σd total oct.distortion	139.19º		range	1.6 – 20.8º	
Mean Σd	11.6º				

As seen in the **L5** complexes, the Cu(II) ion was in a distorted octahedral geometry, (Table 34) with the six coordination sites being filled by the Pz-O-Tz chelation sites of two **L6** ligands. The complex extends indefinitely in a zig-zag, 1D polymer chain of **L6** ligands interlocked by octahedral ions. Again, like the **L5** complexes, hydrophobic interactions arrange the propene tails to stack, but this time in a 'zip' like arrangement, forming 2D sheets. These sheets then form a layered 3D crystal structure, (Figure 72).

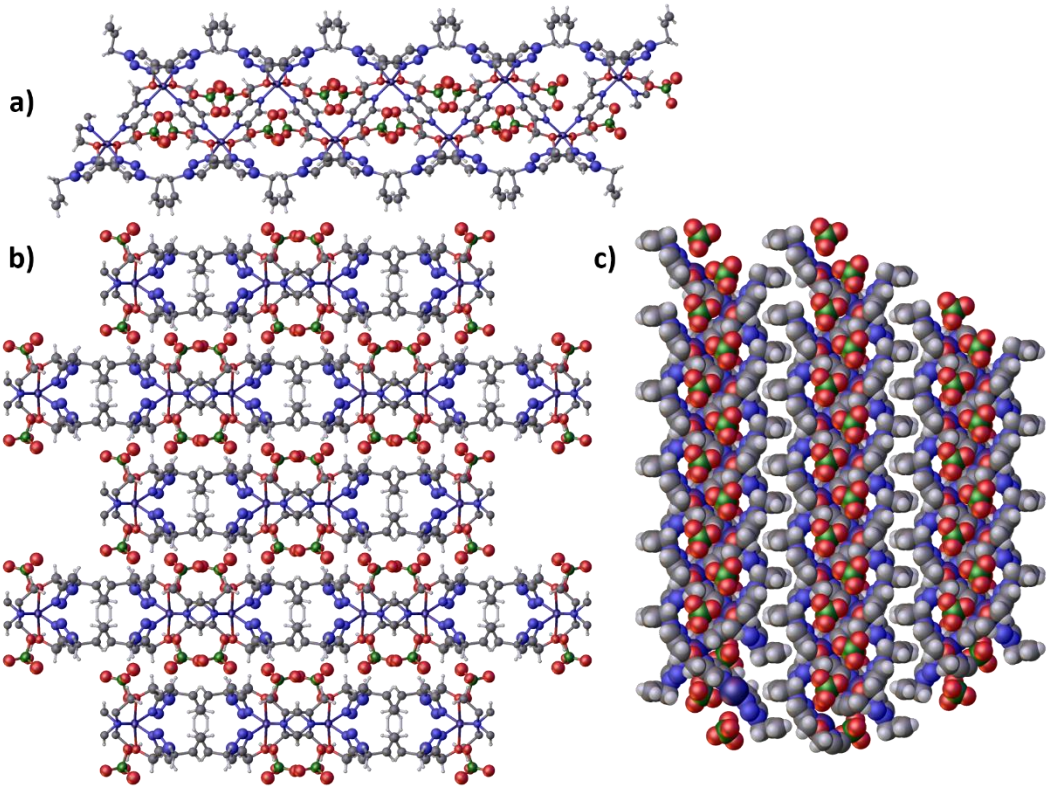

Figure 72: The crystal structures of a) The polymer chain complex of **6F1** b) the cross-section of the 3D structure of the **6F1** crystal in the 001 cell view, and c) the packing of the polymer chains within the 2D sheets.

Some of the immediate future work involves the analysis of the crystal structures that have resulted from the reactions between **L6** and 3*d* metal salts. The $Co(BF_4)_2.6H_2O$ salt in **6B2** resulted in pink plate single crystals. These have been confirmed by an initial X-ray crystallography. However, the full analysis of these complexes needs to be competed, as the crystals only appeared within the last week of research. There is still the possibility of other **L6**-3*d* complexes crystallising out.

4.10 Conclusions of L5 and L6 complexes

'Clicking' a range of azide groups, to the newly synthesised **E1** intermediate has opened up a route to a new array of ligands, with new Pz-O-Tz chelation sites. Of these new possibilities **L5** and **L6** were synthesised using butan azide and 3-azido-prop-1-ene.

The new **L5** ligand was reacted with a wide range of metal salts, and went on to produce ten characterised crystal structures; one Mn(III) monomer, and nine 1D polymer chain complexes. The **L5** metal complexes produced a general zig-zag polymer architecture, with the hydrophobic interactions of the butyl tails arranging these polymer chains into 2D sheets, and counter anions (ClO_4^- and BF_4^-) held within the polymer chains. The 3d ions (excluding Mn(II)) coordinated to the **L5** ligand in distorted octahedral geometries.

The Mn behaved differently in **5A1** and **5B1**, compared to the other complexes that formed. With the Mn(III) forming a a mono-capped trigonal prism shaped coordination. This resulted in the more obtuse angles in ligand arrangement in **5A1** compared to the other ClO_4^- and BF_4^- single chain polymer complexes, discussed later. **5B1** formed a discrete monomer complexes due to the coordination of the Mn(III) ion and the use of NO_3^- as a counter ion.

The **L6** ligand was also reacted with a range of metal salts, of which, three have formed single crystals with the {[Cu**L6**]$(ClO_4)_2$ structure derived from X-ray crystallography. This initial **L6** complex also formed a 1D zig-zag polymer chain complex, similar to the general architecture of the **L5**-metal complexes. It is expected that the other **L6** complexes that are isolated, will likely form this same general architecture.

In the future, the complexes isolated here need to be remade in larger quantities, in order to perform electrochemical and magnetic analyse. These results should then show if there is any possibility of these structures having properties that contribute to metal-metal communication. This was the overall property that was aimed to be produced, to provide a desirable function in new materials.

5.0 Imine Ligands

5.1 Endo- and Exo- Imine Pyrazine Ligands

The investigation into the variations between exo- and endo-imine Schiff base pyrazine ligands, (Figure 73), was started with a recreation of **L1^{endo}**, previously synthesised by Brooker, *et al*. [74]{Hogue, 2017 #73} and Dais *et al*. [75] [60]The triangle cyclohelicate formed by this ligand was discussed in Section 1.4.4.

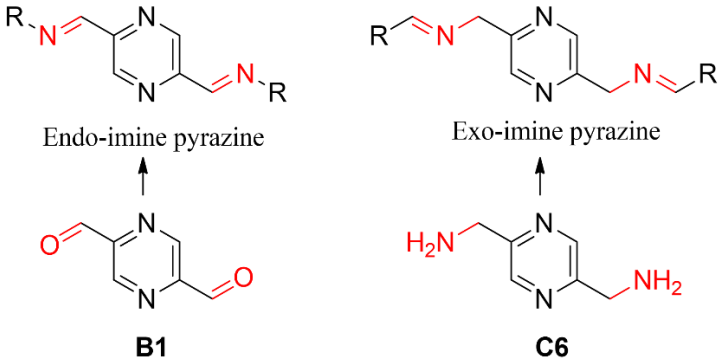

Figure 73: The general chemical structures of Endo-Imine and Exo-imine pyrazine ligands. The differences in the location of the double bond of the imine, are highlighted in red for clarity. The ketone and amine, pyrazine precursors are below the corresponding imine that is formed through Schiff base condensation. **B1**: 2,5-di(formyl) pyrazine, **C6**: 2,5-di(aminomethyl) pyrazine.

The endo-imine ligands are synthesised from the Schiff base condensation of an aldehyde species, 2,5-diformyl pyrazine **B1**, to various primary amine groups. This includes reacting 2-(2-Aminoethyl)pyridine **B2**, to produce the previously synthesised **L1^{endo}**. This required the initial isolation of **B1**. With **B1**, further exo-imine ligands could also be extrapolated.

The synthesis of any exo-imine ligands, including **L1^{exo}** would firstly require the synthesis of 2,5-bis(aminomethyl) pyrazine, **C6**. A synthesis of which has yet to be determined. Isolated **C6**, could then be condensed with a range of carbonyl species, to produce a new family of ligands.

5.2 Schiff Base Condensation

The Schiff base condensation for imine formation is a simple, efficient method for the formation of ligands, that is also usually high yielding. This reaction has been used previously to successfully generate ligands capable of forming cyclohelicate complexes. Schiff base condensations are an excellent way to introduce more donor atoms into a chemical system, where the imine produced can coordinate to a metal centre, such as with the cyclohelicate triangles reported by Brooker *et al.*[59]and Dais *et al.*[60] utilising the exo-imine ligand, **L1^{exo}**.

The introduction of a wide range of function structures, can be joined to pyrazine centres, using complimentary carbonyl or amine functionalities to produce imine linkages. Ligands synthesised from Schiff base condensations, have assembled complexes, exhibiting interesting supramolecular and magnetic properties.[119]

The mechanism for this Schiff base condensation is shown in Scheme 10. Nucleophilic attack by a primary amine occurs on an electrophilic carbonyl, resulting in a carbinolamine species, the loss of water produces the imine product. The production of water in this reaction, means that the reactions should be kept dry to promote high yields. Another point to be kept in mind in the method used is that the imines can be hydrolysed back to starting precursors in aqueous acidic conditions.

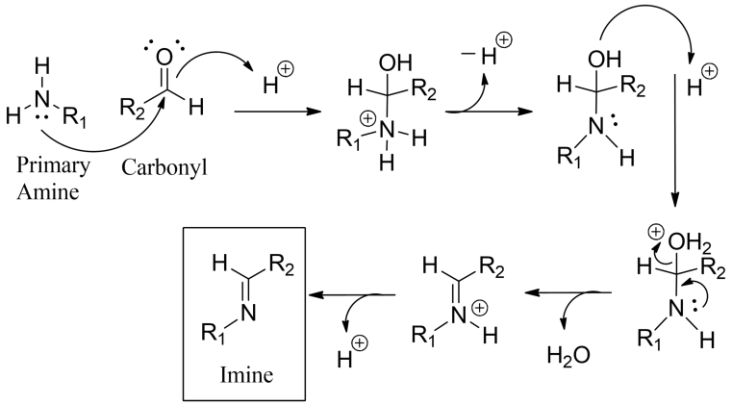

Scheme 10: Mechanism for Schiff Base Condensation, based of Hossain *et al.*[120]

The successful synthesis of Schiff base ligands can be confirmed with a combination of ^{1}H and ^{13}C NMR spectroscopy. The imine bond is distinguished by observing the disappearance of the carbonyl peak (usually around δ = 9.5 – 10 ppm in the ^{1}HNMR spectra); as well as, infrared (IR) spectroscopy, with a peak corresponding to the imine C=N stretch (1690-1640 cm^{-1}) and the absence of the carbonyl C=O stretch (1720-1680 cm^{-1}).[121]

5.3 Pyrazine Centre: 2,5-diformyl pyrazine (B1)

The synthesis of **B1** followed the two-step method developed by Brown, 2018 [20] and Hogue *et al.*[11a] starting from 2,5-dimethyl pyrazine, **A1**. The first step was developed by, a previous member of the Plieger group, Brown, 2018 [20]; a five hour, 175 ºC microwave synthesis, reacting **A1** with, benzoic anhydride and benzaldehyde (Bnz); converting **A1** to 2,5-*E*,*E*-distyrylpyrazine, **A2**. The full method is shown in Apx1.1, with characterisation of **A2** in Apx12.1.1.

This reaction, seen in Scheme 11, was limited by the volume that can be reacted within the microwave vessel, however, this volume is economic in that no solvent was used, and generally produced around 1.2-1.5g 46-68 % yields of **A2**, a bright yellow, crystaline product, which was fluorescent in solution. Due to **A2** decomposing over time and when exposed to UV, it was stored in the freezer and used within a short timeframe.

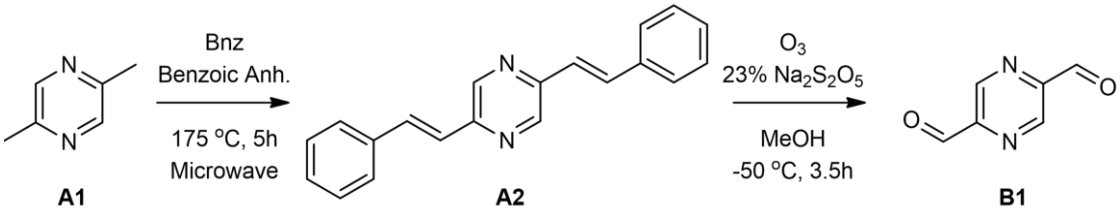

Scheme 11: The reaction scheme for the synthesis of, 2,5-distyryl pyrazine, **A2** and 2,5-diformyl pyrazine, **B1**. Reaction adapted from Brown. [20]

The second reaction, was the ozonolysis of **A2** to the desired **B1** product. This technique, was reported by both Hogue *et al.*[59] and Dais *et al* [60], and involved bubbling ozone through a suspension of fresh **A2** in MeOH, at temperatures below -50 ºC over the course of three and a half hours. This is followed by a reductive workup, wherein aqueous 23% meta-bisulfate was added dropwise, and then the **B1** product was isolated through a series of extractions. The full method for **B1** can be found in Apx1.2 and ^{1}H NMR in Apx12.1.2.

The scale of this synthesis was limited by several factors. Firstly, even though >1g quantities of **A2** could be produced with relative ease, the formation of an explosive intermediate, the ozonide ion, (Scheme 12), in the second synthesis, required that the ozonolysis was never being performed with more than 1.5 g of **A2** starting material. Secondly, during the formation of **B1**, the loss of mass involved during this oxidation,

meant that the yield was only ever a maximum of 0.6219 g, with the largest yield obtained being 61%.

Additionally, there was some evidence that **A2** decomposed at higher temperatures and when exposed to UV. Due to this, the ozonolysis was performed wrapped in tinfoil, and the work up and removal of solvents was performed in amber round bottom flasks, at either RT or below. Ultimately, this resulted in **B1** only being produced in amounts < 200 mg, for use in ligand synthesis.

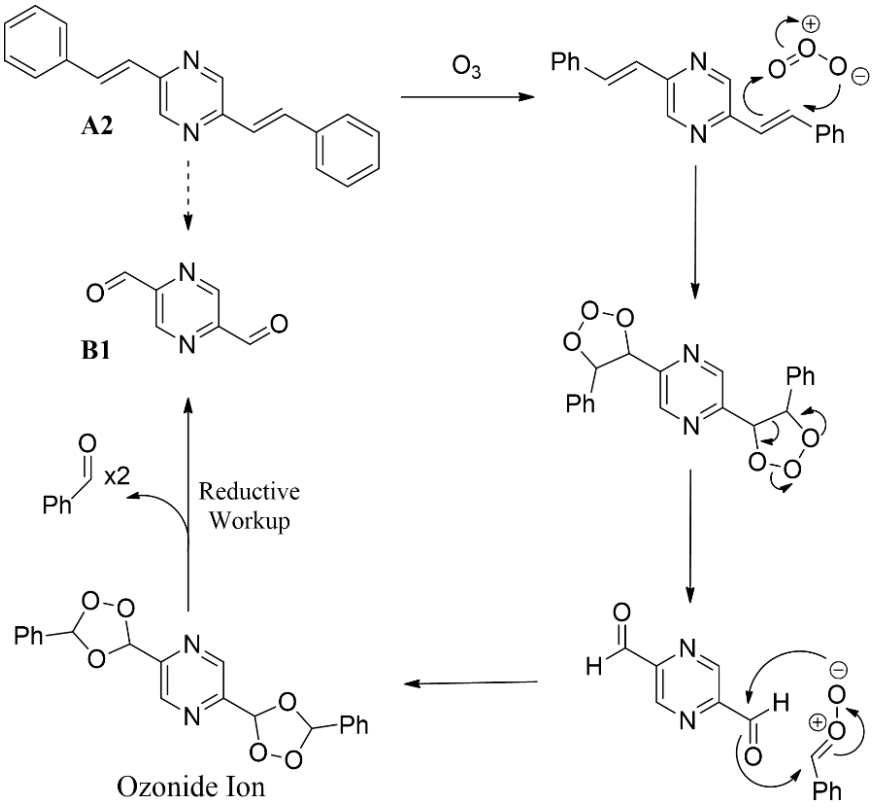

Scheme 12: Ozonolysis oxidation reaction mechanism of **A2** to **B1**

5.4 Remaking of (L1^{endo})

Pyrazine-2,5-diylbis(methanylylidene))bis(2-(pyridin-2-yl)ethanamine

With the successful synthesis of **B1** achieved, exo-imine ligands could be investigated. This began with the synthesis of **L1**, the endo-imine ligand previously synthesised by Brooker *et al*[59] and Dais *et al.* [60] This final step in the ligand synthesis was a Schiff base condensation, previously discussed at the beginning of Section 5.0.

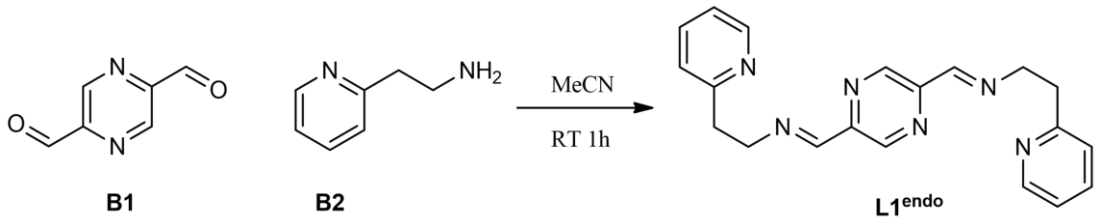

Scheme 13: Reaction Scheme for the synthesis of **L1.**

The **L1^{endo}** ligand resulted from the condensation of 2-(pyridin-2-yl)ethanamine, **B2**, and **B1** in MeCN, Scheme 13. The reaction was stirred at RT for an hour and left to sit at -5 ^{o}C for three hours, producing a pale brown/yellow solid precipitate of **L1^{endo}**. The full method for the synthesis of **L1 ^{endo}** can be found in Apx1.3 and Apx12.1.3. The ^{1}HNMR resulted in δ ($CDCl_3$) = 9.14 (s, 2H), 8.56 (d, 2H), 8.35 (s, 2H), 7.58 (m, 2H), 7.17 (d, 2H), 7.12 (m, 2H), 4.15 (t, 4H), 3.24 (t, 4H). The 10.24 ppm ^{1}H NMR peak of the **B1** aldehyde disappeared. The ^{1}H NMR of the pyrazine peak had shifted from 9.31 to 9.14 ppm. This data indicated the successful synthesis of the imine moiety.

The product was produced with 20-25% yields, which was similar to literature examples.[20] One possibility for the low yield was due to the further decomposition of **B1** between the stages of synthesis, however, the high yields seen with **L2**, indicate that this is not the reason, and that there is something within this reaction causing the low yield.

The colour of **L1^{endo}** behaved unexpectedly; the dry solid became a purple colour over time, but when in solution, it became yellow. It is possible that there is tautomerisation in the highly conjugated, structure, and that conversion between the possible conformations results in these alternative colours.

With isolated **L1^{endo}** complexations were attempted using the metal salts as shown in Table 35, dissolved in MeCN. These salts were introduced to **L1^{endo}** dissolved in MeCN at RT and stirred for half an hour, following the complexation methods used by Dais *et al.*[60] These samples were set up for isolation by the vapour diffusion of Et_2O into the reaction solution, and left for two months.

Only the results discussed in Section 5.5, resulted in crystals.

Table 35: Complexations of **L1** and various metal salts, with the respective solvent system used, the colour changes observed and the complexation code

Metal Salt	Solvent	Colour Δ	Complex Code
$Co(ClO_4)_2 \cdot 6H_2O$	MeCN	Red/Brown	**C1A**
$Mn(ClO_4)_2 \cdot 6H_2O$	MeCN	Orange/Red	**C1B**
$Co(BF_4)_2 \cdot 6H_2O$	MeCN	Red	**C1C**

5.5 Oxidation of (L1^{endo}) – (L1b)

Over the process of vapour diffusion for **C1B**, there was an unexpected result from the extended length of diffusion. A large, light-brown, needle-shaped X-ray quality crystal was grown, which X-ray crystallography revealed as a ligand other than the expected **L1^{endo}**. Instead of the imine group, there were amide groups. (Figure 74).

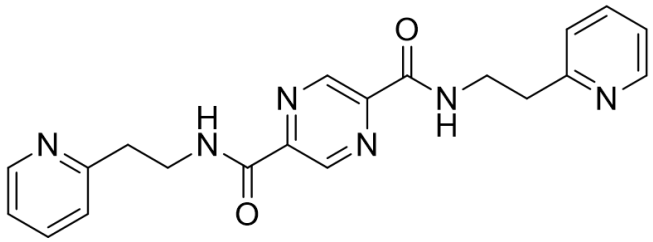

Figure 74: **L1b** Ligand isolated from crystal growth.

This **L1b** ligand was not new, having previously been published by Brooker *et al.*[56, 122] who complexed this ligand with $Co(BF_4)_2 \cdot 6H_2O$ to create [2x2] square cyclohelicates. However, this group synthesised **L1b** through a more traditional method of synthesis that is, by reacting dimethyl pyrazine-2,5-dicarboxylate, with 2-(2-aminoethyl)pyridine, resulting in colourless crystalline solids.

It appears that in the **C1B** complexation attempt, the $Mn(ClO_4)_2 \cdot 6H_2O$, metal salt has oxidised the **L1^{endo}** ligand to **L1b** over the two month period of diffusion.

The previously mentioned needle-shaped crystals were suitable for single crystal X-ray diffraction (SCXRD). The structure was triclinic, crystalising in the $P\bar{1}$ space group. The full crystal data is shown in Apx1.4. The asymmetric unit consists of one half of the ligand and a ClO_4^- counterion. The full ligand structure is shown in (Figure 75), and was generated by inversion centred on the pyrazine ring. The amide group and the pyrazine group are planar, with the pyridine groups held at an angle of 90.4º relative to the pyrazine ring.

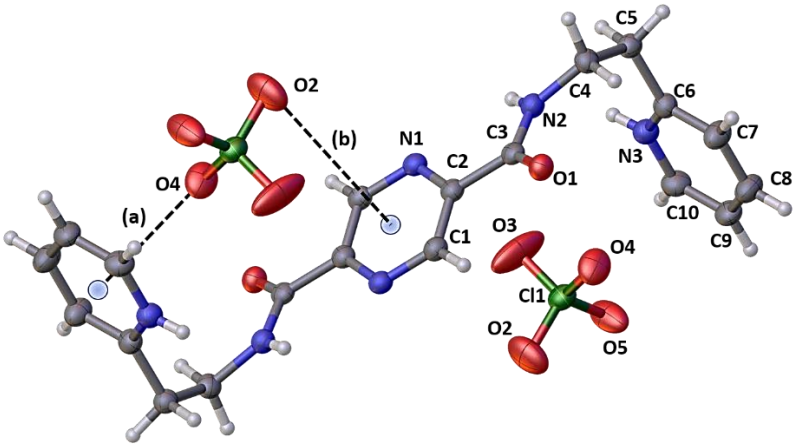

Figure 75: The crystal structure of the **L1b** ligand, with the asymmetric unit labelled. Colour Code: C = grey, N = blue, Cl = green, O = red, H = white. The black dashed lines indicate the O-π intramolecular bonds.

The angled conformation of the ligand is caused by π-anion interactions (Table 36) between the **L1b** ligand and the perchlorate counter anions. Each anion interacts with two sides of the ligand, to a pyridine and pyrazine centre, creating the [C3-C5-C6] angle of 90.42º. The O4 of the ClO_4^- anion interacts with the pyridine centre, at a distance of 3.33 Å, which is a relatively strong interaction. The O2 of the same anion also interacts with the pyrazine centre, at a distance of 3.98 Å, which is a more moderate strength interaction.

The ligands are held slightly off-set in parallel stacks. Each ligand is held by four [N3-H^{N3}-O1] hydrogen bonds, with two connecting to each adjacent ligand. The bonds each between the donor N3 nitrogen of one ligand to the acceptor O1 oxygen of the adjacent ligand resulting in a O1-N3 distance of 2.762 Å, and an O-H-N angle of 163.7º. The hydrogen-acceptor distances for this bond, is between 1.5-2.2 Å, which indicate moderate strength, mostly electrostatic hydrogen bonds.[108] This creates a 1D stack of ligands held by hydrogen bonds (Figure 76).

Table 36: Selected intermolecular bond lengths (Å)and angles (º) for the **L1b** ligand.

Hydrogen bonding					
	D-H-A	D-H(Å)	H ··· A (Å)	D ··· A (Å)	D-H ··· A (º)
1	$N3_1$ - $H^{N3}{}_1$ – $O1_4$	0.83 (4)	1.96 (4)	2.764 (3)	164 (4)
π-anion bonding					
		Cent-O (Å)	Cl1-O-Cent (º)		
a)	Pyr(cent)-O4	3.33	103.6		
b)	Pz(cent)-O2	3.98	82.3		

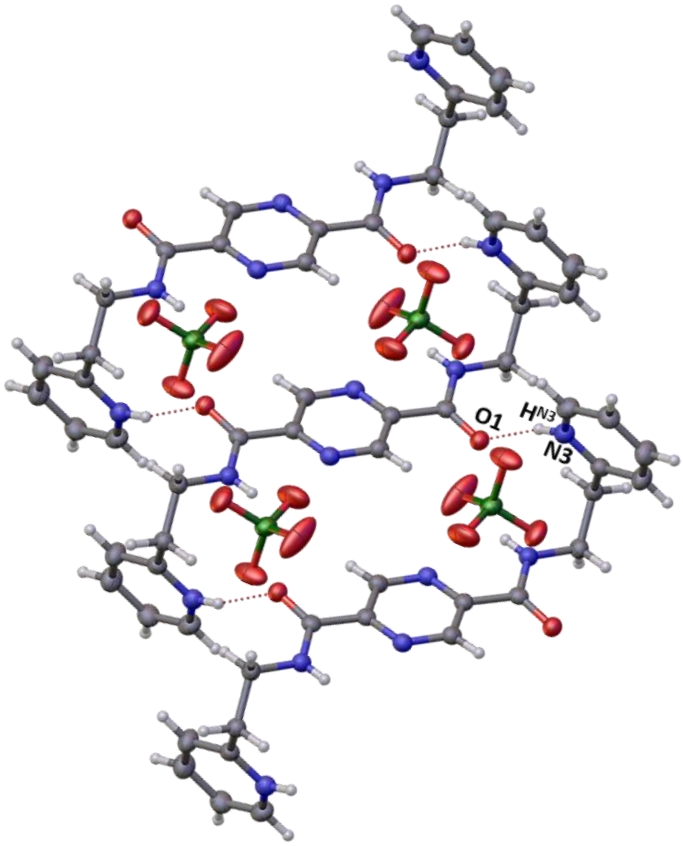

Figure 76: The crystal structure of L1b. Hydrogen bonds between the O1 and N3 of adjacent ligands, indicated by a red line. Colour Code: C = grey, N = blue, Cl = green, O = red, H = white.

5.5 Synthesis and Characterisation of L2

2,2'-(pyrazine-2,5-diylbis(methanylylidene))bis(azanylylidene))bis(methylene))diphenol

With the isolation of **B1**, other endo-imine pyrazine ligands could be synthesised, apart from the recreation of **L1**. Michael Brown[20] had previously synthesised, **L2b**, seen in Scheme 13, but at the time had not successfully complexed these with any metal salts. This could have been due to the fact any resulting complexes would form two five-membered cheltating rings, which are not favoured for an octahedral metal cation to coordinate to. For increased flexibility, an alternate Schiff base ligand, **L2**, could be synthesised.

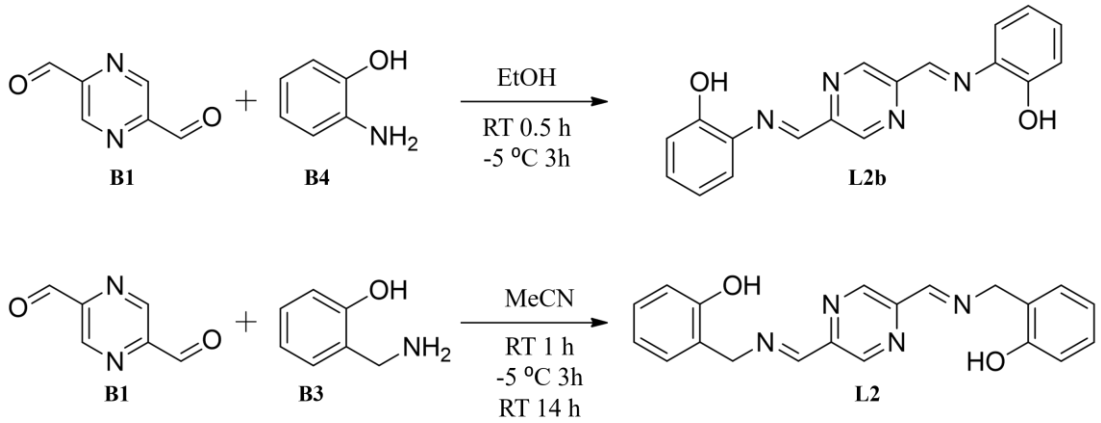

Scheme 14: The Schiff base condensation of **B1** and **B3** (2-(aminomethyl)phenol) scheme for **L2,** and the previous reaction scheme of **B1** and **B4** (2-aminophenol) to synthesise **L2b**.[20]

The reaction to make **L2** proceeded by stirring **B1** with the alternate amine reagent, 2-(aminomethyl)phenol, **B3**, in MeCN at RT for one hour, followed by cooling and standing. **L2** was successfully synthesised, as a peach coloured, solid precipitated out of solution in high yield, 95 %, (Scheme 14). The full details for this synthesis are shown in Apx1.5.

The new **L2** ligand was fully characterised, with ^{1}H NMR and ^{13}C NMR spectroscopy being the primary method used to determine the success and purity of the ligand. The 10.24 ppm ^{1}H NMR peak of the **B1** aldehyde disappeared. Two ^{1}H NMR singlets at 9.18 ppm and 8.48 ppm, could have belonged to either the pyrazine or the imine. Although 9.18 ppm was high compared to other pyrazine protons recorded, the COSY indicated that the 8.48 ppm proton was associated with the 4.84 ppm, 2H peak, belonging to the methyl peak on the other side of the imine. Therefore, the 8.48 ppm

singlet was likely the imine, and the pyrazine peak had shifted from 9.31 to 9.18 ppm. This data indicated the successful synthesis of the imine moiety.

The appearance of the peaks at 4.84 ppm (s, 4H) in the ^{1}H NMR and the 59.33 ppm in the ^{13}C NMR spectra, confirmed the new **L2** ligand, compared to the previously synthesised **L2b,** where these peaks were not present. The assignment of the results of the ^{1}H NMR and ^{13}C NMR are summarised in the Table 37. The full spectra are shown in Apx12.1.5-12.1.8.

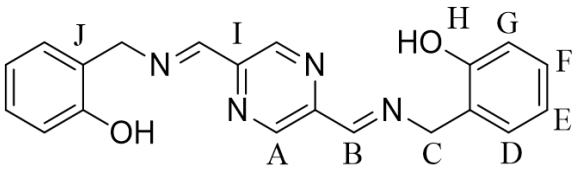

Figure 77 The assignments of the ^{1}H NMR and ^{1}C NMR peaks (ppm) to their locations in **L2.**

Table 37: The ^{1}H and ^{13}C NMR Assignment of **L2**.

	A	**B**	**C**	**D**	**E**	**F**	**G**	**H**	**I**	**J**
*^{1}H NMR**	9.18	8.48	4.84	7.20	6.78	7.13	6.78	9.54	-	-
	s 1H	s 1H	s 2H	d 1H	t 1H	t 1H	T 1H	Br 1H		
J (Hz)				7.65	7.35	7.35	7.35			
^{13}C NMR$^{\intercal}$	149.8	142.25	59.35	130.3	199.4	128.9	199.4	155.7	160.9	124.8

**(500 MHz, DMSO): δ ppm* $^{\intercal}$ *(126 MHz; DMSO): δ ppm*

The results from the NMR spectra were verified with ATR-IR spectroscopy, and MS, as seen in Apx1.5. The appearance of a sharp peak around 1640 cm^{-1} in the ATR-IR spectrum showed the appearance of the imine, while the disappearance of the aldehyde peak (found around 1700 cm^{-1}) proved that the reaction had come to completion. The MS resulted in masses with splitting patterns that show the presence of [**L2**, H], [**L2**, Na] and [2**L2**, Na]. Attempts to grow single crystals of **L2**, through the slow vapour diffusion of Et_2O, were made in an attempt to get confirmation of the structure; however, this was unsuccessful.

5.5.2: Attempted Synthesis of L2 Complexes

With the successful synthesis of the pyrazine-based Schiff base ligand, **L2,** with antiparallel bis-terdentate chelating environments, attempts were made to synthesise cyclohelicate structures $[M_xL_x]$ with assorted transition metal 3*d* octahedral ions.

Due to the similarly proportioned **L1** imine ligand forming cyclohelicate triangles, it was expected that any cyclohelicates formed would adopt a square or triangular arrangement.

5.5.3 General synthesis of complexes

In these complexation attempts **L2** was introduced to 3*d* octahedral metal salts, both dissolved in MeCN, in a 1:1 ratio. The preferred counterion in these attempts was the perchlorate anion (ClO_4^-) due to its propensity to crystallise and act as a non-coordinating counterion. The full method used can be found in Apx1.6.

The metal salts used, and their results are shown in Table 38. The introduction of the metal salts resulted in colour changes, indicating coordination had occurred. The reaction solutions were set up in a slow vapour diffusion of Et_2O, to isolate any single crystals of these products.

Over a period of two weeks, the complexes had precipitated with corresponding colours shown in Table 38. The precipitate was collected, checked with mass spec, and other methods of crystallisation were investigated.

Table 38: **L2** Complexation Results with various metal salts, the resulting colour change, ppt and ms.

Metal Salt	*Complex Code*	*Solvent*	*Colour Change*	*ppt*	*MS (m/z):*
$Ni(ClO_4)_2$	**L2A**	MeCN	orange	dark orange	654.26 1299.78 1360.41
$Mn(ClO_4)_2$	**L2B**	MeCN	orange	brown	311.08 552.88 626.10 1393.43
$Co(ClO_4)_2$	**L2C**	MeCN	dark purple	Black	538.87 641.88 1348.66 1602.48

The MS results indicated that multiple ligands must be coordinated to result in the high masses shown, however, it is yet to be determined what the architecture of these complexes was.

Solubility of the precipitates were then investigated, (Table 39), with partial solubility found in both MeOH and DMF. These solvents were used in further crystallisation attempts (Table 40), however none of these attempts resulted in the formation of single crystals suitable for structural determination.

Although the specifics of the architectures of these complexes is yet to be determined, the large MS results of the resulting precipitate indicate that the **L2** ligand coordinated to some of the 3*d* ions and further investigation in the future may produce results.

Table 39: Solubility investigation of **L2** complexes.

Solubility	**L2A**	**L2B**	**L2C**
MeOH	**P**	**P**	**P**
THF	**X**	**X**	**X**
DMF	**P**	**P**	**P**
$CHCl_3$	**X**	**X**	**X**

X – indicating no solubility **P** – indicating partial solubility

Table 40: Recrystallisation attempts with **L2** complexes

Crystallisation	**L2A**	**L2B**	**L2C**
MeCN - vapour diffusion of Et_2O	**Ppt**	**Ppt**	**Ppt**
MeCN slow air-evaporation	**Ppt**	**Ppt**	**Ppt**
MeOH - vapour diffusion of Et_2O	**X**	**X**	**X**
DMF - vapour diffusion of Et_2O	**X**	**X**	**X**
Hot recrystallisation EtOH	**X**	**X**	**X**
Hot recrystallisation MeCN	**X**	**X**	**X**
Hot recrystallisation MeOH	**X**	-	**X**

ppt – indicating solid precipitate crashed out, **X –** indicating no crystallisation

5.6 Imine Ligands: Conclusions

Three ligands **L1**, **L1b**, and **L2**, were synthesised through Schiff base condensation reactions, using the **B1** aldehyde as the central pyrazine group. These ligands were characterised with a range of techniques to confirm the presence of the imine, and the surprising amide moiety. This was followed by unsuccessful complexation attempts with assorted 3*d* metal ions with ligands **L1** and **L2**, using varying conditions. The large masses seen in the (m/z) of the **L2** complex ppts, have left **L2** as a promising ligand for 3*d* ion coordination and further investigation.

Complexation attempts led to the formation of single needle-shaped crystals of **L1b**, which was used to obtain SCXRD results, revealing its molecular structure, its intermolecular H-bonding within molecule stacks, it's zig-zag conformation, and the pyridine π-stacking interactions within the packing of the molecules.

Although these endo-imine ligands were unsuccessfully complexed with 3*d* ions, there are still a large range of other potential derivatives that could be synthesised via the variety of primary amines remaining.

6.0 Synthesis Pathway for Exo Imine centre (C6)

2,5-bis(aminomethyl)pyrazine (C6): and other Pyrazine Centres: (C3) and (D1)

6.10 Introduction

The initial aim for this section was the synthesis of 2,5-bis(aminomethyl)pyrazine (**C6**), in large enough quantities so that **C6** could then be used to investigate the synthesis of exo-imine pyrazine ligands. This 2,5- arrangement of primary amines would facilitate Schiff-base condensation reactions with an endless variety of primary carbonyl groups, to open up a pathway for a wide range of novel ligands. This was expanded upon in Section 5.0.

Following this aim, a range of reactions were attempted to find a successful pathway to **C6**, as shown in Scheme 15. Ultimately, this route did not isolate the desired **C6** product. However, during this investigation other pyrazine centres, **D1** and **E1**, were isolated, which were used in the synthesis of other successful ligands, explored in Sections 2.0 and 3.0.

6.11 Full Synthesis Pathway

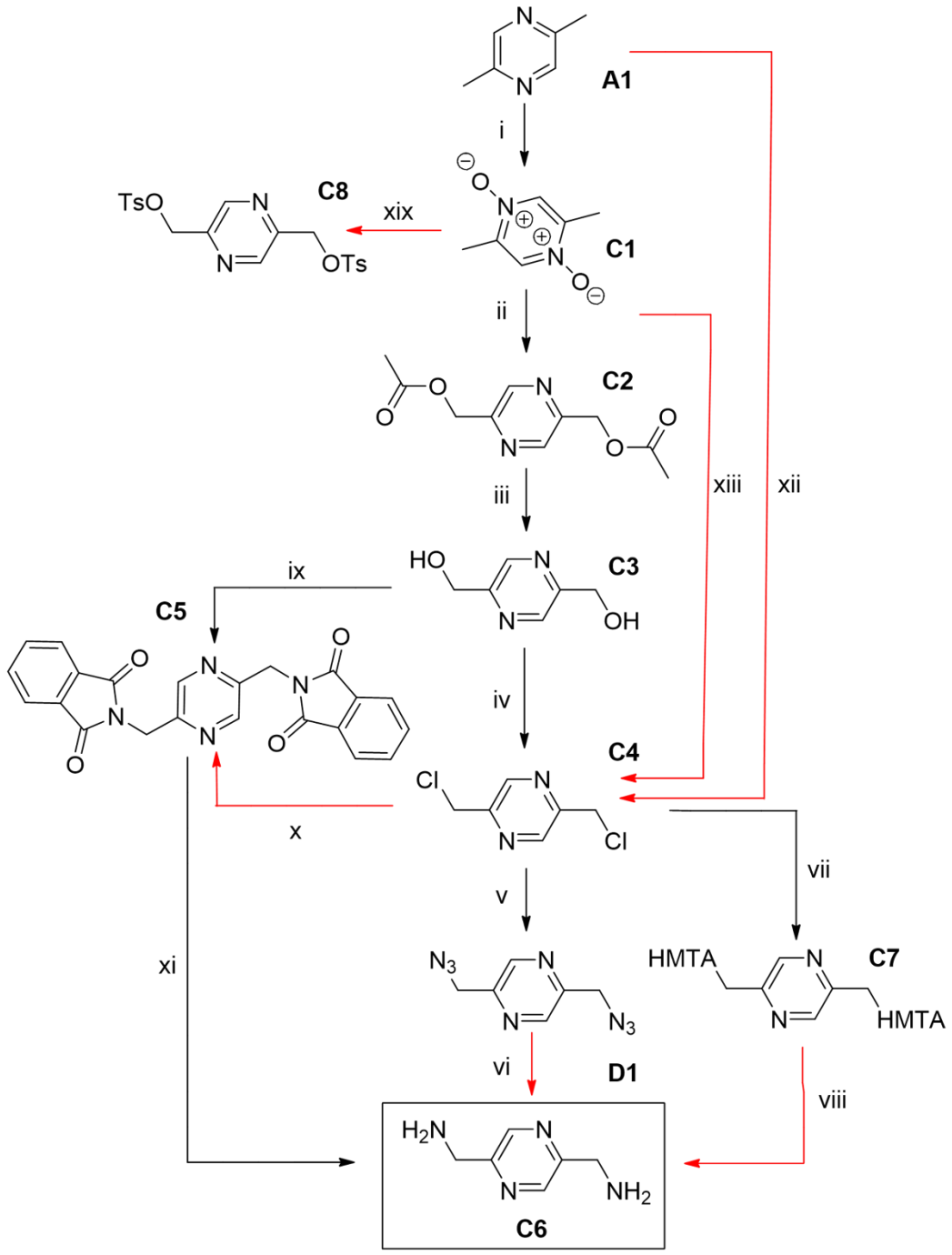

Scheme 15: The overall route in the pathway to **C6**. I) m-CPBA, EtOAc, RT, 24h; ii) Acetic Anhydride, 158 ºC 7h, RT 18h; iii) NaOMe, MeOH, RT, 3h; iv) $SOCl_2$, DCM, RT, 18h; v) NaN_3, TBAHS, DCM:H_2O (1:1) RT, 48h; vi) PPh_3, THF/H_2O, RT, 24h; HCl, RT 2h; vii) KI, HMTA, DCM, 65 ºC, 44h; viii) DCM, NaOH ix) Phth, PPh_3, DIAD, THF, 0 ºC, RT, 16h; x) KPhth, DMF, 110 ºC; xi) NH_2NH_2, EtOH, 70 ºC, 16h; xii) NCS, BzO_2, CCl_4, 66 ºC, 24 h; xiii) $POCl_3$, Et_3N, DCE, 85 ºC, 2h; xix) TsCL, Et_3N, THF, 0 ºC, RT, 16h.

Black reaction pathway arrows indicate the successful detection of products; Red reaction pathway arrow indicates an unsuccessful reaction pathway.

6.2 The 2,5-di(hydroxymethyl) pyrazine Pathway (C1) (C2) (C3)

Initially, the aim was to isolate, 2,5-bis(chloromethyl)pyrazine (**C4**) in as few steps as possible. It began with the reactions xii and xiii in Scheme 15. These reactions never proved fruitful. The reactions that were not ultimately used in the final pathway and the reasons they were not used are discussed in Apx 2.0.

However, the oxidation pathway (i, ii, and iii) and chlorination (iv) rather than direct chlorination was successful, and led to the utilisation of these reactions. Despite a sequential low yield, this series of reactions were scalable. The three initial steps were all adapted from work previously done by Das *et al.*[123]

Firstly, an *N*-oxidation, using m-CPBA of **A1** in EtOAc for 24h produced 2,5-dimethylpyrazine 1,4-dioxide **C1** as a white solid in ~70-87% yields. This reaction could be readily done on large scales and **C1** could be stored at RT without decomposition. Full details of this reaction can be found in Apx4.1 and the ^{1}H NMR in Apx12.2.1.

A Boekelheide rearrangement and Claisen condensation of **C1** with acetic acid, to give 2,5-bis(acetoxymethyl)pyrazine, **C2** followed.[124] A suspension of **C1** in acetic anhydride was heated to 158 °C for 7 hours, resulting in a dark, brown solution which was cooled to RT and stirred for 16 hours. The *N*-oxide functionality allowed for the acetylation of the methyl groups, the mechanism for this is shown in Scheme 16. The *N*-oxide is acetylated, and produces a carboxylate anion. The *N*-acetylated intermediate, can then produce, **C2** in two ways, the rearrangement of the acetylated N-oxide, or the nucleophilic attack of an acetoxy group onto the methylene. The **C2** product was extracted in Et_2O, by being stirred vigorously for two hours, then sat for three hours. The filtrate was then collected and concentrated *in vacuo*.

Two methods of purification were used, depending on the initial purity of the crude product. If the crude product was able to solidify as a dark brown crystallised solid, it was initially washed (with a 3:7 EtOAc:*n*-Hexane) solvent mix then the remaining dark orange product could be hot recrystallised in the same solvent mixture, to give the desired light yellow, crystalline product, in a yield of 30%.

If the crude produce would not solidify when left to air dry, it was run through a silica plug. An initial wash of (1:4) EtOAc:Hexane removed the first fraction then a solvent

gradient was applied, increasing to (4:6) EtOAc:Hexane to collect the product (RF= 0.15). The yellow/orange filtrate was concentrated under reduced vacuum to obtain an orange crystallised solid, which was then hot recrystallised as described previous. Full details of this reaction are found in Apx4.2, and the ^{1}H NMR is shown in Apx12.2.2.

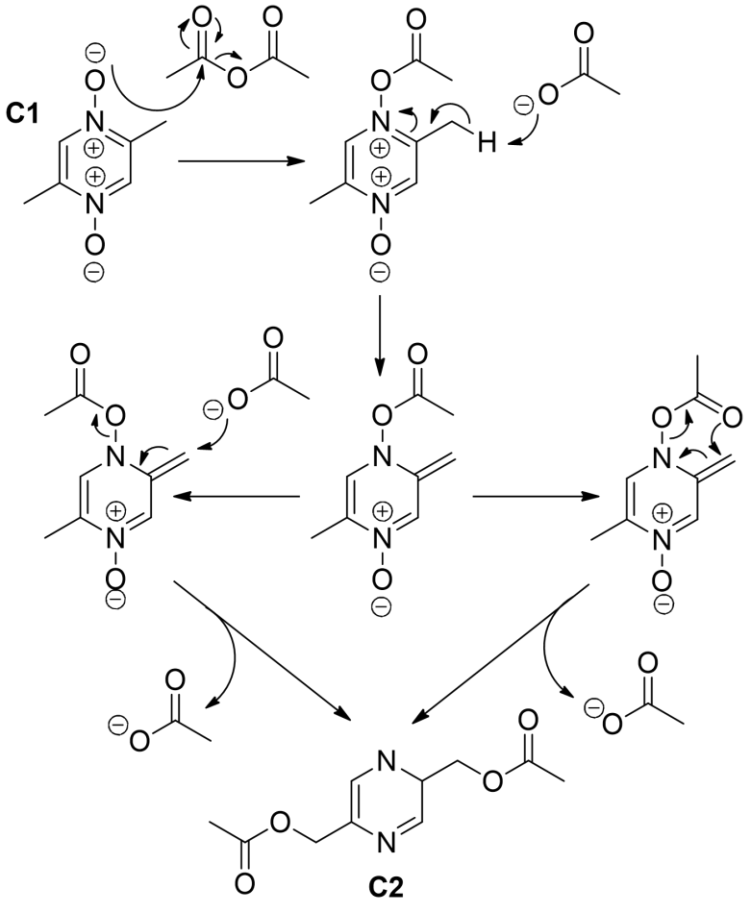

Scheme 16: Proposed Mechanism of an Acetate addition to a Pyrazine N-oxide, through a Boekelheide reaction combined with a Claisen Rearrangement. Adapted from Li, J. J. [125] and Miserazzi, *et al.* [124]

The third step involved the hydrolysis of the **C2** ester to cleave ethanoic acid and produce 2,5-bis(hydroxymethyl)pyrazine, **C3**. Firstly, this required the preparation of NaOMe, using a method documented by Armarego.[126] The reaction was first flushed with Ar, and **C2**, dissolved in dry MeOH under Argon, was then added to the NaOMe solution. The reaction was stirred at RT for three hours, then quenched with a small amount of NH_4Cl. The solvent was reduced *in vacuo*, and the beige solid **C3**, was isolated in an 93% yield. This product could be easily stored for long periods of time. Full details of this reaction are found in Apx4.3, and the ^{1}H NMR is shown in Apx12.2.3.

6.3 Chlorination of (C3) to 2,5-di(chloromethyl) pyrazine (C4)

The next step in the path towards **C6**, was the chlorination of **C3** to **C4**. The method used was adapted from Penteado, *et al.* [127] and Zhang, *et al.*[128] who chlorinated pyridin-2-ylmethanol. To begin, the **C3** was ground into a fine powder using a mortar and pestle, and was suspended in dry DCM, then cooled to 0 °C in an ice bath. A solution of $SOCl_2$, diluted in dry DCM, cooled to 0 °C, was added dropwise to the **C3** suspension and was stirred at 0 °C, for one hour, then brought to RT and stirred for an additional 18 hours. As shown in the mechanism, (Scheme 17.) there is a production of HCl and SO_2, which meant that rubber septum and balloons could not be used, as they would deteriorate.

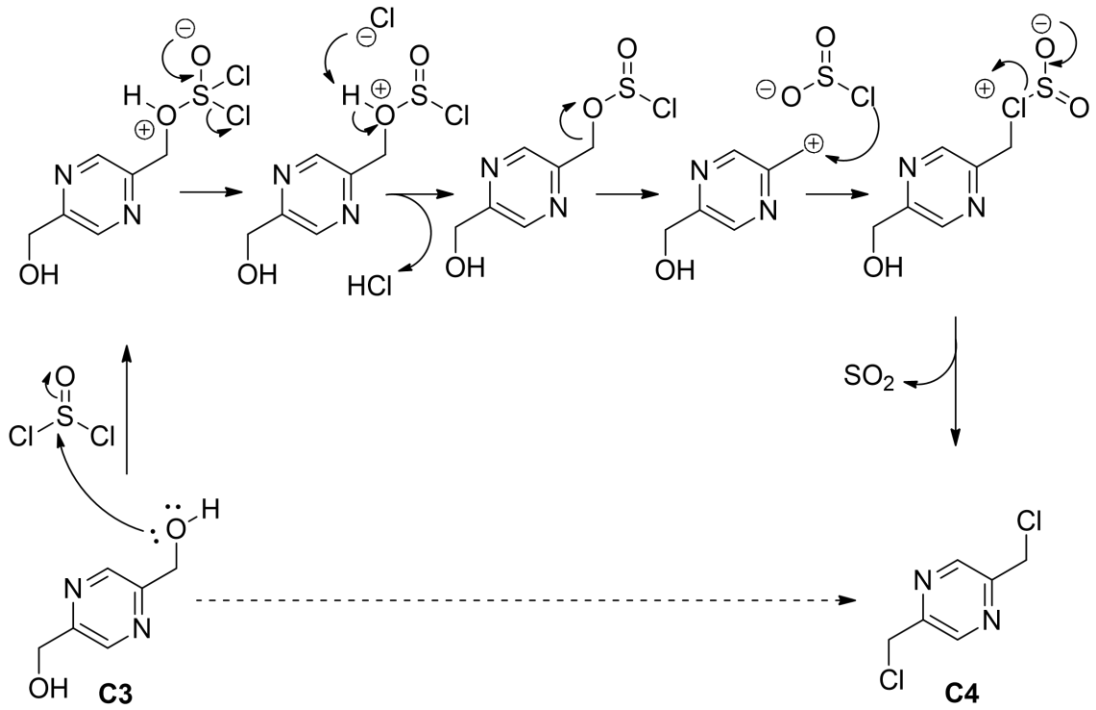

Scheme 17: The chlorination mechanism of **C4**.

The reaction was poured over ice, and quenched with saturated aq. $NaHCO_3$ solution, and left until gas production had ceased. The **C4** product was collected with a DCM extraction, and concentrated *in vacuo*, as an orange-brown oil, in 90 % yield. Full details of this reaction are found in Apx.4.4, and the ^{1}H NMR is shown in Apx12.2.4, which agreed with literature values.[129] The **C4** product was kept in the fridge until desired, with no further purification required as the ^{1}H NMR showed that it was isolated in high purity.

6.4 Azide Synthesis of 2,5-di(azidomethyl) pyrazine (D1)

With the preparation of azides there are hazards that need to be identified and prepared for, especially with the high ratio of 8N to 6C in **D1**. One of the hazards when using sodium azide, with DMSO and DCM, is the formation of diazidomethane $CH_2(N_3)_2$ and triazidomethanes $CH(N_3)_3$, where explosion can happen upon the evaporation of the solvents. This outcome has been previously reported in caution by those who have had explosions in the lab and had resulting injuries.[130]

The damages documented by Conrow *et al.*[130b] occurred when they scaled their reactions up to multigram quantities. These hazards meant that all reactions were done on small scales, resulting in 200 mg of **D1**, kept dilute in DCM.

As **D1** was likely highly energetic the following reaction pathway was the second choice. Initially, 2,5-bis(hexamethyl-tetraamine)pyrazine (**C7**) was attempted to be isolated from **C4**. (Scheme 15: vii, viii). Ultimately, **C7** was only able to be detected as a chlorine salt in the MS results, as (m/z): 421.26 (100), 422.41 (20), 423.19 (30), 423.28 (28) [**C7**+Cl] but not isolated as a lone product, nor was is able to be taken to **C6** when the crude product was attempted to be reduced in situ. (Apx3.1). With this in mind, the synthesis of **D1** was attempted.

Knowing that there was a highly likely explosive nature to the target molecule, was only synthesized in small amount, and was kept stored in a DCM solution in the fridge.

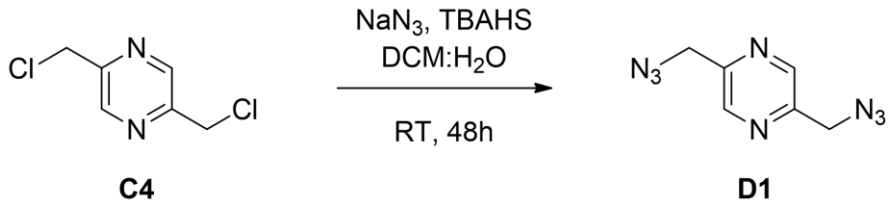

C4 **D1**

Scheme 18: Schematic of **D1** synthesis.

The method for this reaction was adapted from, Abushanab *et al.*[131] and Amadio *et al.*[132] Abushanab *et al.* substituted an azide onto 2-chloromethyl pyrazine, in a MeCN : H_2O (1:1) solution, then refluxed for 12 hours, while Amadio *et al,* completed their reaction on the same product at RT over 48 hours. When both methods were adapted for the synthesis of **D1**, and tested on a small scale, the latter conditions resulted in a higher yield, 46%, and the RT reaction also minimised possible energetic risks.

The final agreed method for this reaction took NaN_3 and TBAHS, dissolved in H_2O, and added to **C4**, dissolved H_2O:DCM (1:1) and stirred at RT for 48 hours. The product was extracted with DCM, and stored in a dilute solution, where the molar amount was calculated from ^1H NMR. (Apdx 12.2.9). To obtain a clean ^1H NMR spectra a small volume of **D1** dilution was left to partially air-dry in a MS vial, revealing **D1** as an orange oily product. The ^1H NMR revealed that the **D1** product had been made, and in very high purity. The full method is shown in Apx4.7.

With the isolation of **D1**, conversion to **C6** (di amine) was attempted by using methods adapted from, Kwan, *et al.*[133] and Palanichamy, *et al.*[134], were used in an attempt to change the azide moieties to amines. These routes were ultimately unsuccessful, as discussed in (Apx4.7.2). While this pathway was being explored, a phthalimide intermediate option was providing some success from **C3**, (see Section 6.5) so further attempts from **D1** were abandoned.

Even though **D1** was not used in the final **C6** synthetic route, its isolation provided the pathway to generate triazole ligands, **L3** and **L4** as discussed in Section 2.0.

6.5 Synthesis of the C5 Intermediate

With the synthesis of **C6** via **C7** and **D1** proving unsuccessful, an alternate pathway was investigated. The aim was to use a Gabriel reaction to form a phthalimide (Phth) intermediate (**C5**), then use an Ing-Manske reduction to the di amine, **C6**.

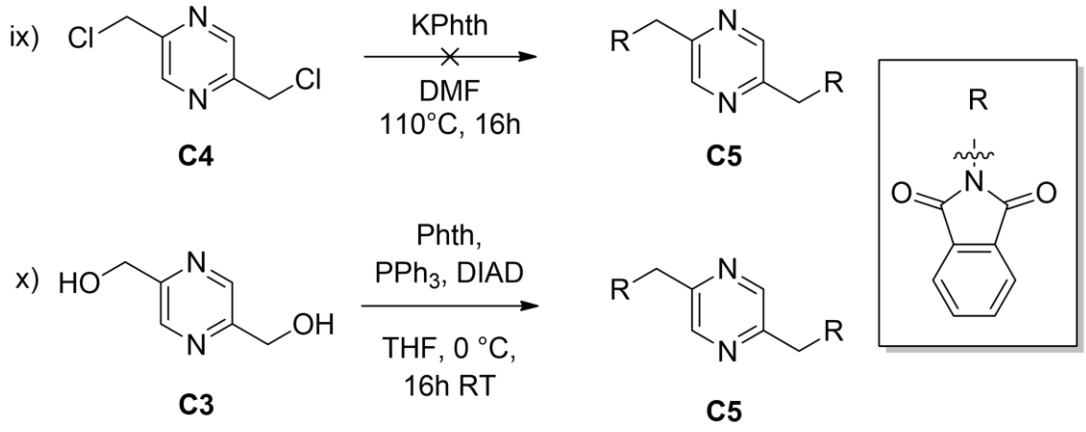

Scheme 19: Synthesis of **C5**. ix) Gabriel Synthesis of **C5** via **C4**: DMF, 110 C, 16h, adapted from Liu *et al.*[135] x) Mitsunobu reaction of **C3** to synthesise **C5**: PPh_3, DIAD, THF, 0 C, RT 16h, adapted from Wessel *et al.*[136]

6.5.1 Gabriel Synthesis via (C4)

Initially, the conversion of **C4** to **C5** was attempted (Scheme 19 (ix)) using a Gabriel synthesis method adapted from *Liu et al.*[135]

The stoichiometry of this reaction was adapted for use with a di-substitution on **C4**. Before this method could be fully tested, the supply of potassium phthalimide (KPhth) needed to be purified, Armarego[126] recommends recrystallisation in a large volume of EtOH, and washing the produced solid product with acetone. The H NMR had a 4H singlet peak at 7.83 ppm, indicating the presence of the potassium phthalimide, but a 0.6 H broad singlet peak at 11.3 ppm indicated that at least some of the product was the protonated form. From this, the reagent was not able to be fully purified, and was most likely degraded as the source was from 1986.

An attempt was made with the isolated KPhth isolated, and reacted with **C4** in DMF, stirred at 100 ºC overnight. But the crude product never indicated success when analyzed with MS and ^{1}H NMR. It was here that this pathway was set aside. (Apx4.5.)

6.5.2 Gabriel Synthesis via (C3)

As the **C4** pathway made little progress. The difficulties encountered led to a Mitsunobu reaction of Phth and **C3**, (x) which was successful in forming the novel **C5** intermediate.

The successful synthesis of **C5**, was adapted from a Mitsunobu reaction of 2,6-bis(hydroxymethyl)pyridine and phth as published by Wessel *et al.*[136] (Scheme 19 (x)). While, Wessel *et al.* used a diethyl azodicarboxylate ester as the catalyst, this was unavailable, so was substituted with diisopropyl azodicarboxylate (DIAD). The mechanism for this Mitsunobu reaction, is shown in Scheme 20.

This method involved the injection of DIAD into a suspension of Phth, PPh_3 and **C3** in THF, at 0 °C under Argon; then stirred at RT for 16 hours. The white, solid **C5** product was isolated by filtration, in an 18 % yield. The specifics of this reaction method can be found in Apx4.5.1. The **C5** compound was characterised by ^{1}H NMR, ^{13}C NMR, MS and IR (Apdx.12.2.5-8), with the NMR results summarised in Table 41.

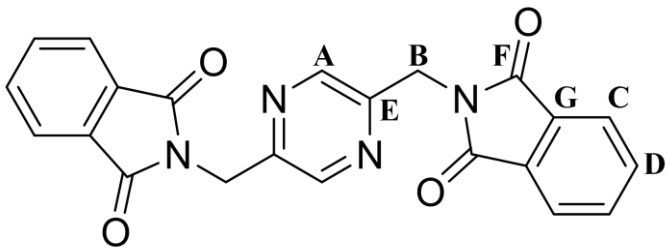

Figure 78: Characterisation of **C5** and assignment of ^{1}H NMR, ^{13}C NMR

Table 41: Assignments of **C5**, ^{1}H NMR, ^{13}C NMR

	A	**B**	**C**	**D**	**E**	**F**	**G**
*^{1}H NMR**	8.62	4.97	7.90	7.87	-	-	-
	s 2H	s 4H	m 4H				
^{13}C NMR$^{\intercal}$	143.3	40.2	123.9	135.1	132.1	168.1	126.4

**(500 MHz, DMSO): δ ppm* *$^{\intercal}$ (126 MHz; DMSO): δ ppm*

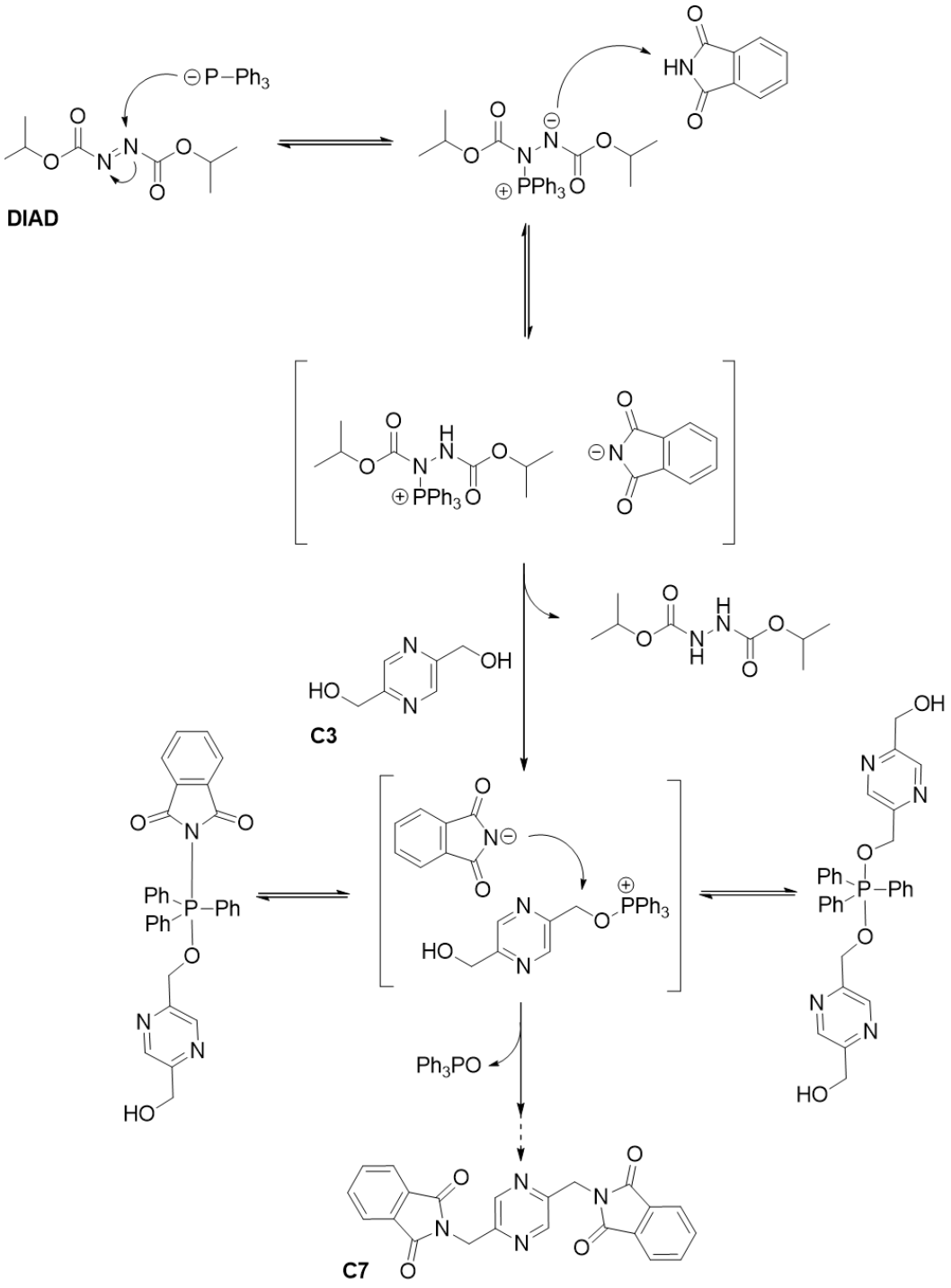

Scheme 20: Mitsunobu Mechanism of **C3**, DIAD and Phth, to form **C5**.

6.6 Ing-Manske Reduction of (C5) to produce the goal amine (C6)

With the isolation of **C5**, Ing-Manske reductions were attempted. The method used was adapted from Wessel *et al.*[136] and Ariffin, *et al.*[137] as part of their Gabriel synthesis. The mechanism for this reduction is shown in Scheme 21.[138] The reduction of the Phth moiety, results in the formation of the primary amine, **C6.**

The method for this reaction involved the initial deprotonation of the Phth moiety, by the hydrazine hydrate base, which was added to a solution of **C5** in EtOH:H_2O (2:1). This reaction was refluxed for half an hour, resulting in a white solid, which was removed via filtration. The filtrate was then concentrated *in vacuo*, and the crude residue then dissolved in $CHCl_3$, and the solids removed and filtrate was concentrated *in vacuo*. This gave a white solid, in 23 % yield. The ^{1}H NMR showed promise, with peaks indicating the **C6** product, however, this was not completely clean. The full method is described in Apx 4.6.

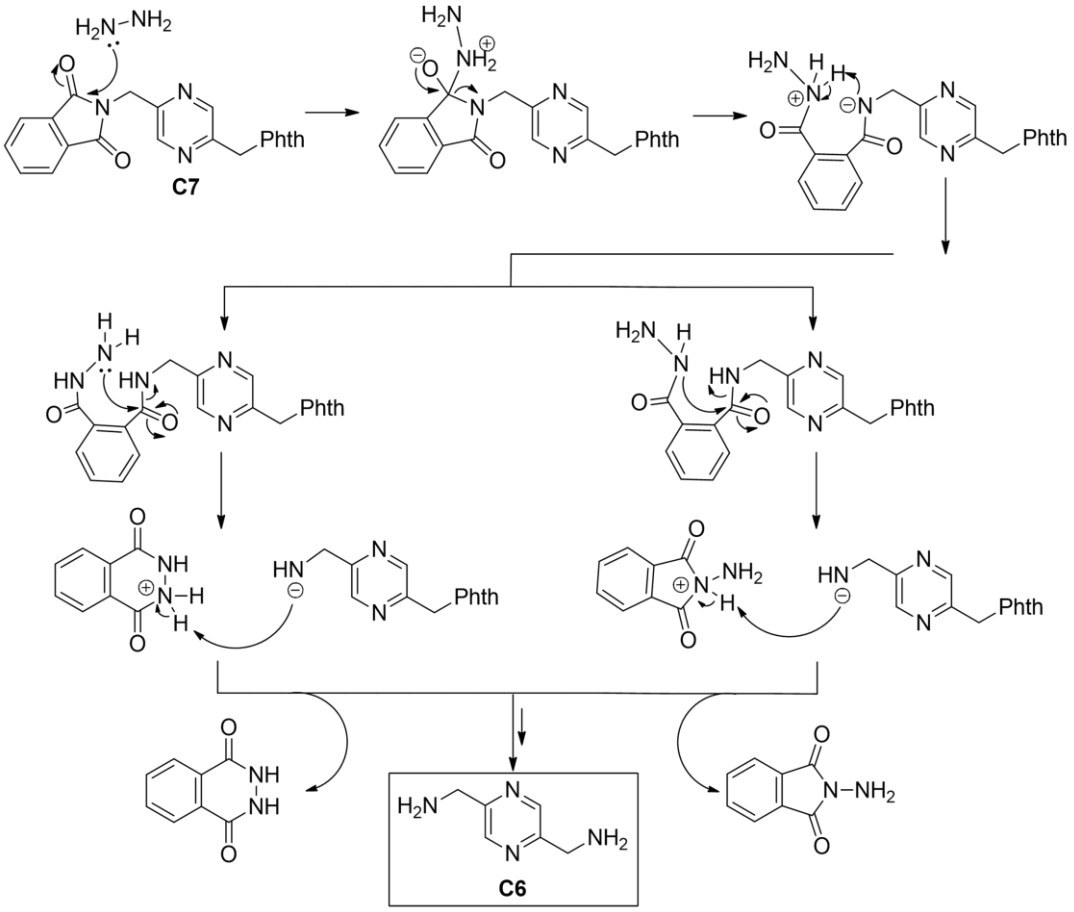

Scheme 21: The Ing-Manske Reduction Mechanism, adapted from Curley *et al.*[138]

6.7 Conclusions and Future Synthesis of (C6)

With the isolation of **C6** almost achieved, the future work for this molecule would be open to build a catalogue of exo-imine pyrazine ligands. All that would be required is a range of primary carbonyl groups, as illustrated in Figure 79. This area of future work would be able to explore if changes in architecture will result in changes in angles within the ligand and hence new supramolecular arrangements.

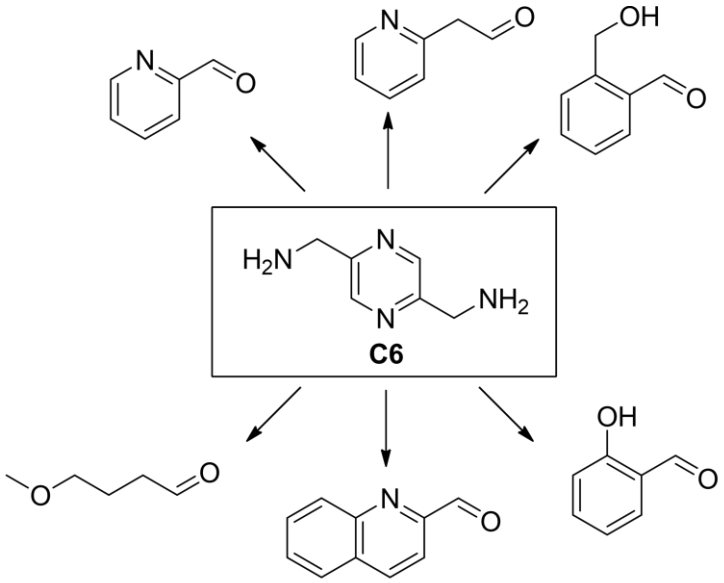

Figure 79: **C6** (central) and the potential future primary carbonyls, with which **C6** could form future exo-imine pyrazine ligands. Clockwise from top left (TL): picolinaldehyde, (TC): 2-(pyridin-2-yl)acetaldehyde, (TR): 2-(hydroxymethyl)benzaldehyde, bottom right (BR): 2-hydroxybenzaldehyde, (BC): quinoline-2-carbaldehyde, (BL): 4-methoxybutanal.

7.0 Conclusions

The aim of this research was to design and synthesise novel pyrazine-based ligands, explore their complexations with 3d ions and the supramolecular structures that they produce. This aim was achieved with the synthesis, isolation and characterisation of four novel ligands; the imine based **L2**, (Section 5.5) the immediate pyrazine click ligand, **L3**, (Section 2.2) and the ligands utilising the new Pz-O-Tz chelation site, ligands **L5** and **L6** (Section 3.4). These ligands are summarised in Figure 80.

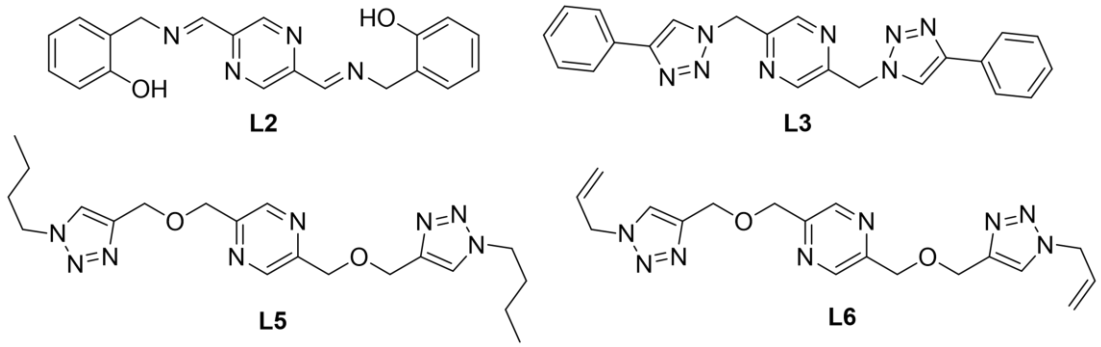

Figure 80: Successfully synthesised ligands over the course of this research, **L2**, **L3**, **L5** & **L6**.

The development of exo-imine pyrazine-based ligands was not completed, but a synthesis pathway towards the di amine intermediate, **C6**, was established. During the investigation into the synthesis of **C6**, a novel **C5** molecule was isolated, (Figure 81) and with the preparation of larger amounts of **C5**, more experimentation can be done to refine a process to isolate **C6**.

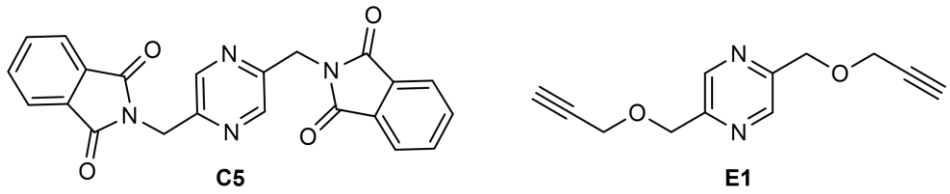

Figure 81: Novel molecules, **C5** and **E1**, synthesised and characterised during this research.

Although, exo-imine pyrazine-based ligands were not produced in this time, a new endo-imine pyrazine-based ligand **L2** was. While **L2** did not result in any isolated metal-organic complexes, the colour changes and mass spec results indicate that some form of complexation was occurring. Revisiting this ligand and reacting it with a wider range of metal salts could result in the isolation of possible structures.

The **L3** ligand, contributed to a collection of triazole and *N*-heterocycle ligands already published. This ligand had very limited solubility, but was able to be reacted with $Ag(NO_3)$ to produce a 3D polymer network complex, $\{[Ag_2(\mathbf{L3})](NO)_4\}_\infty$. The isolation of crystals of this complex resulted in very small pink crystals, which enabled a structure to be derived, but this complex should be remade to get more accurate data. This complex has a very interconnected network, that held a lot of metal ions close together, and presumable also occurred in the **L3** gel that was made with the $[Cu(MeCN)_4]PF_6$. Networks made with **L3** has the possibility of having interesting electric and magnetic properties that could be investigated in the future.

The synthesis of the novel **E1** (Figure 79) allowed for the development of the new Pz-O-Tz chelation site ligands, **L5** and **L6**. These ligands successful achieved the aim of using pyrazine-based ligands complexed to metal ions to create supramolecular coordination complexes. Here the supramolecular structures created were 1D polymer chains. The **L5** ligand generated nine 1D polymer chains and one Mn monomer complex, while **L6** generated three complexes, one of which has been analysed.

The click reaction of **E1**, used to create **L5** and **L6**, also opens a door for the generation of more ligands, as more azide-molecules can be used to finish the ligands.

8.0 Future Work

The synthesis of the di amine intermediate, **C6** is also close to completion. With the synthesis of **C5** being successfully completed, more experimentation can be done on reaction conditions, including higher temperatures and longer reactions times to find the conditions needed for the Ing-Manske reaction of **C5** to result in usable amounts of **C6**. From here future work could be done on synthesising a new range of exo-imine pyrazine-based ligands, and exploring their complexation to 3*d* ions.

Some possible directions for future work with **L3**, is that it could be used in complexation reactions at higher temperatures, and microwave reactions could be explored. There is ongoing work to see if the ligand is suitable to complex to beryllium.

Some of the immediate future work involves the analysis of the crystal structures that have resulted from the reactions between **L6** and 3*d* metal salts. The **6B1** $Co(ClO_4)_2 \cdot 6H_2O$ and **6B2** $Co(BF_4)_2 \cdot 6H_2O$ resulted in pink block single crystals. The initial SCXRD results from these crystals indicate, the now expected, 1D polymer chain structures, but has yet to be fully solved. There is still the possibility of other **L6**-3*d* complexes crystallising out over more time. These **L6** complex results also need to be fully characterised, as they were only collected at the end of this research project, so while the initial SCXRD has been done, IR, MS, and UV-Vis have yet to be collected.

The Pz-O-Tz chelation site, appears to not be flexible enough to encapsulate the 3*d* ions and close into a cyclohelicate. Future work can be done to alter the chelation site, and relax the N3-M-N4 angle from an average angle of 148.1º to an angle closer to 180º. Ligands derived from this altered chelation site can then be examined, and difference in their coordination to 3*d* ions can be discovered.

References

1. Ruben, M.; Rojo, J.; Romero-Salguero, F. J.; Uppadine, L. H.; Lehn, J.-M., Grid-Type Metal Ion Architectures: Functional Metallosupramolecular Arrays. *Angewandte Chemie International Edition* **2004,** *43* (28), 3644-3662.
2. Lemes, M. A.; Stein, H. N.; Gabidullin, B.; Robeyns, K.; Clérac, R.; Murugesu, M., Probing Magnetic-Exchange Coupling in Supramolecular Squares Based on Reducible Tetrazine-Derived Ligands. *Chemistry – A European Journal* **2018,** *24* (17), 4259-4263.
3. Jun-Liang Liu, Y.-C. C., Fu-Sheng Guo, Ming-Liang Tong, Recent advances in the design of magnetic molecules for use as cryogenic magnetic coolants. *Coordination Chemistry Reviews* **2014,** *281*, 26-49.
4. Gusev, D. G.; Peris, E., The Tolman electronic parameter (TEP) and the metal–metal electronic communication in ditopic NHC complexes. *Dalton Transactions* **2013,** *42* (20), 7359-7364.
5. Robertson, N.; Yee, G. T., Molecular Magnetic Materials. In *Molecular Materials*, 2010; pp 143-209.
6. Rančić, M. J.; Burkard, G., Ultracoherent operation of spin qubits with superexchange . *Physical Review B* **2017,** *96* (20), 201304.
7. Andriotis, A. N.; Menon, M., Antiferromagnetic successive superexchange interactions underlying ferromagnetic couplings in codoped diluted magnetic semiconductors. *J. Phys. Condens. Matter* (1361-648X (Electronic)).
8. Tiana, D.; Hendon, C. H.; Walsh, A., Ligand design for long-range magnetic order in metal–organic frameworks. *Chemical Communications* **2014,** *50* (90), 13990-13993.
9. Kumagai, S.; Takaishi, S.; Gao, M.; Iguchi, H.; Breedlove, B. K.; Yamashita, M., MX-Chain Compounds with ReO4 Counterions: Exploration of the Robin–Day Class I–II Boundary. *Inorganic Chemistry* **2018,** *57* (7), 3775-3781.
10. Parthey, M.; Kaupp, M., Quantum-chemical insights into mixed-valence systems: within and beyond the Robin–Day scheme. *Chemical Society Reviews* **2014,** *43* (14), 5067-5088.
11. (a) Hogue, R. W.; Singh, S.; Brooker, S., Spin crossover in discrete polynuclear iron(ii) complexes. *Chemical Society Reviews* **2018,** *47* (19), 7303-7338; (b) Brooker, S., Spin crossover with thermal hysteresis: practicalities and lessons learnt. *Chemical Society Reviews* **2015,** *44* (10), 2880-2892.
12. (a) Ni, Z.-P.; Liu, J.-L.; Hoque, M. N.; Liu, W.; Li, J.-Y.; Chen, Y.-C.; Tong, M.-L., Recent advances in guest effects on spin-crossover behavior in Hofmann-type metal-organic frameworks. *Coordination Chemistry Reviews* **2017,** *335*, 28-43; (b) Shen, F.; Huang, W.; Wu, D.; Zheng, Z.; Huang, X.-C.; Sato, O., Redox Modulation of Spin Crossover within a Cobalt Metallogrid. *Inorganic Chemistry* **2016,** *55* (2), 902-908.
13. (a) Binnemans, K., Physical Properties of Metallomesogens. In *Molecular Materials*, 2010; pp 61-141; (b) Senthil Kumar, K.; Ruben, M., Emerging trends in spin crossover (SCO) based functional materials and devices. *Coordination Chemistry Reviews* **2017,** *346*, 176-205.
14. (a) Aguirre-Etcheverry, P.; O'Hare, D., Electronic Communication through Unsaturated Hydrocarbon Bridges in Homobimetallic Organometallic Complexes. *Chemical Reviews* **2010,** *110* (8), 4839-4864; (b) Dawe, L. N.; Abedin, T. S. M.; Thompson, L. K., Ligand directed self-assembly of polymetallic [n × n] grids: rational routes to large functional molecular subunits? *Dalton Transactions* **2008,** (13), 1661-1675.
15. Thompson, L. K.; Zhao, L.; Xu, Z.; Miller, D. O.; Reiff, W. M., Self-Assembled Supramolecular M9 (Mn(II), Fe(III), Zn(II)), M5 (Fe(III)), and $[M3]_2$ (Pb(II)) Complexes: Structural, Magnetic, and Mössbauer Properties. *Inorganic Chemistry* **2003,** *42* (1), 128-139.

16. Cooke, M. W.; Chartrand, D.; Hanan, G. S., Self-assembly of discrete metallosupramolecular luminophores. *Coordination Chemistry Reviews* **2008,** *252* (8), 903-921.
17. Lakma, A.; Hossain, S. M.; van Leusen, J.; Kögerler, P.; Singh, A. K., Tetranuclear MnII, CoII, CuII and ZnII grid complexes of an unsymmetrical ditopic ligand: synthesis, structure, redox and magnetic properties. *Dalton Transactions* **2019,** *48* (22), 7766-7777.
18. (a) Steel, P. J., Ligand Design in Multimetallic Architectures: Six Lessons Learned. *Accounts of Chemical Research* **2005,** *38* (4), 243-250; (b) Lakma, A.; Pradhan, R. N.; Hossain, S. M.; van Leusen, J.; Kögerler, P.; Singh, A. K., Synthesis, structure and magnetic properties of Ni(II) and Cu(II), [2 × 2] grid complexes of pyrimidine-based symmetric ditopic ligands. *Inorganica Chimica Acta* **2019,** *486*, 88-94.
19. Carmona-Vargas, C. C.; Váquiro, I. Y.; Jaramillo-Gómez, L. M.; Lehn, J.-M.; Chaur, M. N., Grid-type complexes of M^{2+} (M=Co, Ni, and Zn) with highly soluble bis(hydrazone)thiopyrimidine-based ligands: Spectroscopy and electrochemical properties. *Inorganica Chimica Acta* **2017,** *468*, 131-139.
20. Brown, M. Synthesis and Characterisation of Pyrazine-Based Ligands for the Analysis of Metal-Metal Communication. Massey University, New Zealand, 2018.
21. Hanan, G. S.; Volkmer, D.; Schubert, U. S.; Lehn, J.-M.; Baum, G.; Fenske, D., Coordination Arrays: Tetranuclear Cobalt(II) Complexes with [2 × 2]-Grid Structure. *Angewandte Chemie International Edition in English* **1997,** *36* (17), 1842-1844.
22. Casini, A.; Woods, B.; Wenzel, M., The Promise of Self-Assembled 3D Supramolecular Coordination Complexes for Biomedical Applications. *Inorganic Chemistry* **2017,** *56* (24), 14715-14729.
23. Wong, J. W. L.; Demeshko, S.; Dechert, S.; Meyer, F., Heterometallic Ru_2Co_2 [2 × 2] Grid with Localized Single Molecule Magnet Behavior. *Inorganic Chemistry* **2019,** *58* (19), 13337-13345.
24. Tanaka, S.; Tsurugi, H.; Mashima, K., Supramolecular assemblies of multi-nuclear transition metal complexes: Synthesis and redox properties. *Coordination Chemistry Reviews* **2014,** *265*, 38-51.
25. Sautter, A.; Schmid, D. G.; Jung, G.; Würthner, F., A Triangle−Square Equilibrium of Metallosupramolecular Assemblies Based on Pd(II) and Pt(II) Corners and Diazadibenzoperylene Bridging Ligands. *Journal of the American Chemical Society* **2001,** *123* (23), 5424-5430.
26. Würthner, F.; You, C.-C.; Saha-Möller, C. R., Metallosupramolecular squares: from structure to function. *Chemical Society Reviews* **2004,** *33* (3), 133-146.
27. Kalsani, V.; Bodenstedt, H.; Fenske, D.; Schmittel, M., Supramolecular Copper Phenanthroline Racks: Structures, Mechanistic Insight and Dynamic Nature. *European Journal of Inorganic Chemistry* **2005,** *2005* (10), 1841-1849.
28. (a) Baxter, P. N. W.; Lehn, J.-M.; Baum, G.; Fenske, D., Self-Assembly and Structure of Interconverting Multinuclear Inorganic Arrays: A [4×5]-AgI20 Grid and an AgI10 Quadruple Helicate. *Chemistry – A European Journal* **2000,** *6* (24), 4510-4517; (b) Puntoriero, F.; Campagna, S.; Stadler, A.-M.; Lehn, J.-M., Luminescence properties and redox behavior of Ru(II) molecular racks. *Coordination Chemistry Reviews* **2008,** *252* (23), 2480-2492.
29. Stadler, A.-M.; Burg, C.; Ramírez, J.; Lehn, J.-M., Grid–double-helicate interconversion. *Chemical Communications* **2013,** *49* (51), 5733-5735.
30. Nitschke, J. R., Construction, Substitution, and Sorting of Metallo-organic Structures via Subcomponent Self-Assembly. *Accounts of Chemical Research* **2007,** *40* (2), 103-112.
31. (a) Hofmeier, H.; Schubert, U. S., Recent developments in the supramolecular chemistry of terpyridine–metal complexes. *Chemical Society Reviews* **2004,** *33* (6), 373-399; (b) Roberts, D. A.; Pilgrim, B. S.; Nitschke, J. R., Covalent post-assembly modification in metallosupramolecular chemistry. *Chemical Society Reviews* **2018,** *47* (2), 626-644.

32. Holliday, B. J.; Mirkin, C. A., Strategies for the Construction of Supramolecular Compounds through Coordination Chemistry. *Angewandte Chemie International Edition* **2001,** *40* (11), 2022-2043.
33. Chakrabarty, R.; Mukherjee, P. S.; Stang, P. J., Supramolecular Coordination: Self-Assembly of Finite Two- and Three-Dimensional Ensembles. *Chemical Reviews* **2011,** *111* (11), 6810-6918.
34. Jansze, S. M.; Cecot, G.; Wise, M. D.; Zhurov, K. O.; Ronson, T. K.; Castilla, A. M.; Finelli, A.; Pattison, P.; Solari, E.; Scopelliti, R.; Zelinskii, G. E.; Vologzhanina, A. V.; Voloshin, Y. Z.; Nitschke, J. R.; Severin, K., Ligand Aspect Ratio as a Decisive Factor for the Self-Assembly of Coordination Cages. *Journal of the American Chemical Society* **2016,** *138* (6), 2046-2054.
35. Bodman, S. E.; Crowther, A. C.; Geraghty, P. B.; Fitchett, C. M., Structural control: can [2 × 2] silver grids be formed from 4,5-disubstituted 3,6-di(2-pyridyl) pyridazines? *CrystEngComm* **2015,** *17* (1), 81-89.
36. Pitt, M. A.; Johnson, D. W., Main group supramolecular chemistry. *Chemical Society Reviews* **2007,** *36* (9), 1441-1453.
37. Sumby, C. J.; Steel, P. J., 'All twisted up': a dinuclear helicate with a highly contorted pyridazine bridge. *Inorganic Chemistry Communications* **2003,** *6* (2), 127-130.
38. Ramírez, J.; Stadler, A.-M.; Kyritsakas, N.; Lehn, J.-M., Solvent-modulated reversible conversion of a [2×2]-grid into a pincer-like complex. *Chemical Communications* **2007,** (3), 237-239.
39. Schweiger, M.; Seidel, S. R.; Arif, A. M.; Stang, P. J., Solution and Solid State Studies of a Triangle−Square Equilibrium: Anion-Induced Selective Crystallization in Supramolecular Self-Assembly. *Inorganic Chemistry* **2002,** *41* (9), 2556-2559.
40. (a) Lehn, J. M.; Rigault, A.; Siegel, J.; Harrowfield, J.; Chevrier, B.; Moras, D., Spontaneous assembly of double-stranded helicates from oligobipyridine ligands and copper(I) cations: structure of an inorganic double helix. *Proceedings of the National Academy of Sciences* **1987,** *84* (9), 2565; (b) Piguet, C., Helicates and Related Metallosupramolecular Assemblies: Toward Structurally Controlled and Functional Devices. *Journal of inclusion phenomena and macrocyclic chemistry* **1999,** *34* (4), 361-391; (c) Hannon, M. J.; Childs, L. J., Helices and Helicates: Beautiful Supramolecular Motifs with Emerging Applications. *Supramolecular Chemistry* **2004,** *16* (1), 7-22.
41. Williams, A. F.; Piguet, C.; Bernardinelli, G., A Self-Assembling Triple-Helical Co Complex : Synthesis and Structure. *Angewandte Chemie International Edition in English* **1991,** *30* (11), 1490-1492.
42. (a) Zhu, X.; He, C.; Dong, D.; Liu, Y.; Duan, C., Cerium-based triple-stranded helicates as luminescent chemosensors for the selective sensing of magnesium ions. *Dalton Transactions* **2010,** *39* (42), 10051-10055; (b) Albrecht, M., "Let's Twist Again"Double-Stranded, Triple-Stranded, and Circular Helicates. *Chemical Reviews* **2001,** *101* (11), 3457-3498.
43. Kramer, R.; Lehn, J. M.; Marquis-Rigault, A., Self-recognition in helicate self-assembly: spontaneous formation of helical metal complexes from mixtures of ligands and metal ions. *Proceedings of the National Academy of Sciences* **1993,** *90* (12), 5394.
44. Yang, D.; von Krbek, L. K. S.; Yu, L.; Ronson, T. K.; Thoburn, J. D.; Carpenter, J. P.; Greenfield, J. L.; Howe, D. J.; Wu, B.; Nitschke, J. R., Glucose Binding Drives Reconfiguration of a Dynamic Library of Urea-Containing Metal–Organic Assemblies. *Angewandte Chemie International Edition* **2021,** *60* (9), 4485-4490.
45. Schouwey, C.; Scopelliti, R.; Severin, K., An Imine-Based Molecular Cage with Distinct Binding Sites for Small and Large Alkali Metal Cations. *Chemistry – A European Journal* **2013,** *19* (20), 6274-6281.
46. (a) Fang, Y.; Powell, J. A.; Li, E.; Wang, Q.; Perry, Z.; Kirchon, A.; Yang, X.; Xiao, Z.; Zhu, C.; Zhang, L.; Huang, F.; Zhou, H.-C., Catalytic reactions within the cavity of coordination cages. *Chemical Society Reviews* **2019,** *48* (17), 4707-4730; (b) Lewis, J. E. M.; Gavey, E. L.; Cameron, S. A.; Crowley, J. D., Stimuli-responsive

Pd_2L_4 metallosupramolecular cages: towards targeted cisplatin drug delivery. *Chemical Science* **2012,** *3* (3), 778-784.

47. (a) Musser, A. J.; Neelakandan, P. P.; Richter, J. M.; Mori, H.; Friend, R. H.; Nitschke, J. R., Excitation Energy Delocalization and Transfer to Guests within MII 4L6 Cage Frameworks. *Journal of the American Chemical Society* **2017,** *139* (34), 12050-12059; (b) Riddell, I. A.; Smulders, M. M. J.; Clegg, J. K.; Nitschke, J. R., Encapsulation, storage and controlled release of sulfur hexafluoride from a metal–organic capsule. *Chemical Communications* **2011,** *47* (1), 457-459.
48. Symmers, P. R.; Burke, M. J.; August, D. P.; Thomson, P. I. T.; Nichol, G. S.; Warren, M. R.; Campbell, C. J.; Lusby, P. J., Non-equilibrium cobalt(III) "click" capsules. *Chemical Science* **2015,** *6* (1), 756-760.
49. Bolliger, J. L.; Ronson, T. K.; Ogawa, M.; Nitschke, J. R., Solvent Effects upon Guest Binding and Dynamics of a $FeII_4L_4$ Cage. *Journal of the American Chemical Society* **2014,** *136* (41), 14545-14553.
50. Ferguson, J. L.; Fitchett, C. M., N,N′-Dimethylene-2,2′-biimidazole—A Mimic of Carboxylate for the Formation of Complexes with Copper(I) And the Anion Directed Formation of a Solvent Pocket. *Crystal Growth & Design* **2015,** *15* (3), 1280-1288.
51. Manoj, E.; Prathapachandra Kurup, M. R.; Fun, H. K.; Punnoose, A., Self-assembled macrocyclic molecular squares of Ni(II) derived from carbohydrazones and thiocarbohydrazones: Structural and magnetic studies. *Polyhedron* **2007,** *26* (15), 4451-4462.
52. Dey, S. K.; Abedin, T. S. M.; Dawe, L. N.; Tandon, S. S.; Collins, J. L.; Thompson, L. K.; Postnikov, A. V.; Alam, M. S.; Müller, P., Supramolecular Self-Assembled Polynuclear Complexes from Tritopic, Tetratopic, and Pentatopic Ligands: Structural, Magnetic and Surface Studies. *Inorganic Chemistry* **2007,** *46* (19), 7767-7781.
53. Cook, T. R.; Zheng, Y.-R.; Stang, P. J., Metal–Organic Frameworks and Self-Assembled Supramolecular Coordination Complexes: Comparing and Contrasting the Design, Synthesis, and Functionality of Metal–Organic Materials. *Chemical Reviews* **2013,** *113* (1), 734-777.
54. Bassani, D. M.; Lehn, J.-M.; Fromm, K.; Fenske, D., Toposelective and Chiroselective Self-Assembly of [2×2] Grid-Type Inorganic Arrays Containing Different Octahedral Metallic Centers. *Angewandte Chemie International Edition* **1998,** *37* (17), 2364-2367.
55. Wu, Z.; Chen, Q.; Xiong, S.; Xin, B.; Zhao, Z.; Jiang, L.; Ma, J. S., Double-Stranded Helicates, Triangles, and Squares Formed by the Self-Assembly of Pyrrol-2-ylmethyleneamines and ZnII Ions. *Angewandte Chemie International Edition* **2003,** *115* (28), 3393-3396.
56. Hausmann, J.; Brooker, S., Control of molecular architecture by use of the appropriate ligand isomer: a mononuclear "corner-type" versus a tetranuclear [2 × 2] grid-type cobalt(III) complex. *Chemical Communications* **2004,** (13), 1530-1531.
57. Zangrando, E.; Casanova, M.; Alessio, E., Trinuclear Metallacycles: Metallatriangles and Much More. *Chemical Reviews* **2008,** *108* (12), 4979-5013.
58. Neels, A.; Stoeckli-Evans, H., Trinuclear Zinc(II) Complexes and Polymeric Cadmium(II) Complexes with the Ligand 2,5-Bis(2-pyridyl)pyrazine: Synthesis, Spectral Analysis, and Single-Crystal and Powder X-ray Analyses. *Inorganic Chemistry* **1999,** *38* (26), 6164-6170.
59. Hogue, R. W.; Dhers, S.; Hellyer, R. M.; Luo, J.; Hanan, G. S.; Larsen, D. S.; Garden, A. L.; Brooker, S., Self-Assembly of Cyclohelicate $[M_3L_3]$ Triangles Over $[M_4L_4]$ Squares, Despite Near-Linear Bis-terdentate L and Octahedral M. *Chemistry – A European Journal* **2017,** *23* (57), 14193-14199.
60. Dais, T. N.; Brown, M. J.; Coles, M. P.; Laur, F.; Price, J. R.; Rowlands, G. J.; Plieger, P. G., Synthesis and characterization of Co(II) and Mn(II) $[M_3L_3]$ triangles. *Journal of Inclusion Phenomena and Macrocyclic Chemistry* **2019,** *94* (3), 175-182.

61. Zhong, J.; Zhang, L.; August, D. P.; Whitehead, G. F. S.; Leigh, D. A., Self-Sorting Assembly of Molecular Trefoil Knots of Single Handedness. *Journal of the American Chemical Society* **2019,** *141* (36), 14249-14256.
62. Li, L.; Yang, J.; Zhao, Q.; Li, J., One-dimensional interpenetrated coordination polymers showing step gas sorption properties. *CrystEngComm* **2013,** *15* (9), 1689-1692.
63. Zhao, M.; Huang, Y.; Peng, Y.; Huang, Z.; Ma, Q.; Zhang, H., Two-dimensional metal–organic framework nanosheets: synthesis and applications. *Chemical Society Reviews* **2018,** *47* (16), 6267-6295.
64. (a) Li, Y.-z.; Fu, Z.-h.; Xu, G., Metal-organic framework nanosheets: Preparation and applications. *Coordination Chemistry Reviews* **2019,** *388*, 79-106; (b) Zhang, L.; Jia, Y.; Wang, H.; Zhang, D.-W.; Zhang, Q.; Liu, Y.; Li, Z.-T., pH-Responsive single-layer honeycomb supramolecular organic frameworks that exhibit antimicrobial activity. *Polymer Chemistry* **2016,** *7* (10), 1861-1865.
65. Caradoc-Davies, P. L.; Hanton, L. R.; Henderson, W., Coordination polymers and isomerism; a study using silver(i) and a π-stacked ligand. *Journal of the Chemical Society, Dalton Transactions* **2001,** (19), 2749-2755.
66. Chakraborty, B.; Halder, P.; Paine, T. K., Conformational supramolecular isomerism in one-dimensional silver(i) coordination polymer of a flexible bis(bidentate)N,N-donor ligand with p-xylyl spacer. *Dalton Transactions* **2011,** *40* (14), 3647-3654.
67. Caradoc-Davies, P. L.; Gregory, D. H.; Hanton, L. R.; Turnbull, J. M., Probing copper halide supramolecular arrays of a ditopic ligand with complexes of a monotopic analogue. *Journal of the Chemical Society, Dalton Transactions* **2002,** (8), 1574-1580.
68. Cordes, D. B.; Bailey, A. S.; Caradoc-Davies, P. L.; Gregory, D. H.; Hanton, L. R.; Lee, K.; Spicer, M. D., Flexible Ligands and Structural Diversity: Isomerism in Cd(NO3)2 Coordination Polymers. *Inorganic Chemistry* **2005,** *44* (7), 2544-2552.
69. Dong, R.; Zhang, Z.; Tranca, D. C.; Zhou, S.; Wang, M.; Adler, P.; Liao, Z.; Liu, F.; Sun, Y.; Shi, W.; Zhang, Z.; Zschech, E.; Mannsfeld, S. C. B.; Felser, C.; Feng, X., A coronene-based semiconducting two-dimensional metal-organic framework with ferromagnetic behavior. *Nature Communications* **2018,** *9* (1), 2637.
70. Martin, C. R.; Kittikhunnatham, P.; Leith, G. A.; Berseneva, A. A.; Park, K. C.; Greytak, A. B.; Shustova, N. B., Let the light be a guide: Chromophore communication in metal-organic frameworks. *Nano Research* **2021,** *14* (2), 338-354.
71. (a) Bera, S.; Mondal, S.; Rencus-Lazar, S.; Gazit, E., Organization of Amino Acids into Layered Supramolecular Secondary Structures. *Accounts of Chemical Research* **2018,** *51* (9), 2187-2197; (b) Kathalikkattil, A. C.; Subramanian, P. S.; Eringathodi, S., Structural Investigation of Metal-Organic Cu(II) Coordination Frameworks Constructed from N-donor and α, ω-Dicarboxylate Ligands by One Pot Synthesis: Zigzag Strands, Layered Networks and Its Interaction with Lattice Water Molecules. *Journal of Chemical Crystallography* **2010,** *40* (12), 1087-1093.
72. Ghosh, S. K.; Bharadwaj, P. K., Infinite Chains of Quasi-Planar Hexameric Water Clusters Stabilized in a Metal-Organic Framework Built from CoII and Pyrazine-2,3,5,6-tetracarboxylic Acid. *European Journal of Inorganic Chemistry* **2005,** *2005* (24), 4880-4885.
73. Cowan, M. G.; Miller, R. G.; Brooker, S., Pyrazine-imide complexes: reversible redox and MOF building blocks. *Dalton Transactions* **2015,** *44* (6), 2880-2892.
74. Cui, Z.; Lin, H.; Zeng, L.; Lu, J., A new functionalized POM-based MOF containing 1D [Mo3O10]n2n− chains and the flexible bis(pyrazine)-bis(amide) ligand. *Inorganic Chemistry Communications* **2021,** *126*, 108493.
75. Kolb, H. C.; Finn, M. G.; Sharpless, K. B., Click Chemistry: Diverse Chemical Function from a Few Good Reactions. *Angewandte Chemie International Edition* **2001,** *40* (11), 2004-2021.
76. Agalave, S. G.; Maujan, S. R.; Pore, V. S., Click Chemistry: 1,2,3-Triazoles as Pharmacophores. *Chemistry – An Asian Journal* **2011,** *6* (10), 2696-2718.

77. (a) Kappe, C. O.; Van der Eycken, E., Click chemistry under non-classical reaction conditions. *Chemical Society Reviews* **2010,** *39* (4), 1280-1290; (b) Castro, V.; Rodríguez, H.; Albericio, F., CuAAC: An Efficient Click Chemistry Reaction on Solid Phase. *ACS Combinatorial Science* **2016,** *18* (1), 1-14.
78. Moses, J. E.; Moorhouse, A. D., The growing applications of click chemistry. *Chemical Society Reviews* **2007,** *36* (8), 1249-1262.
79. Lewis, J. E. M.; Elliott, A. B. S.; McAdam, C. J.; Gordon, K. C.; Crowley, J. D., 'Click' to functionalise: synthesis, characterisation and enhancement of the physical properties of a series of exo- and endo-functionalised Pd2L4 nanocages. *Chemical Science* **2014,** *5* (5), 1833-1843.
80. Bock, V. D.; Hiemstra, H.; van Maarseveen, J. H., CuI-Catalyzed Alkyne–Azide "Click" Cycloadditions from a Mechanistic and Synthetic Perspective. *European Journal of Organic Chemistry* **2006,** *2006* (1), 51-68.
81. Bryant, J. J.; Bunz, U. H. F., Click To Bind: Metal Sensors. *Chemistry – An Asian Journal* **2013,** *8* (7), 1354-1367.
82. Mindt, T. L.; Struthers, H.; Brans, L.; Anguelov, T.; Schweinsberg, C.; Maes, V.; Tourwé, D.; Schibli, R., "Click to Chelate": Synthesis and Installation of Metal Chelates into Biomolecules in a Single Step. *Journal of the American Chemical Society* **2006,** *128* (47), 15096-15097.
83. Yan, W.; Ye, X.; Akhmedov, N. G.; Petersen, J. L.; Shi, X., 1,2,3-Triazole: Unique Ligand in Promoting Iron-Catalyzed Propargyl Alcohol Dehydration. *Organic Letters* **2012,** *14* (9), 2358-2361.
84. Guha, P. M.; Phan, H.; Kinyon, J. S.; Brotherton, W. S.; Sreenath, K.; Simmons, J. T.; Wang, Z.; Clark, R. J.; Dalal, N. S.; Shatruk, M.; Zhu, L., Structurally Diverse Copper(II) Complexes of Polyaza Ligands Containing 1,2,3-Triazoles: Site Selectivity and Magnetic Properties. *Inorganic Chemistry* **2012,** *51* (6), 3465-3477.
85. Schulze , B.; Brown, D. G.; Robson, K. C. D.; Friebe , C.; Jäger , M.; Birckner, E.; Berlinguette, C. P.; Schubert , U. S., Cyclometalated Ruthenium(II) Complexes Featuring Tridentate Click-Derived Ligands for Dye-Sensitized Solar Cell Applications. *Chemistry – A European Journal* **2013,** *19* (42), 14171-14180.
86. Urankar, D.; Pevec, A.; Turel, I.; Košmrlj, J., Pyridyl Conjugated 1,2,3-Triazole is a Versatile Coordination Ability Ligand Enabling Supramolecular Associations. *Crystal Growth & Design* **2010,** *10* (11), 4920-4927.
87. Schulze, B.; Schubert, U. S., Beyond click chemistry – supramolecular interactions of 1,2,3-triazoles. *Chemical Society Reviews* **2014,** *43* (8), 2522-2571.
88. Herzigkeit, B.; Flöser, B. M.; Meißner, N. E.; Engesser, T. A.; Tuczek, F., Click. Coordinate. Catalyze. Using CuAAC Click Ligands in Small-Molecule Model Chemistry of Tyrosinase. *ChemCatChem* **2018,** *10* (23), 5402-5405.
89. Himo, F.; Lovell, T.; Hilgraf, R.; Rostovtsev, V. V.; Noodleman, L.; Sharpless, K. B.; Fokin, V. V., Copper(I)-Catalyzed Synthesis of Azoles. DFT Study Predicts Unprecedented Reactivity and Intermediates. *Journal of the American Chemical Society* **2005,** *127* (1), 210-216.
90. Rodionov, V. O.; Fokin, V. V.; Finn, M. G., Mechanism of the Ligand-Free CuI-Catalyzed Azide–Alkyne Cycloaddition Reaction. *Angewandte Chemie International Edition* **2005,** *117* (15), 2250-2255.
91. Tornøe, C. W.; Christensen, C.; Meldal, M., Peptidotriazoles on Solid Phase: [1,2,3]-Triazoles by Regiospecific Copper(I)-Catalyzed 1,3-Dipolar Cycloadditions of Terminal Alkynes to Azides. *The Journal of Organic Chemistry* **2002,** *67* (9), 3057-3064.
92. Kilpin, K. J.; Gavey, E. L.; McAdam, C. J.; Anderson, C. B.; Lind, S. J.; Keep, C. C.; Gordon, K. C.; Crowley, J. D., Palladium(II) Complexes of Readily Functionalized Bidentate 2-Pyridyl-1,2,3-triazole "Click" Ligands: A Synthetic, Structural, Spectroscopic, and Computational Study. *Inorganic Chemistry* **2011,** *50* (13), 6334-6346.

93. Brotherton, W. S.; Michaels, H. A.; Simmons, J. T.; Clark, R. J.; Dalal, N. S.; Zhu, L., Apparent Copper(II)-Accelerated Azide−Alkyne Cycloaddition. *Organic Letters* **2009,** *11* (21), 4954-4957.
94. Dou, Y.; Yin, B.; Zhang, P.; Zhu, Q., Copper-Catalyzed Regioselective Nitration and Azidation of 1-Naphthylamine Derivatives via Remote C–H Activation. *European Journal of Organic Chemistry* **2018,** *2018* (33), 4571-4576.
95. Hohenstein, E. G.; Sherrill, C. D., Effects of Heteroatoms on Aromatic π−π Interactions: Benzene−Pyridine and Pyridine Dimer. *The Journal of Physical Chemistry A* **2009,** *113* (5), 878-886.
96. Umezawa, Y.; Tsuboyama, S.; Takahashi, H.; Uzawa, J.; Nishio, M., CHπ interaction in the conformation of organic compounds. A database study. *Tetrahedron* **1999,** *55* (33), 10047-10056.
97. Anderson, C. B.; Elliott, A. B. S.; Lewis, J. E. M.; McAdam, C. J.; Gordon, K. C.; Crowley, J. D., fac-Re(CO)3 complexes of 2,6-bis(4-substituted-1,2,3-triazol-1-ylmethyl)pyridine "click" ligands: synthesis, characterisation and photophysical properties. *Dalton Transactions* **2012,** *41* (48), 14625-14632.
98. Crowley, J. D.; Bandeen, P. H., A multicomponent CuAAC "click" approach to a library of hybrid polydentate 2-pyridyl-1,2,3-triazole ligands: new building blocks for the generation of metallosupramolecular architectures. *Dalton Transactions* **2010,** *39* (2), 612-623.
99. Wu, N.; Melan, C. F. C.; Stevenson, K. A.; Fleischel, O.; Guo, H.; Habib, F.; Holmberg, R. J.; Murugesu, M.; Mosey, N. J.; Nierengarten, H.; Petitjean, A., Systematic study of the synthesis and coordination of 2-(1,2,3-triazol-4-yl)-pyridine to Fe(ii), Ni(ii) and Zn(ii); ion-induced folding into helicates, mesocates and larger architectures, and application to magnetism and self-selection. *Dalton Transactions* **2015,** *44* (33), 14991-15005.
100. Scattergood, P. A.; Roberts, J.; Omar, S. A. E.; Elliott, P. I. P., Observation of an Inversion in Photophysical Tuning in a Systematic Study of Luminescent Triazole-Based Osmium(II) Complexes. *Inorganic Chemistry* **2019,** *58* (13), 8607-8621.
101. Ladouceur, S.; Soliman, A. M.; Zysman-Colman, E., One-Pot Click Synthesis of 1N-Alkyl-4-aryl-1,2,3-triazoles from Protected Arylalkynes and Alkyl Bromides. *Synthesis* **2011,** *2011* (22), 3604-3611.
102. Fu, Y.; Liu, Y.; Fu, X.; Zou, L.; Li, H.; Li, M.; Chen, X.; Qin, J., Synthesis of Click-Chelator via Cu(I)-Catalyzed Alkyne-Azide Cycloaddition. *Chinese Journal of Chemistry* **2010,** *28* (11), 2226-2232.
103. Burke, B. P.; Grantham, W.; Burke, M. J.; Nichol, G. S.; Roberts, D.; Renard, I.; Hargreaves, R.; Cawthorne, C.; Archibald, S. J.; Lusby, P. J., Visualizing Kinetically Robust CoIII4L6 Assemblies in Vivo: SPECT Imaging of the Encapsulated [99mTc]TcO4– Anion. *Journal of the American Chemical Society* **2018,** *140* (49), 16877-16881.
104. Kubas, G. J.; Monzyk, B.; Crumblis, A. L., Tetrakis(Acetonitrile)Copper(1+) Hexafluorophosphate(1-). *Inorganic Syntheses* **1990**, 68-70.
105. (a) Dastidar, P.; Ganguly, S.; Sarkar, K., Metallogels from Coordination Complexes, Organometallic, and Coordination Polymers. *Chemistry – An Asian Journal* **2016,** *11* (18), 2484-2498; (b) Fang, W.; Zhang, Y.; Wu, J.; Liu, C.; Zhu, H.; Tu, T., Recent Advances in Supramolecular Gels and Catalysis. *Chemistry – An Asian Journal* **2018,** *13* (7), 712-729.
106. (a) Steel, P. J.; Fitchett, C. M., Metallosupramolecular silver(I) assemblies based on pyrazine and related ligands. *Coordination Chemistry Reviews* **2008,** *252* (8), 990-1006; (b) Garrison, J. C.; Youngs, W. J., Ag(I) N-Heterocyclic Carbene Complexes: Synthesis, Structure, and Application. *Chemical Reviews* **2005,** *105* (11), 3978-4008.
107. Yang, L.; Powell, D. R.; Houser, R. P., Structural variation in copper(i) complexes with pyridylmethylamide ligands: structural analysis with a new four-coordinate geometry index, τ4. *Dalton Transactions* **2007,** (9), 955-964.

108. Steiner, T., The Hydrogen Bond in the Solid State. *Angewandte Chemie International Edition* **2002,** *41* (1), 48-76.
109. Delso, I.; Valero-Gonzalez, J.; Gomollón-Bel, F.; Castro-López, J.; Fang, W.; Navratilova, I.; van Aalten, D. M. F.; Tejero, T.; Merino, P.; Hurtado-Guerrero, R., Inhibitors against Fungal Cell Wall Remodeling Enzymes. *ChemMedChem* **2018,** *13* (2), 128-132.
110. Hao, E.; Meng, T.; Zhang, M.; Pang, W.; Zhou, Y.; Jiao, L., Solvent Dependent Fluorescent Properties of a 1,2,3-Triazole Linked 8-Hydroxyquinoline Chemosensor: Tunable Detection from Zinc(II) to Iron(III) in the CH3CN/H2O System. *The Journal of Physical Chemistry A* **2011,** *115* (29), 8234-8241.
111. Irfan, M.; Alam, S.; Manzoor, N.; Abid, M. A.-O., Effect of quinoline based 1,2,3-triazole and its structural analogues on growth and virulence attributes of Candida albicans. *Plos one* (1932-6203 (Electronic)).
112. Aneja, B.; Azam, M.; Alam, S.; Perwez, A.; Maguire, R.; Yadava, U.; Kavanagh, K.; Daniliuc, C. G.; Rizvi, M. M. A.; Haq, Q. M. R.; Abid, M., Natural Product-Based 1,2,3-Triazole/Sulfonate Analogues as Potential Chemotherapeutic Agents for Bacterial Infections. *ACS Omega* **2018,** *3* (6), 6912-6930.
113. Gümüş, A. A.-O.; Okumuş, V. A.-O.; Gümüş, S. A.-O., Synthesis, biological evaluation of antioxidant-antibacterial activities and computational studies of novel anthracene- and pyrene-based Schiff base derivatives. (1300-0527 (Print)).
114. Darrah, K.; Wang, T.; Cook, I.; Cacace, M.; Deiters, A.; Leyh, T. S., Allosteres to regulate neurotransmitter sulfonation. *Journal of Biological Chemistry* **2019,** *294* (7), 2293-2301.
115. Yang, B.; Zhang, H.; Peng, H.; Xu, Y.; Wu, B.; Weng, W.; Li, L., Self-healing metallo-supramolecular polymers from a ligand macromolecule synthesized via copper-catalyzed azide–alkyne cycloaddition and thiol–ene double "click" reactions. *Polymer Chemistry* **2014,** *5* (6), 1945-1953.
116. Nguyen, D. M.; Miles, D. H., Copper(I)-Catalyzed Cycloaddition of Methyl O-Propargylpodocarpate and Azides at Room Temperature. *Synthetic Communications* **2011,** *41* (12), 1759-1771.
117. Geary, W. J., The use of conductivity measurements in organic solvents for the characterisation of coordination compounds. *Coordination Chemistry Reviews* **1971,** *7* (1), 81-122.
118. Buron-Le Cointe, M.; Hébert, J.; Baldé, C.; Moisan, N.; Toupet, L.; Guionneau, P.; Létard, J. F.; Freysz, E.; Cailleau, H.; Collet, E., Intermolecular control of thermoswitching and photoswitching phenomena in two spin-crossover polymorphs. *Physical Review B* **2012,** *85* (6), 064114.
119. Frischmann, P. D.; Jiang, J.; Hui, J. K. H.; Grzybowski, J. J.; MacLachlan, M. J., Reversible−Irreversible Approach to Schiff Base Macrocycles: Access to Isomeric Macrocycles with Multiple Salphen Pockets. *Organic Letters* **2008,** *10* (6), 1255-1258.
120. Hossain, M.; Roy, P.; Zakaria, C.; Zahan, M. K.-E., Selected Schiff base coordination complexes and their microbial application: A review. *International Journal of Chemical Studies* **2018,** *6*, 19-31.
121. Suart, B., Infrared spectroscopy: Fundamental and applications. *Google Scholar* **2004**.
122. Klingele, J.; Moubaraki, B.; Murray, K. S.; Boas, J. F.; Brooker, S., Dinuclear Copper(II) Complexes of Two Homologous Pyrazine-Based Bis(terdentate) Diamide Ligands. *European Journal of Inorganic Chemistry* **2005,** *2005* (8), 1530-1541.
123. Das, S. K.; Frey, J., Regioselective double Boekelheide reaction: first synthesis of 3,6-dialkylpyrazine-2,5-dicarboxaldehydes from dl-alanine. *Tetrahedron Letters* **2012,** *53* (30), 3869-3872.
124. Andreotti, D.; Miserazzi, E.; Nalin, A.; Pozzan, A.; Profeta, R.; Spada, S., Reaction of 2-alkyl pyridine N-oxide derivatives with Mosher's acyl chloride: first example of stereoselective Boekelheide rearrangement. *Tetrahedron Letters* **2010,** *51* (50), 6526-6530.

125. Li, J. J., *Name reactions: a collection of detailed mechanisms and synthetic applications*. Springer Science & Business Media: 2010.
126. Armarego, W. L., *Purification of laboratory chemicals*. Butterworth-Heinemann: 2017.
127. Penteado, F.; Gomes, C. S.; Perin, G.; Garcia, C. S.; Bortolatto, C. F.; Brüning, C. s. A.; Lenardão, E. J., Regioselective Synthesis of 1-Sulfanyl-and 1-Selanylindolizines. *The Journal of organic chemistry* **2019,** *84* (11), 7189-7198.
128. Zhang, H.; Yao, Y.; Sun, R.; Sun, C.; Liu, F.; Liu, Y.; Guo, M.; Wang, S.; You, K., Thermally stable pseudo-third-generation Grubbs ruthenium catalysts with pyridine–phosphinimine ligand. *Catalysis Communications* **2014,** *49*, 43-46.
129. Eiermann, U.; Krieger, C.; Neugebauer, F. A.; Staab, H. A., [2.2](2, 6)-and [2.2](2, 5) Pyrazinophanes: Synthesis and Molecular Structure. *Chemische Berichte* **1990,** *123* (3), 523-533.
130. (a) Peet, N.; Weintraub, P., Explosion with Sodium-Azide in DMSO-CH_2Cl_2. *Chemical & Engineering News* **1993,** *71* (16), 4-4; (b) Conrow, R. E.; Dean, W. D., Diazidomethane explosion. *Organic Process Research & Development* **2008,** *12* (6), 1285-1286.
131. Abushanab, E.; Bindra, A. P.; Goodman, L.; Petersen Jr, H., Imidazo [1, 5-a] pyrazine System. *The Journal of organic chemistry* **1973,** *38* (11), 2049-2052.
132. Amadio, E.; Scrivanti, A.; Chessa, G.; Matteoli, U.; Beghetto, V.; Bertoldini, M.; Rancan, M.; Dolmella, A.; Venzo, A.; Bertani, R., Synthesis, characterization and low temperature self assembling of (η^3-allyl) palladium complexes with 2-pyridyl-1, 2, 3-triazole bidentate ligands. Study of the catalytic activity in Suzuki–Miyaura reaction. *Journal of Organometallic Chemistry* **2012,** *716*, 193-200.
133. Kwan, C.-S.; Zhao, R.; Van Hove, M. A.; Cai, Z.; Leung, K. C.-F., Higher-generation type III-B rotaxane dendrimers with controlling particle size in three-dimensional molecular switching. *Nature communications* **2018,** *9* (1), 1-9.
134. Palanichamy, K.; Bravo, M. F.; Shlain, M. A.; Schiro, F.; Naeem, Y.; Marianski, M.; Braunschweig, A. B., Binding Studies on a Library of Induced-Fit Synthetic Carbohydrate Receptors with Mannoside Selectivity. *Chemistry–A European Journal* **2018,** *24* (52), 13971-13982.
135. Liu, S.; Focken, T.; Chahal, N.; Zhang, Z.; Oballa, R. M.; Fonarev, J. Biaryl ether sulfonamides, their preparation and use in treating sodium channel-mediated diseases. 2013.
136. Wessel, A. J.; Schultz, J. W.; Tang, F.; Duan, H.; Mirica, L. M., Improved synthesis of symmetrically & asymmetrically N-substituted pyridinophane derivatives. *Organic & biomolecular chemistry* **2017,** *15* (46), 9923-9931.
137. Ariffin, A.; Khan, M. N.; Lan, L. C.; May, F. Y.; Yun, C. S., Suggested Improved Method for the Ing-Manske and Related Reactions for the Second Step of Gabriel Synthesis of Primary Amines. *Synthetic communications* **2004,** *34* (24), 4439-4445.
138. Curley, O. S.; McCormick, J. E.; McElhinney, R. S.; McMurry, T. B. H., Intermediates in the Ing-Manske reaction. *Arkivoc* **2003,** *7*, 180-189.
139. Bruker, *Apex3*. Computer Program.
140. Palatinus, L.; van der Lee, A., Symmetry determination following structure solution in P1. *Journal of Applied Crystallography* **2008,** *41* (6), 975-984.
141. Sheldrick, G. M., Crystal structure refinement with SHELXL. *Acta Crystallographica Section C: Structural Chemistry* **2015,** *71* (1), 3-8.
142. Dolomanov, O. V.; Bourhis, L. J.; Gildea, R. J.; Howard, J. A.; Puschmann, H., OLEX2: a complete structure solution, refinement and analysis program. *Journal of applied crystallography* **2009,** *42* (2), 339-341.
143. Zhou, F.; Liu, X.; Hao, Y. Preparation of Pharmaceutical intermediate 2-aminomethylpyrazine hydrochloride. 2012.
144. He, S.; Li, K.; Lin, B.; Hu, Z.; Xiao, J.; Hu, X.; Wang, A. Q.; Xu, X.; Ferrer, M.; Southall, N., Development of an aryloxazole class of hepatitis C virus inhibitors

targeting the entry stage of the viral replication cycle. *Journal of medicinal chemistry* **2017,** *60* (14), 6364-6383.
145. Matsuura, K.; Inomata, M.; Oikawa, S.; Jin, K.; Itai, T., Synthesis of Pyrazine Derivatives. I. Reactions of 2, 5-Dimethylpyrazine N-Oxides with Acid Chlorides. *Chemical and Pharmaceutical Bulletin* **1975,** *23* (11), 2913-2917.
146. Wang, C.-S.; Dixneuf, P. H.; Soulé, J.-F., Metal-free C (sp 3)–H bond sulfonyloxylation of 2-alkylpyridines and alkylnitrones. *Organic & biomolecular chemistry* **2018,** *16* (27), 4954-4957.
147. Jacobi, P. A., *Introduction to Heterocyclic Chemistry*. John Wiley & Sons: 2018.
148. Wietzke, R.; Mazzanti, M.; Latour, J.-M.; Pécaut, J.; Cordier, P.-Y.; Madic, C., Lanthanide (III) complexes of tripodal N-donor ligands: structural models for the species involved in solvent extraction of actinides (III). *Inorganic chemistry* **1998,** *37* (26), 6690-6697.

Appendices

Appendices 141

General Experimental Methods 145

G.1 General Procedures 145
Appendix 1.0: Method and Characterisation of L1, L1b and L2 147

A1.0: Preparing the pyrazine ketone: (B1) 147
A1.1: 2,5- bis((E)-styryl)pyrazine: (A2) 147
A1.2 Synthesis of 2,5-diformyl pyrazine (B1) 148
A1.3 Synthesis of endo-imine ligand ($L1^{endo}$) 149
A1.4 SXRD Characterisation of (L1b) 150
A1.5 Synthesis of novel endo-imine ligand (L2) 151

Appendix 2.0: Alternate routes of C4 synthesis 152

A2.0 Initial attempts at the synthesis of 2,5-dichloromethyl pyrazine 152
A2.1 Full attempted routes to C6 153
A2.2 Wohl Ziegler Radical Chlorination 154

A2.2.2 Synthesis of C4 – Wohl-Ziegler Mechanism 155

A2.2.3 Method Synthesis of 2,5- bis(chloromethyl)pyrazine 156

A2.3 $POCl_3$ Chlorination 157

A2.4 Boekelheide rearrangement of TOSYL – (C6) 159

Appendix 3.0: Alternate routes of C6 synthesis 160

A3.1 2,5-bis(HMTA-methyl)pyrazine synthesis (C6) 160

Appendix 4.0: Methods from Section 3.0 163

A4.1: *N*-oxidation: 2,5-dimethylpyrazine-1,4-N-oxide (C1) 163
A4.2 Synthesis of 2,5-bis(acetoxymethyl)pyrazine (C2) 164
A4.3 2,5-bis(hydroxymethyl)pyrazine (C3) 165
A4.4 Synthesis of 2,5-bis(chloromethyl)pyrazine (C4) 166
A4.5 Synthesis of 2,5-bis(phthalamidemethyl)pyrazine C5 167
A4.5.1 C5 from C4 167
A4.5.1 Mitsunobu reaction of C3 to C5 168
A4.6 Ing-Manske Reaction: C5 – C6 169

A4.7 2,5-bis(azidomethyl)pyrazine (D1) 170

A4.7.2 Unsuccessful (D1) reduction to (C6) 171

Appendix 5.0: Synthesis Methods of (L3) and (L4) 172

A5.1 Synthesis of L3 172

A5.1a Synthesis of $[Cu(MeCN)_4]PF_6$ 173

A5.1b Complexation of L3 and NO_3 (AgL3) 174

A5.2 Synthesis of D3 175

A5.3 Synthesis of L4: 176

Appendix6.0: Synthesis Method of L5 and Reagents 177
A6.1 Synthesis of F1: 2,5-bis((prop-2-yn-1-yloxy)methyl)pyrazine 177
A6.2 Synthesis of: azido butane (E2) 178

Appendix 7.0: L5 Crystallisation Methods 183
A7.01: {[Mn_2(L5, H_2O)](ClO_4)$_2$}$_\infty$ (5A1) 183
A7.02: {[Co(L^5)](ClO_4)$_2$}$_\infty$ (5B1) 184
A7.03 {[Fe(L5)](H_2O)(ClO_4)$_2$}$_\infty$ (5C1) 185
A7.04 {[Ni(L^5)](ClO_4)$_2$}$_\infty$ (5D1) 186
A7.05 {[Cu(L^5)](ClO_4)$_2$}$_\infty$ (5F1) 187
A7.06 [Mn_2(L^5)](NO_3)$_3$(H_2O)$_4$ (5A3) 188
A7.07 {[Co(L^5)](BF_4)$_2$}$_\infty$ (5B2) 189
A7.08 {[Fe(L5)](BF_4)$_2$}$_\infty$ (5C2) 190
A7.09 {[Zn(L5)](BF_4)$_2$}$_\infty$ (5E2) 191
A7.10 {[Cu(L^5)](BF_4)$_2$}$_\infty$ (5F2) 192
A9.0 Full L5 Complexation Attempts 194

A10.0 L6 Complexes 195
A10.1 {[Cu(L6)](ClO_4)$_2$}$_\infty$ (6D1) 195

A11.0 X-ray crystallography data 197

A12.0 Appendix: NMR and Other Characterisation 201
A12.1 Characterisation of Endo-imine molecules: (A2) (B1) ($L1^{endo}$) (L2) 201
A12.1.1 ^{1}H NMR of 2,5-distyryl pyrazine (A2) 201
A12.1.2 ^{1}H NMR of 2,5-diformyl pyrazine (B1) 202
A12.1.3 ^{1}H NMR of ($L1^{endo}$) 202
A12.1.5 ^{1}H NMR of (L2) 203
A12.1.6 ^{13}C NMR of (L2) 203
A12.1.7 COSY of (L2) 204
A12.1.8 HMQC of (L2) 204
A12.2 Characterisation of the amine synthesis pathway: (C1) (C2) (C3) (C4) (C5) (C6) (D1) 205
A12.2.0 ^{1}H NMR Pathway Molecules Comparison: 205
A12.2.1 ^{1}H NMR of 2,5-dimethylpyrazine-1,4-N-oxide (C1) 205
A12.2.2 ^{1}H NMR of 2,5-di(acetoxymethyl)pyrazine (C2) 206
A12.2.3 ^{1}H NMR of 2,5-di(hydroxymethyl)pyrazine (C3) 206
A12.2.4 ^{1}H NMR of 2,5-di(chloromethyl)pyrazine (C4) 207
A12.2.5 ^{1}H NMR of 2,5-bis(phthalamidemethyl)pyrazine (C5) 207
A12.2.6 ^{13}C NMR of 2,5-bis(phthalamidemethyl)pyrazine (C5) 208

A12.2.7 HMQC of 2,5-bis(phthalamidemethyl)pyrazine (C5) 208

A12.2.8 AT-FIR of 2,5-bis(phthalamidemethyl)pyrazine (C5) 209

A12.2.9 ^{1}H NMR of 2,5-di(azidomethyl)pyrazine (D1) 209

A12.3.0 Characterisation of (L3) and (L4) 210
A12.3.1 ^{1}H NMR of (L3) 210
A12.3.2 COSY of (L3) 210
A12.3.3 HMQC of (L3) 211
A12.3.4 ^{1}H NMR of (D3) 211
A12.3.5 ^{1}H NMR of (L4) 212
A12.5.0 IR Spectra of (L5) Complexations 220
A12.5.0 Table of IR Spectra data of L5 Complexations 220

A12.5.01 (L5) IR Spectra 221

A12.5.02 (5A1) IR Spectra 222

A12.5.03 (5B1) IR Spectra 222

A12.5.03 (5C1) IR Spectra 223

A12.5.04 (5D1) IR Spectra 223

A12.5.05 (5F1) IR Spectra 224

A12.5.06 (5A3) IR Spectra 224

A12.5.07 (5B2) IR Spectra 225

A12.5.08 (5C3) IR Spectra 225

A12.5.09 (5E2) IR Spectra 226

A12.5.10 (5F2) IR Spectra 226

General Experimental Methods

G.1 General Procedures

All starting materials purchased from commercial sources were used without purification unless stated otherwise. Analytical grade solvents were used as purchased unless stated otherwise. Dry MeOH, was stored over 3 Å sieves for a week before use.

All reactions were carried out in acetone washed, oven dried glassware under ambient conditions, unless stated otherwise. Glassware utilised in crystallisation attempts were either used straight from purchase, or washed with deionsied H_2O, soaked in KOH/IPA base bath, rinsed with H_2O and acetone, and air dried. Column chromatography and silica plugs performed, utilised silica gel (grade 60, mesh size 230-400, Scharlau) in a slurry of the eluent. Celite 545 was used from Serva. Drying tubes used calcium chloride, in a fused granular size of about a 8-16 mesh.

All new organic compounds have been characterized by NMR, ESI-MS, and ATR-FTIR. New 3*d* complexes have been characterized by a combination of X-ray, IR, UV-Vis, ESI-MS and conductivity measurements.

^{1}H and ^{13}C NMR Spectra were recorded on Bruker-400 and Bruker-500 Avance instruments, (solutions in DMSO-d_6, $CDCl_3$, or D_2O at RT) with the ^{1}H shift of the solvents being used as internal standards. ESI-MS spectra were collected on a Dionex Ultimate 3000 and run in positive mode, ATR-FTIR spectra were collected on a Nicolett 5700 FT-IR; UV-Vis spectroscopy was performed on a Shimadzu UV-3101PC Spectrophotometer. Conductivity measurements were run on a Philips PW9509 conductivity meter. The following settings were imposed on the conductivity meter: frequency (Hz) = 2,000, MTC depression, cell constant = 3, coefficient % ($°C^{-1}$) = 2.50, temperature (°C) = 20.0. Samples were dissolved in A.R grade MeOH. κ_s values were recorded with A.R grade dry MeOH prior to analysis of the sample.

The Microwave synthesis performed, used a CEM Discovery Monomode microwave synthesizer. Ozonolysis was performed using a CD10/AD Corona Discharge Ozone Generator.

The X-ray data for the ligands and complexes were collected at 100K, unless otherwise stated, on a Bruker D8 Venture diffractometer equipped with a IμS Diamond, microfocus X-ray source. Crystals were mounted on Mitigen loops using Fombin (R), and transferred into the cold gas stream of the detector. Data was collected and processed using APEX3[139]. The structures were solved by SHELXT[140] and refined using SHELXL [141] in Olex2.[142]

For all complexes, non-hydrogen atoms were refined anisotropically; hydrogen atoms were calculated to their ideal positions unless stated otherwise, and refined by using a rising model with fixed isotropic U_{iso} values. The crystallographic data are summarised in Apx11.0.

Appendix 1.0: Method and Characterisation of L1, L1b and L2

A1.0: Preparing the pyrazine ketone: (B1)

A1.1: 2,5- bis((E)-styryl)pyrazine: (A2)

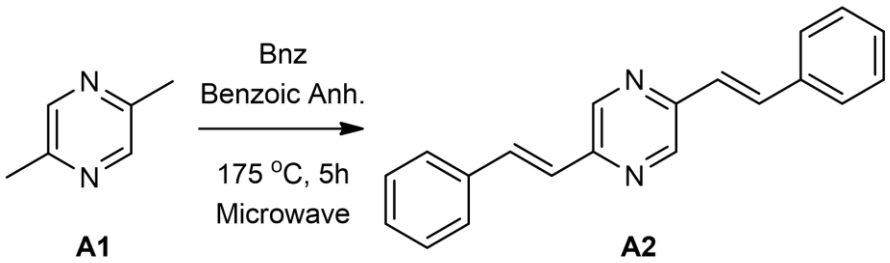

Scheme A1.1: Schematic of synthesis of (**A2**)

Method from Brown 2018. [20]

Benzoic anhydride (4.97 g, 22.0 mmol, 2.4 eq) was dissolved in benzaldehyde (4.18 g, 4.00 mL, 39.4 mmol, 4.3 eq) and 2,5-Dimethylpyrazine (0.99 g, 9.15 mmol, 1.0 eq) in a 35 mL microwave tube, and was stirred until all benzoic anhydride had dissolved. Argon was bubbled through the mixture for two minutes, then sealed with the microwave tube lid. The yellow solution was maintained at 175 °C for 5 hrs in the microwave, with high stirring and no set pressure. The resulting dark brown solid was cooled to RT. The crude product was suspended in ice cold EtOH (10 mL), filtered, and washed with ice cold EtOH (10 x 10 mL). A yellow crystalline solid was isolated (1.76 g, 6.19 mmol, 67.6 %). The product obtained was sufficiently pure to proceed to the following reaction; therefore, no further purification was performed.

^{1}H NMR (400 MHz, $CDCl_3$): δ = δ 8.60 (2H, s, pz), 7.74 (2H, d, J = 16 Hz, CH, 7.63 - 7.59 (4H, m, ArH), 7.43 – 7.31 (6H, m, ArH), 7.19 (2H, d, J = 16Hz, CH). **– Spectra A12.1.1**

A1.2 Synthesis of 2,5-diformyl pyrazine (B1)

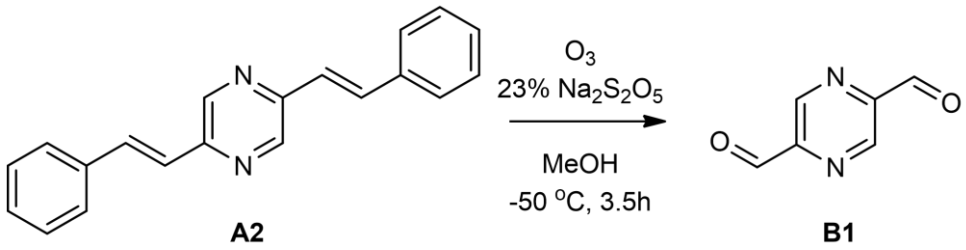

Scheme A1.2: Ozonolysis of (**A2**) to (**B1**).

Method from Brown 2018. [20]

2,5-Distyrylpyrazine (1.00 g, 3.5 mmol, 1.0 eq) was suspended in MeOH (200 mL) and cooled to -50 °C, using a diethylene glycol diethyl ether – dry ice bath. The temperature was maintained while ozone was bubbled through the mixture until the solution presented a pale blue colour of dissolved ozone (3.5 hrs). Excess ozone was displaced by bubbling nitrogen through the solution until it became pale yellow. A solution of 23 % sodium meta-bisulfate in H_2O (12 mL) was added dropwise. The mixture was warmed to room temperature whilst still under an argon atmosphere. The mixture was filtered and washed with MeOH (3 x 30 mL). The yellow filtrate was concentrated under reduced pressure at rt until an oily residue remained. Brine (45 mL) was added to the yellow oil and extracted with Et_2O (3 x 150 mL) to remove the benzaldehyde by-product and the remaining MeOH. The aqueous layer was then extracted with $CHCl_3$ (4 x 30 mL). The organic extracts were combined, dried ($MgSO_4$) and evaporated under reduced pressure at rt, yielding pyrazine-2,5-dicarbaldehyde (**A1**) as a yellow/brown solid (0.24 g, 1.7 mmol, 49.0 %). No further purification was necessary.

^{1}H NMR (400 MHz, $CDCl_3$): δ = 10.24 (2H, s, CHO), δ 9.31 (2H, s, pz). Data is comparable to that of literature. – **Spectra A12.1.2**

A1.3 Synthesis of endo-imine ligand ($L1^{endo}$)

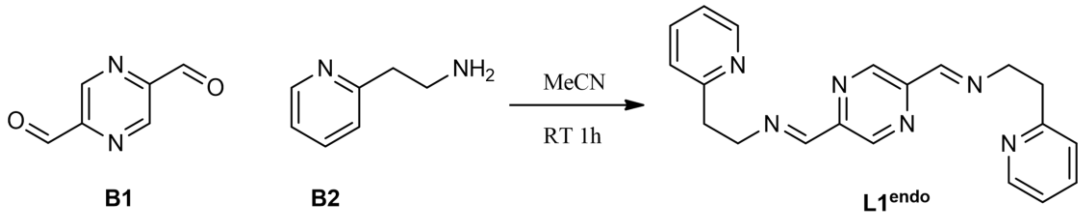

Scheme A1.2: Schiff base condensation to **$L1^{endo}$**

Method from Brown [20]

2-(2-aminoethyl)pyridine (1.02 g, 8.28 mmol, 2.3 eq) was added to a stirred solution of pyrazine-2,5-dicarbaldehyde (485.5 mg, 3.57 mmol, 1.0 eq) in MeCN (10 mL) at rt, and stirred for 30 minutes. The mixture was then left to stand for 3 hours at -5 °C. The precipitated solid was filtered and washed with ice cold CH_3CN affording **L3** as white crystalline solid (260 mg, 21.4%).

δH (500 MHz; $CDCl_3$; solvent) 9.14 (2 H, s, imH), 8.55 (2 H, d, J = 4.10 Hz, pyH), 8.35 (2 H, t, J = 1.27 Hz, pzH), 7.58 (2 H, td, J = 1.57, 7.6 Hz, pyH), 7.18 (2 H, d, J = 7.87 Hz, pyH), 7.12 (2 H, qd, J = , pyH), 4.13 (4 H, td, J = 1.26, 7.26 Hz, CH_2), 3.24 (4 H, t, J = 7.1 Hz, CH_2). δC (125.7 MHz; $CDCl_3$; solvent) 160.37 (pzH), 159.47 (pz), 149.6 (pyN), 149.53 (pyCN), 142.69 (CHN), 136.43 (py), 123.81 (py), 121.58 (py), 61.39 (CH_2N), 39.3 (CH_2py). m/z 345 (M^+, 100%). **– Spectra A12.13**

A1.4 SXRD Characterisation of (L1b)

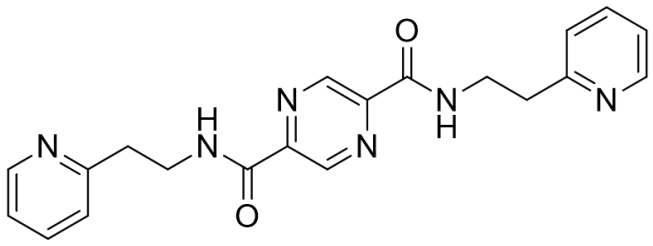

Scheme A1.4 **L1b** Ligand isolated from crystal growth.

In a (1:1) ratio, the ligand **L1^{endo}** and pink $Mn(ClO_4)_2.6H_2O$, dissolved in EtOH, and stirred at RT for two hours. The reaction solution changed to a pale brown colour. The product was precipitated out by vapour diffusion of Et_2O into the reaction solution.

After a period of two and a half months, the **L1^{endo}** ligand crystalised out as a large, off-white needle shaped crystal structure. The crystal was of a high enough quality for X-ray crystallography.

Crystal Data for $C_{20}H_{22}Cl_2N_6O_{10}$ (M =577.33 g/mol): triclinic, space group $P\bar{1}$ (no. 2), a =5.4780(4) Å, b =8.0950(6) Å, c =13.4428(11) Å, α =97.598(3)°, β =93.434(3) °, γ = 101.508(3)°, V = 576.71(8) Å^3, Z = 1, T = 100.0 K, μ(CuKα) = 3.185 mm^{-1}, *Dcalc* = 1.662 g/cm^3, 8144 reflections measured (6.66° ≤ 2Θ ≤ 152.144°), 2198 unique (R_{int} = 0.0414, R_{sigma} = 0.0394) which were used in all calculations. The final R_1 was 0.0607 (I > 2σ(I)) and wR_2 was 0.1755 (all data).

A1.5 Synthesis of novel endo-imine ligand (L2)

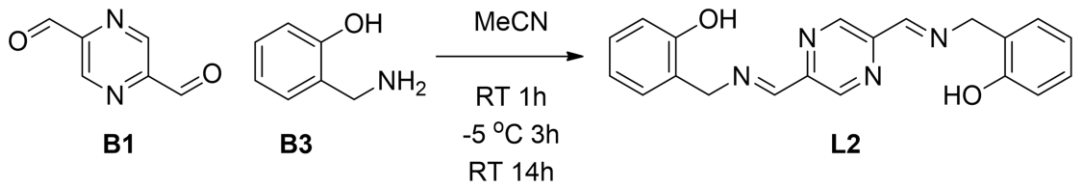

Scheme A1.5: Schiff base condensation to **L1^{endo}**

Adapted from Brown [20]

A solution of 2-aminomethyl phenol (39.6 mg, 0.32 mmol, 2.1 equiv.) was added to a stirred solution of pyrazine-2,5-dicarbaldehyde (20.8 mg, 0.15 mmol, 1.0 equiv.) in MeCN (3 mL) at RT, for 30 minutes. The mixture was then left to stand for 2 hours at -5 °C., then stood for 14 h at RT. The product precipitated was a peach coloured solid, which was filtered and washed with ice cold EtOH, affording a peach powder, **L2** (49.7 mg, 0.14 mmol, 94.8 %).

δ ^{1}H NMR (500 MHz, DMSO): 9.55 (s br, 1H) 9.19 (s 1H), 8.49 (s, 1H) 7.22 (d, 1H, J = 7.65 Hz), 7.12 (t, 1H, J = 7.35 Hz), 6.85 (d, 1H, J = 8.00 Hz), 6.80 (t, 1H, J = 7.35 Hz), 4.85 (s, 2H) δ ^{13}C NMR (125.7 MHz; DMSO): 160.89 (pzC), 155.75 (phC), 149.78 (imC), 142.25 (pzC), 130.37 (ArC), 128.82 (ArC), 124.78 (ArC), 119.49 (ArC), 115.53 (ArC), 59.33 (MeC) m/z: [M+H] 347.04 (100), 347.82 (20), 349.35 (2); [M Na] 368.92 (100), 369.73 (20) [2M Na] 715.05 (100), 716.02 (40), 717.02 (10) ν_{max}/cm^{-1} : 3225.35 (m)(ν Phenol); 2979.36 (w) (ν Pz); 1605.55 (m) (ν Imine), 1580.37 (m) (ν Aromatic), 1343.08 (m) (-OH), 1261.72 (s) (ν CN Ar), 1230.39 (s), 934.25 (s), 906.99 (s), 750.32 (m)(ν C-H bending) MP: 154.5-155.1 °C **– Spectra A12.15-A12.18**

Appendix 2.0: Alternate routes of C4 synthesis

A2.0 Initial attempts at the synthesis of 2,5-dichloromethyl pyrazine

Initially, the short pathway of (**A1**) through (**C4**) to (**C7**) to (**C6**) was investigated. This was because the synthesis of (**C6**) has previously been completed by Eiermann *et al.* 1990[129]; who used Wohl-Ziegler radical chlorination of (**A1**) to produce (**C4**), which was substituted with HMTA to produce (**C7**), which was finally reduced to produce (**C6**).

With this the first reaction, (i) in Apx2.1, was attempted. This would ultimately prove unsuccessful, and so followed other attempts at chlorination reactions to produce (**C4**).

A2.1 Full attempted routes to C6

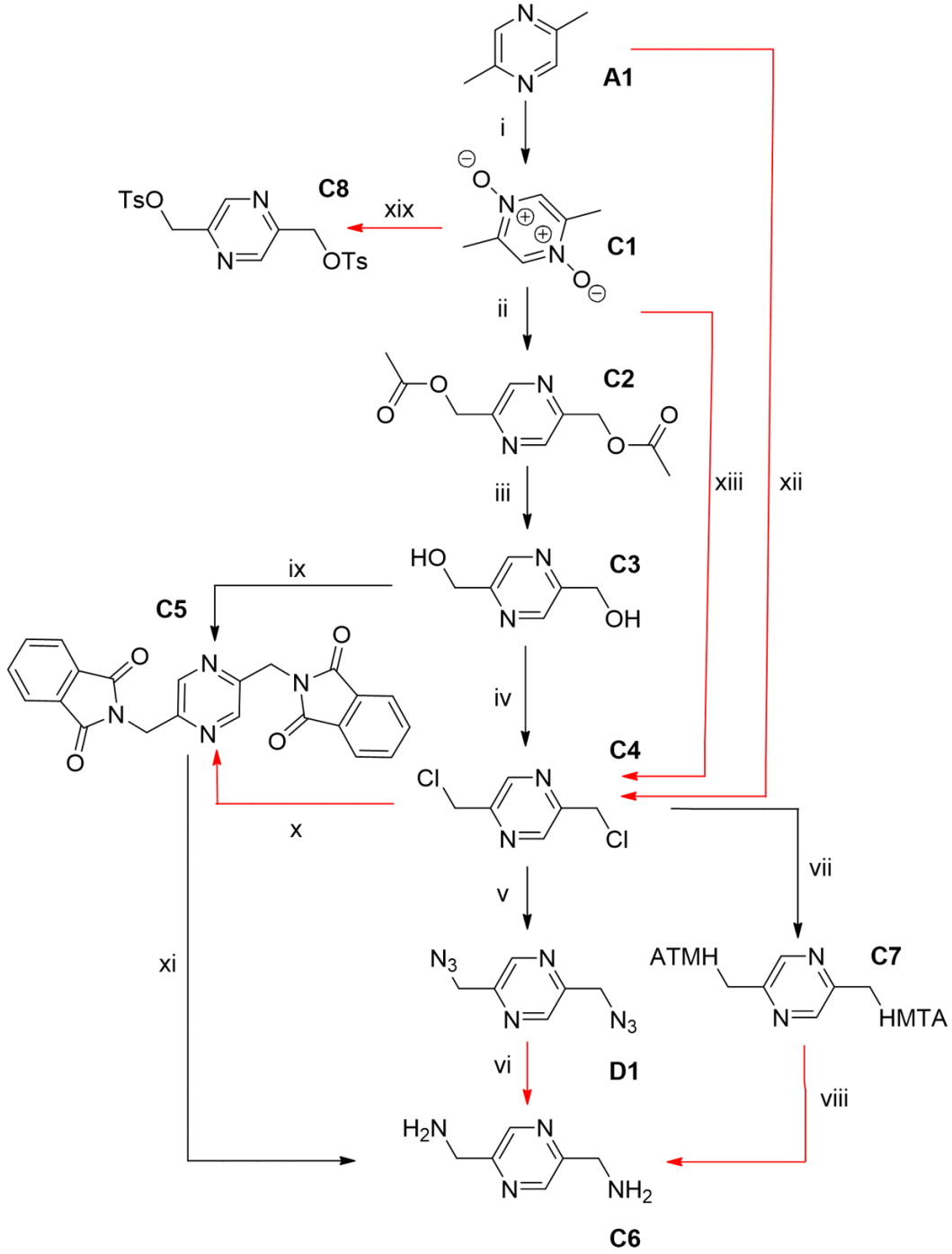

Scheme A2.1: The overall route in the pathway to **C6**. I) m-CPBA, EtOAc, RT, 24h; ii) Acetic Anhydride, 158 ºC 7h, RT 18h; iii) NaOMe, MeOH, RT, 3h; iv) $SOCl_2$, DCM, RT, 18h; v) NaN_3, TBAHS, DCM:H_2O (1:1) RT, 48h; vi) PPh_3, THF/H_2O, RT, 24h; HCl, RT 2h; vii) KI, HMTA, DCM, 65 ºC, 44h; viii) DCM, NaOH ix) Phth, PPh_3, DIAD, THF, 0 ºC, RT, 16h; x) KPhth, DMF, 110 ºC; xi) NH_2NH_2, EtOH, 70 ºC, 16h; xii) NCS, BzO_2, CCl_4, 66 ºC, 24 h; xiii) $POCl_3$, Et_3N, DCE, 85 ºC, 2h; xix) TsCL, Et_3N, THF, 0 ºC, RT, 16h.

Black reaction pathway arrows indicate the successful detection of products; Red reaction pathway arrow indicates an unsuccessful reaction pathway.

A2.2 Wohl Ziegler Radical Chlorination

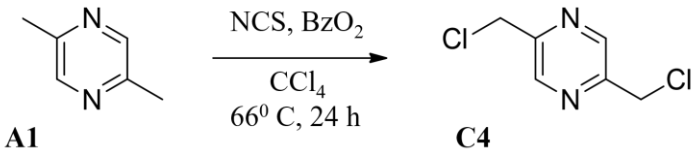

Scheme A2.2: Wohl-Ziegler Chlorination to **C4**: NCS, BzO_2, CCl_4, 66 ºC, 24 h.

Based on; Eiermann *et al.* 1990[129]; and Zhou, et al. 2009. [143]

In this method, two equiv. of N-chlorosuccinimide (NCS) was finely ground with a mortar and pestle, divided and added to boiling CCl_4 (10 ml) in four portions in a 2-necked-rbf, and was stirred until dissolved. Dibenzoyl peroxide (BzO_2), 0.028 equiv. was added to the solution. The BzO_2 was weighed and transferred in small portions using wooden spatulas due to its explosive properties. The solution was put under Ar, and 1 equiv. of **A1** was injected through a septum. The reaction was refluxed at 76ºC for 24 hours, then left to return to RT. Solid NCS product was removed by filtration and washed with CCl_4 (2 x 5ml). A yellow filtrate was collected and concentrated *in vacuo* to give a crude yellow oil product.

MS spectra indicated that, **C4** was present in the sample (m/z): 177.38(100), 179.51(58) [M+H], along with other products, 2-(chloromethyl)-5-methylpyrazine (**C4b**); (m/z) 143.21(100), 145.02(30), [M+H] and 2,5-bis(dichloromethyl)pyrazine (**C4c**), (m/z) 246.26 [M+H]. The crude product was separated into components through silica chromatography (10:1 dichloromethane: ethyl acetate).

The portion that was able to be cleanly isolated resulted in a single methyl chlorinated product, 2-(chloromethyl)-5-methylpyrazine. ^{1}HNMR (400 MHz, $CDCl_3$): δ = 8.66, (s 1H), 8.54, (s 1H), 5.74, (s, 3H) 4.82, (s, 2H). (m/z): 143.38(100), 145.38(30) [M+H].

This Wohl-Zielger chlorination concluded with **C4** unable to be isolated. While, (**C4b**) was isolated, it could not be further selectively chlorinated without over-chlorination, due to the nature of the mechanism, Scheme A2.2.2, in which radical formation can occur on each methyl arm up to three times. Another disadvantage of

this reaction, and similar reactions found in literature, was the limited supply of required CCl_4, which had recently become a restricted substance nationally. Previous work within the lab group had also had difficulty in isolating **C4** through this process. For these reasons this reaction was ultimately shelved.

A2.2.2 Synthesis of C4 – Wohl-Ziegler Mechanism

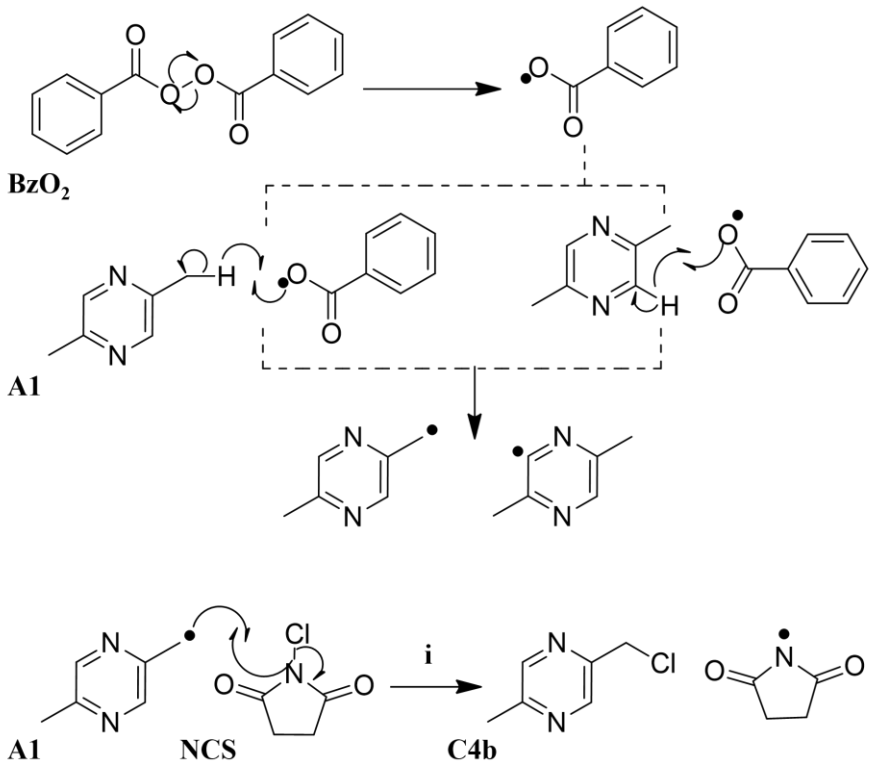

Scheme A2.22 Wohl-Ziegler Chlorination Mechanism [125]

A2.2.3 Method Synthesis of 2-chloromethyl-5-methyl pyrazine C4b – Wohl-Ziegler (i)

N-chlorosuccinimide (NCS), (2.511 g, 18.8 mmol, 2 equiv.) was finely ground with a mortar and pestle, divided and added to boiling CCl_4 (10 ml) in four equal portions, and was stirred until dissolved. Dibenzoyl peroxide (BzO_2), 0.0631 g (0.26 mmol, 0.028 equiv.) was added to the solution.

Caution Note: The BzO_2 was weighed and transferred in small portions using wooden spatulas due to its explosive properties.

The reaction was degassed using Argon and **A1** (1.01 ml, 9.2 mmol, 1 equiv.) was injected through a septum. The reaction was refluxed at 76ºC for 24 hours, then left to return to RT. The NCS waste product was removed by filtration and washed CCl_4. The yellow filtrate was collected and concentrated *in vacuo* to give a crude yellow oil product 1.584 g of

Mass spec of the crude product indicated that the desired 2,5-bis(chloromethyl)pyrazine (m/z): 177.38(100), 179.51(58) [M+H] was present, along with; 2-(chloromethyl)-5-methylpyrazine (**C4b**) (m/z): 143.21(100), 145.02(30) [M+H] and trace 2,5-bis(dichloromethyl)pyrazine (m/z): 246.26 [M+H].

The crude product was separated into components through silica chromatography (10:1 dichloromethane: ethyl acetate). The largest portion that was able to be isolated resulted in a single methyl chlorinated product, 2-(chloromethyl)-5-methylpyrazine, **C4b** with an Rf = 0.3, in yield of (0.28 g 22%).

^{1}HNMR (400 MHz, $CDCl_3$): δ = 8.66, (s 1H), 8.54, (s 1H), 5.74, (s, 3H) 4.82, (s, 2H) Mass (m/z): [M+H]: 143.38(100), 145.38(30) Agrees with the literature for **C4b.**

A2.3 $POCl_3$ Chlorination

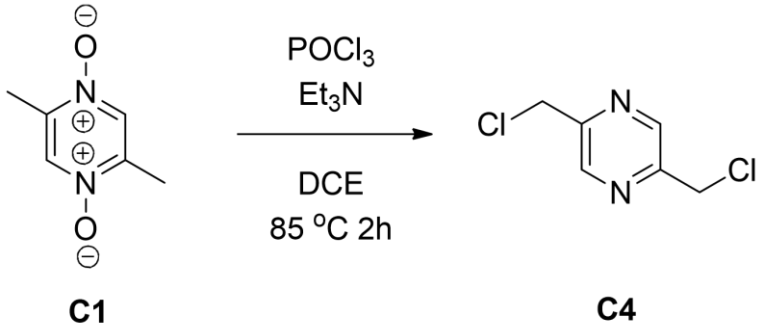

Scheme A2.3 Proposed $POCl_3$ chlorination reaction

Another attempt at the synthesis of **C4**, was through a chlorination of **C1**, the N-oxide species. This methodology was based on the work of Kimera, and He *et al.* [144] This was investigated due to the successful formation of a variety of N-oxide pyrazine and tetrazole species allowing for ortho-methyl groups to be chlorinated with $POCl_3$. It was assumed that this method could be adapted for pyrazines, and the chlorination of the two sides could be accomplished simultaneously, shown in the mechanism in A2.32.

To one equiv. of **C1** dissolved in 10 mL of DCM, two equiv. of $POCl_3$ and 1.8 equiv. of NEt_3 were simultaneously added dropwise at RT. The reaction was stirred at 85°C for a range of tested time periods, from 0.5 to 8 h. The reaction was poured over ice and neutralised with saturated $NaHCO_3$ solution. Product was extracted with $CHCl_3$, and the organic layers was concentrated *in vacuo*.

As well as changes in time under reflux; the mol equivalence of $POCl_3$ was varied; and, DCM and DCE solvents were tested. All variations, resulted in the singularly chlorinated, **C4b**.

It was found that Matsuura *et al.*[145], had previously investigated the chlorination of pyrazine N-oxides, and found that, while one of the N-oxides was used in a chlorination, the second N-oxide would be simultaneously reduced. Thus, preventing the **A1** from being chlorinated on both sides simultaneously.

The use of this pathway for **C4**, may not be possible, but more experimentation could be performed to determine if a sequential chlorination--N-oxidation--chlorination pathway could be performed.

^{1}HNMR (400 MHz, $CDCl_3$): δ = 8.66, (s 1H), 8.54, (s 1H), 5.74, (s, 3H) 4.82, (s, 2H). (m/z): 143.38(100), 145.38(30) [M+H]. The 1HNMR and Mass Spec data agreed with that obtained using the NCS method.

At this time, investigations into **C3** were proving more successful. Focus was shifted to this alternate route, and the $POCl_3$ chlorination was put aside, but this is a route that could be open for further investigation within organic synthesis.

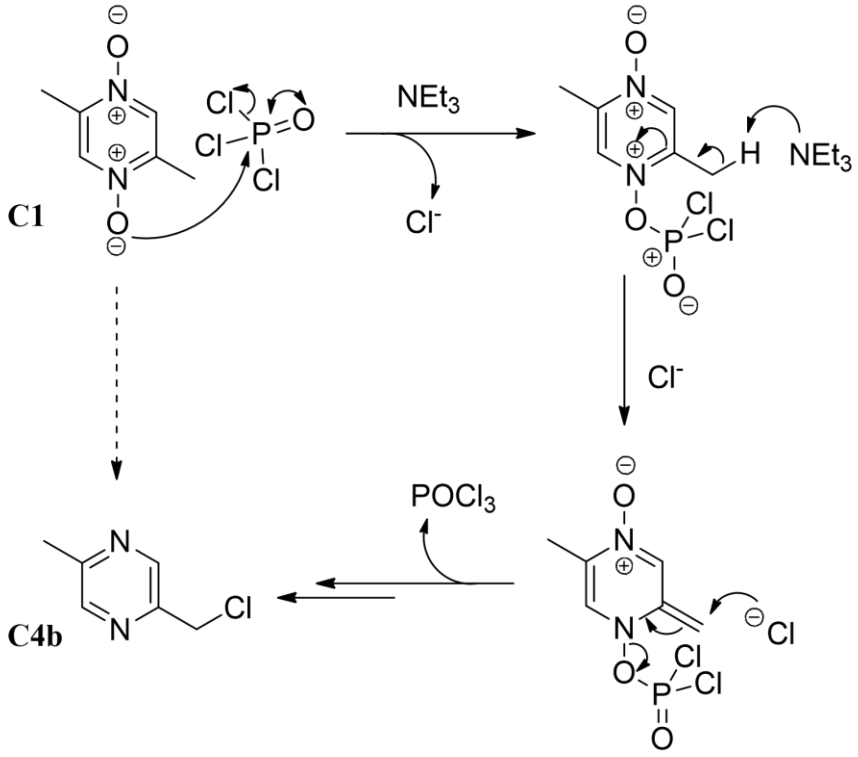

Scheme A2.32 Proposed mechanism for $POCl_3$ chlorination, with the second *N*-oxide reducing at an unknow point.

A2.4 Boekelheide rearrangement of TOSYL – (C6)

Another attempt at chlorination from the N-oxide, **C1**, was attempted. In this case, a method was adapted from Wang, *et al.*[146] to add a toluenesulfonyl, TsO, group to the methyl arms of the pyridine, through a boekelheide rearrangement and Claisen reduction Ideally, the success of this reaction should have made it possible to bypass the lower yield (20-30%) in **C2** synthesis, and go on to reduce to **C4**.

The reaction mechanism for this Boekelheide addition proposed that of the products 2,5-dichloromethylpyrazine and 2,5-ditosylmethylpyrazine could be possible.[147] Both products can be directly used to form the azide group, but would require purification steps. If the TOSYL had an increased equivalency, the TOSYL product may become more favourable. These are other aspects to consider when planning the next immediate future steps.

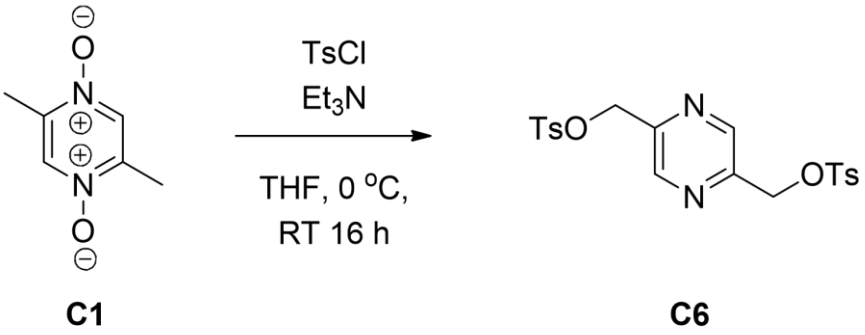

Scheme A2.32 The Proposed Reaction for 2,5- bis(tosylmethyl)pyrazine synthesis.

C1 (0.2018 g, 1.44 mmol, 1 equiv.), dissolved in THF (5.75 mL) was stirred with Et_3N (2.99 ml, 5 equiv.). The solution was cooled down at 0 ° C, toluenesulfonyl chloride (0.831 g, 4.36 mmol, 3 equiv.) was slowly added. The solution was raised to RT and stirred over 16 h. The precipitate (expected to be Et_3NHCl) was removed via a thin layer Celite filtration, and was washed with EtOAc (3 x 30 ml). The crude mixture was concentrated *in vacuo*, to a crude yellow oil, of 0.2 g. There was no indication that the desired product was in this crude material.

Appendix 3.0: Alternate routes of C6 synthesis

A3.1 2,5-bis(HMTA-methyl)pyrazine synthesis (C6)

An alternate route to **C6** was attempted via **C7**, where the pyrazine had a HMTA (hexamethyl tetraamine) moiety. The isolation of **C7** could then be reduced to the **E1** amine. Methods were adapted from Wietzke, *et al.* [148], Zhou, *et al*. [143] and Hoffman.

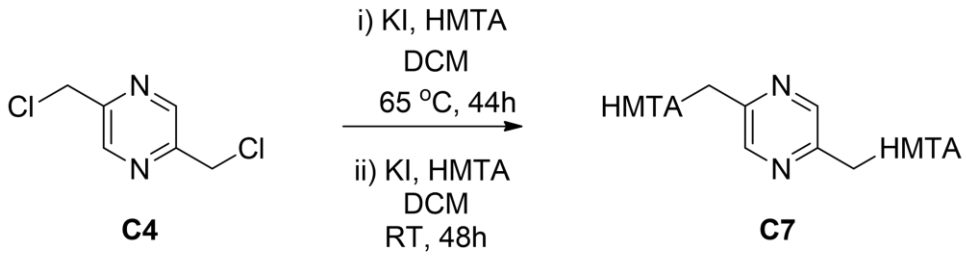

Scheme A3.1 Final Reaction for Cl to HMTA Substitution

Route A: Wietzke, *et al.*[148]

Wietzke, *et al.* performed a substitution of Cl with HMTA on a 2-chloromethylpyrazine. Wietzke, *et al.'s* method was adapted so that the relative equivalents would be enough for two substitutions. The 3 h reflux, of 2-chloromethylpyrazine (1 equiv.) and hexamethyl tetraamine (HMTA) (2.2 equiv.) in DCM under stirring and was then left to stand overnight. These reactions should have resulted in the product salt visibly precipitating out of the reaction solution, but this did not occur.

Route B: Zhou, *et al.*[143]

Zhou, et al's patent included the addition of 0.1 equiv. of KI, with the 2.0 equiv. HMTA, which they used to act as a catalyst. Zhou, et al. also had an increased length of reflux. These two factors were incorporated separately into the reaction design, but neither alteration resulted in the product precipitation.

Trace amounts of the 2,5- bis(hexamethyl-tetraamine)pyrazine chlorine salt, was detected. Mass (m/z): [M+Cl]: 421.26 (100), 422.41 (20), 423.19 (30), 423.28 (28). Showing the predicted peak distribution for the 2,5-bis(hexamethyl-tetraamine)pyrazine chlorine salt.

From this, another option that was tried, was to assume that the product may be forming at some points in the reaction, and so to move on to the amine synthesis steps without isolating the 2,5- bis(hexamethyl-tetraamine)pyrazine. Initially, 0.1 equiv. of KI, with the 2.5 equiv. HMTA were added to a dropwise addition to 1.0 equiv. 2,6- bis(chromemethyl)pyridine in $CHCl_3$ at reflux, then reflux was carried out at an additional 44 h. Then this was cooled to RT over 6 h, and concentrated *in vacuo*. The residue was dissolved in EtOH and HCl (3 equiv.) was added, with the reaction heating on a boiling plate for 4 hours. This did not give any indication of the desired product.

Wietzke, *et al.*[148] and Zhou, *et al.*[143] both used very similar methods to try and achieve this; the RT reaction solution was concentrated *in vacuo*, and then resolved in EtOH, with 5 equiv. of HCl from 35% added. This mixture was brought to the boil in an open beaker, for 5 hours, with the solvent layer being maintained with the addition of EtOH. The results were evaporated to dryness. The residue was dissolved in Water:DCM (1:2) and 5 M NaOH was added until the pH was basic. An extraction of the product was attempted with more DCM. The organic phases were separated and dried with Na_2SO_4. This resulted in a small amount of beige solid and some dark oil. Neither gave any indication of the 2,5- bis(aminomethyl)pyrazine product by ^{1}HNMR.

Even with different attempts, only trace amounts of desired product was identified in the mass spectrum, and only from the very lengthy versions of the reaction attempts, but was not able to be isolated. The hexamethyl tetraamine (HMTA), route was attempted prior to the azido route, due to the (carbon:nitrogen) ratios of the intermediates. 2,5- bis(hexamethyl-tetraamine) pyrazine, has less explosive potential than the 2,5- bis(azidomethyl)pyrazine, and so was investigated first as the safer option, for when synthesis would be completed in larger quantities. Once it was established that this product could not be achieved, by this route investigation into the azide synthesis began.

In the samples produced by this altered 44h reflux route, that were then left again to stir at RT for periods of 24h and 48h, there was an increase in the trace amounts of the desired product detected by mass spectrometry. However, these trace amounts could not be isolated, and after 5-8 further days sitting at RT the trace amounts had disappeared from the mass spectra as well.

Appendix 4.0: Methods from Section 6.0

A4.1: *N*-oxidation: 2,5-dimethylpyrazine-1,4-N-oxide (C1)

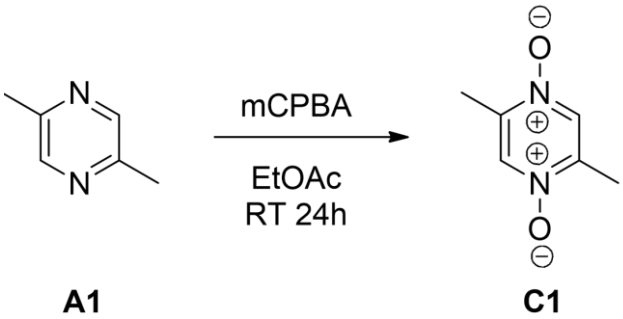

Scheme A4.1 Synthesis reaction for 2,5-dimethylpyrazine-1,4-N-oxide

Method from Das *et al.*[123]

A solution of m-CPBA 77% (39.955 g, 178.28 mmol 3 equiv.) in ethyl acetate (EtOAc) (66 ml) was washed with brine (66 ml). The organic layer was separated, dried with $MgSO_4$ and filtered. To the filtrate was added 2,5-dimethylpyrazine (6.5 ml, 59.428 mmol, 1 equiv.). The reaction was stirred for 24 hours at RT. White precipitate was collected in a glass sintered frit, and washed with EtOAc (3x15ml), to remove any m-CPBA waste products resulting in a yellow filtrate. The white solid **C1** product, was dried to give a mass of 7.266 g, (51.80 mmol) in an 87.3 % yield.

^{1}HNMR (400 MHz, D_2O): δ = 8.48, (s 1H), 2.43, (s, 3H). Mass (m/z): [M+H]: 141.19 (100), 142.16 (6) These results agreed with literature values.[123] **Spectra – A12.2.1**

A4.2 Synthesis of 2,5-bis(acetoxymethyl)pyrazine (C2)

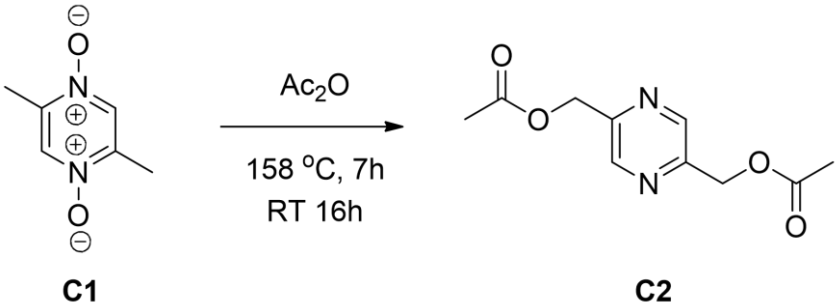

Scheme A4.2: Reaction synthesis of 2,5-bis(acetixymethyl)pyrazine

Adapted from Das *et al.*[123]

A stirred suspension of **C1** (5.001 g, 35.7 mmol, 1 equiv.) in acetic anhydride (25 ml, 260 mmol, 7.4 equiv.) was heated at 158°C for 7 hours, the reduced to RT and stirred for a further 16 hours. Acetic anhydride was removed under reduced pressure to give a crude viscous, black/brown liquid. Diethyl ether (125 ml) was added to the crude product, as an extraction solvent, and stirred vigorously for 2 hours, then sat undisturbed for 3 hours at RT. The solution was then filtered through a 4 mm layer of Celite, and a yellow filtrate collected. The remaining black residue and was recollected and stirred with Et_2O (100 ml) for 0.3 hours, followed by filtering through Celite again, process was repeated until minimal colour was extracted with Et_2O. The combined filtrate was concentrated under reduced pressure.

Two methods of purification were used, depending on the purity of the crude product. If the crude product was able to solidify as a dark brown crystalized solid, it was washed with a 3:7 EtOAc:*n*-Hexane, and the remaining dark orange product was hot recrystallized in the some ratio eluent, to give a light yellow, crystalline solid, of **C2**, in a yield of 28.2%.

If the crude produce would not solidify when left to air dry, it was run through a silica plug. An initial wash of (1:4) EtOAc:Hexane removed the first fraction (rf = 0.65), then a gradient of increased EtOAc to 4:6 was used to collect the product (rf = 0.15). The yellow/orange filtrate was concentrated under reduced vacuum to obtain an orange crystallised solid, which was then hot recrystallised as described previous.

^{1}H NMR (400 MHz, $CDCl_3$): δ = 8.61, (s, 2H), 5.25 (s, 2H), 2.15 (s, 3H). Mass (m/z): [M+H]: 225.13 (100), 226.10 (9) [M, Na]: 247.16 (100), 248.16 (11). These results agreed with literature values.[123] **Spectra – A12.2.2**

A4.3 2,5-bis(hydroxymethyl)pyrazine (C3)

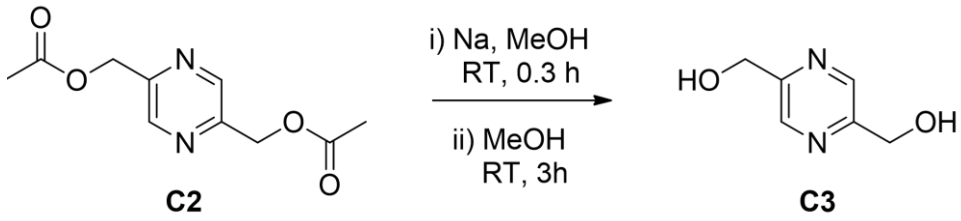

Scheme A4.3: Reaction of 2,5-bis(acetoxymethyl)pyrazine producing 2,5-bis(hydroxymethyl)pyrazine.

Preparation of NaOMe. Method from Armarego, W. L. F.[126]

Dry MeOH (3 ml) was added to solid Na (0.3236 g, 14.1 mmol 2 equiv.), and stirred at RT under dry conditions for 0.25 hours, until no more solid remained.

Adapted from Das, *et al.*[123]

The drying tube was removed and a solution of **C2** (1.5781 g, 7.04 mmol, 1 equiv.) in dry MeOH (35 ml) was added under argon and the reaction stirred for 3 hours at RT. The reaction was quenched by adding solid NH_4Cl (0.05 g). The solvent reduced *in vacuo*, resulting in a beige-white solid, later identified as the 2,5-bis(hydroxymethyl)pyrazine product (0.9152g, in a 92.8%). This **C3** product, did not require further purification.

^{1}H NMR (400 MHz, $CDCl_3$): δ = 8.57, (s 1H, Ar-H), 4.84, (s, 2H, CH_2), 2.98 (br, 1H, -OH). Mass (*m*/*z*): [M+H] 141.17 (100), 142.11 (7) These results agreed with literature values.[123]
Spectra – A12.2.3

A4.4 Synthesis of 2,5-bis(chloromethyl)pyrazine (C4)

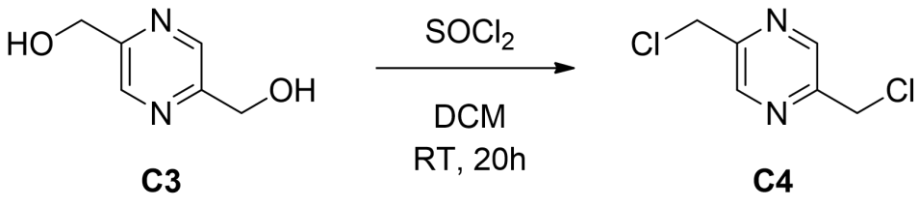

Scheme A4.4: Chlorination Reaction of 2,5-bis(hydroxymethyl)pyrazine to 2,5-bis(chloromethyl)pyrazine

Adapted from; Penteado, *et al.*[127] and Zhang, *et al.*[128]

In a 25 mL round-bottomed flask containing a solution of 2,5-bis(hydroxymethyl)pyrazine (0.0703 g; 0.5016 mmol, 1.0 equiv.) in dry dichloromethane (DCM) (4 mL) at 0 °C (ice bath) was added dropwise $SOCl_2$ (0.17 ml, 2.25 mmol, 4.5 equiv.) in dry DCM (2 mL). After the addition, the system was warmed to RT and stirred for an additional 18 h. The solution was then poured over ice and neutralised with saturated $NaHCO_3$ solution (2 ml). The product was extracted with $CHCl_3$, and the orange filtrate was dried with $MgSO_4$. Solvents were reduced *in vacuo*, to give the desired 2,5-bis(chloromethyl)pyrazine product as a brown oil, 0.355 g (90.1%). Product was pure enough to continue without further purification.

^{1}H NMR (400 MHz, $CDCl_3$): δ = 8.71, (s, 1H), 4.71 (s, 2H). Mass (m/z): [M+H]: 177.38(100), 179.51(58) Agreeable with literature values. [129] **Spectra – A12.2.4**

A4.5 Synthesis of 2,5-bis(phthalamidemethyl)pyrazine C5

A4.5.1 C5 from C4

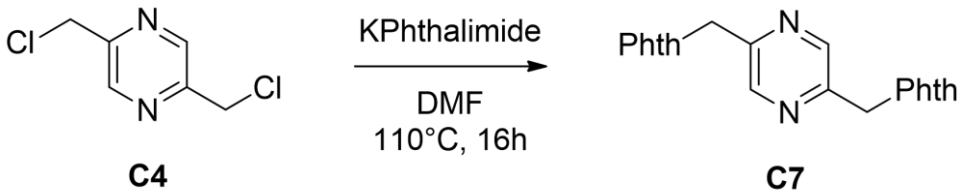

C4 **C7**

Scheme A4.5: The initial attempt at synthesising **C5** from **C4**

The method for cleaning the potassium phthalimide was obtained from Armarego, W. L. F.[126] The initial attempt at synthesising **C5** from **C4**, was adapted from the method from Liu *et al.* *135*

To a solution of **C4** (0.1098 g, 0.62 mmol, 1 equiv.) in DMF (4 mL) was added potassium phthalimide (0.2426 g, 1.31 mmol, 2.1 equiv.). The reaction mixture was heated for 16 h at 110 °C, allowed to cool to ambient temperature and concentrated *in vacuo*.

The residue was partitioned between DCM (5 mL) and H_2O (2 mL). The organic phase was washed with water (3 mL) and brine (2 x 2 mL), dried with $MgSO_4$, filtered and concentrated *in vacuo*, to give a crude beige solid (0.2912 g). The residue was washed in a mixture of ethyl acetate and hexane (1:1) (5 ml) to give a light brown solid (0.2131 g).

The 1HNMR analysis of the isolated product did not indicate any success. The potassium phthalimide equivalence was raised to 3 and 4, but the reaction still did not work.

A4.5.1 Mitsunobu reaction of C3 to C5

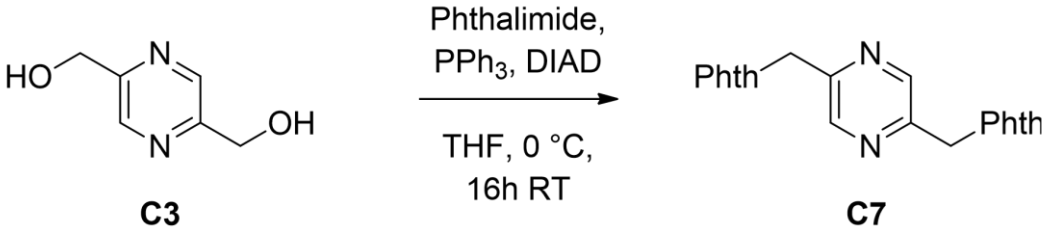

Scheme A4.5: The mitsunobu reaction of **C3** to **C5**.

This mitsunobu reaction of Phth and **C3**, was adapted form Wessel *et al*. [136]

Triphenylphospine (0.7570 g, 2.89 mmol, 2 equiv.) and **C3** (0.200 g, 1.4 mmol, 1 equiv.) were dissolved in THF (12 mL), flushed with argon and chilled to 0 °C. Once cooled, phthalimide (0.4409 g, 3.0 mmol, 2.1 equiv.) was added. DIAD (1.52 ml, 40% in toluene, 3.1 mmol, 2.2 equiv.) was added dropwise. Upon completion of the addition, the reaction was allowed to slowly warm to RT and left to stir overnight.

The solvent was removed by filtration and 5mL of DCM/THF (8 : 1) (5 ml) was added to the residue and stirred for 30 min. This solution was filtered to obtain white powder, which NMR confirmed to be **C7** (0.1029 g) in a 18.1 % yield. The product was used without further purification.

δ ^{1}H NMR (400 MHz, $CDCl_3$): δ = 8.63 (s, 2H), 7.89 (m, 4H), 7.87 (m, 4H), 4.96 (s, 4H). δ ^{13}C NMR (125.7 MHz; DMSO): 168.1, 143.3, 135.0, 123.9, 40.2 m/z: 421.05 [M, Na] 398.1 [M] ν_{max}/cm^{-1} : 3585.01 (s) 3461.59 (m) 3441.39 (m) 3200.53, 1768.80 (m) 1701.24 (s) 1482.48 (w), 1470.56 (w), 1416.94 (m) 1368.28 (s), 1323.63 (m) 1313.09 (m), 1193.43 (m), 1151.91 (w), 1107.15 (m), 1090.43 (m), 1026.81 (m), 956.59 (s), 745.28 (m), 725.30 (s), 710.79 (s). **Spectra – A12.2.5- A12.2.8**

A4.6 Ing-Manske Reaction: C5 – C6

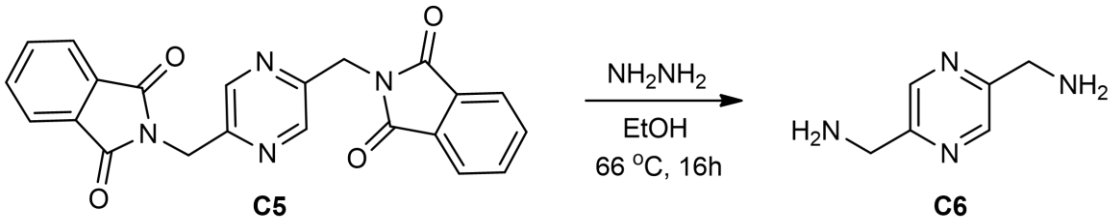

Scheme A4.6: The Ing-Manske reduction of Phth to **C6**, was adapted from Wessel *et al*.[136]

Hydrazine hydrate (0.055 ml, 1.7 mmol, 9.5 equiv.) was added to a solution of **C5** (0.0703 g, 0.18 mmol, 1 equiv.) in 95% ethanol (3 ml) and refluxed overnight upon which a a white solid presipitated.

The solution was filtered and the filtrate was concentrated under reduced pressure. The residue was washed with $CHCl_3$ (10 mL), filtered and concentrated *in vacuo*, and the crude beige powder was collected (5.7 mg, 23.4 % yield).

^{1}H NMR (400 MHz, $CDCl_3$): δ = 8.69 (s, 2H), 4.33 (s, 4H). **Spectra – A12.2.4**

A4.7 2,5-bis(azidomethyl)pyrazine (D1)

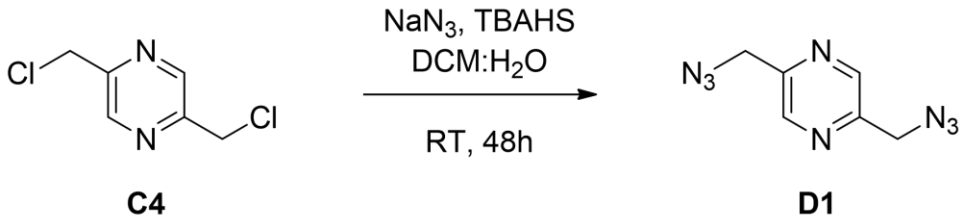

Scheme A4.7: 2,5-bis(azidomethyl)pyrazine Route B reaction.

Adapted from, Amadio *et al.* [132] and Abushanab, *et al.*[131]

To a solution of, NaN_3 (0.0531 g, 0.8 mmol 4.8 equiv.) and tetrabutylammonium hydrogensulfate (TBAHS) (0.0071 g, 0.02 mmol, 0.12 equiv.) in CH_2Cl_2/H_2O (10 mL, 1:1), was added 2,5-bis(Chloromethyl)pyridine (**C4**) (0.0304 g, 0.17 mmol 1.0 equiv.).

The reaction mixture was vigorously stirred at RT for 48 h. The mixture was extracted with DCM (25 mL); the combined organic phases were dried ($MgSO_4$), filtered and the solvent removed by evaporation and 2,5-bis(azidomethyl)pyridine (**D1**) was collected as a yellow oil (54% yield), diluted to 10 ml DCM.

^{1}H NMR (400 MHz, $CDCl_3$): δ = 8.64 (s, 1H), 4.58 (s, 2H). **Spectra – A12.2.9**

A4.7.2 Unsuccessful (D1) reduction to (C6)

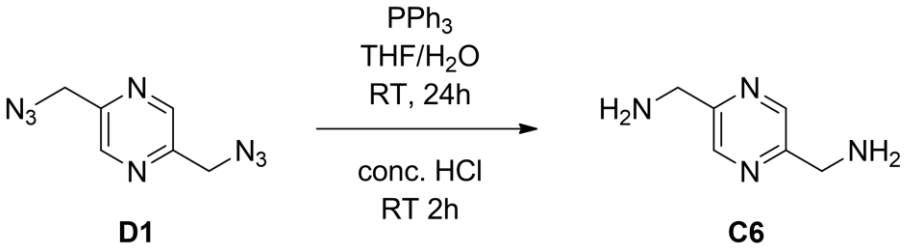

Scheme A4.8. 2,5- bis(azidomethyl)pyrazine Route B reaction.

A number of methods were attempted to convert the azides of **D1** to amine of **C6**. Methods were attempted, using Kwan, *et al.* [133] and Palanichamy, *et al.*[134] who both used PPh_3 and HCl to convert azidomethyls on aromatic rings, to aminomethyls. However, benzenes, not pyrazines were used in these examples.

Different lengths of time, temperature, and concentration of HCl were attempted, but none of these reactions resulted in any indication of **C6**.

Appendix 5.0: Synthesis Methods of (L3) and (L4)

A5.1 Synthesis of L3

Scheme A5.1: Reaction scheme for the synthesis of **L3**

Adapted from, Herzigkeit *et al.*[88] and Brotherton, *et al.*[93]

To a deoxygenated solution of 2,5-bis(Azidomethyl)pyridine (**D1**) (144.9 mg, 0.76 mmol, 1.0 equiv.), in DCM (5ml) and tBuOH (0.5 ml). was added phenylacetylene (**D2**) (23.3, 2.3 mmol 3 equiv.) and an aqueous $Cu(OAc)_2$ solution (0.5M, 0.09 ml). The blue $Cu(OAc)_2$ solution turned green upon addition. The reaction was stirred vigorously at RT for 18 h, after which time a brown-grey precipitate had formed. The reaction was diluted with water (6 mL) and DCM (10 mL), and the organic phase was washed until no more blue copper solution was extracted. The precipitate was collected by filtration, isolating a pure **L3**, as a greyish solid (168.8 mg in a 56.2 % yield). The ligand was used for complexation with no further purification.

^{1}H NMR (500 MHz, DMSO): δ = 8.74 (s, 2H); 8.67 (s, 2H); 7.89 (d, 4H, J = 7.50 Hz); 7.46 (t, 4H, J = 7.28 Hz); 7.34 (t, 2H, J = 7.32 Hz); 5.88 (s, 4H). ^{13}C NMR (126 MHz; DMSO): δ = 150.5; 147.0; 144.0; 131.1; 129.4; 138.3, 122.8; 125.6; 52.8; (m/z): 395.16 (100), 395.63 (24), 396.29 (3) [M+H]; High Res (m/z): 417.1548 [M, Na], *IR:* ν_{max}/cm^{-1}*:* 3127.79 (m br), 1304.05 (m), 3085.53 (m br), 2430.78 (w), 2272.28 (w), 1611.06 (w), 1482.16 (m), 1464.33 (m), 1441.14 (w), 1304.05 (w), 1222.60 (m), 1198.72 (w), 1158.77 (m), 1076.44 (m), 1035.22 (s), 977.05 (w), 763.15 (s), 692.73 (s). **Spectra – A12.3.1- A12.3.3**

The **L3** ligand was also characterised by SXRD, as discussed in Section 3.

Crystal Data for $C_{11}H_9N_4$ (M =197.22 g/mol): monoclinic, space group $P2_1/c$ (no. 14), a = 16.8966(6) Å, b = 5.5208(2) Å, c = 9.9782(4) Å, β = 102.079(2)°, V = 910.19(6) Å^3, Z = 4, T = 100.0 K, μ(CuKα) = 0.741 mm^{-1}, *Dcalc* = 1.439 g/cm^3, 10503 reflections measured (5.348° ≤ 2Θ ≤ 151.674°), 1769 unique (R_{int} = 0.0342, R_{sigma} = 0.0245) which were used in all calculations. The final R_1 was 0.0373 (I > 2σ(I)) and wR_2 was 0.0998 (all data)

A5.1 Synthesis of $[Cu(MeCN)_4]PF_6$

Method from Kubas. *et al.*[104]

Caution Note: The following procedures should be carried out in a well-ventilated fume hood because of the toxicity of acetonitrile and the HF fumes evolved from HPF_6. With this in mind, a 7% solution of calcium gluconate was prepared and kept on hand in case of exposure to HF.

$$Cu_2O + 2HPF_6 \xrightarrow{MeCN} 2[Cu(MeCN)_4)][PF_6] + H_2O$$

To a stirred suspension of Cu_2O (4.0 g, 28 mmol) of in of MeCN (80 mL), in an Erlenmeyer flask, HPF_6 (10 mL of 60-65%) was added, in 2-mL portions. This caused an exothermic reaction, a tray of cold water was on hand, to cool the base of the Erlenmeyer if the reaction boiled in excess, however this was not needed. After addition of the final portion of HPF, the solution was stirred for about 3 min and then filtered hot through a medium-porosity frit to remove small amounts of undissolved black solid. The pale-blue solution is cooled in a freezer to about – 20 ºC, in a salt ice bath, for several hours, with an addition of Et_2O (20 ml) after three hours. White $[Cu(MeCN)_4]PF_6$ crystalised out, which was collected by filtration, and washed with Et_2O. The material was transferred to a sealable container and flushed with Ar, to prevent oxidation. The product was stored in the freezer, even in a desiccator, the product would slowly turn blue, indicating oxidation. This reaction resulted in 2.746 g (7.37 mmol) of product in a 13.2 % yield and confirmed through an X-ray crystallography screening.

A5.1b Complexation of L3 and NO_3 (AgL3)

L3, (8.3 mg, 0.021 mmol, 1 equiv.) was suspended in THF (3 ml), in a sealed Ar flushed container. $AgNO_3$ (3.8 mg, 0.022 mmol, 1.06 equiv.) dissolved in MeOH (1 ml) was added by injection. The resulting solution was stirred for two hours. Isolation of the complex was achieved by either slow evaporation, or vapour diffusion of Et_2O into a THF solution containing the crude material resulting in very small red/pink, block-shaped crystals after one week yield. The crystals were barely sufficient quality to be characterised by X-ray crystallography.

Crystal Data for $C_{24}H_{24}N_{12}O_4Ag_2$ (*M* =760.273 g/mol): monoclinic, space group $P2_1/n$ (no. 14), *a* = 9.594(5) Å, *b* = 12.263(8) Å, *c* = 10.309(5) Å, β = 90°, *V* = 1212.9(12) $Å^3$, *Z* = 2, *T* = 102.0 K, μ(Cu Kα) = 13.501 mm^{-1}, *Dcalc* = 2.082 g/cm^3, 9073 reflections measured (11.22° ≤ 2Θ ≤ 145.38°), 2205 unique (R_{int} = 0.2758, R_{sigma} = 0.3058) which were used in all calculations. The final R_1 was 0.1880 (I>=2u(I)) and wR_2 was 0.5216 (all data).

(m/z): 317.39; 395.14; (100), 396.14 (20) [**L3** + H]; 416.90; 606.41; 810.80. IR: ν_{max}/cm^{-1}:3421.02 (br), 2981.21 (m), 2879.50 (m), 1650.85 (w), 1463.29 (w), 1390.50 (w), 1066.04 (s), 1029.79 (s), 903.07 (w), 760.35 (w).

A5.2 Synthesis of D3: 2-((prop-2-yn-1-yloxy)methyl)pyridine

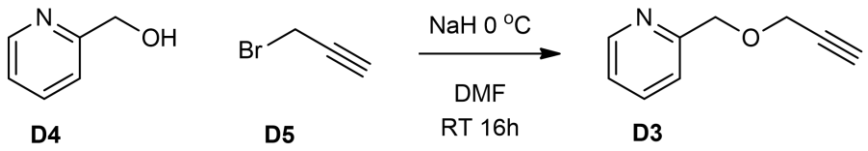

Scheme A5.2: Williamson ether reaction for the synthesis of **D3**

Adapted from Delso *et al.* [109]

Pyridin-2-ylmethanol (**D4**) (0.1 g, 0.73 mmol, 1 equiv.) was dissolved in argon flushed DMF (9 mL) then cooled to 0ºC. Sodium hydride (60% wt) (0.0572 g, 1.43 mmol, 1.95 equiv.) was added. When hydrogen liberation had stopped, propargylbromide (**D5**) (0.160 ml, 1.09 mmol, 1.48 equiv.) was added and the mixture was stirred overnight at RT. Afterwards, water (100 mL) was added and the solution extracted with hexane (3 x 30 mL). The combined organic layers were dried with $MgSO_4$, filtered and the solvent was removed under vacuum. A pale yellow crude oil of was collected, in a (0.122 g, 90 % yield).

^{1}H NMR (400 MHz, DMSO): δ = 8.55 (d, 1H, J = Hz), 7.68 (t, 1H, J = Hz), 7.44 (d, 1H, J = Hz), 7.20 (t, 1H, J = Hz), 4.73 (s, 2H), 4.28 (d, 2H, J = Hz), 2.46 (t, 1H, J = Hz). The ^{1}H NMR of **D3** agreed with the literature values.[109] **Spectra – A12.3.4**

A5.3 Synthesis of L4:

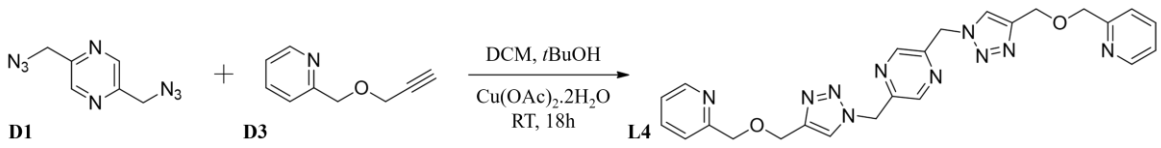

Scheme A5.3: The click reaction scheme for the synthesis of **L4**.

To an argon flushed rbf, 2,5-bis(Azidomethyl)pyridine (**D1**) (27.26 mg, 0.14 mmol, 1.0 equiv.), in DCM (1 ml) and tBuOH (0.5 ml) was added 2-((prop-2-yn-1-yloxy)methyl)pyridine (**D3**) (63.2 mg, 0.43 mmol 3 equiv.) and an aqueous solution of $Cu(OAc)_2$ (0.5 M, 0.03 ml), were added. The blue aqueous $Cu(OAc)_2$ solution turned green upon addition. The reaction was stirred vigorously at RT for 18 h, during which the organic layer became brown-grey in colour. The reaction was diluted with water (4 mL) and DCM (3 mL), and the organic phase was washed until no more blue copper solution was extracted. The crude product was concentrated *in vacuo*, as a tacky brown-yellow solid (55 mg in an 84 % yield).

The ^{1}HNMR of the crude reaction mix indicated the successful synthesis of **L4**, however further investigation would be required to characterise this ligand. ^{1}H NMR (400 MHz, DMSO): δ = 8.65 (s, 1H), 8.51 (m, 1H), 8.26, (s, 1H), 7.78 (m, 1H), 7.42 (m, 1H), 7.29 (m, 1H), 5.81 (s, 2H), 4.65 (s, 2H), 4.60 (s, 2H). **Spectra – A12.3.5**

Appendix6.0: Synthesis Method of L5 and Reagents

A6.1 Synthesis of F1: 2,5-bis((prop-2-yn-1-yloxy)methyl)pyrazine

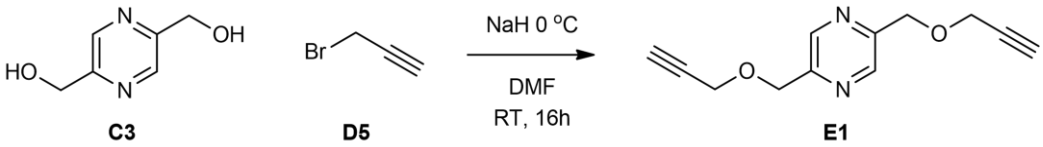

Scheme A6.1: Williamson Ether reaction scheme for the synthesis of **E1**.

Adapted from Delso *et al.*[109]

The 2,5-dimethoxy pyrazine (**C3**) (0.500 g, 3.57 mmol, 1 equiv.), was ground with a mortar and pestle, into a fine, very pale beige powder. This powdered **C3** was suspended in DMF (40 mL), cooled to 0ºC, and deoxygenated with argon gas.

NaH (0.3125 g, 13.0 mmol, 3.65 equiv.) was carefully measured and added in portions. When hydrogen liberation has stopped, propargylbromide (**D5**) (0.95 ml, 10.75 mmol, 3 equiv.) was then added. The reaction was shielded from UV and stirred overnight at RT. Next, water (100 mL) was added and the solution extracted with hexane (3 x 55 mL). The combined organic layers were dried with $MgSO_4$, filtered and the solvent was removed under vacuum.

A clear oil was collected, with some staining of orange inside. The crude product was collected (0.5704 g, 73.6% yield) and used with no further purification.

^{1}H NMR (400 MHz, DMSO): δ = 8.63 (s, 2H), 4.68 (s, 4H), 4.30 (d, 4H, J = 2.33 Hz), 3.52 (t, 2H, J = Hz); δ ^{13}C NMR (125.7 MHz; DMSO): 152.21, 142.97, 80.31, 78.29, 70.29, 58.16 (*m/z*): 239.14 (100) 240.14 (14) [M, Na]. **Spectra – A12.4.01- A12.4.03** This NMR data confirmed the synthesis of this new compound.

A6.2 Synthesis of: azido butane (E2)

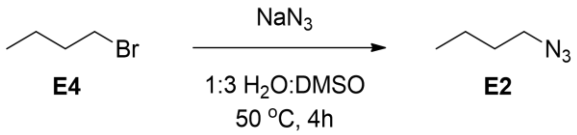

Scheme A6.2: The synthesis of **E2**

Adapted from, Darrah *et al.*[114]

Caution Note: The close C:N ratio, as discussed previously in Section 3.2, introduces an explosive risk, requiring that this reaction was done on no larger than 0.8 ml of azido butane.

Sodium azide (0.7116 g, 10.95 mmol, 1.5 equiv.) is dissolved in water (2 mL) at RT. DMSO (6 mL) is added to the solution. 1-Bromopropane (**E4**) (0.789 mL, 7.30 mmol, 1 equiv.) is added dropwise to the solution, which was then heated to 50 ºC for 4hours, upon which two layers formed. The top layer, a clear oil (containing a mixture of **E4** and **E2**) was decanted and used crude in the subsequent click reaction.

The crude product was characterised by ^{1}H NMR, and had a calculated mass of 0.44 g, 97.5% yield based on **E2**. The molar amount was calculated from the ^{1}H NMR spectra, and the crude product was used in the subsequent click reaction without further purification.

^{1}H NMR (400 MHz, $CDCl_3$): δ = 3.26 (t, 2H, J = 6.89 Hz), 1.59 (m, 2H, J = 7.21 Hz; J = 6.66 Hz), 1.41 (m, 2H, J = 7.49 Hz; J = 7.60 Hz), 0.94 (t, 3H, J = 7.23 Hz). Mass (*m*/*z*): 122.05 (100), 123.05 (5) [M, Na] The ^{1}H NMR values agree with the literature values.[116] **Spectra – A12.4.04**

A6.3 Synthesis of: Allyl azide (E3)

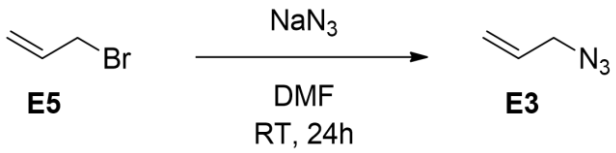

Scheme A6.3: The synthesis of **E3**

Adapted from: Method from Yang *et al.* [115]

The method used by Yang *et al.* [115] was followed. To a suspension of sodium azide (0.7437 g, 11.44 mmol, 1.29 equiv.) and DMF (6 mL); 3-bromo-1-propene (**E5**) (0.790 ml, 8.89 mmol, 1 equiv.) was added. After stirring at RT for 1 day, the product was extracted with CH_2Cl_2/H_2O (3x). The combined organic phases were concentrated by rotary evaporator (below 10 ºC) to half volume, and sealed for storage. From the weight in DCM in the ^{1}H NMR, a mass of 0.286 g was calculated, (41.6 % yield). The crude **E3** was used without further purification.

^{1}H NMR (400 MHz, $CDCl_3$): δ = 5.87 (ddt, 1H, J = 5.79 Hz, J = 10.30 Hz, J = 6.05 Hz), 5.33 (s, 2H), 3.77 (d, 2H, J = 5.76 Hz, $=CH_2$) Results agree with lit. values.[115] **Spectra – A12.4.05-A12.4.06**

A6.4 Synthesis of L5

2,5-bis(((1-butyl-1H-1,2,3-triazol-4-yl)methoxy)methyl)pyrazine

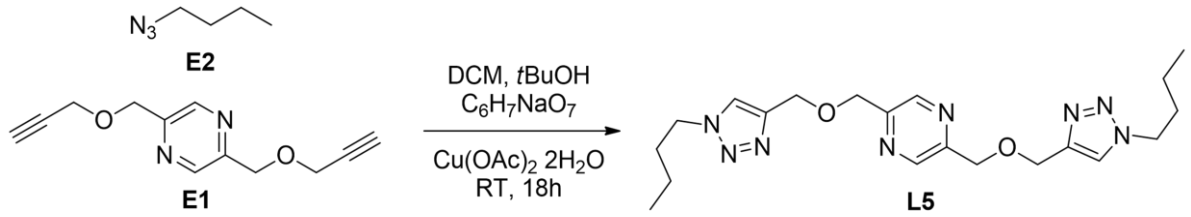

Scheme A6.4: The click reaction for the synthesis of **L5**

To the azide, **E2** (0.280 g 2.82 mmol, 3.5 equiv.) in degassed DCM (20 ml), was added the di-alkyne **E1** (0.1740 g, 0.8 mmol, 1 equiv.) and sodium citrate (0.0328 g, 0.13 mmol, 0.16 equiv.) and stirred for ten minutes. Then an aqueous $Cu(OAc)_2.H_2O$ solution (0.5 M, 0.16 ml) was injected to the reaction, turning from a blue to green immiscible layer. The reaction was stirred vigorously so that the aqueous layer was not able to fully settle as a separate layer, and was stirred for 18h at RT.

The organic layer was washed with water, until no further blue copper was extracted. The **L5** yellow-brown precipitate was collected by filtration, (0.2614 g, 78.38 % yield). The product did not require further purification.

^{1}H NMR (500 MHz, DMSO): δ = 8.63 (s, 2H), 8.17 (s, 2H), 4.67 (s, 4H), 4.66 (s, 4H), 4.34 (t, 4H, J = 7.05 Hz), 1.78 (q, 4H, J = 7.33, Hz, J = 7.11 Hz) 1.23 (m, 4H, J = 7.45), 0.86-0.88-0.89 (t, 6H, J = 7.38 Hz). δC (126 MHz; DMSO): δ = 152.53; 143.91; 142.81; 124.50; 70.74; 64.06; 49.46; 32.15; 19.52; 13.76. m/z: 415.21(100) 416.18 (22) [M+H]; 437.19 (100) 438.19 (20) [M Na]; 851.37 (100) 852.36 (50) [2M Na]. *IR:* ν_{max}/cm^{-1}: 3430.81 (br), 3118.84 (s), 2955.45 (s), 2931.07 (s), 2872.06 (s), 1669.37 (w), 1484.80 (w), 1458.67 (m), 1375.35 (m), 1349.86 (m), 1255.46 (w), 1218.73 (m), 1143.69 (m), 1091.34 (s), 1056.73 (s), 1035.50 (m), 1027.66 (m), 991.22 (m), 941.85 (w), 870.35 (w), 802.73 (w), 776.12 (w). **Spectra – A12.4.07- A12.4.10** This NMR data confirmed the synthesis of this new compound.

A6.5 Synthesis of L6

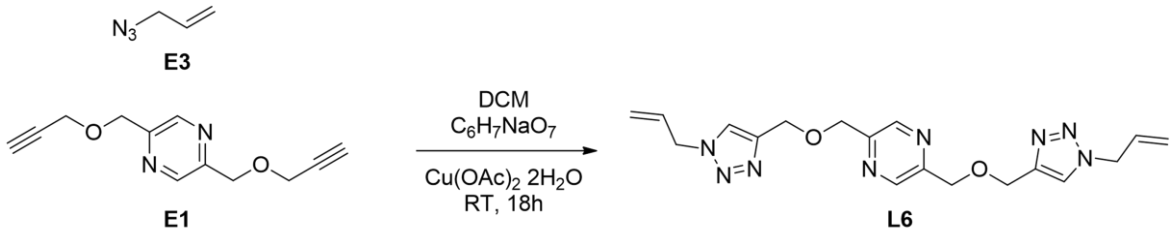

Scheme A6.5: The click reaction for the synthesis of **L6**

To the crude deoxygenated DCM solution of **E3**, (of calculated 0.286g 3.44 mmol, 3.04 equiv.) was added the di-alkyne **E1** (0.2443g, 1.13 mmol, 1 equiv.) and sodium citrate (0.007g, mmol) and stirred for ten minutes. To this an aqueous $Cu(OAc)_2.H_2O$ (0.5 M, 0.02 ml) was injected into the reaction, turning from a blue to green immiscible layer. The reaction was stirred so that the aqueous layer was not able to fully settle as a separate layer, and was stirred for 18h at RT.

The organic layer was washed with water, until no further blue copper was extracted. The organic layer was concentrated, to a dark brown tacky solid, 0.440g, 102%. There is some crude material left in the product, as seen in the ^{1}H NMR.

^{1}H NMR (500 MHz, DMSO): δ = 8.63 (s, 2H), 8.14 (s, 2H), 6.02-6.07 (dq, 2H, J = 6.29, 10.38, 5.26 Hz), 5.24-5.26 (d, 2H, J = 10.2 Hz), 5.14-5.18 (d, 2H, J = 16.94 Hz) 5.00-5.02 (d, 4H, J = 5.93 Hz), 4.68 (s, 8H). δC (126 MHz; DMSO): δ = 152.52, 144.14, 142.82, 133.23, 124.66, 119.17, 70.76, 63.99, 52.10, 36.24, 31.23 *(m/*z): 383.05 [**L6**H]; 405.12 [**L6** Na]; 420.99 [**L6**K]; 787.28 [2**L6** Na]. *IR:* ν_{max}/cm^{-1}: 3430.73 (br), 3143.29 (m), 2929.04 (m), 1664.71 (s), 1490.69 (w), 1463.86 (w), 1419.61 (w), 1389.95 (m), 1338.13 (m), 1260.15 (w), 1223.47 (m), 1140.10 (m), 1095.00 (s), 1049.91 (s), 1033.23 (m) 993.46 (m), 94269 (m), 886.43 (w), 834.71 (w), 793.76 (w). **Spectra – A12.4.11- A12.4.14** This NMR data confirmed the synthesis of this new compound.

Appendix 7.0: L5 Crystallisation Methods

A7.01: $\{[Mn_2(L5, H_2O)](ClO_4)_2\}_\infty$ (5A1)

To **L5** (0.0173 g, 0.173 mmol, 1.0 eq.) in MeCN (0.6 mL) was added a pink, $Mn(ClO_4)_2.6H_2O$ (0.0065 g, 0.017 mmol, 1.035 eq.) in MeOH (0.6 mL). The pink solution was stirred at 60 ºC for 30 minutes, during which time the solution turned yellow. Isolation of the complex was achieved by the diffusion of Et_2O into the reaction solution. Yellow, block shaped X-ray quality crystals were produced after four weeks.

Crystal Data for $C_{20}H_{32}Cl_2MnN_8O_{11}$ (M =686.37 g/mol): monoclinic, space group C2/*c*, a = 18.2220(5) Å, b = 13.9035(4) Å, c = 23.6049(7)Å, β = 94.870(2)°, V = 5958.7(3)$Å^3$, Z = 8, T = 100 K, μ(MoKα) = 5.857mm^{-1}, ρcalc = 1.530 g/cm^3, 17486 reflections measured (8.01° ≤ 2Θ ≤ 130.158°), 5006 unique (Rint = 0.0402, Rsigma = 0.0404) which were used in all calculations. The final R1 was 0.0617 (I > 2σ(I)) and wR2 was 0.1458 (all data).

The crystals were crushed and dried prior to further analysis.

IR: ν_{max}/cm^{-1}; 3430.81 (br), 2962.24 (m), 2876.17 (w), 1641.37 (w), 1467.19 (w), 1363.18 (w), 1302.38 (w), 1158.63 (m), 1090.82 (s), 1063.36 (s), 950.62 (w), 816.26 (w), 779.04 (w) MS: m/z; 414.65 [L], 441.77, 648.6, 828.92, 981.81 $[[Mn^{2+}(2L)](ClO_4^-)(H^+)]$ UV/Vis (ε, L/mol cm) in MeOH: 270 nm (3984.04), 210.2 nm (7064.81), 309.5 nm (489.27) Conductivity of MeOH (A.R) = 7.89 μS cm^{-1}; Conductivity of **5A1** in MeOH (A.R) = 44.6 μS cm^{-1}. Leading to a molar conductivity of 65.79 S cm^2 mol^{-1}.

A7.02: $\{[Co(L^5)](ClO_4)_2\}_\infty$ (5B1)

To **L5** (0.0173 g, 0.173 mmol, 1.0 eq.) in MeCN (0.6 mL) was added pink $Co(ClO_4)_2.6H_2O$ (0.0065 g, 0.017 mmol, 1.035 eq.) in MeOH (0.6 mL). The pink solution was stirred at 60 ºC for 30 minutes, during which time the solution turned orange. Isolation of the complex was achieved by the diffusion of Et_2O into the reaction solution. Pink, block shaped X-ray quality crystals were produced after four weeks.

Crystal Data for $C_{20}H_{29}Cl_2CoN_8O_{10}$ (M =671.339 g/mol): monoclinic, space group $P2_1/c$ (no. 14), a =18.8050(14) Å, b =15.4107(11) Å, c =9.5941(7) Å, β =103.818(4)°, V =2699.9(3) Å^3, Z = 4, T = 100.0 K, μ(Cu Kα) = 7.426 mm^{-1}, *Dcalc* = 1.652 g/cm^3, 12441 reflections measured (4.84° ≤ 2Θ ≤ 144.84°), 5004 unique (R_{int} = 0.0540, R_{sigma} = 0.0788) which were used in all calculations. The final R_1 was 0.0891 (I>=2u(I)) and wR_2 was 0.2751 (all data).

The crystals were crushed and dried prior to further analysis.

IR: ν_{max}/cm^{-1}; 3422.88 (br), 3155.68 (w), 2962.76 (m), 1510.14 (w), 1465.93 (w), 1307.59 (w), 1087.99 (s), 846.80 (w). MS: m/z; 414.15 [L], 443.65[Co^{2+}(2L)] 603.41, 650.79, 779.97 [2Co^{2+}(3L)](2ClO_4^-)]], 857.80, 985.81[[Co^{2+}(2L)](ClO_4^-)]. UV/Vis (ε, L/mol cm) in MeOH: 269.5 nm (8700.66), 221.0 nm (8428.98), 310.5 nm (1057.05). Conductivity of MeOH (A.R) = 7.73 μS cm^{-1}; Conductivity of **5B1** in MeOH (A.R) = 66.7 μS cm^{-1}. Leading to a molar conductivity of 134.63 S cm^2 mol^{-1}.

A7.03 {[Fe(L5)](H$_2$O)(ClO$_4$)$_2$}$_\infty$ (5C1)

To **L5** (0.0173 g, 0.173 mmol, 1.0 eq.) in MeCN (0.6 mL) was added yellow,Fe(ClO$_4$)$_2$.6H$_2$O (0.0060 g, 0.0165 mmol, 0.95 eq.) in MeOH (0.6 mL). The yellow solution was stirred at 60 ºC for 30 minutes. Isolation of the complex was achieved by the diffusion of Et$_2$O into the reaction solution. Orange, block shaped X-ray quality crystals were produced after four weeks.

Crystal Data for $C_{20}H_{28}Cl_2FeN_8O_{10}$ (*M* =667.25 g/mol): monoclinic, space group P2$_1$/c (no. 14), *a* =18.8195(10) Å, *b* =15.1945(8) Å, *c* =10.0460(5) Å, *β* =103.644(3)°, *V* =2791.6(3) Å^3, *Z* = 4, *T* = 100.0 K, μ(CuKα) = 6.694 mm^{-1}, *Dcalc* = 1.588 g/cm^3, 54335 reflections measured (4.832° ≤ 2Θ ≤ 152.5°), 5547 unique (R_{int} = 0.0736, R_{sigma} = 0.0444) which were used in all calculations. The final R_1 was 0.0750 (I > 2σ(I)) and wR_2 was 0.2356 (all data)

The crystals were crushed and dried prior to further analysis.

IR: ν_{max}/cm^{-1}; 3485.40 (br), 3151.25 (w), 2964.28 (m), 2876.66 (w), 1511.69 (w), 1465.63 (w), 1303.64 (w), 1238.66 (w), 1087.38 (s), 834.12 (w). MS: m/z; 414.02 [L], 442.27 [Fe^{2+}(2L)], 649.29, 829.05, 982.81 [[Fe^{2+}(2L)](ClO$_4^-$)]. UV/Vis (ε, L/mol cm) in MeOH: 269.0 nm (6743.31), 310.5 nm (947.60). Conductivity of MeOH (A.R) = 7.65 μS cm^{-1}; Conductivity of **5C1** in MeOH (A.R) = 23.4 μS cm^{-1}. Leading to a molar conductivity of 44.14 S cm^2 mol^{-1}.

A7.04 $\{[Ni(L^5)](ClO_4)_2\}_\infty$ (5D1)

To **L5** (0.0173 g, 0.173 mmol, 1.0 eq.) in MeCN (0.6 mL) was added pink $Ni(ClO_4)_2.6H_2O$ (0.0063 g, 0.017 mmol, 0.99 eq.) in MeOH (0.6 mL). The green solution was stirred at 60 ºC for 30 minutes, during which time the solution turned slightly blue. Isolation of the complex was achieved by the diffusion of Et_2O into the reaction solution. Blue, block shaped X-ray quality crystals were produced after four weeks.

Crystal Data for $C_{20}H_{30}Cl_2N_8NiO_{10}$ (M = 672.13 g/mol): monoclinic, space group C2/*c*, a = 18.5166(11) Å, b =16.2958(9) Å, c = 9.3201(5) Å, β = 92.768(4)°, V = 2809.0(3)Å^3, Z = 4, T = 100 K, μ(MoKα) = 3.344mm^{-1}, ρcalc = 1.589 g/cm^3, 27595 reflections measured (7.23° ≤ 2Θ ≤ 145.314°), 2572 unique (Rint = 0.0781, Rsigma = 0.0400) which were used in all calculations. The final R1 was 0.0890 (I > 2σ(I)) and wR2 was 0.1900 (all data).

The crystals were crushed and dried prior to further analysis.

IR: ν_{max}/cm^{-1}; 3408.83 (br), 3160.47 (m), 2965.06 (m), 2876.70 (m), 1641.15 (w), 1507.91 (w), 1464.31 (m), 1310.83 (w), 1244.23 (w), 1083.54 (s), 898.18 (w), 833.46 (w). MS: m/z; 415.16 [L], 437.08 [LNa], 585.13, 650.95, 698.18, 764.50, 851.42, 999.25. UV/Vis (ε, L/mol cm) in MeOH: 373.0 nm (2.56), 310.0 nm (215.11), 270.0 nm (1576.50), 210.0 nm (3080.79). Conductivity of MeOH (A.R) = 7.32 μS cm^{-1}; Conductivity of **5D1** in MeOH (A.R) = 34.2 μS cm^{-1}. Leading to a molar conductivity of 40.44 S cm^2 mol^{-1}.

A7.05 {[Cu(L^5)](ClO$_4$)$_2$}$_\infty$ (5F1)

To **L5** (0.0173 g, 0.173 mmol, 1.0 eq.) in MeCN (0.6 mL) was added blue Cu(ClO$_4$)$_2$.6H$_2$O (0.0064 g, 0.017 mmol, 1.00 eq.) in MeOH (0.6 mL). The blue solution was stirred at 60 ºC for 30 minutes, during which time the solution turned green. Isolation of the complex was achieved by the diffusion of Et$_2$O into the reaction solution. Green, block shaped X-ray quality crystals were produced after four weeks.

Crystal Data for $C_{20}H_{24.7}Cl_2CuN_8O_{10}$ (M = 671.62 g/mol): monoclinic, space group C2/*c*, a = 18.6303(10) Å, b = 16.1633(8) Å, c = 9.4784(5) Å, β = 92.415(4) V = 2851.7(3) Å^3, Z = 4, T = 100 K, μ(MoKα) = 3.393mm^{-1}, ρcalc = 1.564 g/cm^3, 9442 reflections measured (7.244° ≤ 2Θ ≤ 151.946°), 2763 unique (Rint = 0.0509, Rsigma = 0.0501) which were used in all calculations. The final R1 was 0.0712 (I > 2σ(I)) and wR2 was 0.2206 (all data).

The crystals were crushed and dried prior to further analysis.

IR: ν_{max}/cm^{-1}; (br), 3159.33 (m), 2960.97 (m), 2873.62 (w), 1575.03 (w), 1506.86 (w), 1465.45 (m), 1308.56 (m), 1240.35 (w), 1153.38 (m), 1091.52 (s), 989.13 (m), 836.93 (w). MS: m/z; 414.27 [L], 445.77 [Cu^{2+}(2L)], 577.78 [Cu^{2+}(L+H)](ClO$_4^-$)], 652.91, 783.92 [2 Cu^{2+}(3L)](2 ClO$_4^-$)], 991.43 [[Cu^{2+}(2L+H)](ClO$_4^-$)]. UV/Vis (ε, L/mol cm) in MeOH: 271.50 nm (6293.14). Conductivity of MeOH (A.R) = 7.68 μS cm^{-1}; Conductivity of **5F1** in MeOH (A.R) = 18.17 μS cm^{-1}. Leading to a molar conductivity of 42.92 S cm^2 mol^{-1}.

A7.06 $[Mn_2(L5)](NO_3)_2(H_2O)_4](NO_3)_2$ (5A3)

To **L5** (0.0173 g, 0.173 mmol, 1.0 eq.) in MeCN (0.6 mL) was added pink $Mn(NO_3)_2.6H_2O$ (0.0060 g, 0.019 mmol, 1.18 eq.) in MeOH (0.6 mL). The pink solution turned yellow, and was then stirred at 60 ºC for 30 minutes. Isolation of the complex was achieved by the diffusion of Et_2O into the reaction solution. Very pale yellow, block shaped X-ray quality crystals were produced after four weeks.

Crystal Data for $C_{20}H_{38}Mn_2N_{12}O_{18}$ M = 844.471 g/mol): triclinic, space group $P\bar{1}$, a = 9.6194(3) Å, b = 9.7752(3) Å, c = 10.2915(3)Å, β = 91.685(4) º, V = 854.74(5) $Å^3$, Z = 1, T = 120 K, μ(MoKα) = 6.851 mm^{-1}, ρcalc = 1.641 g/cm^3, 14781 reflections measured (9.1 ° ≤ 2Θ ≤ 151.92°), 3273 unique (Rint = 0.0529, Rsigma = 0.0443) which were used in all calculations. The final R1 was 0.0612 (I > 2σ(I)) and wR2 was 0.1749 (all data).

The crystals were crushed and dried prior to further analysis.

IR: ν_{max}/cm^{-1}; 3399.33 (br), 3103.83 (m), 2962.78 (m), 2878.37 (w), 2257.60 (w), 1611.41 (m), 1489.03 (s), 1446.91 (m), 1373.51 (s), 1342.62 (s), 1296.16 (s), 1245.66 (w), 1158.16 (w),1110.83 (m), 1081.43 (m), 1060.85 (s), 1038.35 (w), 854.36, 814.46 (w), 773.20 (w). MS: m/z: 266.89, 414.27 [L], 441.65, 531.03, 648.66, 709.79 $[Mn^{2+}(L)](H_2O)(2ClO_4^-)$, 792.05, 855.80, 944.93. UV/Vis (ε, L/mol cm) in MeOH: 310.50 nm (919.49), 269.50 nm (7430.87). Conductivity of MeOH (A.R) = 9.19 μS cm^{-1}; Conductivity of **5A3** in MeOH (A.R) = 69.8 μS cm^{-1}. Leading to a molar conductivity of 190.52 S cm^2 mol^{-1}.

A7.07 $\{[Co(L^5)](BF_4)_2\}_\infty$ (5B2)

To **L5** (0.0173 g, 0.173 mmol, 1.0 eq.) in MeCN (0.6 mL) was added red $Co(BF_4)_2.6H_2O$ (0.0058 g, 0.017 mmol, 0.98 eq.) in MeOH (0.6 mL). The red solution was stirred at 60 ºC for 30 minutes, during which time the solution turned orange. Isolation of the complex was achieved by the diffusion of Et_2O into the reaction solution. Purple/red, block shaped X-ray quality crystals were produced after four weeks.

Crystal Data for $C_{20}H_{30}B_2CoF_8N_8O_2$ (M = 647.07 g/mol): triclinic, space group $P\bar{1}$, a = 10.0286(5) Å, b = 11.4663(7) Å, c = 12.5989(7) Å, α= 76.679(4)º β = 88.465(4)º V = 1391.91(14) $Å^3$, Z = 2, T = 100 K, μ(MoKα) = 5.644mm^{-1}, ρcalc = 1.544 g/cm^3, 17184 reflections measured ($8.022° \leq 2\Theta \leq 152.708°$), 5370 unique (Rint = 0.0601, Rsigma = 0.0727) which were used in all calculations. The final R1 was 0.0849 ($I > 2\sigma(I)$) and wR2 was 0.2612 (all data).

The crystals were crushed and dried prior to further analysis.

IR: ν_{max}/cm^{-1}; 3464.39 (br), 3156.77 (w), 2964.84 (m), 2877.58 (w), 1642.28 (w), 1508.83 (w), 1468.25 (m), 1360.96 (w), 1306.91 (m), 1246.60 (w), 1064.64 (s), 892.13 (w), 845.63 (w). MS: m/z; 268.89, 443.65 $[Co^{2+}(2L)]$, 650.66 $[[Co^{2+}(L+2H)](2BF_4^-)]$, 857.80, 973.93 $[[Co^{2+}(L)](BF_4^-)]$. UV/Vis (ε, L/mol cm) in MeOH: 310.5 nm (503.98), 270.0 nm (4096.97), 212.2 nm (8437.24). Conductivity of MeOH (A.R) = 7.26 μS cm^{-1}; Conductivity of **5B2** in MeOH (A.R) = 23.8 μS cm^{-1}. Leading to a molar conductivity of 51.22 S cm^2 mol^{-1}.

A7.08 $\{[Fe(L5)](BF_4)_2\}_\infty$ (5C2)

To **L5** (0.0173 g, 0.173 mmol, 1.0 eq.) in MeCN (0.6 mL) was added white $Fe(BF_4)_2.6H_2O$ (0.0060 g, 0.018 mmol, 1.02 eq.) in MeOH (0.6 mL). The yellow solution turned a brighter yellow, and was then stirred at 60 ºC for 30 minutes. Isolation of the complex was achieved by the diffusion of Et_2O into the reaction solution. Orange, block shaped X-ray quality crystals were produced after four weeks.

Crystal Data for $C_{40}H_{62}B_4F_{16}Fe_2N_{16}O_5$ (M = 1305.99 g/mol): triclinic, space group $P\bar{1}$, a = 10.0668(7)) Å, b = 11.9380(9) Å, c = 12.1166(10) Å, α= 70.664(5)º, β = 89.417(6)º, V = 1373.93(19) $Å^3$, Z = 1, T = 106 K, μ(MoKα) = 5.245mm^{-1}, ρcalc = 1.578 g/cm^3, 13189 reflections measured (7.732 ° ≤ 2Θ ≤ 144.294°), 5128 unique (Rint = 0.0589, Rsigma = 0.0827) which were used in all calculations. The final R1 was 0.0745 (I > 2σ(I)) and wR2 was 0.2271 (all data).

The crystals were crushed and dried prior to further analysis.

IR: ν_{max}/cm^{-1}; 3497.13 (br), 3160.18 (m), 2964.54 (m), 2877.00 (w), 1576.63 (w), 1510.78 (w), 1467.38 (m), 1362.85 (w), 1304.55 (m), 1240.56 (w), 1068.23 (s), 886.87 (w), 837.84 (w), 769.53 (w). MS: m/z; 414.15 [L], 437.02[LNa], 649.16, 850.92, 996.93. UV/Vis (ε, L/mol cm) in MeOH: 310.5 nm (1078.56), 270.0 nm (7585.00), 210.0 nm (151178.78). Conductivity of MeOH (A.R) = 7.45 μS cm^{-1}; Conductivity of **5C2** in MeOH (A.R) = 9.11 μS cm^{-1}. Leading to a molar conductivity of 20.75 S cm^2 mol^{-1}.

A7.09 $\{[Zn(L5)](BF_4)_2\}_\infty$ (5E2)

To **L5** (0.0173 g, 0.173 mmol, 1.0 eq.) in MeCN (0.6 mL) was added white $Zn(BF_4)_2.6H_2O$ (0.0052 g, 0.0177 mmol, 1.02 eq.) in MeOH (0.6 mL). The solution was then stirred at 60 ºC for 30 minutes. Isolation of the complex was achieved by the diffusion of Et_2O into the reaction solution. Clear, needle-shaped X-ray quality crystals were produced after four weeks.

Crystal Data for $C_{20}H_{30}B_2F_8N_8O_2Zn$ (M = 653.51g/mol): monoclinic, space group C2/c, a = 19.5350(9) Å, b = 14.0069(7) Å, c = 10.0241(5) Å, β = 90.699(2) º, V = 2742.6(2) $Å^3$, Z = 4, T = 100 K, μ(MoKα) = 2.066 mm^{-1}, ρcalc = 1.583 g/cm^3, 9423 reflections measured (7.766° ≤ 2Θ ≤ 152.346°), 2774 unique (Rint = 0.0426, Rsigma = 0.0411) which were used in all calculations. The final R1 was 0.0816 (I > 2σ(I)) and wR2 was 0.2417 (all data).

The crystals were crushed and dried prior to further analysis.

IR: ν_{max}/cm^{-1}; 3510.27 (br), 3173.97 (m), 2937.11 (m), 1577.46 (w), 1521.78 (w), 1467.65 (m), 1307.79 (m), 1243.50 (w), 1154.44 (m), 1072.13 (s), 1050.84 (s), 890.13 (w), 837.20 (w), 768.23 (w). MS: m/z; 414.02 [L], 437.02 [LNa], 446.27 $[Zn^{2+}(2L)]$, 653.79 $[Zn^{2+}(LH)](2BF_4^-)]$, 828.92, 978.93. UV/Vis (*ε*, L/mol cm) in MeOH: 310.5 nm (43.00), 270.0 nm (3394.00), 209.0 nm (7102.84). Conductivity of MeOH (A.R) = 7.67 μS cm^{-1}; Conductivity of **5E2** in MeOH (A.R) = 13.2 μS cm^{-1}. Leading to a molar conductivity of 30.27 S cm^2 mol^{-1}.

A7.10 $\{[Cu(L^5)](BF_4)_2\}_\infty$ (5F2)

To **L5** (0.0173 g, 0.173 mmol, 1.0 eq.) in MeCN (0.6 mL) was added blue $Cu(BF_4)_2.6H_2O$ (0.0060 g, 0.019 mmol, 1.18 eq.) in MeOH (0.6 mL). The blue solution turned green, and was then stirred at 60 ºC for 30 minutes. Isolation of the complex was achieved by the diffusion of Et_2O into the reaction solution. Turquois, block shaped X-ray quality crystals were produced after four weeks.

Crystal Data for $C_{20}H_{30}B_2CuF_8N_8O_2$ (M = 651.68 g/mol): monoclinic, space group C2/c, a = 18.2228(10) Å, b = 16.2157(9) Å, c = 9.4651(6) Å, β = 91.685(4) º, V = 2795.7(3) $Å^3$, Z = 4, T = 100 K, μ(MoKα) = 1.910 mm^{-1}, ρcalc = 1.548 g/cm^3, 11335 reflections measured (7.298 ° ≤ 2Θ ≤ 152.184 °), 2639 unique (Rint = 0.0446, Rsigma = 0.0441) which were used in all calculations. The final R1 was 0.0596 (I > 2σ(I)) and wR2 was 0.1809 (all data).

The crystals were crushed and dried prior to further analysis.

IR: ν_{max}/cm^{-1}; 3486.45 (br), 3167.97 (m), 2963.67 (m), 2876.68 (m), 1576.63 (w), 1508.16 (w), 1466.71 (m), 1311.61 (m), 1244.04 (w), 1156.21 (m), 1060.83 (s), 900.03 (w), 842.54 (w), 765.56 (w). **MS:** m/z; 445.65 $[Cu^{2+}(2L)]$, 522.03, 653.16 $[Cu^{2+}(L+2H)](2BF_4^-)]$, 771.79$[2Cu^{2+}(3L)]$, 890.80, 977.93. **UV/Vis** (ε, L/mol cm) in MeOH: 310.5 nm (937.25), 271.0 nm (5437.66), 213.0 nm (8167.72). Conductivity of MeOH (A.R) = 8.22 μS cm^{-1}; Conductivity of **5F2** in MeOH (A.R) = 24.1 μS cm^{-1}. Leading to a molar conductivity of 46.22 S cm^2 mol^{-1}.

(**5G1**): $NaClO_4.H_2O$

The first ion alteration, was with **G1,** with the introduction of 2.50 equiv. of $Na(ClO_4)_2.H_2O$ to 1 equiv. of **L5** and 0.96 equiv. of $Co(ClO_4)_2.6H_2O$, to investigate whether the introduction of excess anions would act as building templates. This reaction produced pink, block-shaped crystals, after one week of slow diffusion of Et_2O.

The X-ray data collected from this crystal matched the cell of the **5A2** crystals, therefore it was presumed that the introduction of Na^+ cations had no effect on the supramolecular assembly of the **5A2** metal-organic polymer chain architecture.

(**5G2**): $Na(ClO_4)_2.H_2O$

The first ion alteration, was with **G2,** with the introduction of 1.96 equiv. of $Na(ClO_4)_2.H_2O$ to 1 equiv. of **L5** and 0.76 equiv. of $Fe(ClO_4)_2.6H_2O$, to investigate whether the introduction of Na^+ cations act as building templates. This reaction produced pink, block-shaped crystals, after one week of slow diffusion of Et_2O.

The X-ray data collected from this crystal matched the cell of the **5A3** crystals, therefore it was presumed that the introduction of Na^+ cations had no effect on the supramolecular assembly of the **5A3** metal-organic polymer chain architecture.

(**5H1**): $Ba(ClO_4)_2$

One equiv. of **L5** in MeCN was introduced to 0.96 equiv. of $Co(ClO_4)_2.6H_2O$ and 1.04 equiv. of $Ba(ClO_4)_2$, dissolved in MeOH. The mixture was heated at 60 ºC for half and hour, and left to cool. This reaction produced pink, block-shaped crystals, after one week of slow diffusion of Et_2O.

The X-ray data collected from this crystal did not quite match the cell of **5A2**, however when the structure of **H1** was solved, it was the same structure as **5A2**. The introduction of the large Ba^{2+} cation had no effect on the assembly of the supramolecular structure of **5A2**.

A9.0 Full L5 Complexation Attempts

	Metal Salt	M equiv.	M	equiv.		Colour Δ	Crystal	Ppt
5A1	$Mn(ClO_4)_2.6H_2O$	1.04				Yellow	√	
5A2	$Co(ClO_4)_2.6H_2O$	1.09				Pink	√	
5A3	$Fe(ClO_4)_2.6H_2O$	0.95				Orange	√	
5A4	$Ni(ClO_4)_2.6H_2O$	0.99				Blue	√	
5A5	$Mn(ClO_4)_2.6H_2O$	0.48	$Co(ClO_4)_2.6H_2O$	0.43		Yellow	√	
5A6	$Cu(ClO_4)_2.6H_2O$	1.00				Green	√	
5A7	$Cr(ClO_4)_2.6H_2O$					Brown		
5B4	$Fe(ClO_4)_2.6H_2O$		$Co(ClO_4)_2.6H_2O$			Orange	√	
A58	$Eu(NO_3)_3.5H_2O$					Yellow		
5B1	$Mn(NO_3)_3.4H_2O$	1.04				Yellow	√	
5B2	Co(acac)	0.97				Pink		
5B3	Fe(acac)	1.08				Orange		
5B5	Zn(acac)	1.05				Yellow		
5B6	$Cu(NO_3)$	1.10				Green		
5B7	$Dy(NO_3)$	1.10				Yellow	√*	
5B8	$Gd(NO_3)_3.H_2O$	1.01				Yellow		
5B9	$La(NO_3)$	1.03				Yellow	√*	
5C1	$Mn(OAc)_3$					Brown		
5C2	$Co(BF_4)_2.H_2O$	0.98				Pink	√	
5C3	$Fe(BF_4)_2.H_2O$	1.02				Orange	√	
5C4	$Ni(BF_4)_2.H_2O$	0.98				Blue		
5C5	$Zn(BF_4)_2.H_2O$	1.02				White	√	
5C6	$Cu(BF_4)_2.H_2O$	1.19				Green	√	
5C7	$DyCl_3.H_2O$	1.12				Yellow	√*	
5C8	$ErCl_3$	0.95				Yellow	√*	
5C9	Co(acac)					Brown		
5D1	$MnCl_2$	0.96				Yellow		Gel
5D2	$CoCl_2$	1.11				Orange		
5D3	$Fe(SO_4)_2.7H_2O$	1.02				-		
5D4	$NiCl_2$	1.02				Green		
5D5	$Co(BF_4)_2xH_2O$		$Fe(BF_4)_2.H_2O$			Pink		
5D6	$CuCl_2$	1.13				Green		Gel
5D7	$LaCl_3.H_2O$					Yellow		
5D8	$EuCl_3.6H_2O$	0.99				Yellow		
5E1	$Mn(OAc)_2$	0.77			White	-		Ppt
5E2	$Co(OAc)_2$					-		
5E3	CrCl3	0.89			Green	-		
5E4	$Ni(OAc)_2$	0.94			Turquois	-		
5E5	$Zn(Oac)_2$					-		
5E6	$Cu\ (Oac)_2$	1.11			Blue	-		
5E7	$La(Oac)_3$	1.02			White	-		
5F1	$Mn(acac)_3$	0.98			Brown	-		
5F2	$Co(SO_4)_2$	1.04			Red	-		
5F3	$HoCl_3.6H_2O$	0.97			Yellow	brown	√*	
5F5	$Zn(SO_4)_2.7H_2O$	0.97			White	-		
5F6	$Cu(SO_4).5H_2O$	1.07			Blue	-		

*crystal was the original metal salt. -

A10.0 L6 Complexes

A10.1 {[Cu(L6)](ClO$_4$)$_2$}$_\infty$ (6F1)

To **L6** (3.88 mg, 0.101 mmol, 1.0 eq.) in MeCN (0.6 mL) was added a blue, Cu(BF$_4$)$_2$.6H$_2$O (2.95 mg, 0.101 mmol, 1 eq.) in MeOH (0.6 mL). The blue solution turned yellow, and was then stirred at 60 ºC for 30 minutes. Isolation of the complex was achieved by the diffusion of Et$_2$O into the reaction solution. Green, block shaped crystals of barely, X-ray quality were produced after three weeks.

Crystal Data for C$_{12}$H$_{0.25}$Cl$_2$CuN$_{12}$O$_{10}$ (*M* =606.93 g/mol): monoclinic, space group C2/c (no. 15), *a* = 18.306(9) Å, *b* = 15.039(7) Å, *c* = 9.695(5) Å, *β* = 111.18(3)°, *V* = 2489(2) Å^3, *Z* = 4, *T* = 100.0 K, μ(CuKα) = 3.881 mm^{-1}, *Dcalc* = 1.620 g/cm^3, 7478 reflections measured (7.834° ≤ 2Θ ≤ 135.714°), 2180 unique (R_{int} = 0.1302, R_{sigma} = 0.1614) which were used in all calculations. The final R_1 was 0.2280 (I > 2σ(I)) and wR_2 was 0.5949 (all data).

A11.0 X-ray crystallography data

Identification code	**5A1**	**5B1**	**5C1**	**5D1**	**5F1**
	$\{[Mn(L^5,H_2O)](ClO_4)_3\}_\infty$	$\{[Co(L^5)](H_2O)(ClO_4)_3\}_\infty$	$\{[Fe(L^5)](H_2O)(ClO_4)_3\}_\infty$	$\{[Ni(L^5)](ClO_4)_3\}_\infty$	$\{[Cu_2(L^5)](ClO_4)_3\}_\infty$
Empirical formula	$C_{20}H_{32}Cl_2MnN_8O_{11}$	$C_{20}H_{29}Cl_2CoN_8O_{10}$	$C_{20}H_{28}Cl_2FeN_8O_{10}$	$C_{20}H_{30}Cl_2N_8NiO_{10}$	$C_{20}H_{24.7}Cl_2CuN_8O_{10}$
Formula weight	686.37	671.339	667.25	672.13	671.62
Temperature/K	100.0	100.0	100.0	100.0	100.0
Crystal system	monoclinic	monoclinic	monoclinic	monoclinic	monoclinic
Space group	C2/c	$P2_1/c$	$P2_1/c$	C2/c	C2/c
a/Å	18.2220(5)	18.8050(14)	18.8195(10)	18.5166(11)	18.6303(10)
b/Å	13.9035(4)	15.4107(11)	15.1945(8)	16.2958(9)	16.1633(8)
c/Å	23.6049(7)	9.5941(7)	10.0460(5)	9.3201(5)	9.4784(5)
α/°	90	90	90	90	90
β/°	94.870(2)	103.818(4)	103.644(3)	92.768(4)	92.415(4)
γ/°	90	90	90	90	90
Volume/$Å^3$	5958.7(3)	2699.9(3)	2791.6(3)	2809.0(3)	2851.7(3)
Z	8	4	4	4	4
$\rho_{calc}g/cm^3$	1.530	1.652	1.588	1.589	1.564
μ/mm^{-1}	5.857	7.426	6.694	3.344	3.393
F(000)	2840.0	1382.8	1376.0	1392.0	1375.0
Crystal size/mm^3	0.21 × 0.1 × 0.1	0.21 × 0.20 × 0.17	0.10 × 0.08 × 0.01	0.07 × 0.05 × 0.02	0.45 × 0.4 × 0.2
Radiation	CuKα (λ = 1.54178)	Cu Kα (λ = 1.54178)	CuKα (λ = 1.54178)	CuKα (λ = 1.54178)	CuKα (λ = 1.54178)
2Θ range for data collection/°	8.01 to 130.158	4.84 to 144.84	4.832 to 152.5	7.23 to 145.314	7.244 to 151.946
Index ranges	$-21 \le h \le 18$, $-9 \le k \le 16$, $-27 \le l \le 27$	$-18 \le h \le 23$, $-18 \le k \le 16$, $-11 \le l \le 6$	$-22 \le h \le 23$, $-17 \le k \le 19$, $-12 \le l \le 11$	$-21 \le h \le 22$, $-19 \le k \le 19$, $-11 \le l \le 10$	$-21 \le h \le 23$, $-20 \le k \le 17$, $-11 \le l \le 10$
Reflections collected	17486	12441	54335	27595	9442
Independent reflections	5006 [R_{int} = 0.0402, R_{sigma} = 0.0404]	5004 [R_{int} = 0.0540, R_{sigma} = 0.0788]	5547 [R_{int} = 0.0736, R_{sigma} = 0.0444]	2572 [R_{int} = 0.0781, R_{sigma} = 0.0400]	2763 [R_{int} = 0.0509, R_{sigma} = 0.0501]
Data/restraints/parameters	5006/30/418	5004/105/421	5547/0/385	2572/0/187	2763/6/206
Goodness-of-fit on F^2	1.068	1.065	1.083	1.076	1.118
Final R indexes [I>=2σ (I)]	R_1 = 0.0481, wR_2 = 0.1326	R_1 = 0.0895, wR_2 = 0.2374	R_1 = 0.0750, wR_2 = 0.2041	R_1 = 0.0617, wR_2 = 0.1674	R_1 = 0.0712, wR_2 = 0.2002
Final R indexes [all data]	R_1 = 0.0617, wR_2 = 0.1458	R_1 = 0.1304, wR_2 = 0.2710	R_1 = 0.1123, wR_2 = 0.2356	R_1 = 0.0890, wR_2 = 0.1900	R_1 = 0.0857, wR_2 = 0.2206
Largest diff. peak/hole / e $Å^{-3}$	0.91/-0.43	1.27/-0.93	1.10/-0.56	0.55/-0.55	0.80/-0.99

Identification code	**5A3**	**5B2**	**5C2**	**5E2**	**5F2**	**6F1**
	$[Mn_2(\mathbf{L5})](NO_3)_2(H_2O)_4](NO_3)_2$	$\{[Co(L^5)](BF_4)_3\}_\infty$	$\{[Fe(L^5)](BF_4)_3\}_\infty$	$\{[Zn(L^5)](BF_4)_3\}_\infty$	$\{[Cu(L^5)](BF_4)_3\}_\infty$	$\{[Cu_2(\mathbf{L6})](ClO_4)_2\}_\infty$
Empirical formula	$C_{20}H_{38}Mn_2N_{12}O_{18}$	$C_{20}H_{30}B_2CoF_8N_8O_2$	$C_{40}H_{62}B_4F_{16}Fe_2N_{16}O_5$	$C_{20}H_{30}B_2F_8N_8O_2Zn$	$C_{20}H_{30}B_2CuF_8N_8O_2$	$C_{12}H_{0.25}Cl_2CuN_{12}O_{10}$
Formula weight	844.471	647.07	1305.99	653.51	651.68	606.93
Temperature/K	120.0	100.0	106.0	100.0	100.0	100.0
Crystal system	triclinic	triclinic	triclinic	monoclinic	monoclinic	monoclinic
Space group	$P\bar{1}$	$P\bar{1}$	$P\bar{1}$	C2/c	C2/c	C2/c
a/Å	9.6194(3)	10.0286(5)	10.0668(7)	19.5350(9)	18.2228(10)	18.306(9)
b/Å	9.7752(3)	11.4663(7)	11.9380(9)	14.0069(7)	16.2157(9)	15.039(7)
c/Å	10.2915(3)	12.5989(7)	12.1166(10)	10.0241(5)	9.4651(6)	9.695(5)
α/°	106.319(2)	76.679(4)	70.664(5)	90	90	90
β/°	93.715(2)	88.465(4)	89.417(6)	90.699(2)	91.685(4)	111.18(3)
γ/°	110.610(1)	80.886(3)	89.948(6)	90	90	90
Volume/Å^3	854.74(5)	1391.91(14)	1373.93(19)	2742.6(2)	2795.7(3)	2489(2)
Z	1	2	1	4	4	4
ρ_{calc}g/cm^3	1.641	1.544	1.578	1.583	1.548	1.620
μ/mm^{-1}	6.851	5.644	5.245	2.066	1.910	3.881
F(000)	436.9	662.0	670.0	1336.0	1332.0	1197.0
Crystal size/mm^3	0.34 × 0.28 × 0.28	0.2 × 0.15 × 0.08	0.14 × 0.12 × 0.10	0.45 × 0.35 × 0.2	0.25 × 0.2 × 0.1	0.14 × 0.1 × 0.1
Radiation	Cu Kα (λ = 1.54178)	CuKα (λ = 1.54178)	CuKα (λ = 1.54178)	CuKα (λ = 1.54178)	CuKα (λ = 1.54178)	CuKα (λ = 1.54178)
2Θ range for data collection/°	9.1 to 151.92	8.022 to 152.708	7.732 to 144.294	7.766 to 152.346	7.298 to 152.184	7.834 to 135.714
Index ranges	-12 ≤ h ≤ 11, -11 ≤ k ≤ 11, -12 ≤ l ≤ 12	-11 ≤ h ≤ 11, -14 ≤ k ≤ 13, -14 ≤ l ≤ 15	-12 ≤ h ≤ 11, -13 ≤ k ≤ 14, -14 ≤ l ≤ 14	-24 ≤ h ≤ 21, -17 ≤ k ≤ 17, -12 ≤ l ≤ 12	-19 ≤ h ≤ 22, -19 ≤ k ≤ 20, -11 ≤ l ≤ 11	-21 ≤ h ≤ 20, -13 ≤ k ≤ 17, -10 ≤ l ≤ 11
Reflections collected	14781	17184	13189	9423	11335	7478
Independent reflections	3273 [R_{int} = 0.0529, R_{sigma} = 0.0443]	5370 [R_{int} = 0.0601, R_{sigma} = 0.0727]	5128 [R_{int} = 0.0589, R_{sigma} = 0.0827]	2774 [R_{int} = 0.0426, R_{sigma} = 0.0411]	2639 [R_{int} = 0.0446, R_{sigma} = 0.0441]	2180 [R_{int} = 0.1302, R_{sigma} = 0.1614]
Data/restraints/parameters	3273/2/241	5370/0/373	5128/0/385	2774/0/188	2639/6/206	2180/122/168
Goodness-of-fit on F^2	1.120	1.086	1.099	1.098	1.139	1.402
Final R indexes [I>=2σ (I)]	R_1 = 0.0612, wR_2 = 0.1730	R_1 = 0.0849, wR_2 = 0.2297	R_1 = 0.0745, wR_2 = 0.1992	R_1 = 0.0816, wR_2 = 0.2364	R_1 = 0.0596, wR_2 = 0.1554	R_1 = 0.2280, wR_2 = 0.5080
Final R indexes [all data]	R_1 = 0.0630, wR_2 = 0.1749	R_1 = 0.1201, wR_2 = 0.2612	R_1 = 0.1116, wR_2 = 0.2271	R_1 = 0.0855, wR_2 = 0.2417	R_1 = 0.0835, wR_2 = 0.1809	R_1 = 0.4061, wR_2 = 0.5949
Largest diff. peak/hole / e Å^{-3}	1.26/-1.01	1.05/-0.49	0.76/-0.77	1.36/-0.89	0.53/-0.83	0.95/-0.66

Identification code	**L1b**	**L3**	$\{[Ag_2(\mathbf{L^3})](NO)_4\}_\infty$	
Empirical formula	$C_{20}H_{22}Cl_2N_6O_{10}$	$C_{11}H_9N_4$	$C_{24}H_{24}N_{12}O_4Ag_2$	
Formula weight	577.33	197.22	760.273	
Temperature/K	100.0	100.0	102.0	
Crystal system	triclinic	monoclinic	monoclinic	
Space group	$P\bar{1}$	$P2_1/c$	$P2_1/n$	
a/Å	5.4780(4)	16.8966(6)	9.594(5)	
b/Å	8.0950(6)	5.5208(2)	12.263(8)	
c/Å	13.4428(11)	9.9782(4)	10.309(5)	
α/°	97.598(3)	90	90	
β/°	93.434(3)	102.079(2)	90	
γ/°	101.508(3)	90	90	
Volume/Å^3	576.71(8)	910.19(6)	1212.9(12)	
Z	1	4	2	
ρ_{calc}g/cm^3	1.662	1.439	2.082	
μ/mm^{-1}	3.185	0.741	13.501	
F(000)	298.0	412.0	759.4	
Crystal size/mm^3	0.45 × 0.35 × 0.15	0.27 × 0.10 × 0.08	0.18 × 0.14 × 0.10	
Radiation	CuKα (λ = 1.54178)	CuKα (λ = 1.54178)	Cu Kα (λ = 1.54178)	
2Θ range for data collection/°	6.66 to 152.144	5.348 to 151.674	11.22 to 145.38	
Index ranges	-6 ≤ h ≤ 6, -10 ≤ k ≤ 9, -16 ≤ l ≤ 15	-21 ≤ h ≤ 19, -6 ≤ k ≤ 6, -11 ≤ l ≤ 10	-11 ≤ h ≤ 10, -15 ≤ k ≤ 10, -11 ≤ l ≤ 12	
Reflections collected	8144	10503	9073	
Independent reflections	2198 [R_{int} = 0.0414, R_{sigma} = 0.0394]	1769 [R_{int} = 0.0342, R_{sigma} = 0.0245]	2205 [R_{int} = 0.2758, R_{sigma} = 0.3058]	
Data/restraints/parameters	2198/0/181	1769/0/137	2205/163/164	
Goodness-of-fit on F^2	1.156	1.048	1.139	
Final R indexes [I>=2σ (I)]	R_1 = 0.0607, wR_2 = 0.1717	R_1 = 0.0373, wR_2 = 0.0970	R_1 = 0.1880, wR_2 = 0.4076	
Final R indexes [all data]	R_1 = 0.0634, wR_2 = 0.1755	R_1 = 0.0403, wR_2 = 0.0998	R_1 = 0.3515, wR_2 = 0.5216	
Largest diff. peak/hole / e Å^{-3}	0.50/-0.57	0.21/-0.20	2.08/-1.84	

A12.0 Appendix: NMR and Other Characterisation

A12.1 Characterisation of Endo-imine molecules: (A2) (B1) ($L1^{endo}$) (L2)

A12.1.1 ^{1}H NMR of 2,5-distyryl pyrazine (A2)

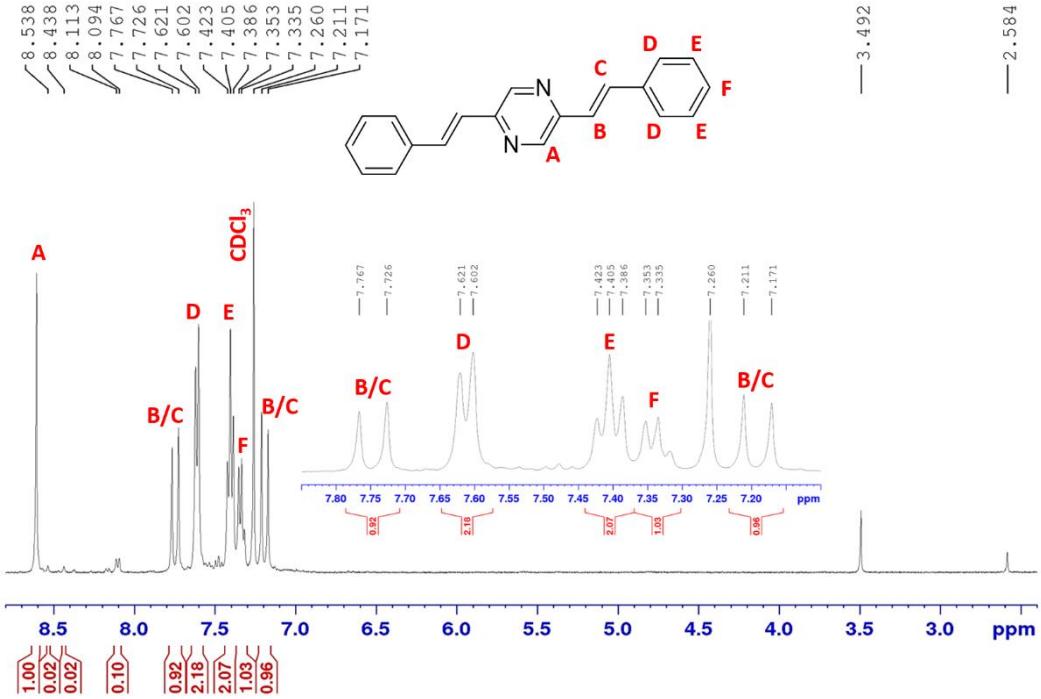

^{1}HNMR of **A2**. Reference solvent peak ($CDCl_3$) at 7.260 ppm

A12.1.2 ^{1}H NMR of 2,5-diformyl pyrazine (B1)

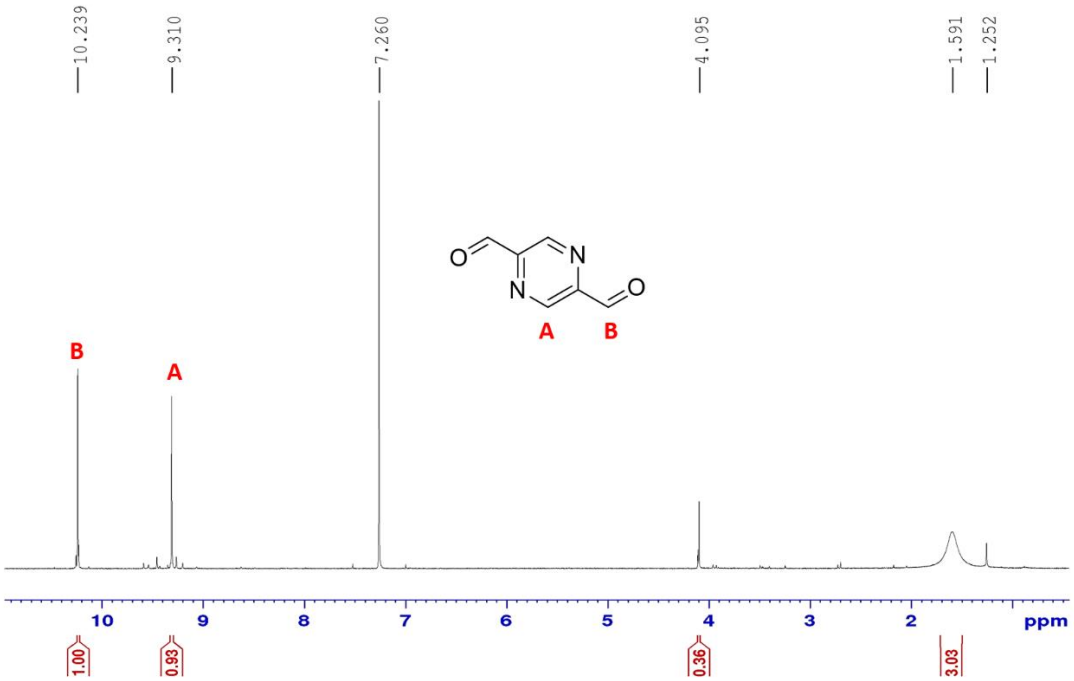

^{1}HNMR of **A2**. Reference solvent peak ($CDCl_3$) at 7.260 ppm

A12.1.3 ^{1}H NMR of ($L1^{endo}$)

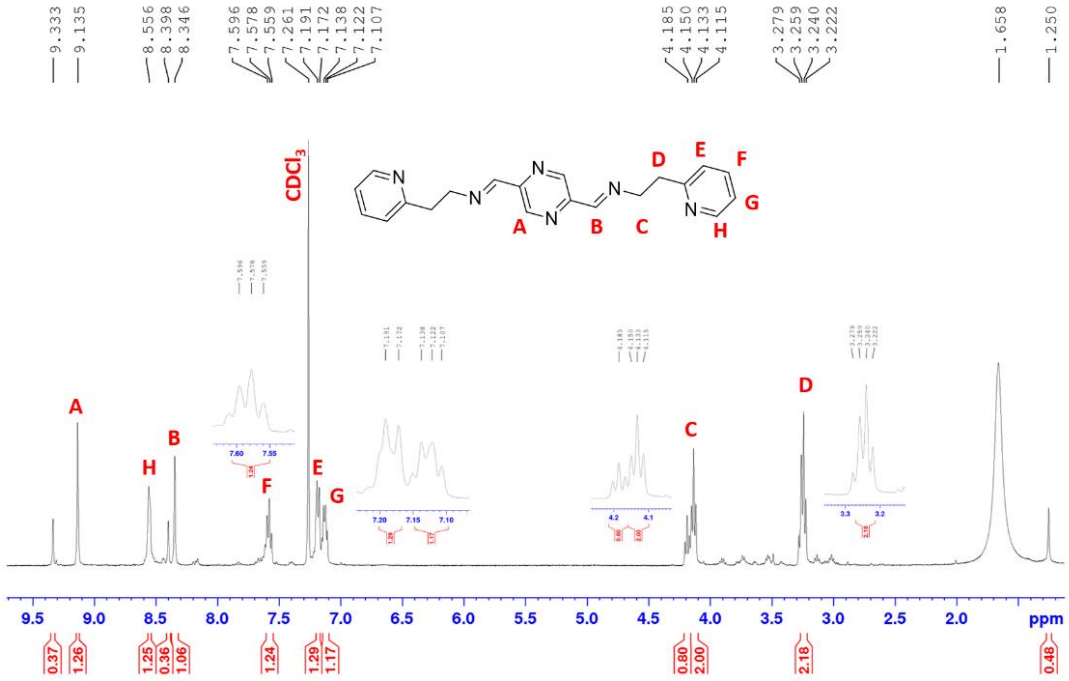

^{1}HNMR of **$L1^{endo}$**. Reference solvent peak ($CDCl_3$) at 7.260 ppm

A12.1.5 ^{1}H NMR of (L2)

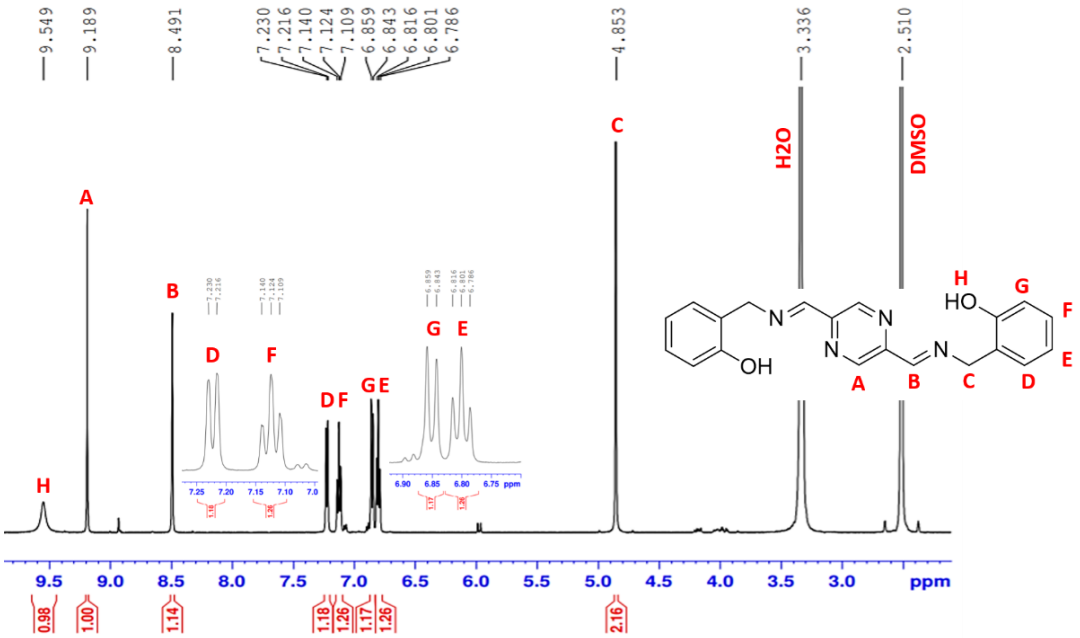

^{1}HNMR of **L2**. Reference solvent peak (DMSO) at 2.510 ppm.

A12.1.6 ^{13}C NMR of (L2)

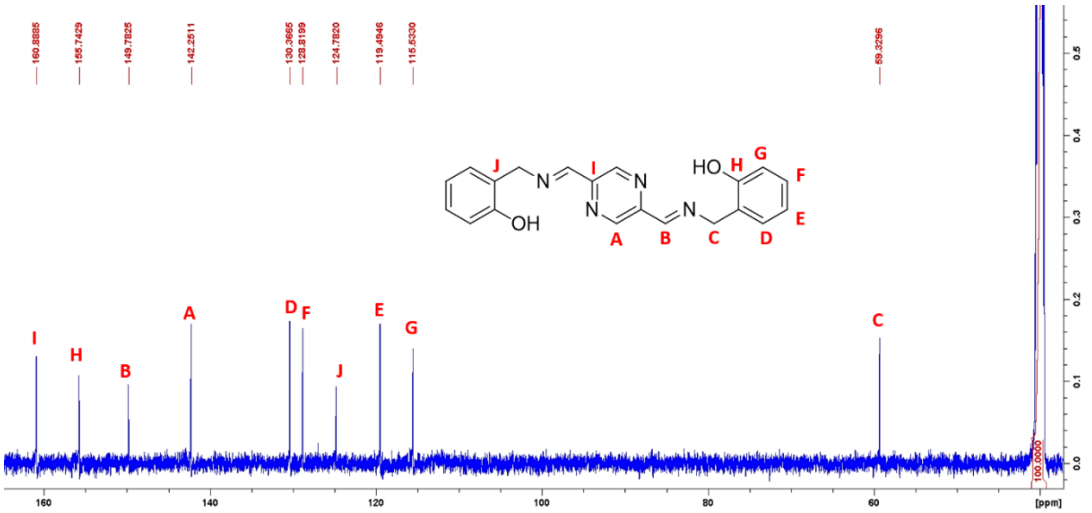

^{13}CNMR of L2. Reference solvent peak (DMSO) at 40 ppm.

A12.1.7 COSY of (L2)

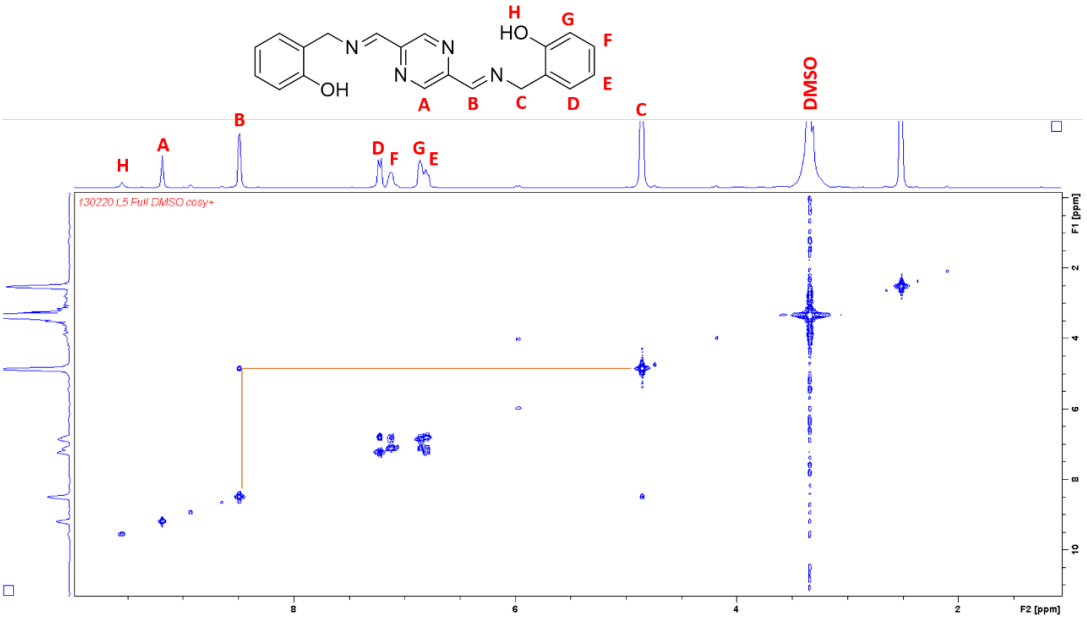

COSY of **L2**. Reference solvent peak (DMSO) at 2.50 ppm

A12.1.8 HMQC of (L2)

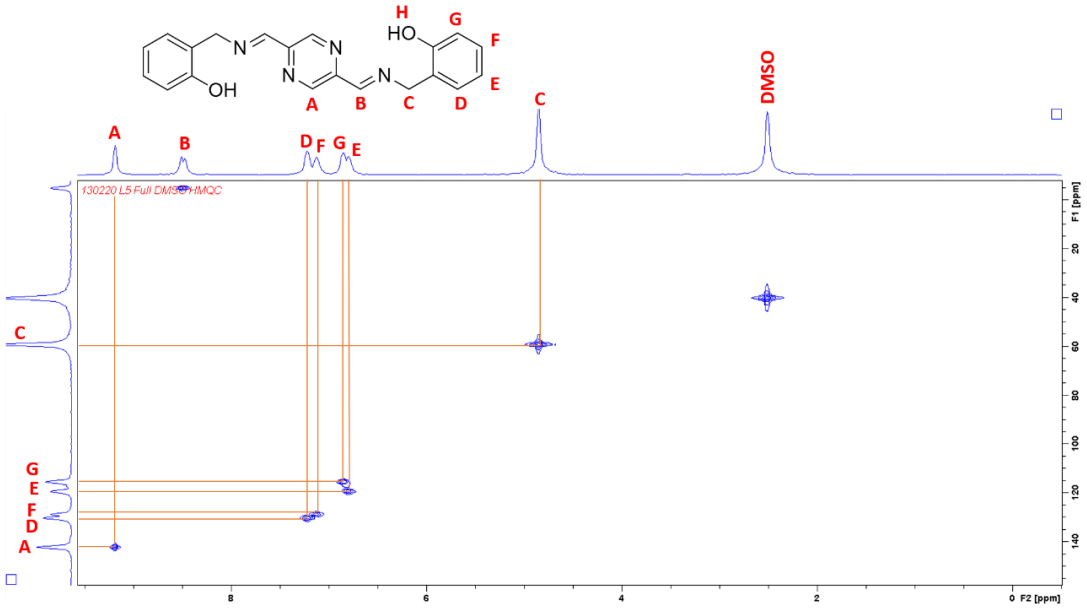

HMQC of **L2**. Reference solvent peak (DMSO) at 2.50 ppm

A12.2 Characterisation of the amine synthesis pathway: (C1) (C2) (C3) (C4) (C5) (C6) (D1)

A12.2.0 ^{1}H NMR Pathway Molecules Comparison:

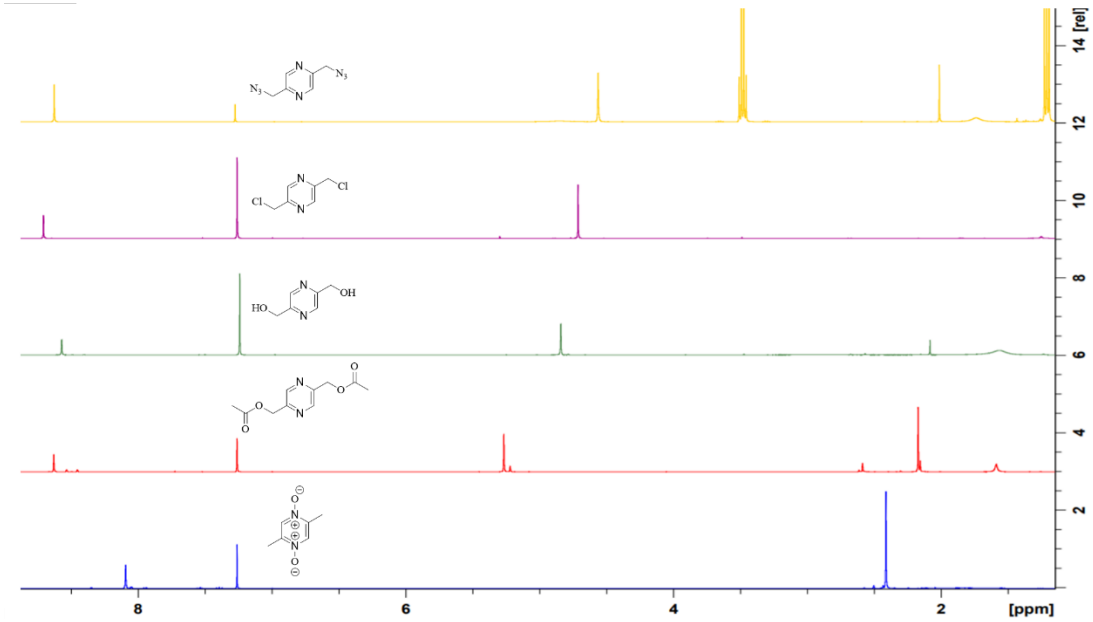

^{1}HNMR of **C1-C4, and D1**. Reference solvent peak ($CDCl_3$) at 7.26 ppm

A12.2.1 ^{1}H NMR of 2,5-dimethylpyrazine-1,4-N-oxide (C1)

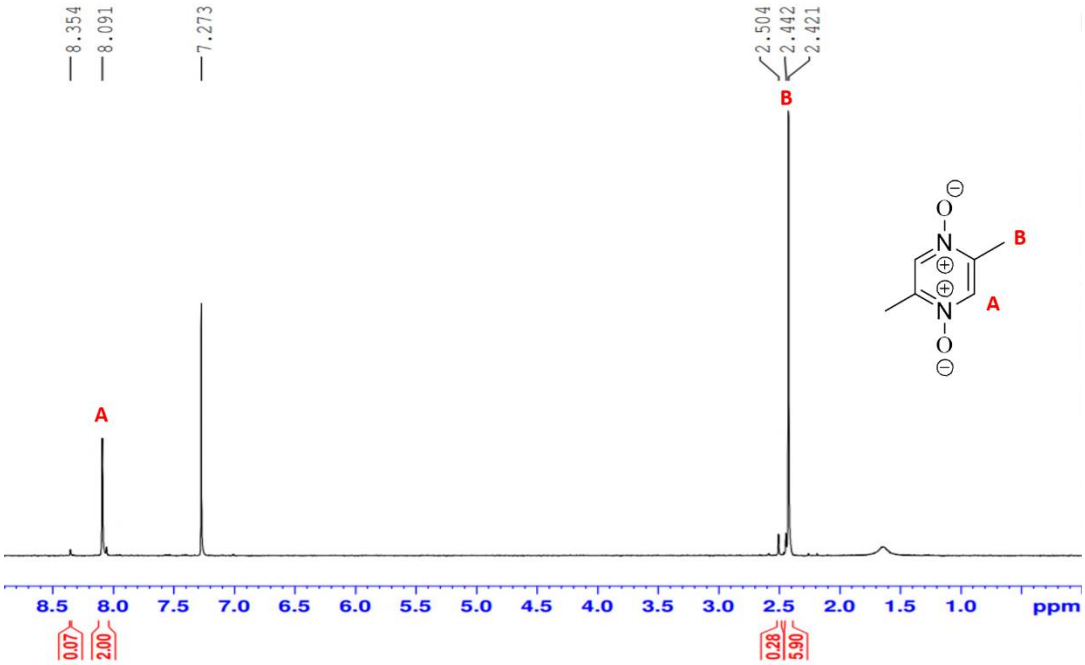

^{1}HNMR of **C1**. Reference solvent peak ($CDCl_3$) at 7.273 ppm

A12.2.2 ^{1}H NMR of 2,5-di(acetoxymethyl)pyrazine (C2)

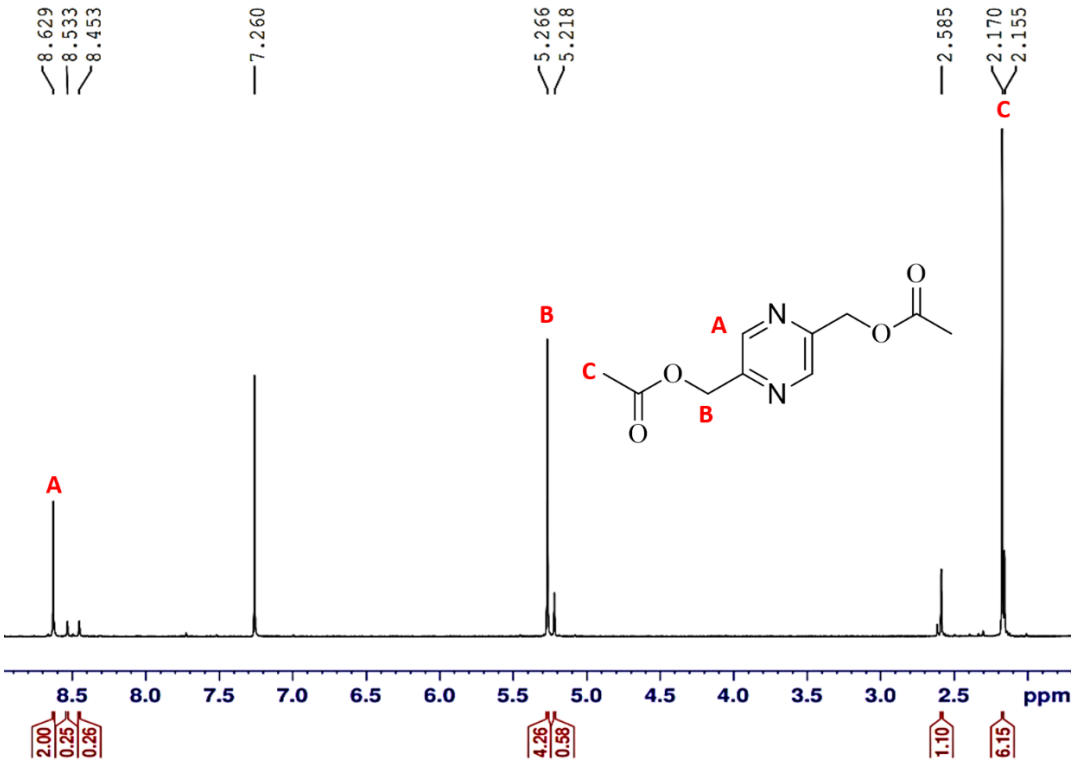

^{1}HNMR of **C2**. Reference solvent peak ($CDCl_3$) at 7.260 ppm

A12.2.3 ^{1}H NMR of 2,5-di(hydroxymethyl)pyrazine (C3)

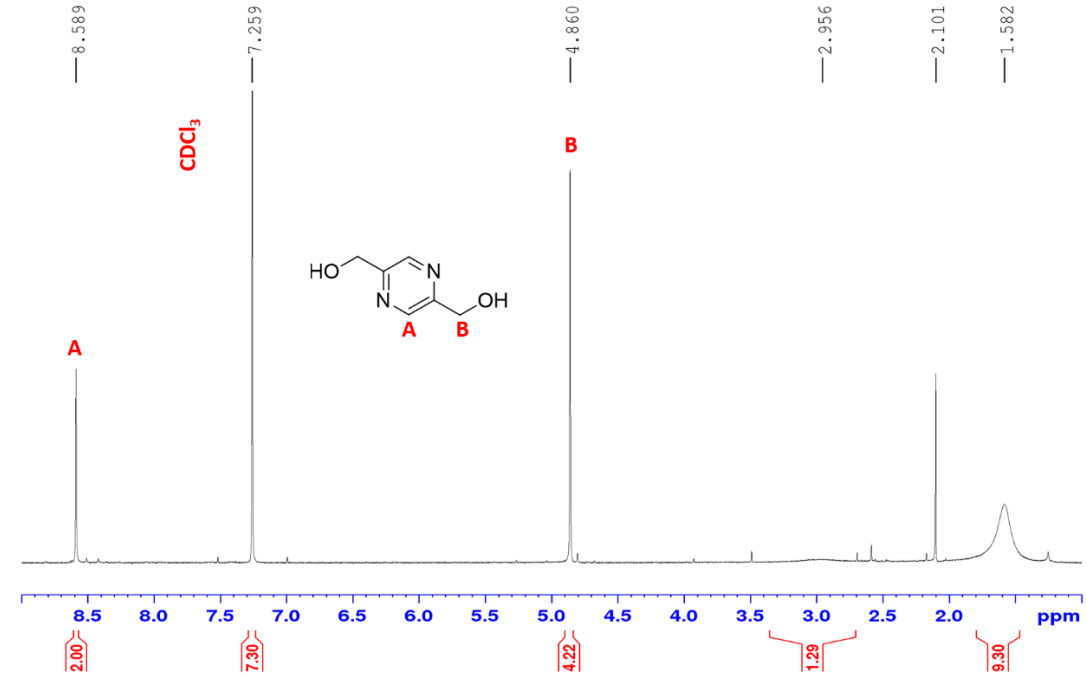

^{1}HNMR of **C3**. Reference solvent peak ($CDCl_3$) at 7.259 ppm

A A12.2.4 [1]H NMR of 2,5-di(chloromethyl)pyrazine (C4)

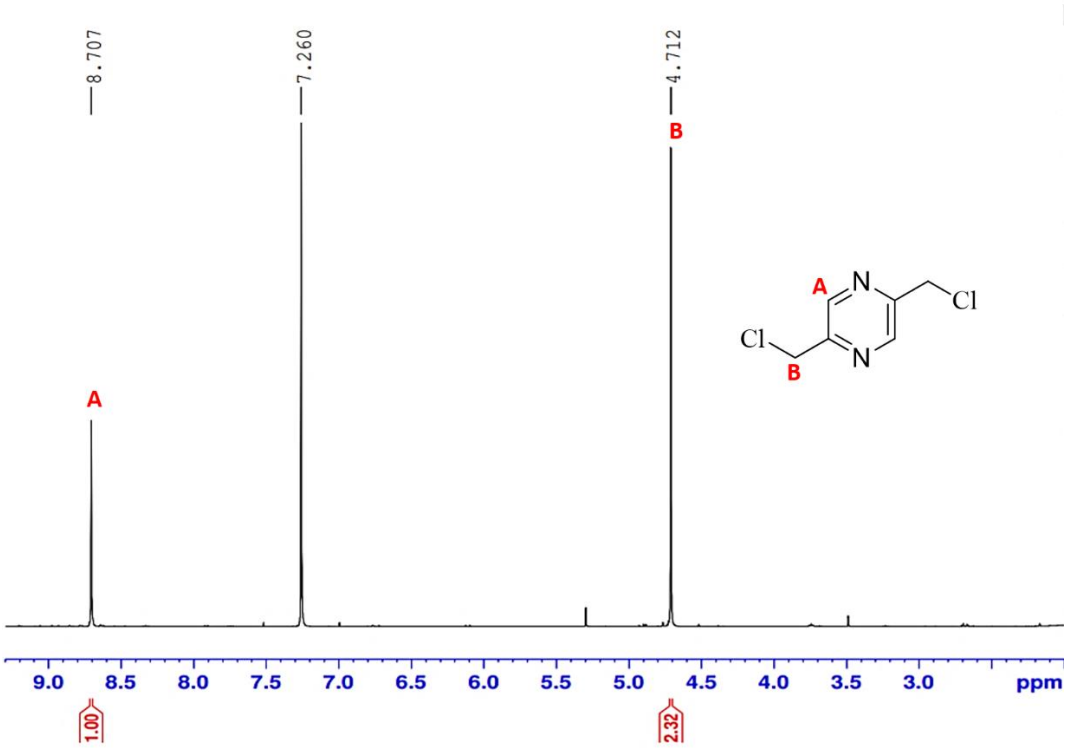

[1]HNMR of **C4**. Reference solvent peak ($CDCl_3$) at 7.260 ppm

A12.2.5 [1]H NMR of 2,5-bis(phthalamidemethyl)pyrazine (C5)

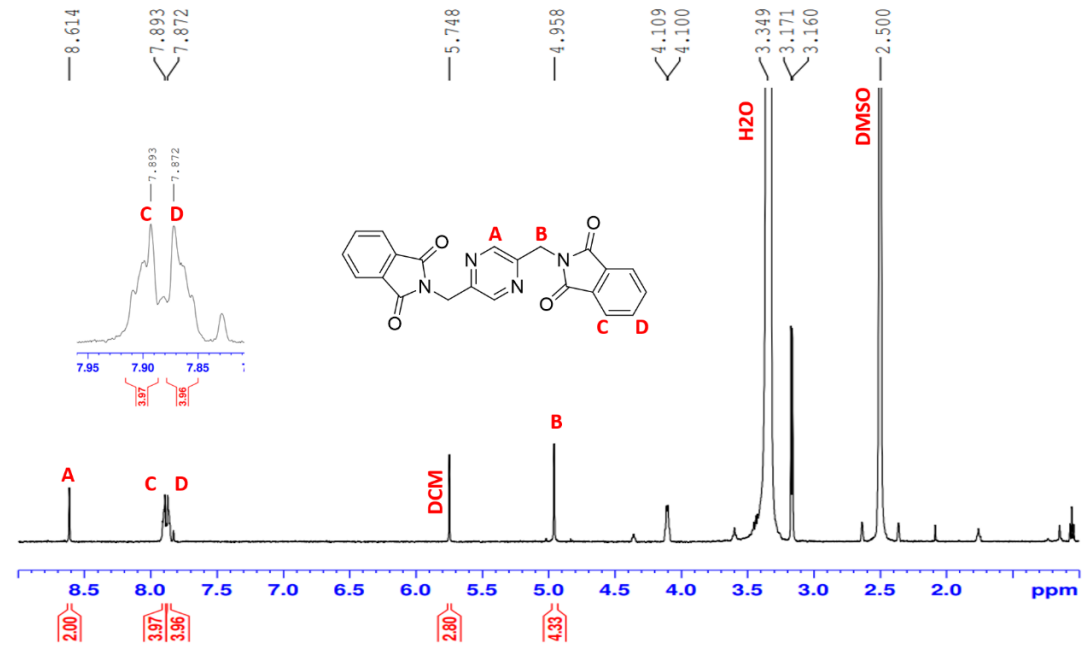

[1]HNMR of **C5**. Reference solvent peak (DMSO) at 2.50 ppm

A12.2.6 ^{13}C NMR of 2,5-bis(phthalamidemethyl)pyrazine (C5)

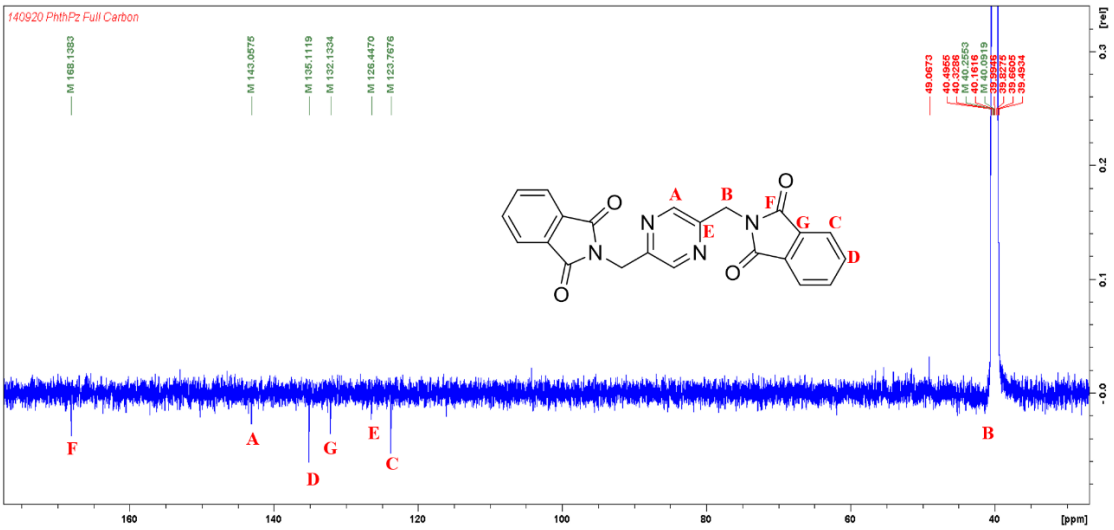

^{13}CNMR of **C5**. Reference solvent peak (DMSO) at 40 ppm.

A12.2.7 HMQC of 2,5-bis(phthalamidemethyl)pyrazine (C5)

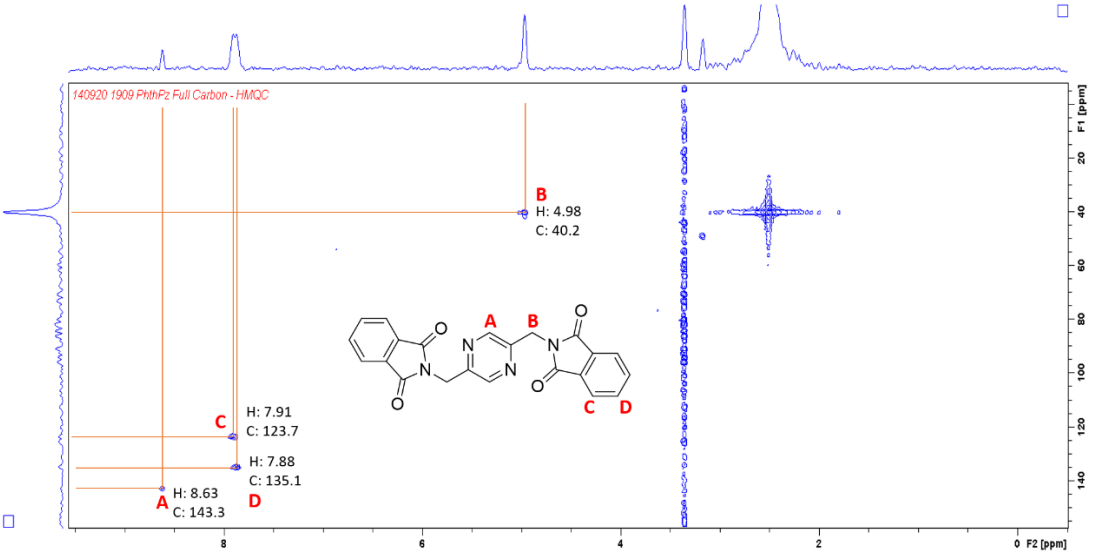

HMQC of **C5**. Reference solvent peak (DMSO) at 40 ppm.

A12.2.8 AT-FIR of 2,5-bis(phthalamidemethyl)pyrazine (C5)

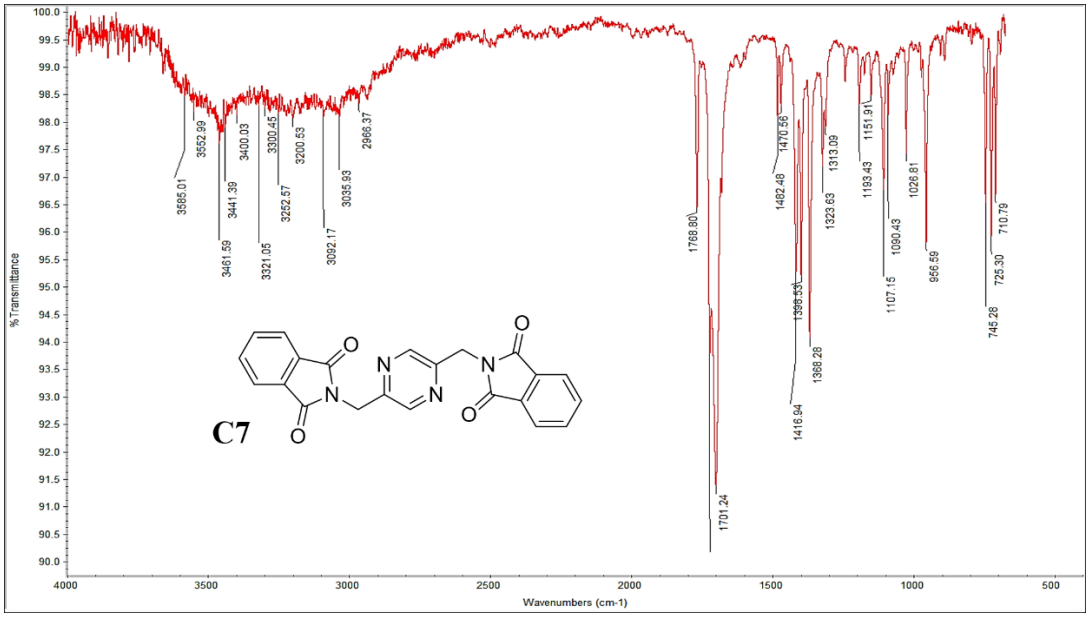

ATR-IR of **C5**.

A12.2.9 ^{1}H NMR of 2,5-di(azidomethyl)pyrazine (D1)

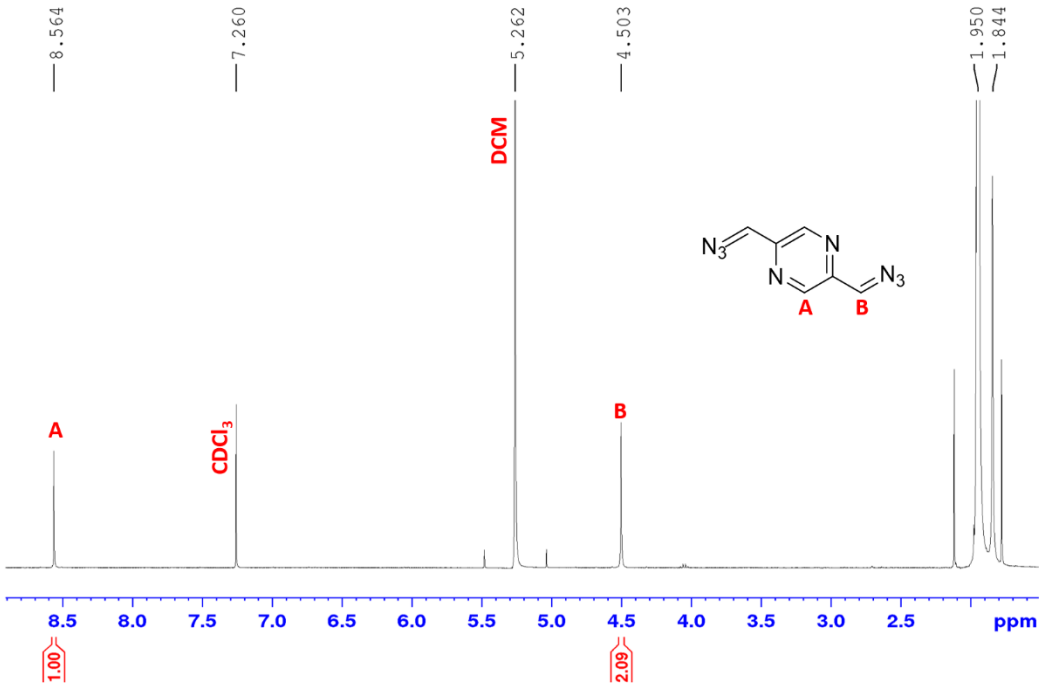

^{1}HNMR of **D1**. Reference solvent peak ($CDCl_3$) at 7.260 ppm

A12.3.0 Characterisation of (L3) and (L4)

A12.3.1 ^{1}H NMR of (L3)

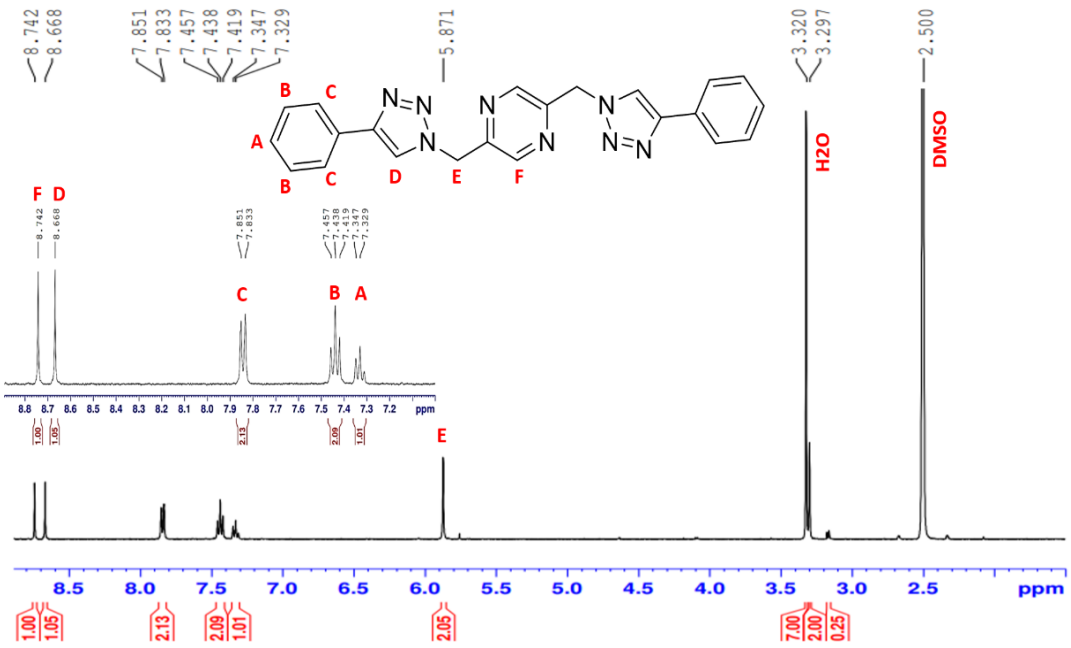

^{1}HNMR of **L3**. Reference solvent peak (DMSO) at 2.50 ppm

A12.3.2 COSY of (L3)

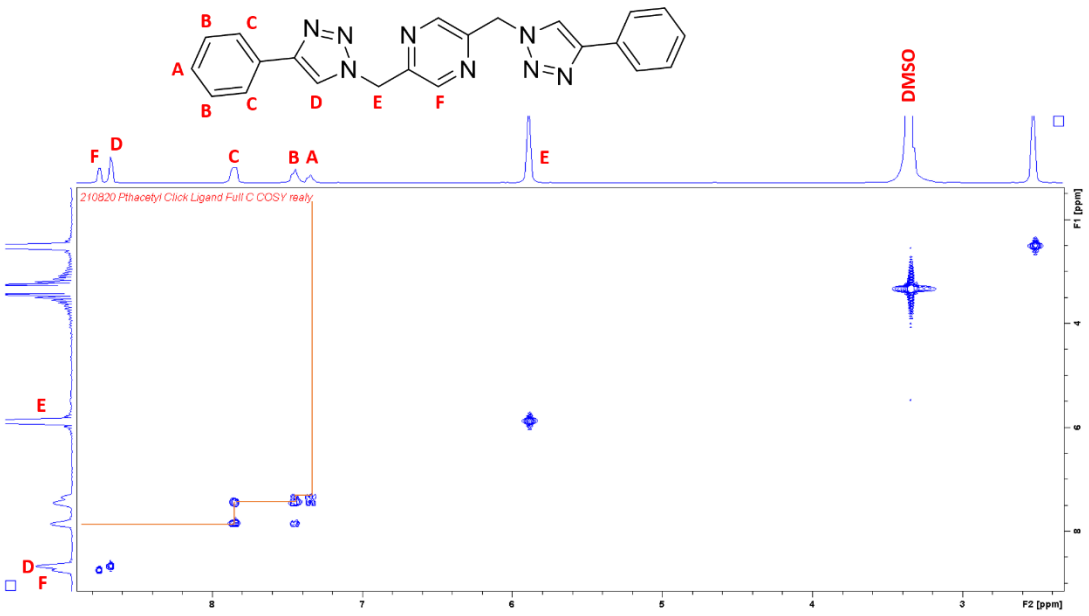

COSY of **L3**. Reference solvent peak (DMSO) at 2.50 ppm

A12.3.3 HMQC of (L3)

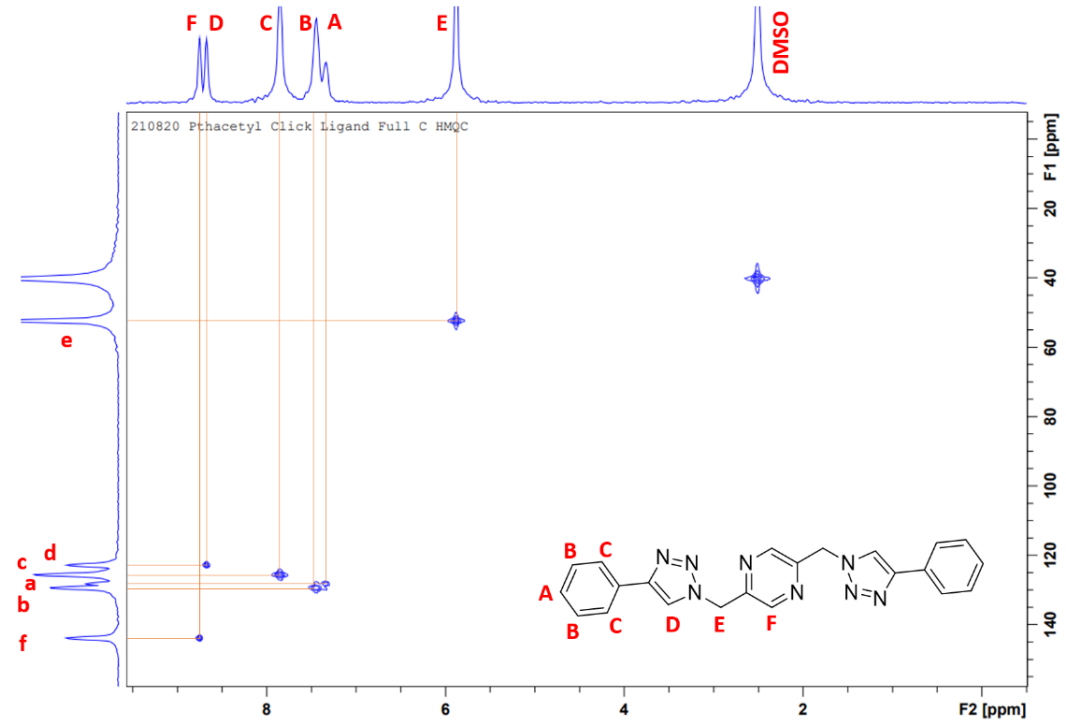

HMQC of **L3**. Reference solvent peak (DMSO) at 2.50 ppm

A12.3.4 ^{1}H NMR of (D3)

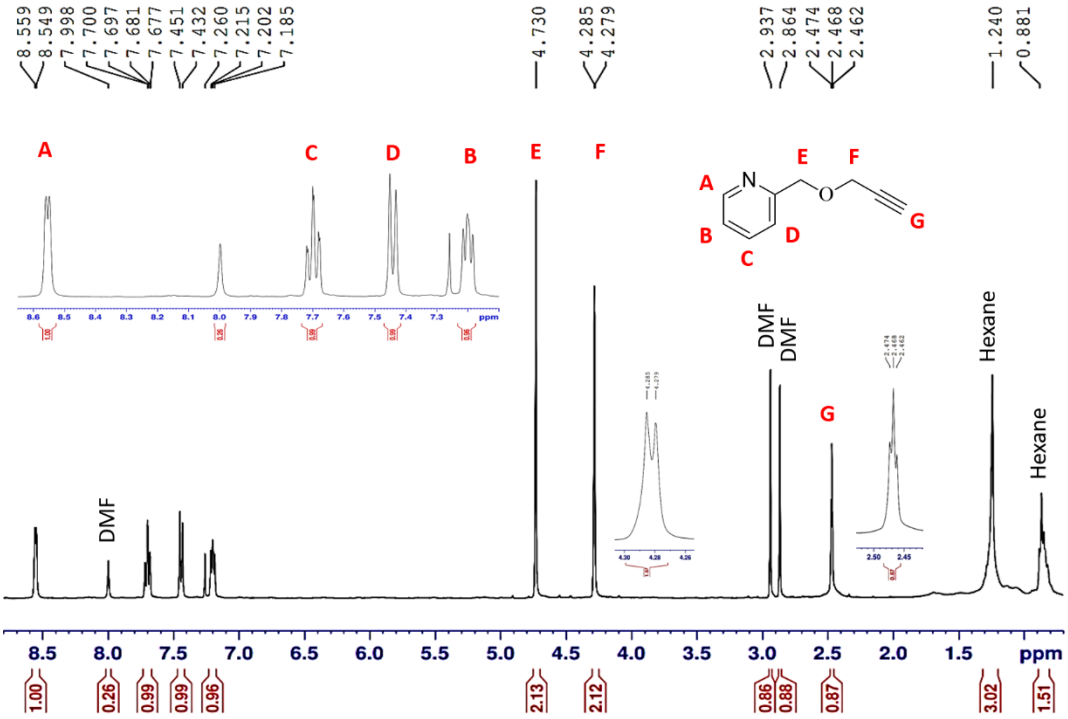

^{1}HNMR of **D3**. Reference solvent peak ($CDCl_3$) at 7.260 ppm

A12.3.5 ^{1}H NMR of (L4)

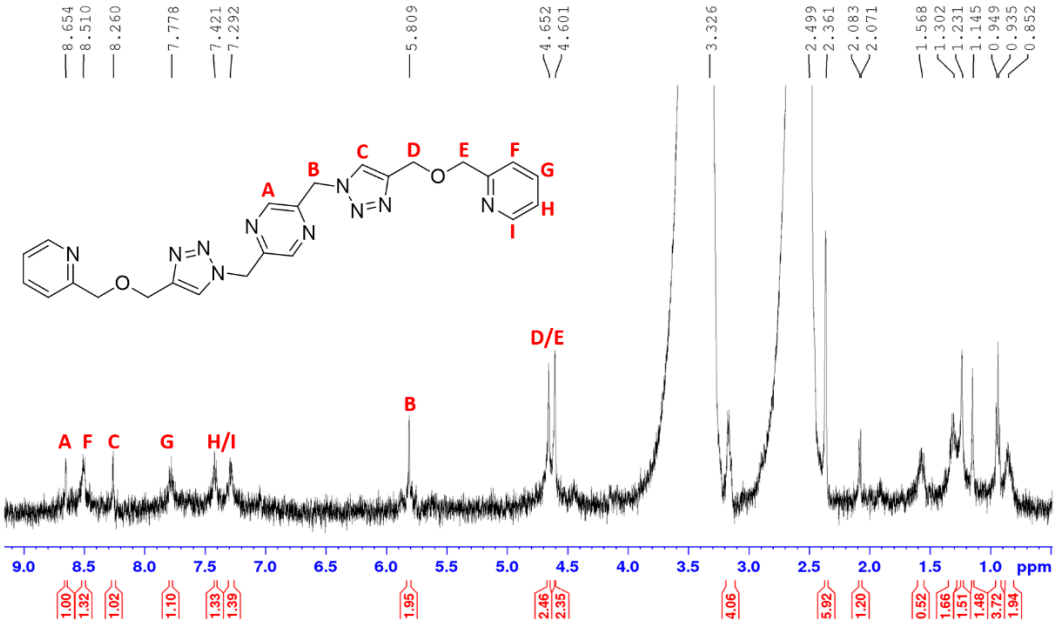

^{1}HNMR of **L4**. Reference solvent peak (DMSO) at 2.49 ppm

A12.4.0 Characterisation of (L5) and (L6)

A12.4.01 ^{1}H NMR of (E1)

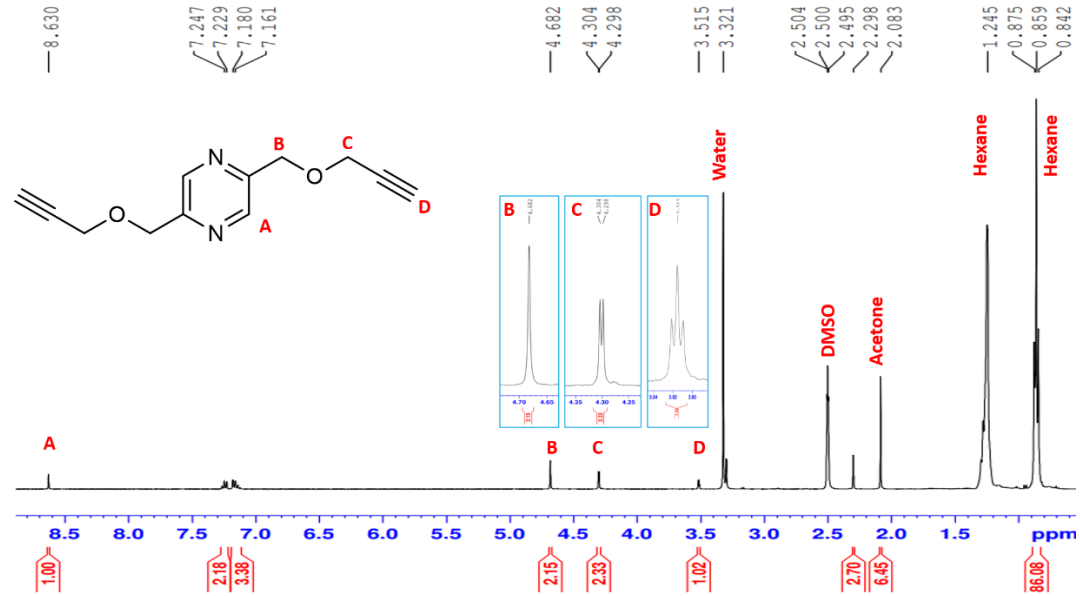

^{1}HNMR of **E1** Reference solvent peak (DMSO) at 2.50 ppm

A12.4.02 ^{13}C NMR of (E1)

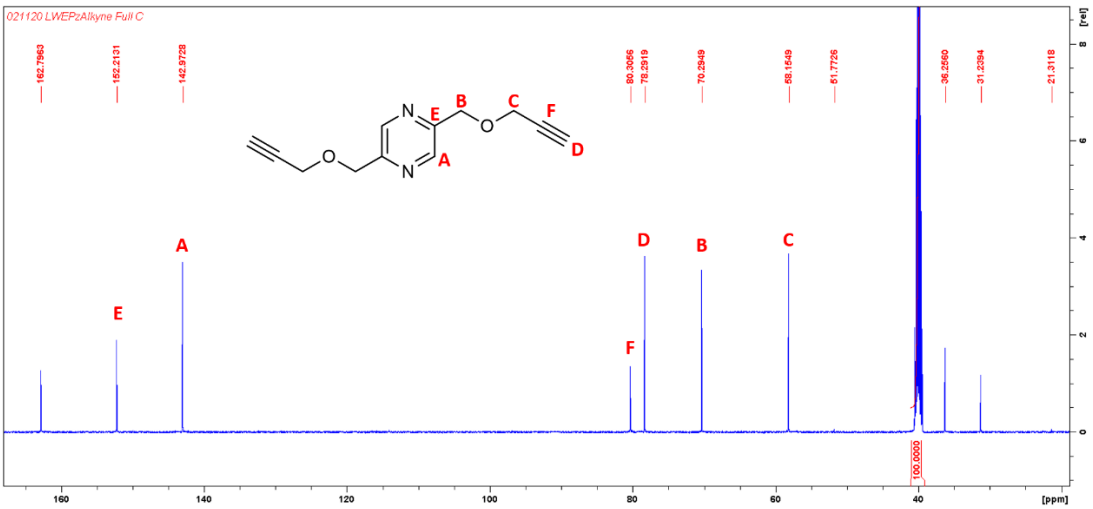

^{13}CNMR of E1. Reference solvent peak (DMSO) at 40 ppm.

A12.4.03 HMQC of (E1)

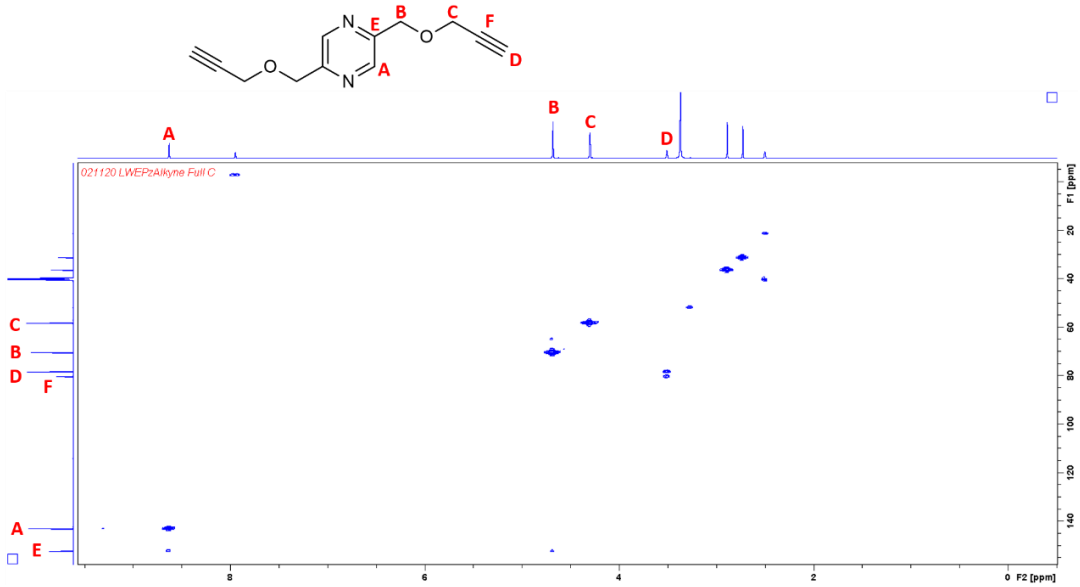

HMQC of **L3**. Reference solvent peak (DMSO) at 2.50 ppm

A12.4.04 ^{1}H NMR of (E2)

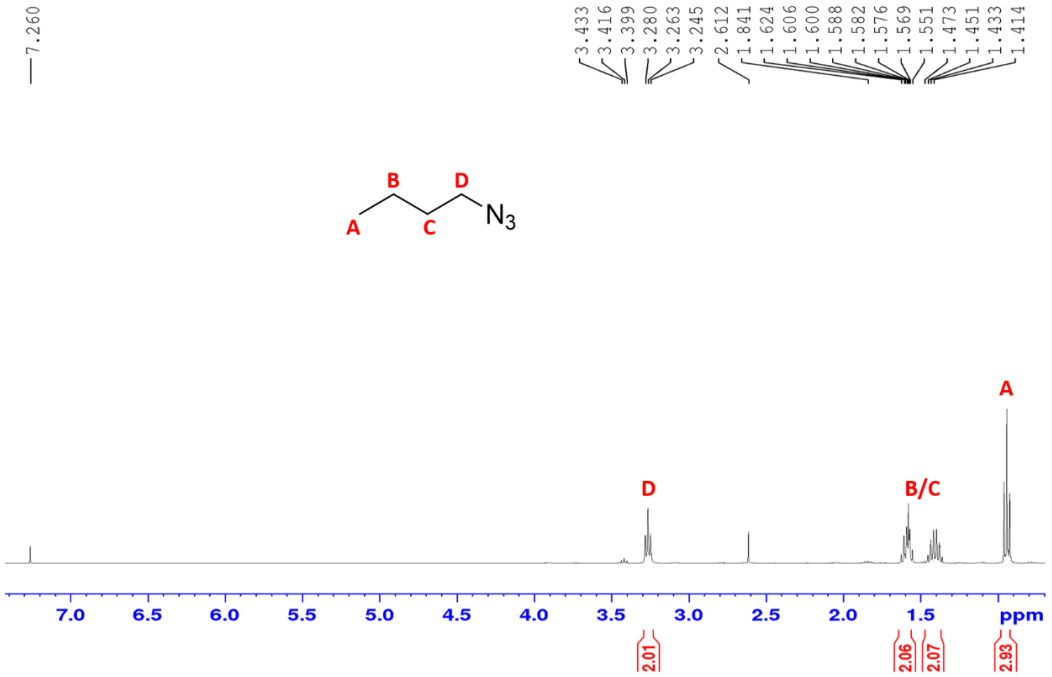

^{1}HNMR of **E2**. Reference solvent peak ($CDCl_3$) at 7.260 ppm.

A12.4.05 ^{1}H NMR of (E3)

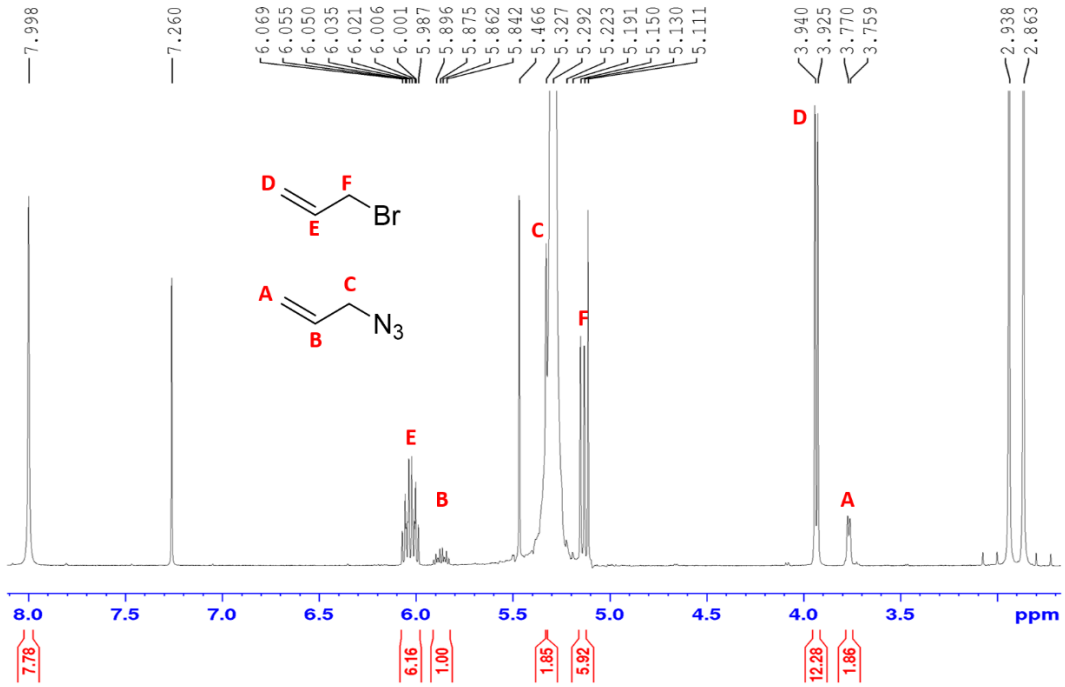

^{1}HNMR of **E3** and allyl bromide reagent. Reference solvent peak ($CDCl_3$) at 7.260 ppm

A12.4.06 ^{1}H NMR of (E3)

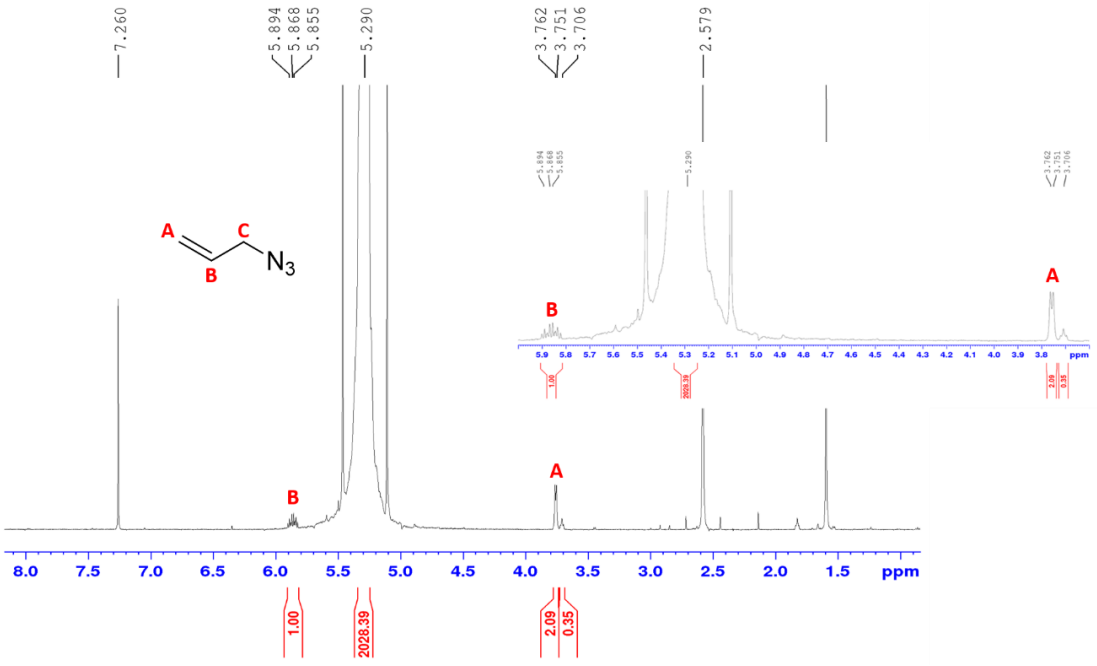

^{1}HNMR of **E3**. Reference solvent peak ($CDCl_3$) at 7.260 ppm

A12.4.07 ^{1}H NMR of (L5)

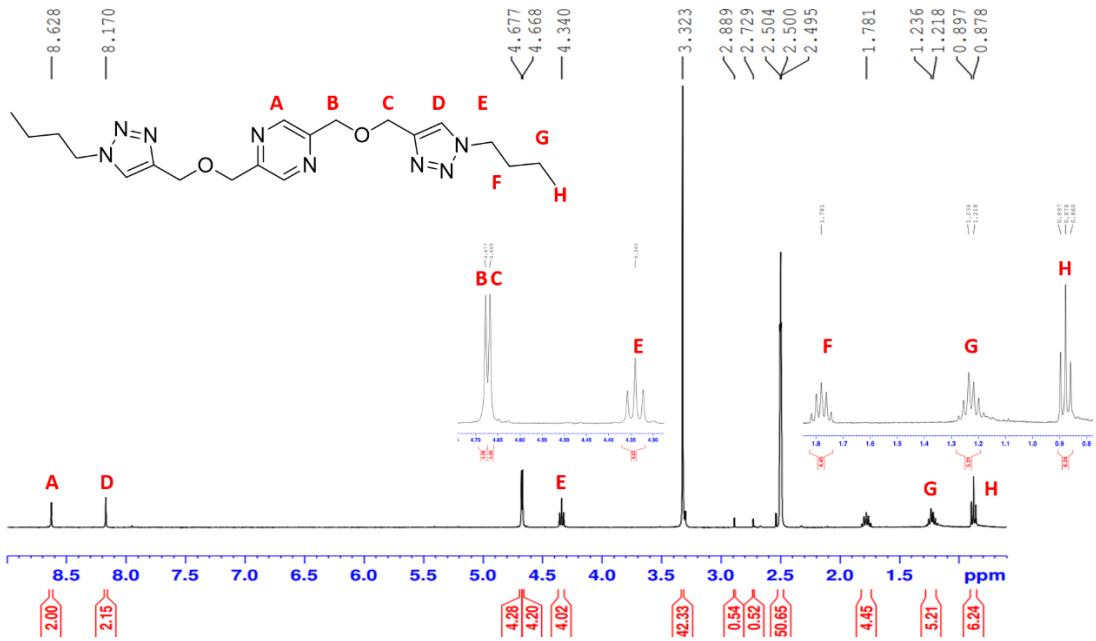

^{1}HNMR of **L5**. Reference solvent peak (DMSO) at 2.50 ppm

A12.4.08 ^{13}C NMR of (L5)

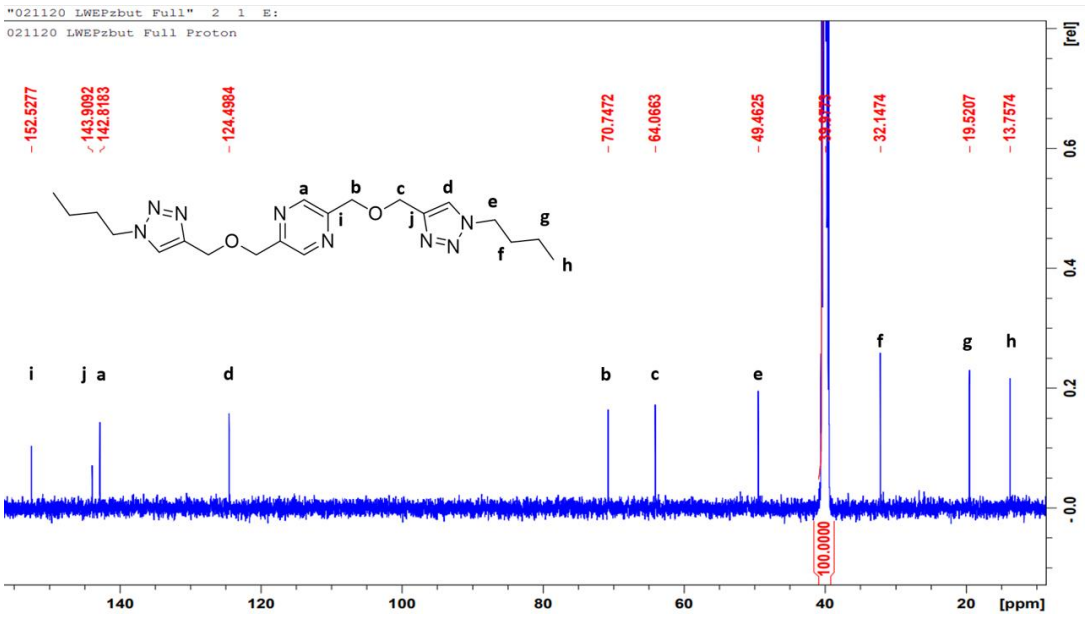

^{13}CNMR of **L5**. Reference solvent peak (DMSO) at 39.97 ppm

A12.4.09 COSY of (L5)

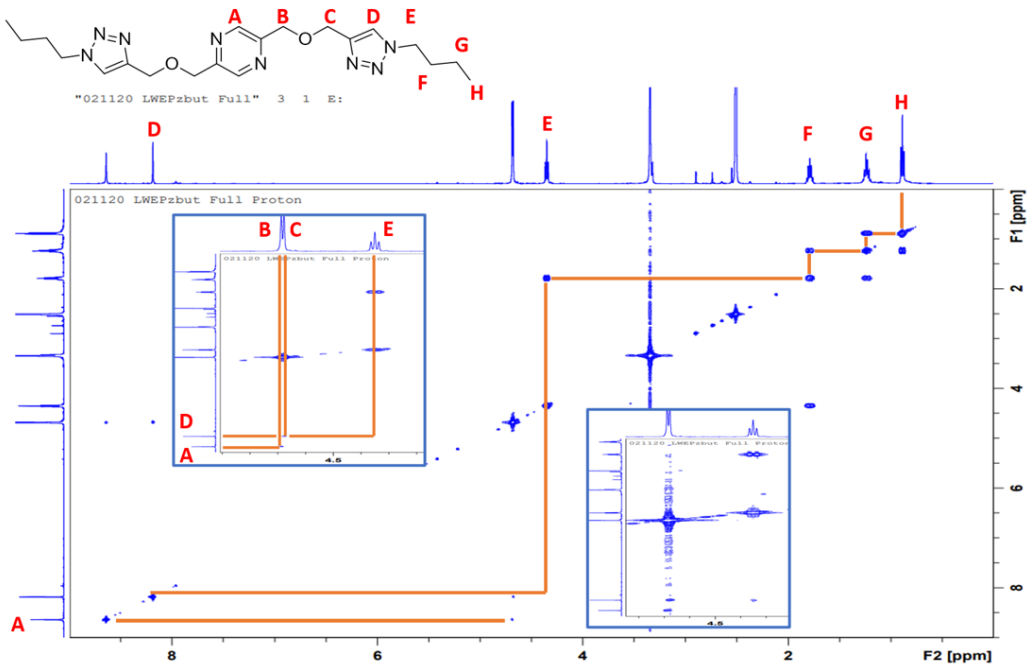

COSY of **L5**. Reference solvent peak (DMSO) at 39.97 ppm

A12.4.10 HMQC of (L5)

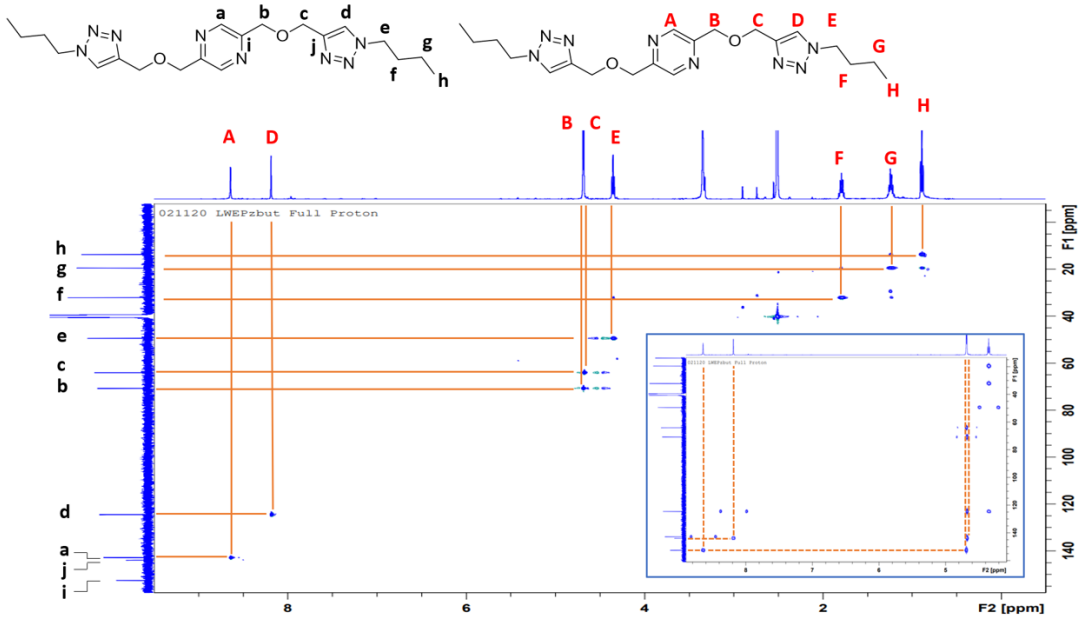

HMQC of **L5**. Reference solvent peak (DMSO) at 39.97 ppm

A12.4.11 ^{1}H NMR of (L6)

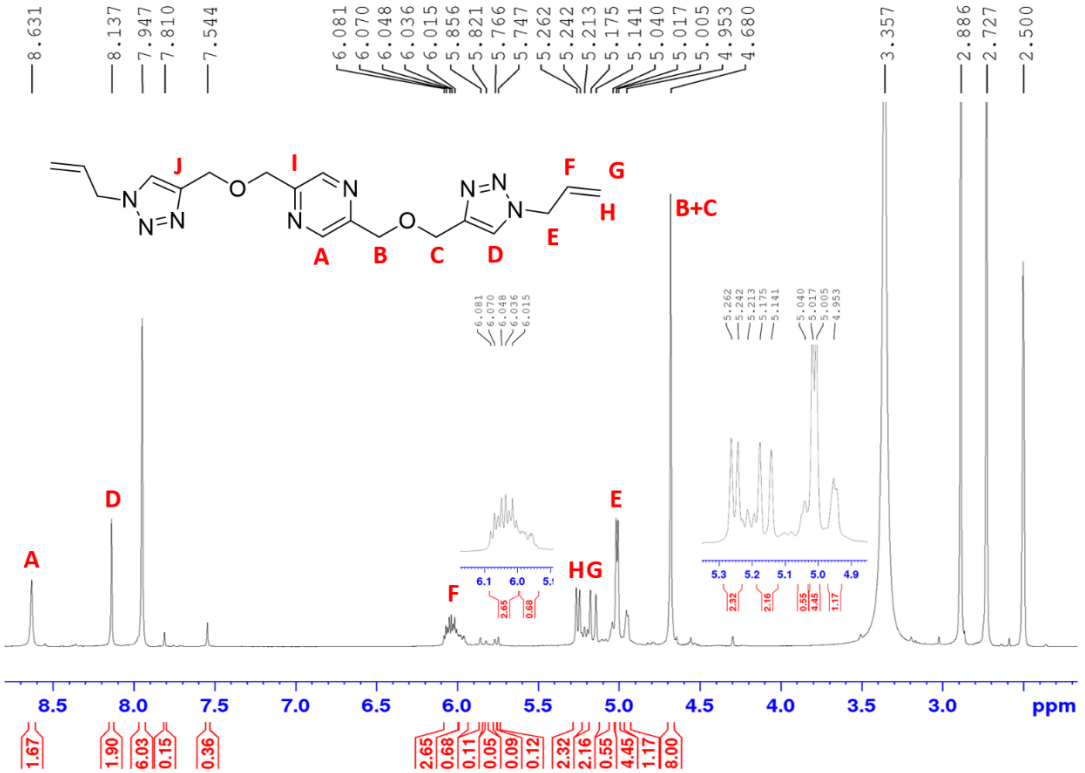

[1]HNMR of **L6**. Reference solvent peak (DMSO) at 2.50 ppm

A12.4.12 ^{13}C NMR of (L6)

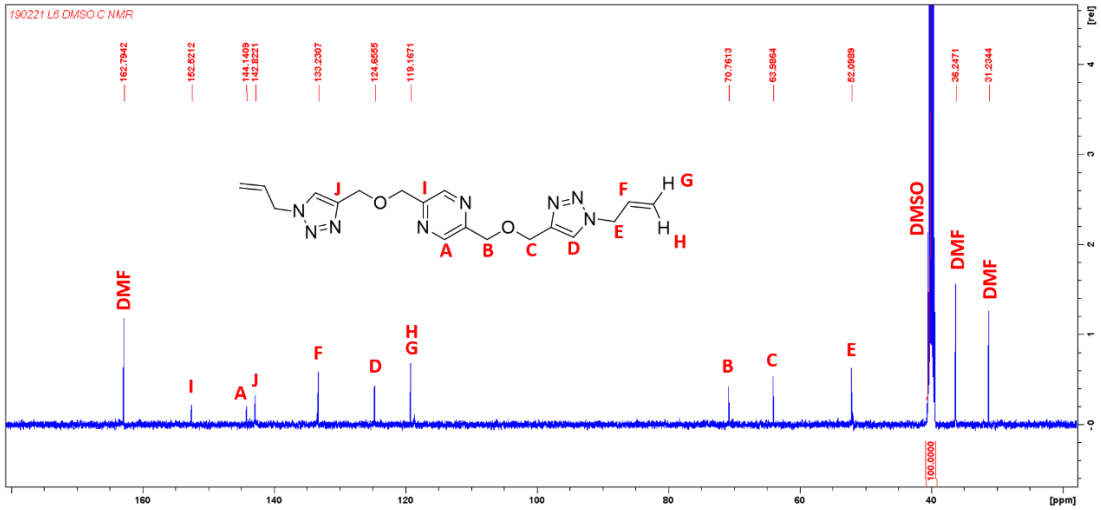

[13]CNMR of **L6**. Reference solvent peak (DMSO) at 39.97 ppm

A12.4.13 COSY of (L6)

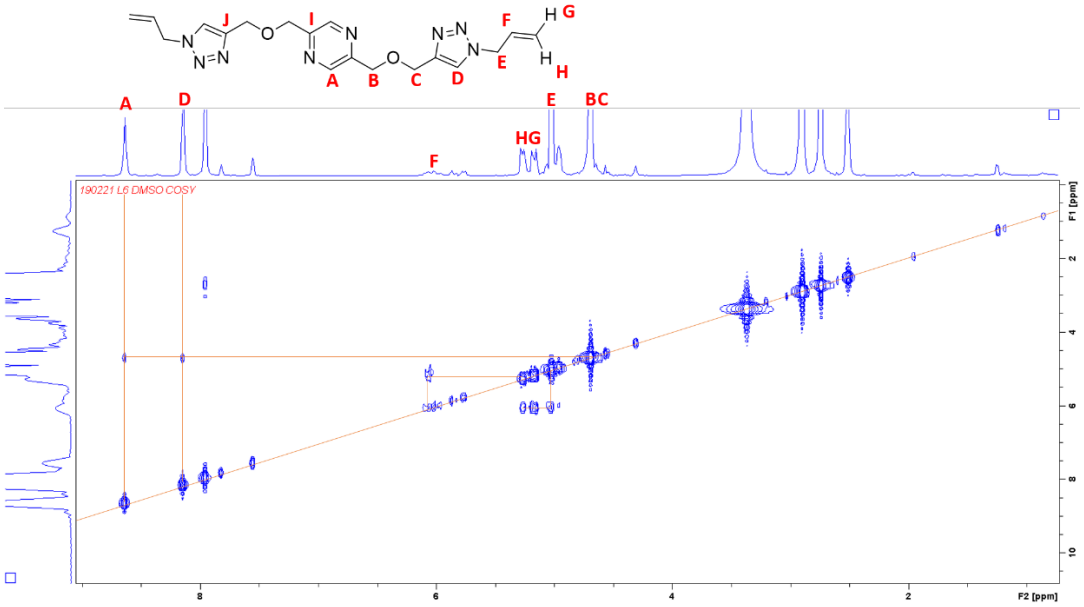

COSY of **L6**. Reference solvent peak (DMSO) at 39.97 ppm

A12.4.14 HMQC of (L6)

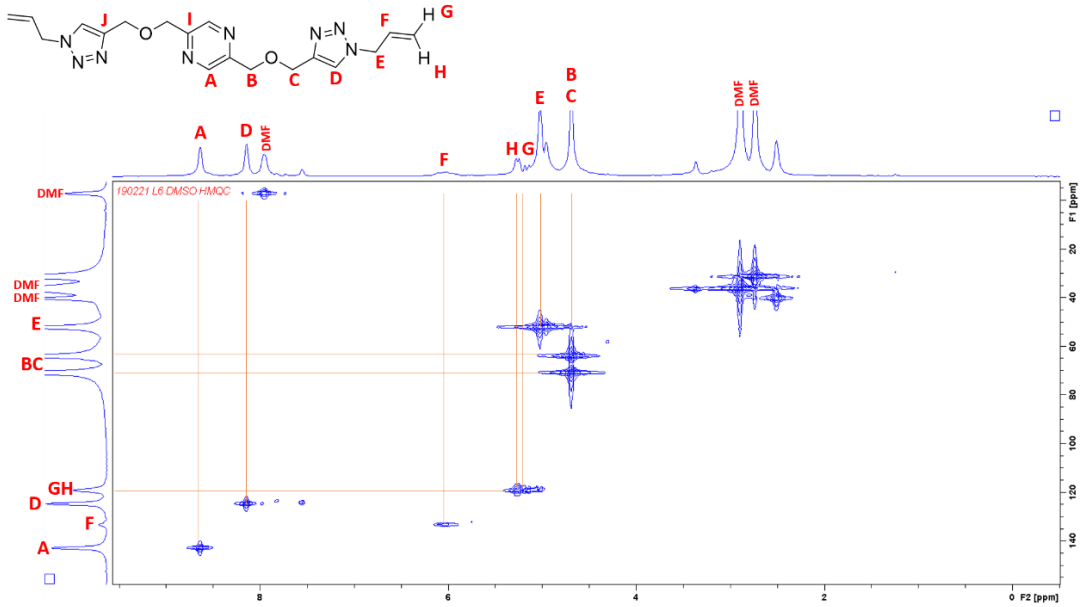

HMQC of **L6**. Reference solvent peak (DMSO)

A12.5.0 IR Spectra of (L5) Complexations

A12.5.0 Table of IR Spectra data of L5 Complexations

	L5	5A1	5B1	5C1	5D1	5F1	5A3	5B2	5C2	5E2	5F2
N-H	3430.81 br	3437.61 br	3422.88 br	3485.40 br	3408.83 br	br	3399.33 br	3464.39 br	3497.13 br	3510.27 br	3486.45 br
C-H Ar Stretch	3118.84 s		3155.68 w	3151.25 w	3160.47 m	3159.33 m	3103.83 m	3156.77 w	3160.18 m	3173.97 m	3167.97 m
N-H stretch	2955.45 s	2962.24 w	2962.76 m	2964.28 m	2965.06 m	2960.97 m	2962.78 m	2964.84 m	2964.54 m	2937.11 m	2963.67 m
	2931.07 s				2876.70 m						
	2872.06 s	2876.17 w		2876.66 w		2873.62 w	2878.37 w	2877.58 w	2877.00 w		2876.68 m
							2257.60 w				
C=C stretch	1669.37 w	1641.37 w			1641.15 w	1575.03 w	1611.41 m	1642.28 w	1576.63 w	1577.46 w	1576.63 w
C=C (Tz)	1484.80 w		1510.14 w	1511.69 w	1507.91 w	1506.86 w	1489.03 s	1508.83 w	1510.78 w	1521.78 w	1508.16 w
N=N (Tz)	1458.67 m	1467.19 w	1465.93 w	1465.63 w	1464.31 m	1465.45 m	1446.91 m	1468.25 m	1467.38 m	1467.65 m	1466.71 m
	1375.35 m	1363.18 w					1373.51 s	1360.96 w	1362.85 w		
C-N	1349.86 m	1302.38 w	1307.59 w	1303.64 w	1310.83 w	1308.56 m	1342.62 s	1306.91 m	1304.55 m	1307.79 m	1311.61 m
C-N aromatic	1255.46 w	1158.63 m		1238.66 w	1244.23 w	1240.35 w	1296.16 s	1246.60 w	1240.56 w	1243.50 w	1244.04 w
C-O	1218.73 m					1153.38 m	1245.66 w				
	1143.69 m						1158.16 w				
							1110.83 m			1154.44 m	1156.21 m
C-O-C ether stretch	1091.34 s	1090.82 s	1087.99 s	1087.38 s	1083.54 s	1091.52 s	1081.43 m	1064.64 s	1068.23 s	1072.13 s	1060.83 s
	1056.73 s	1063.36 s					1060.85 s			1050.84 s	
	1035.50 m										
	1027.66 m										
	991.22 m	950.62 w				989.13 m	1038.35 w				
	941.85 w										
C-O-C Sym stretch	870.35 w		846.80 w	834.12 w	898.18 w	836.93 w	854.36 w	892.13 w	886.87 w	890.13 w	900.03 w
C-H	802.73 w	816.26 w			833.46 w		814.46 w	845.63 w	837.84 w	837.20 w	842.54 w
	776.12	779.04 w					773.20 w		769.53 w	768.23 w	765.56 w

A12.5.01 (L5) IR Spectra

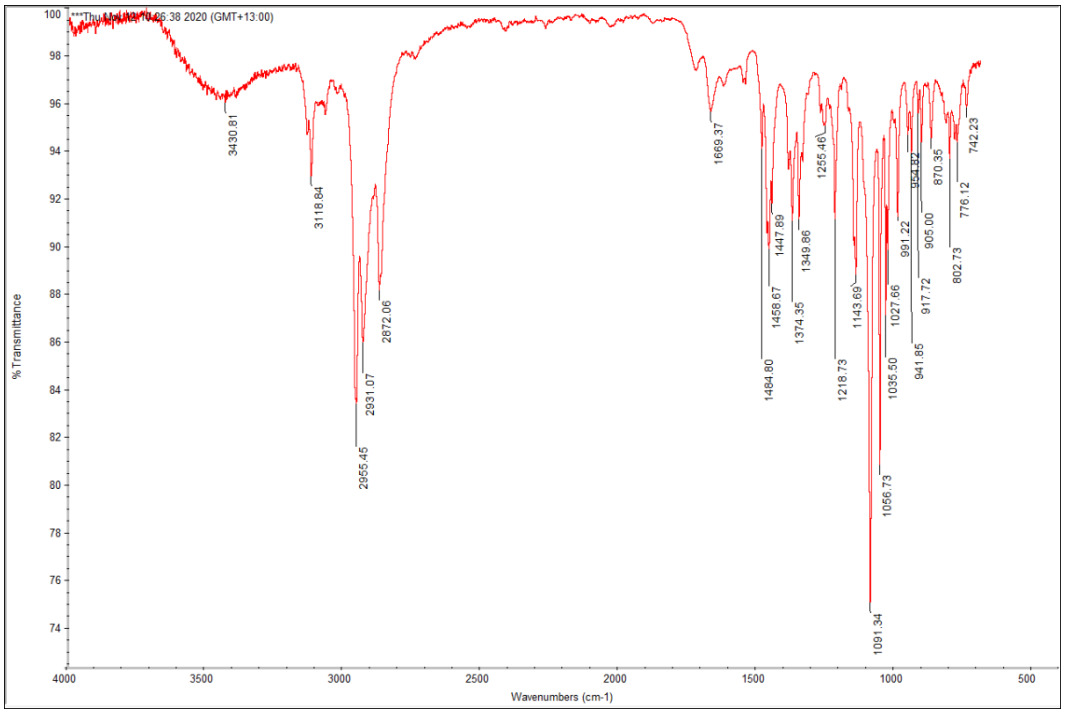

The IR spectra of (**L5**)

A12.5.10 (L6) IR Spectra

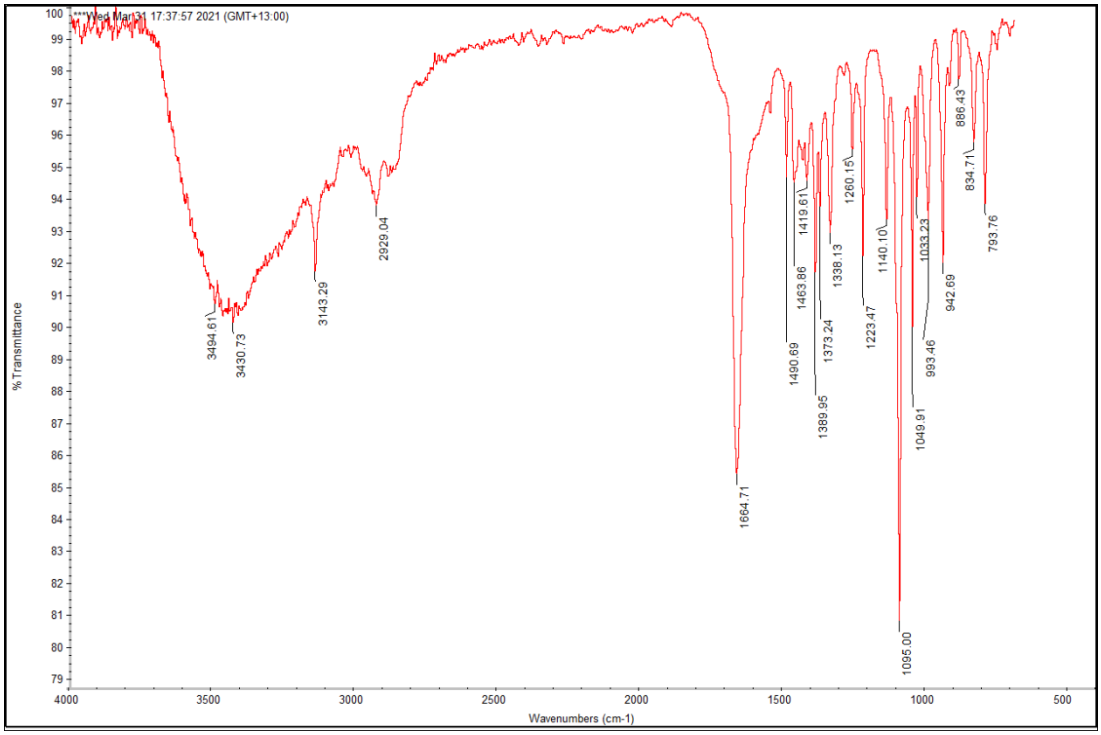

A12.5.02 (5A1) IR Spectra

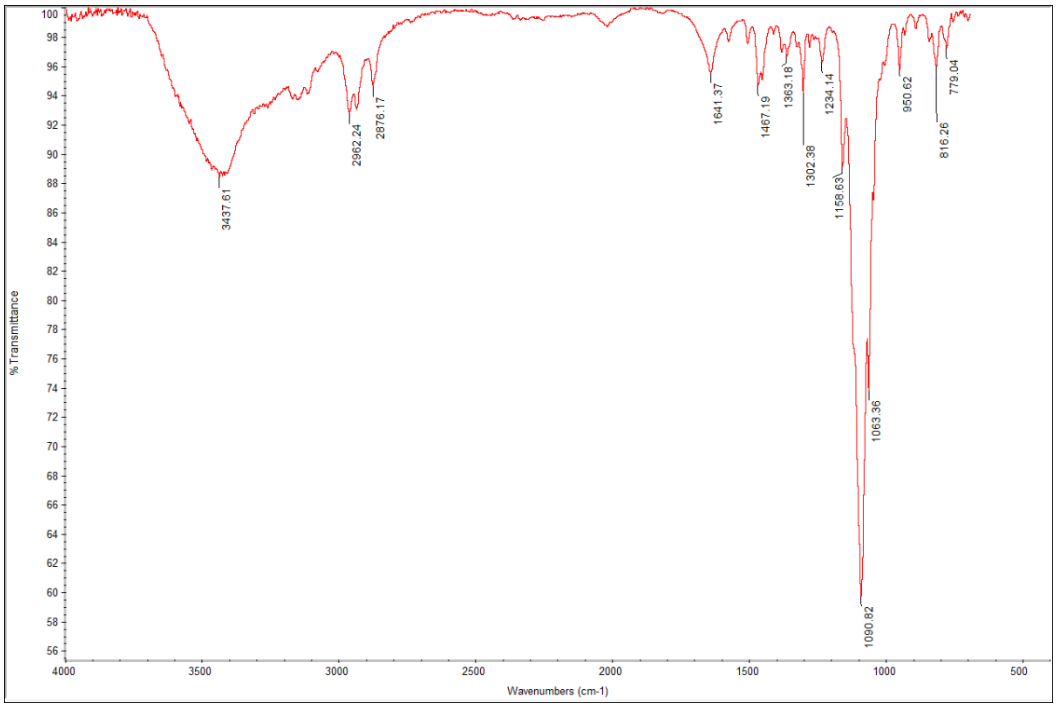

The IR spectra of (**5A1**)

A12.5.03 (5B1) IR Spectra

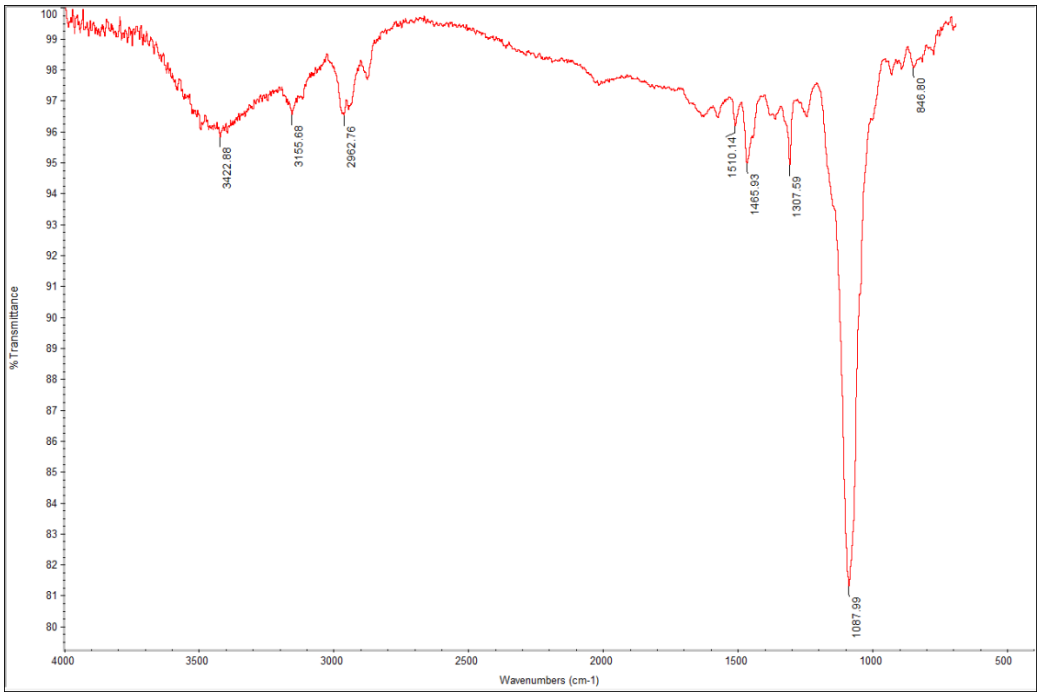

The IR spectra of (**5B1**)

A12.5.03 (5C1) IR Spectra

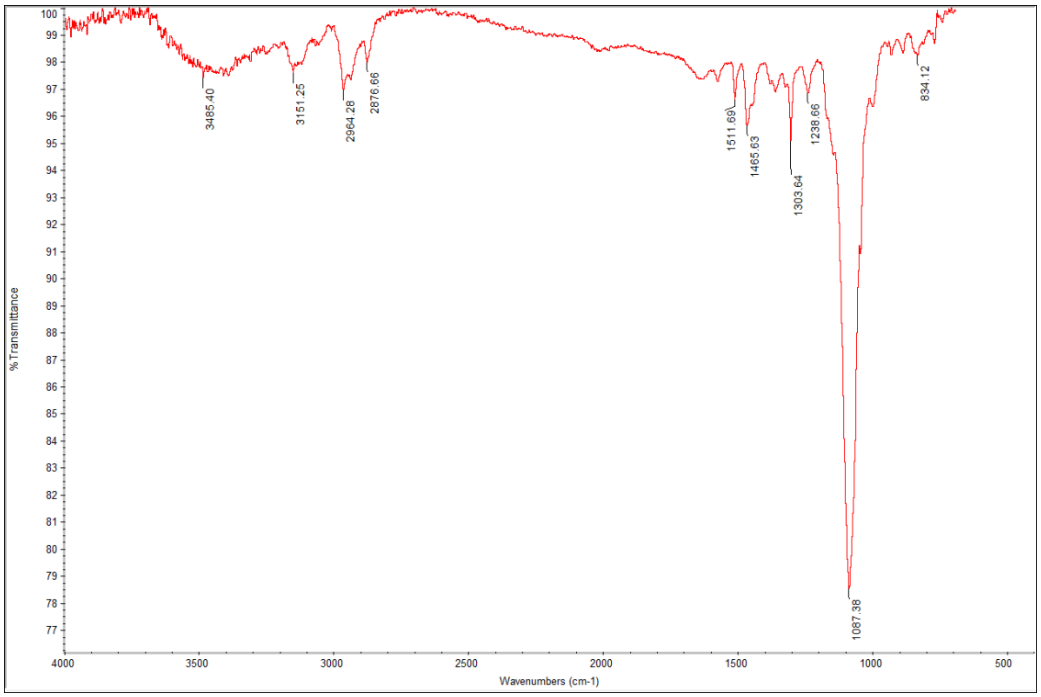

The IR spectra of (**5C1**)

A12.5.04 (5D1) IR Spectra

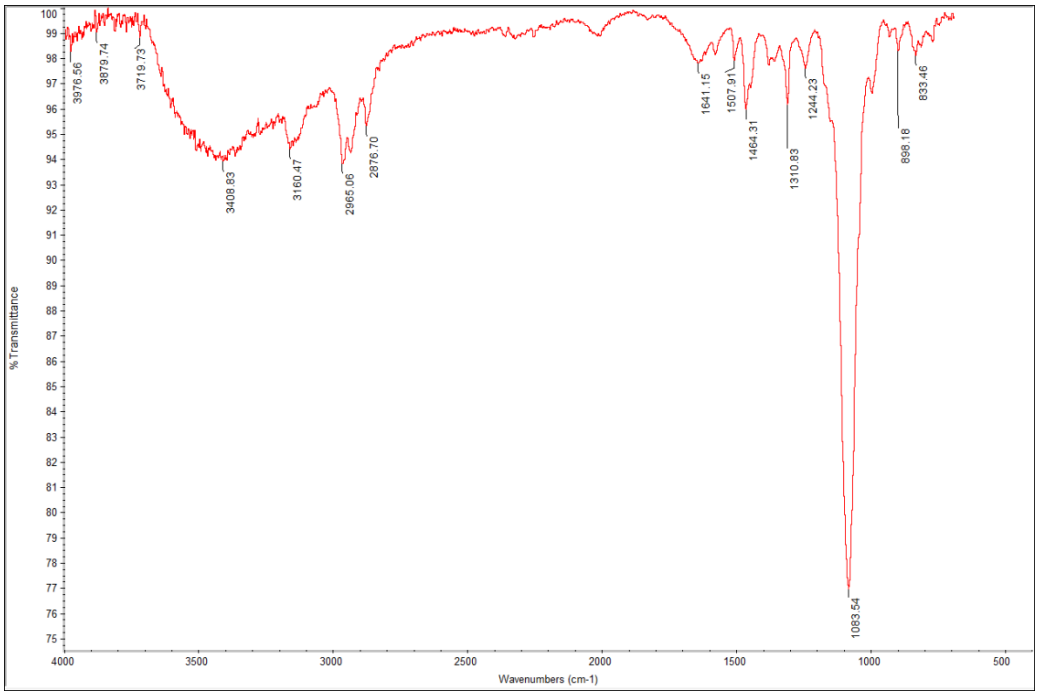

The IR spectra of (**5D1**)

A12.5.05 (5F1) IR Spectra

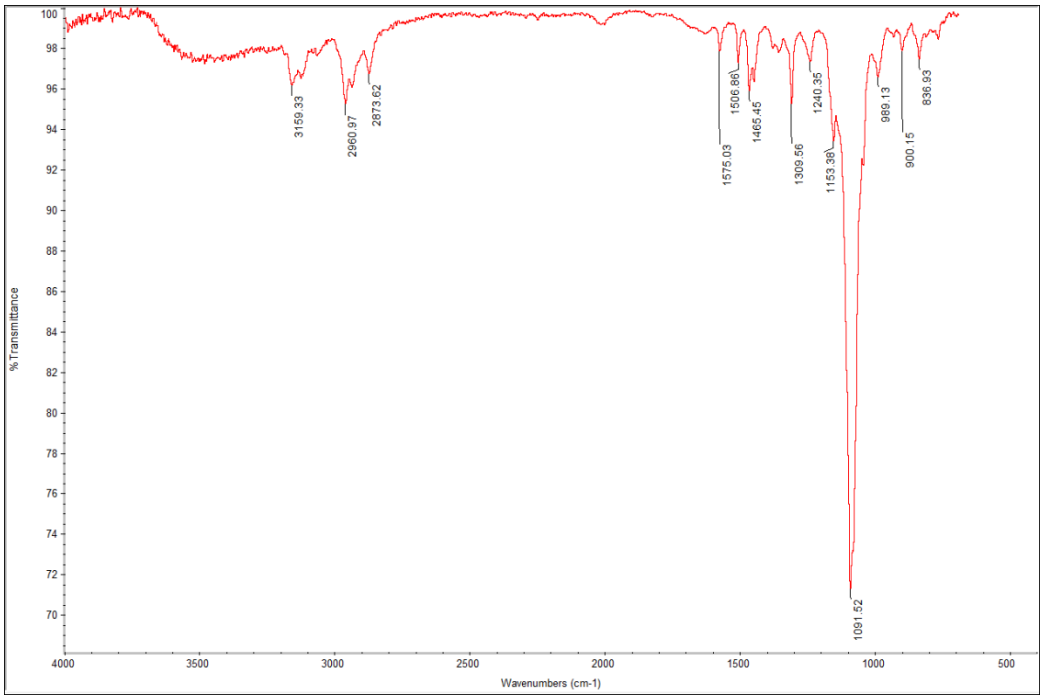

The IR spectra of (**5F1**)

A12.5.06 (5A3) IR Spectra

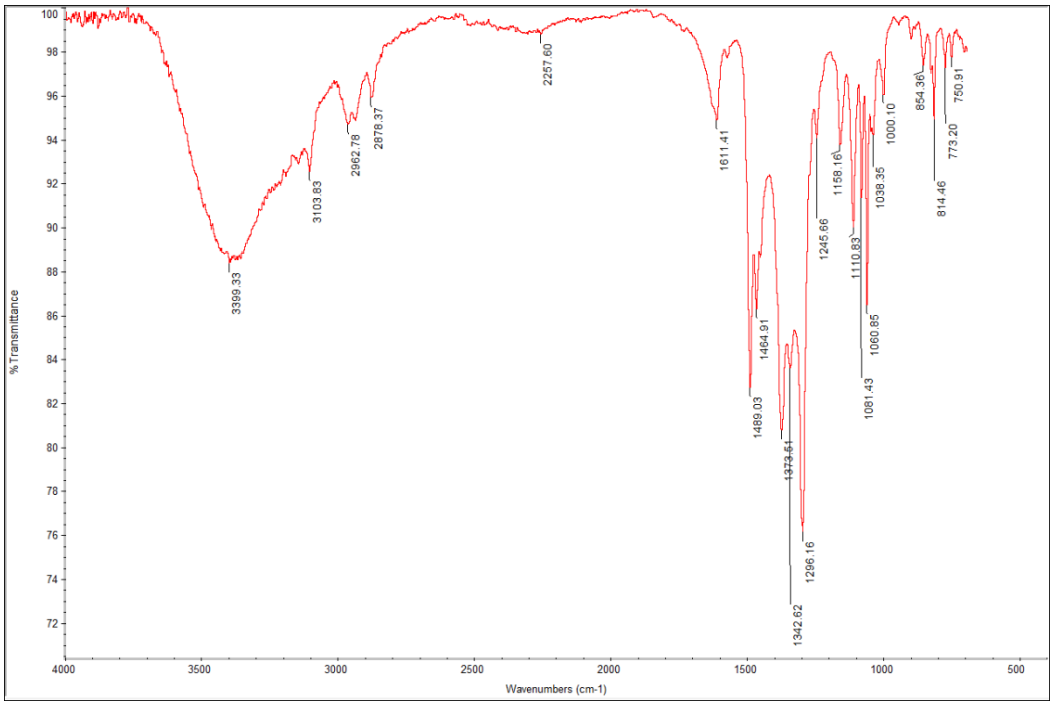

The IR spectra of (**5A3**)

A12.5.07 (5B2) IR Spectra

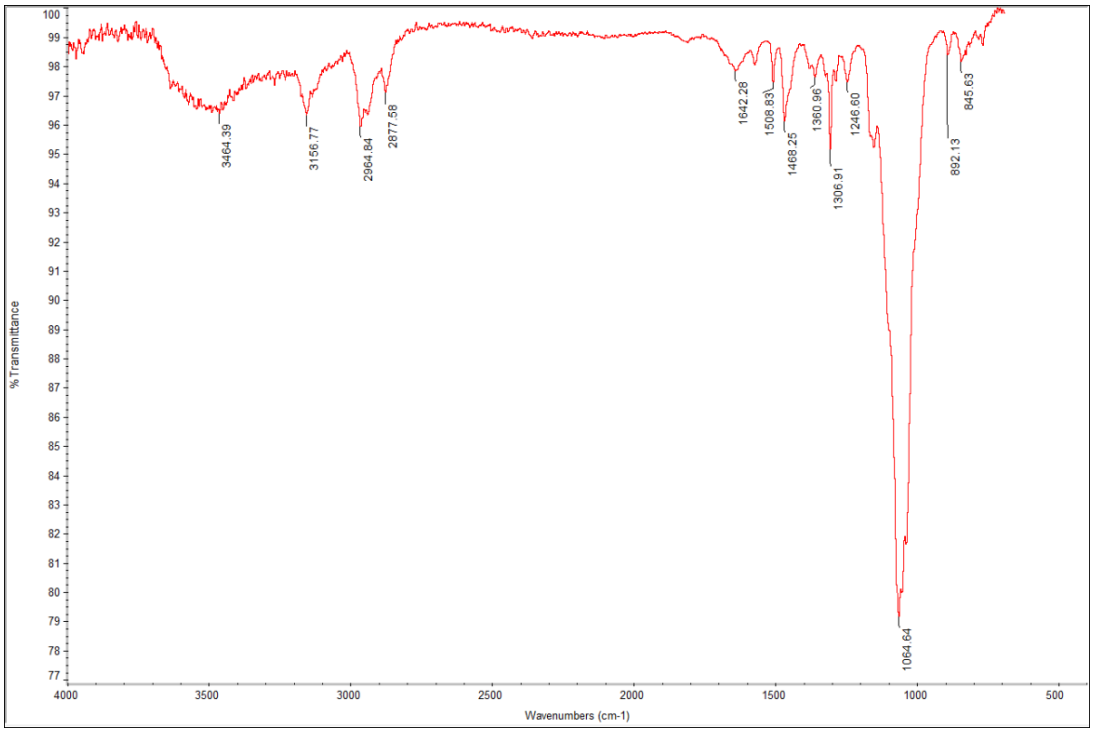

The IR spectra of (**5B2**)

A12.5.08 (5C3) IR Spectra

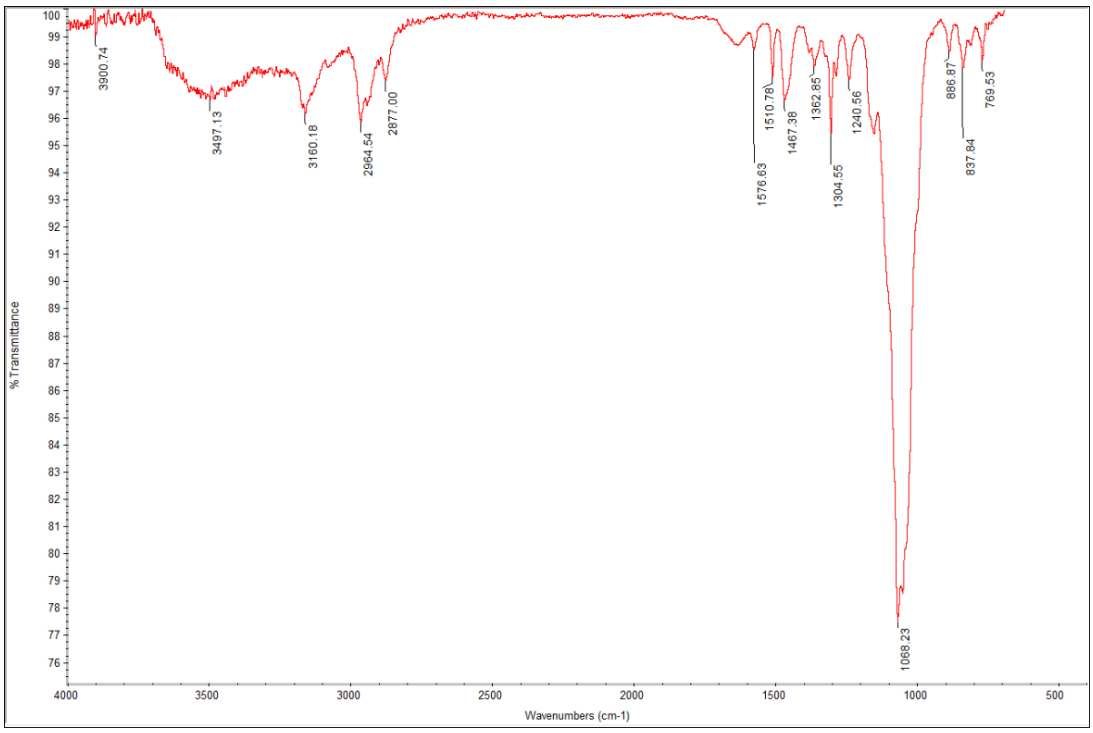

The IR spectra of (**5C3**)

A12.5.09 (5E2) IR Spectra

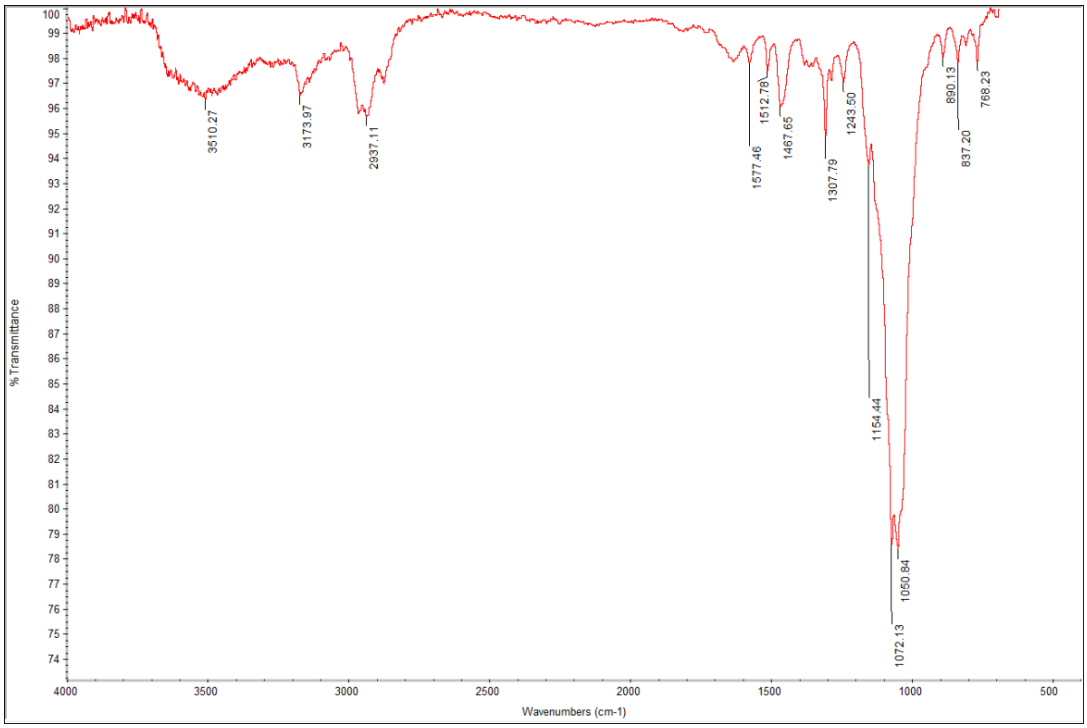

The IR spectra of (**5E2**)

A12.5.10 (5F2) IR Spectra

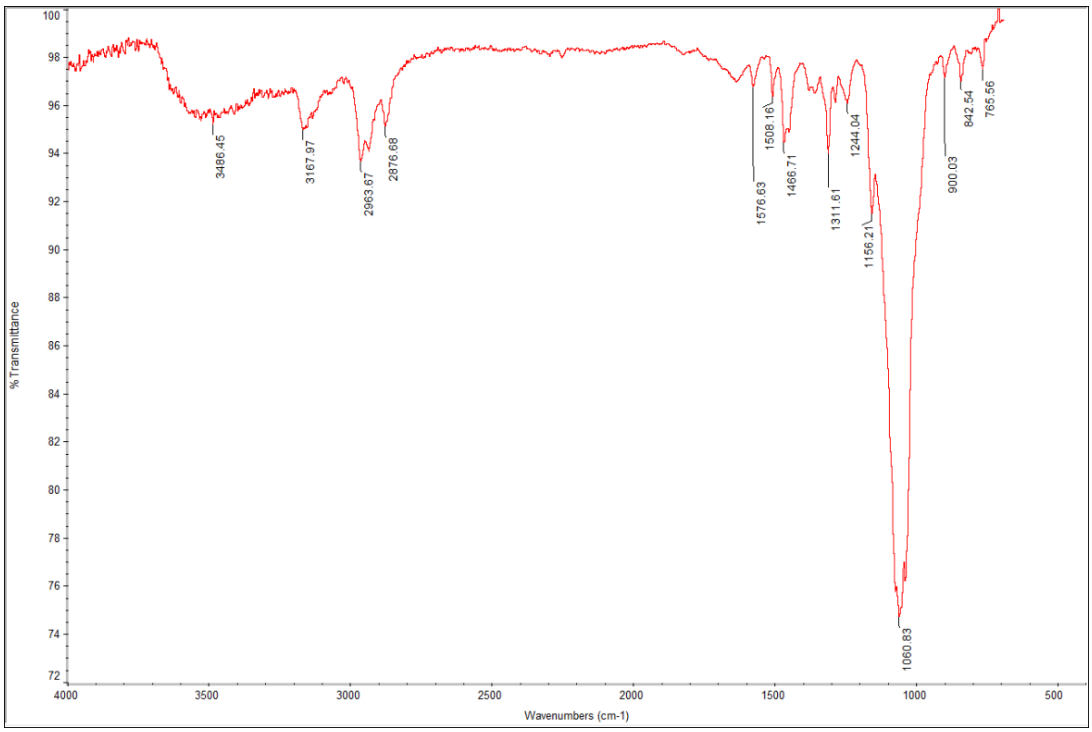

The IR spectra of (**5F2**)

List of molecule codes.

A1	2,5-dimethylpyrazine
A2	2,5-bis((E)-styryl)pyrazine
B1	2,5-bis(formyl)pyrazine
B2	2-(pyridin-2-yl)ethanamine
B3	2-(aminomethyl)phenol
B4	2-aminophenol
C1	2,5-dimethylpyrazine 1,4-dioxide
C2	2,5-bis(acetoxymethyl)pyrazine
C3	2,5-bis(hydroxymethyl)pyrazine
C4	2,5-bis(chloromethyl)pyrazine
C4a	2-chloromethyl-5-methyl pyrazine
C5	2,2'-(pyrazine-2,5-diylbis(methylene))bis(isoindoline-1,3-dione)
C6	2,5-bis(aminomethyl)pyrazine
HMTA	Hexamethyl tetraamine
C7	2,5-bis(HMTA-methyl)pyrazine
C8	pyrazine-2,5-diylbis(methylene) bis(4-methylbenzenesulfonate)
D1	2,5-bis(azidomethyl)pyrazine
D2	Phenylacetylene
D3	2-((prop-2-yn-1-yloxy)methyl)pyridine
D4	2-hydroxymethyl pyridine
D5	Propargyl bromine
E1	2,5-bis((prop-2-yn-1-yloxy)methyl)pyrazine
E2	1-azidobutane
E3	3-azido prop-1-ene
E4	1-bromobutane
E5	3-bromo prop-1ene
$L1^{endo}$	(*N*,*N'E*,*N*,*N'E*)-*N*,*N'*-(pyrazine-2,5-diylbis(methanylylidene))bis(2-(pyridin-2-yl)ethanamine)
$L1^{exo}$	(*NE*,*N'E*)-1,1'-(pyrazine-2,5-diyl)bis(N-(2-(pyridin-2-yl)ethylidene)methanamine)
L1b	*N*2,*N*5-bis(2-(pyridin-2-yl)ethyl)pyrazine-2,5-dicarboxamide
L2	2,2'-(((1*E*,1'*E*)-(pyrazine-2,5-diylbis(methanylylidene))bis(azanylylidene))bis(methylene))diphenol
L2b	2,2'-((1*E*,1'*E*)-(pyrazine-2,5-diylbis(methanylylidene))bis(azanylylidene))diphenol
L3	2,5-bis((4-phenyl-1H-1,2,3-triazol-1-yl)methyl)pyrazine
L4	2,5-bis((4-((pyridin-2-ylmethoxy)methyl)-1H-1,2,3-triazol-1-yl)methyl)pyrazine
L5	2,5-bis((2-(1-butyl-1H-1,2,3-triazol-4-yl)ethoxy)methyl)pyrazine
L6	2,5-bis((2-(1-allyl-1H-1,2,3-triazol-4-yl)ethoxy)methyl)pyrazine

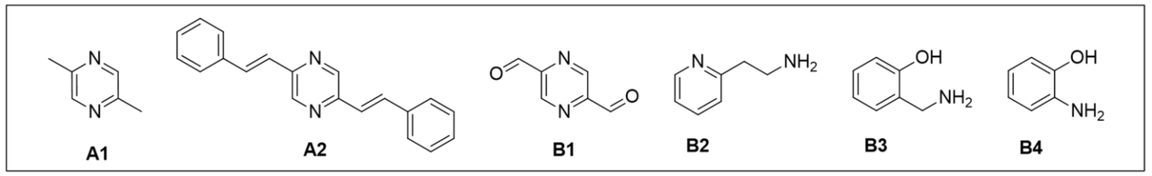
A1

A2

B1

B2

B3

B4

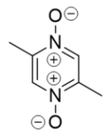
C1

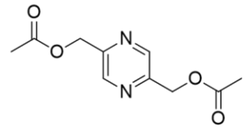
C2

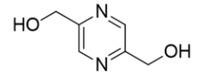
C3

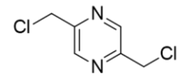
C4

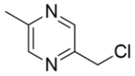
C4b

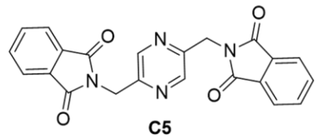
C5

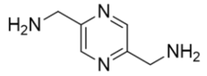
C6

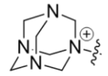
HMTA

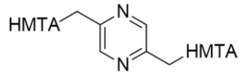
C7

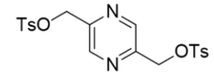
C8

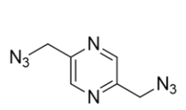
D1

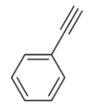
D2

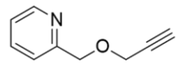
D3

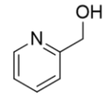
D4

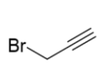
D5

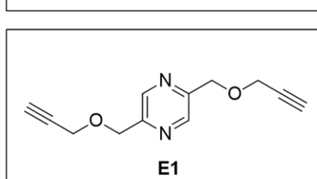
E1

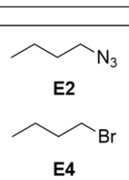
E2

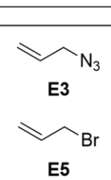
E3

E4

E5

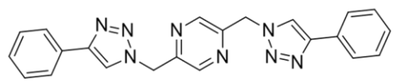
L3

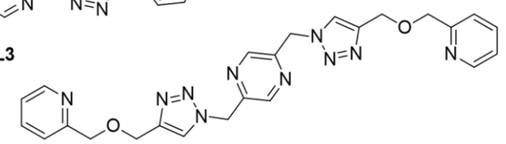
L4

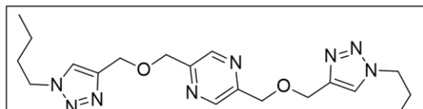
L5

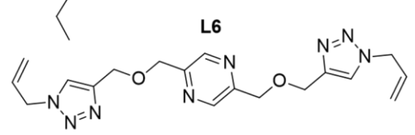
L6

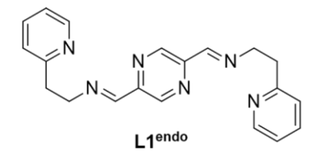
L1endo

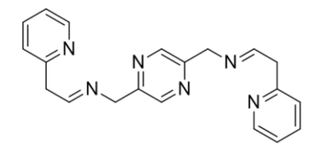
L1exo

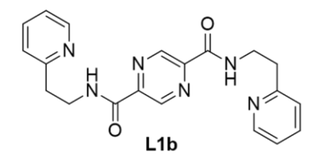
L1b

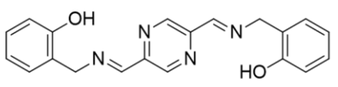
L2

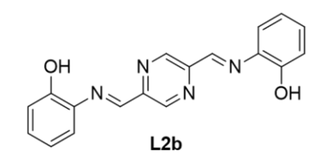
L2b